SOURCE AND PROPAGATION EFFECTS OF RAYLEIGH WAVES FROM CENTRAL ASIAN EARTHQUAKES

by

Howard John Patton

A. B., Franklin and Marshall College

(1971)

SUBMITTED IN PARTIAL FULFILLMENT
OF THE REQUIREMENTS FOR THE
DEGREE OF

DOCTOR OF PHILOSOPHY

at the

MASSACHUSETTS INSTITUTE OF TECHNOLOGY

(April 1978)

Signature of Author.....

Department of Earth and Planetary Sciences, April 28, 1978

Certified by.....

Thesis Supervisor

Accepted by.....

Chairman, Department (or Interdepartmental) Committee

SOURCE AND PROPAGATION EFFECTS OF RAYLEIGH WAVES FROM CENTRAL ASIAN EARTHQUAKES

by

HOWARD JOHN PATTON

Submitted to
the Department of Earth and Planetary Sciences
on April 28, 1978
in partial fulfillment of the requirements for the
degree of Doctor of Philosophy

ABSTRACT

A reference point equalization method has been developed which enables the separation of source and propagation effects of surface waves. The method works on seismic events located in a small source region, which allows us to assume that all events share the same path effects to a given receiver. Two important steps in the method are initialization and iteration. Initialization obtains the first "reference events" in order to compute initial estimates of phase velocity and attenuation coefficient. Iteration simultaneously refines the propagation parameters and determines the source parameters of new earthquakes in the vicinity of the reference point. This method was applied to earthquakes in the Pamir mountains, Central Asia (reference point: 39.58N, 73.55E).

In the initialization step, the method of Weidner and Aki (1973) was applied to obtain focal depths and revise fault plane parameters of the first two earthquakes. The residuals obtained from fitting the observed amplitude ratios and phase differences indicate that the crust and upper mantle in Central Asia is more laterally heterogeneous than near the ocean rifts, the site of Weidner and Aki's experiment. We computed heterogenity quotients of .46 vs .80 x 10^{-4}Napier^2/km and .93 vs 2.4 x 10-^{4}radian^2/km for ocean versus continent as a measure of the increasing scatter in amplitude and phase of 20-60sec Rayleigh waves due to lateral heterogeneities.

To determine source parameters in the iteration, we applied the linear moment tensor inversion on Rayleigh wave complex source spectra. The presence of random additive errors in the

complex spectra does not pose difficulties for recovering reliable source parameters using the linear inversion method. However, amplitude magnification errors in the complex spectra will lead to over-estimation of the moment tensor elements and phase incoherency will lead to under-estimation. In applying this method to our dataset, it was necessary to modify the straight least squares inversion method because of its sensitivity to even a few bad data points.

The residuals obtained from the repeated application of the moment tensor inversion over trial focal depth showed two minima: one minima at depths less than 20km and the other at depths greater than 70km. The values of the residuals at these minima were close enough to cast doubt on the determination of focal depth. One way to resolve this ambiguity is to compare the geometry of the moment tensor obtained for shallow and deep focus inversions with observed P-wave polarities.

The focal depths of eight out of the nine events in our dataset were found to be shallow, between 5-15km. Their principal compressive stress axes are aligned north-south and nearly horizontal, consistent with the interpretation of plate tectonics in Central Asia. The moment tensor inversion generally gives three-couple force systems having significant non-zero intermediate component. However, in light of errors in our data and the similarities of the double couple models to the three-couple models, it can not be established convincingly that these results are caused by departures of source from the double couple model.

We interpret the propagation parameters in terms of lateral variation of phase velocity and Q on the Eurasian continent. A phase velocity regionalization is proposed involving five continental provinces: Indian Shield, Northern Platforms, Coastal Plains, Tectonic and Plateau. Phase velocities on the Indian Shield are 20% higher than velocities on the Plateau province at 26sec period and 5% higher at 90sec period. Stable provinces in Eurasia are found to have significantly higher phase velocity than tectonic provinces out to 150sec period.

Interpretations of the phase velocities on the Indian Shield show a lithosphere thickness of about 120km, considerably thicker than the lithosphere under the Northern Platforms ($\sim$75km). The lowest shear velocity in the upper mantle is found under the Tectonic province with a value about 4.3km/sec over depths between 83-240km. The crustal thickness of the Plateau province is as great as 70km provided that shear velocity in the lower half of the crust is about 3.8km/sec. The upper mantle structure under this province is very similar to James' (1971) for the Andes mountains region.

Surface wave amplitudes on the Eurasian continent are strongly affected by horizontal refraction as well as intrinsic Q of the medium. Average Rayleigh wave Q has very different character on paths over northern platforms and tectonic provinces east and west of the reference point. Under platforms Q is found to increase with depth from a Q between 200-300 in the crust to

300-500 in the lid and asthenosphere. West of the reference point Q is low ($\sim$60) in the bottom 20km of the crust and extending $\sim$35km into the mantle. East of the reference point Q appears to be $\sim$60 in a layer 35km thick at the base of the crust. Deeper in the mantle Q increases suggesting that the low Q zone is concentrated at shallow depths in the upper mantle under the tectonic provinces of Asia.

Thesis Supervisor: Keiiti Aki
Title: Professor of Geophysics

ACKNOWLEDGEMENTS

First and foremost, I would like to thank my advisor, Keiiti Aki, for his patience, encouragement, and for the guidance he offered through the completion of this thesis. I feel quite fortunate to have been a student of Professor Aki who has a great breadth of knowledge of seismology and keen instincts about research.

Secondly, I am grateful to the people of Group 22, Lincoln Laboratory, specifically Drs. Michael Chinnery and Richard Lacoss, for permitting me to use their facilities. Among those at Group 22, I extend special thanks to: Dr. Robert North for helpful discussions about surface wave propagation in Eurasia and for the use of his digitized Moho contours shown in Figure 5-2.1, to Dr. Douglas McCowan for helpful discussions about the moment tensor representation of the seismic source, to Mr. Michael Shields for assisting me in the literature search, and to the technical staff for coming to the rescue at various times when the PDP-7's were misbehaving.

Among my graduate student colleagues, I extend special thanks to: Tony Shakal, Jim Scheimer, and Mai Yang for many stimulating discussions which enriched my experience at MIT in ways that are not mentioned in the graduate student catalogue, to Dr. Barnard Chouet for critically reading several chapters of this thesis, and to Ken Anderson for discussions on robust estimation.

Finally, to my wife, Mary, who not only kept my spirits up but also drew most of the figures and typed the thesis, I cannot find words to adequately convey my thanks.

I am grateful to the National Science Foundation for supporting this research under the grants 73-00425EAR and 77-13632EAR and to the Air Force grant AFSOR F44620-75-C-0064.

TABLE OF CONTENTS

CHAPTER I

INTRODUCTION

Only recently have we realized the significance of the continental collision between the Eurasian and Indian plates in the interpretation of the structure and tectonics of Asia. The formation of orogenic belts (Dewey and Bird, 1970), the seismicity, stress field, faulting (Molnar et al., 1973; Molnar and Tapponnier, 1975) and the mechanical and thermal evolution of structures in southern Asia (Bird, 1976) are all seen as consequences of the closing of the Tethys Sea and subsequent collision of the continents. Among the implications of the continental convergence, Molnar and Tapponnier cite that 1500km of crustal shortening must have occurred by deformation solely in the continental lithosphere. This deformation is believed to have occurred over a broad zone extending as far as 3000km northeast of the Himalayan mountains. Some old features on the continent, such as the Ural mountains, are believed to have been sites of convergence of proto-lithospheric plates (Hamilton, 1970). The description of Eurasia as "a composite continent" (Kropotkin, 1971) is appropriate in light of its tectonic history.

In this paper, we investigate the source and propagation effects of surface waves from earthquakes in Central Asia. In doing so, we learned more about the structure of the crust and upper mantle of the Eurasian continent.

We present the analysis methods applied in this study in

Chapter 2. A reference point equalization method is developed, which isolates the source effects from amplitude and phase spectra of surface waves. We discuss the advantages of the joint use of amplitude and phase spectra and the extension of the linear moment tensor inversion (Gilbert, 1970) to surface wave complex source spectra. Finally, we address the problem of estimating source and propagation parameters from seismograms contaminated by noises.

The surface wave dataset and auxiliary data collected for this study is presented in Chapter 3. It is important to test the performance of our analysis methods before applying them to our dataset. We do so for the moment tensor inversion method through a series of numerical experiments using synthetic data. We evaluate the effects of both random errors and systematic errors on the results of the inversion.

The application of the analysis methods to our data is described in Chapter 4. We present this in three parts: results from the initialization, results from the iteration, and the final estimates of propagation parameters. In the iteration part, we successfully apply the linear moment tensor inversion to Rayleigh wave complex source spectra. The results of the analysis are given in detail.

In Chapter 5, we interpret the source and propagation data in terms of the tectonics and structure of the Eurasian continent. A phase velocity regionalization is carried out involving five continental provinces. We obtain estimates of Rayleigh

wave Q for stable platform and two tectonic areas. The results of our interpretation are layered structural models of medium velocity and Q.

CHAPTER II

METHOD OF ANALYSIS

The information obtained from the study of surface waves has contributed heavily to our understanding of the nature of the solid earth and the seismic source. The use of surface waves for this purpose is well established by the numerous advances in theory and methods of analysis. A major step in the analysis is the separation of source and propagation effects since both can drastically alter the character of the surface wave. In Sections 2-1 and 2-2 we describe a new method to separate these effects from the amplitude and phase spectrum of surface waves.

Theoretical studies show that the amplitude and phase of surface waves supply complementary information about the seismic source. For example, the amplitude can be used to determine the orientation of the fault planes but not the direction of fault slip motion. Phase can resolve this ambiguity. In Section 2-3, we discuss the advantages of analyzing both of these data particularly in the case of small earthquakes which rarely have reliable fault plane solutions.

A deficiency in the practical aspect of using surface waves to study the source is the great expense of trial and error search procedures for obtaining the slip angle, dip angle, and the strike of the fault planes. An advantage of the seismic moment tensor formalism obtained for free oscillations by Gilbert (1970) is that the tensor elements are linearly related to ob-

servable quantities on the seismogram. The recovery of the seismic moment tensor, as demonstrated by Dziewonski and Gilbert (1974), is very simple and fast via linear inversion methods. In Section 2-4 we describe the extension of the linear relationship to surface waves and present a method to invert the observations of complex spectra.

An assumption underlying methods of analysis concerns the noise on the seismogram. For example, the linear inversion described in Section 2-4 is amenable to the estimation of the moment tensor elements when additive noise, such as the background recording noise, is the primary contaminant on the seismogram. The statistical properties of noise vary depending on the noise source. Section 2-5 addresses the problem of estimating source and propagation parameters in the presence of two important types of noise occurring on the seismogram.

1. REFERENCE POINT...SEPARATION OF SOURCE AND PATH

Our method requires seismic events in a small area with a lateral dimension, D, much smaller than the epicentral distance and comparable to or less than the shortest analyzed wavelength. This requirement allows us to safely assume that all events in the source region share the same wavepath to a given receiver except for small differences in the path length in the source region. These differences will be corrected for by introducing a reference point as shown schematically in Figure 2-1.1.

The reference point is defined as the point with coordinates

equal to the mean of coordinates of all the events. Then the distance, $\bar{X}_i$, from the reference point to the i^{th} receiver can be written as

$$\bar{X}_i = \frac{1}{N} \sum_{j=1}^{N} X_{ji} \qquad (2\text{-}1.1)$$

where X_{ji} is the epicentral distance between the j^{th} event and the i^{th} station, and N is the number of events in the source region. The effect of the correction will be to equalize the Fourier transform of the surface wave record to $\bar{X}_i$. Specifically, we compute the Fourier transform of a record, $f_{ji}(t)$, over a time interval t_1 to t_2, as follows:

$$A^o_{jik} e^{-i\phi^o_{jik}} \equiv A^o_{ji}(\omega_k) e^{-i\phi^o_{ji}(\omega_k)} = \int_{t_1}^{t_2} f_{ji}(t) e^{-i\omega_k t} dt \qquad (2\text{-}1.2)$$

where k refers to frequency ω_k, A^o_{jik} is the amplitude spectral density, and ϕ^o_{jik} is phase delay in cycles. The observed amplitude and phase spectra are equalized to the reference point as follows:

$$A^E_{jik} \simeq A^o_{jik}$$

and

$$\phi^E_{jik} = \phi^o_{jik} + \frac{\omega_k (\bar{X}_i - X_{ji})}{C(\omega_k)} \qquad (2\text{-}1.3)$$

where the superscript E indicates the equalized quantity. Since path differences are small, the effects of attenuation are ignored. Phase equalization is made using a phase velocity curve, $C(\omega_k)$, appropriate for the source region.

After correction for instrumental response is removed, the equalized quantities A^E_{jik} and ϕ^E_{jik} are separated into source and medium effects:

$$A^E_{jik} = H_i(\omega_k)S_{ji}(\omega_k) = H_i S_{jik}$$

and

$$\phi^E_{jik} + \omega_k T_{ji} = \phi_i(\omega_k) + \phi^F_{ji}(\omega_k) \pm n = \phi_{ik} + \phi^F_{jik} \pm n \qquad (2\text{-}1.4)$$

where S_{jik} is the source amplitude factor and ϕ^F_{jik} is the source or focal phase delay. This is the phase of the Rayleigh wave at the origin time and epicenter of the earthquake and is sometimes referred to as the first motion of the Rayleigh wave (e.g. Weidner, 1972). H_{ik} is the path amplitude transfer function which corrects for anelastic attenuation and ϕ_{ik} is the propagation phase delay. T_{ji} refers to the time interval between the origin time of the j^{th} earthquake and the start of the digitization window, t_1, on the i^{th} record. The integer, n, represents the order number (Brune et al., 1960).

Earthquakes in the source region with known source parameters (i.e., fault plane geometry, depth, seismic moment) shall be called reference events. For reference events, we can calculate

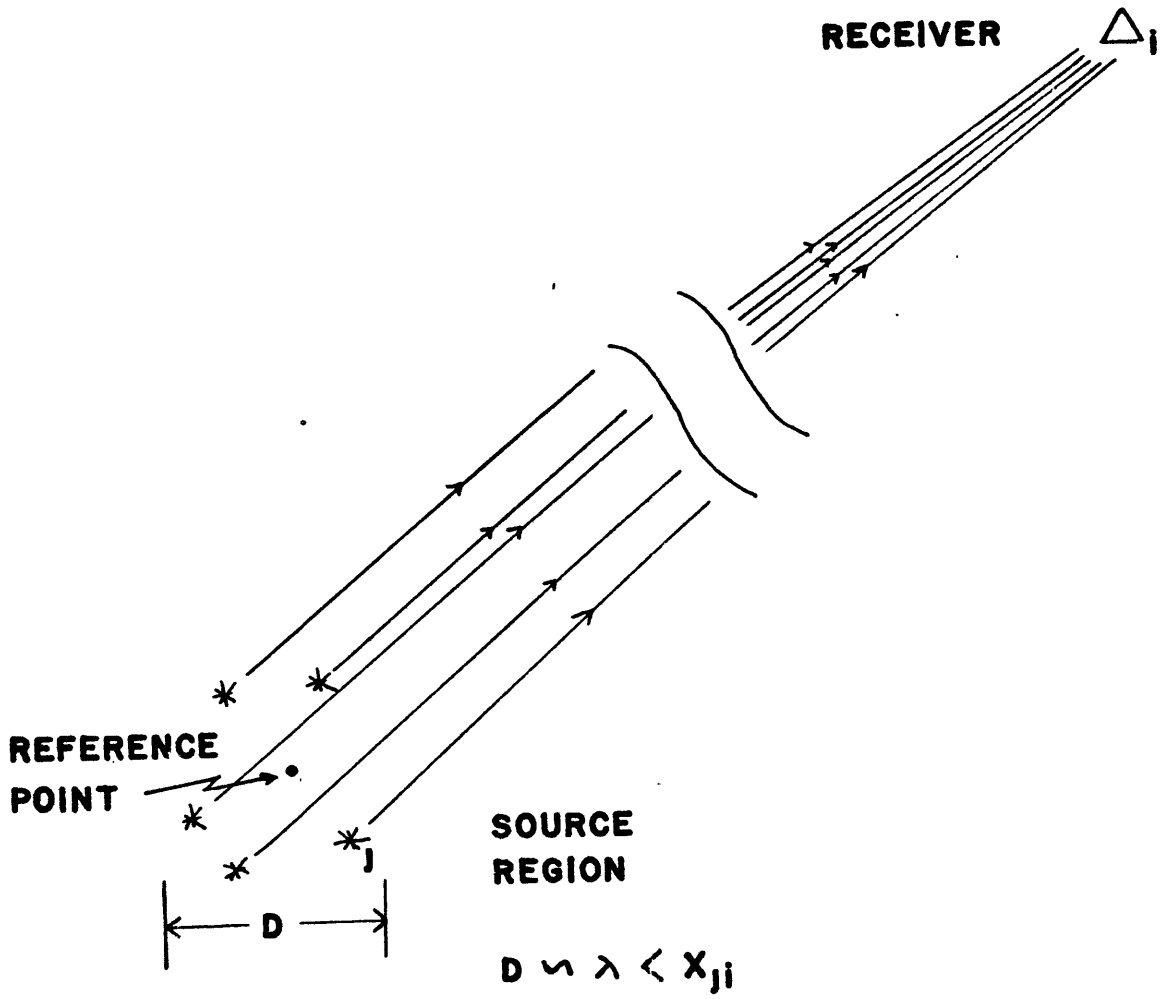

Fig. 2-1.1: Schematic of the source region having lateral dimension D; λ is the shortest analyzed wavelength and X_{ji} is the epicentral distance between the j^{th} earthquake and the i^{th} receiver.

S_{jik} and ϕ^F_{jik} using the theory of surface wave excitation (e.g. Saito, 1967). Thus, if there are M reference events, we obtain by Equation 2-1.4 above, M equations at each frequency which relate source parameters with the observed spectra at the i^{th} station through a common "earth filter" parameterized by H_{ik} and ϕ_{ik}. The errors in the observations and assumptions in our model will require a statistical method to estimate these filter parameters. Let us call $\hat{H}_{ik}$ and $\hat{\phi}_{ik}$ the estimates of the filter parameters determined by an appropriate statistical method.

If a new earthquake, say the 1^{th}, does not have known source parameters, the estimates, $\hat{H}_{ik}$ and $\hat{\phi}_{ik}$, will be used to isolate its source spectra by the following equation:

$$A^s_{lik} e^{-i\phi^s_{lik}} = A^E_{lik} e^{-i(\phi^E_{lik}+\omega_k T_{li})} / \hat{H}_{ik} e^{-i\hat{\phi}_{ik}} \qquad (2\text{-}1.5)$$

where A^s_{lik} is identified as the source amplitude factor and ϕ^s_{lik} as the focal phase delay of the 1^{th} earthquake. Source spectra obtained in this manner are used to recover the source parameters of this new earthquake.

2. INITIALIZATION AND ITERATION

The reference point equalization introduced in the previous section allows the separation of path and source effects for earthquakes in the source region, provided that reference events are available to compute the propagation parameters. The initial

estimates of H_{ik} and ϕ_{ik} are obtained from a method that does not require reference events or are based on apriori knowledge of the propagation effects. Further refinement of the estimates of H_{ik} and ϕ_{ik} are made as new events are supplied from the region of the current reference point. The purpose of this section is to describe our computation scheme, shown in Figure 2-2.1, and a method to initialize it.

The initialization makes use of an independent surface wave method, of which there are several available to us. The method of Weidner and Aki (1973) offers the most advantages in this particular application for reasons that become evident upon reviewing it.

Initialization via Weidner and Aki. The method of Weidner and Aki requires two earthquakes located close together and having different focal mechanisms. Forming spectral ratios between earthquakes at a given receiver will cancel the propagation effects but not the source effects if the two earthquakes have different focal mechanisms. Under these conditions the ratios can be used to revise their source parameters.

The source parameters of both earthquakes are revised to minimize the residuals between the observed log amplitude ratio, $\ln(A^o_{1ik}/A^o_{2ik})$, and the calculated, as well as between the observed differential phase, $\Delta\phi_{1-2,ik}$:

$$\Delta\phi^o_{1-2,ik} = \phi^o_{1ik} - \phi^o_{2ik} + \omega_k(T_{1i}-T_{2i}-\frac{(X_{1i}-X_{2i})}{C(\omega_k)} \qquad (2\text{-}2.1)$$

and its calculated counterpart. The residuals are simply a weighted sum of squared differences with the weights chosen to minimize the contribution from stations near the nodal directions. A systematic search through an 8-dimensional parameter space (2 depths, 2 slips, 2 dips, and 2 strikes) is carried out to find source parameters that minimize the residuals.

By virtue of the cancelation of propagation effects, apriori knowledge of H_{ik} and ϕ_{ik} is not required. The source region structure must be known though errors in the phase velocity curve, $C(\omega)$, due to poor knowledge of this structure will not significantly affect the calculation of $\Delta\phi^{o}$, because of the small distances between events.

The source parameters that minimized the residuals are used to calculate initial estimates of H_{ik} and ϕ_{ik}.

Iterative Process. As shown in the flow chart in Figure 2-2.1, the iterative process starts after initial estimates of H_{ik} and ϕ_{ik} are determined. Once a new event has been introduced and its source parameters determined, this event is placed in the pool of reference events to be used in revising $\hat{H}_{ik}$ and $\hat{\phi}_{ik}$. The revision that occurs in each iteration results in refined estimates of these propagation parameters. Finally, with improved estimates of the propagation parameters, it will be possible to revise the source parameters of some events in the pool.

We anticipate that the greatest chance of instability will arise at the outset when estimates of H_{ik} and ϕ_{ik} are based on just a few observations. A fully developed reference point will

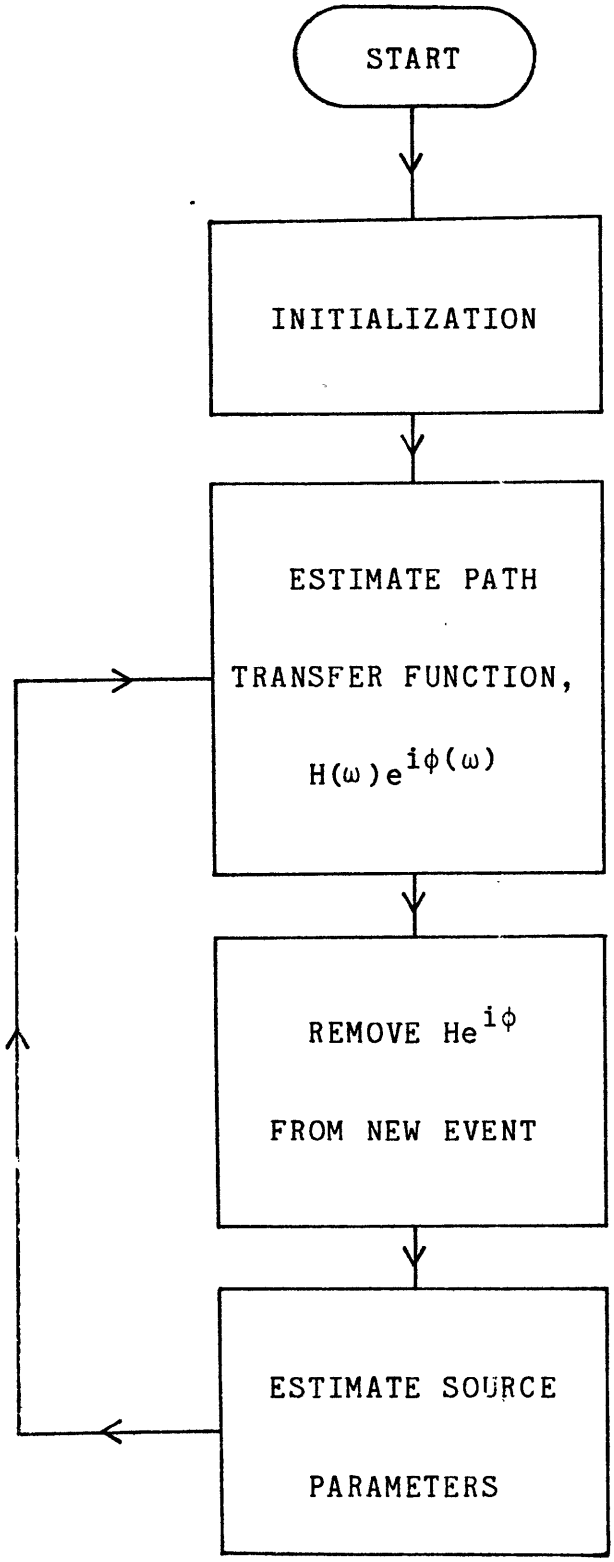

Fig. 2-2.1: Major computational steps of the iterative method.

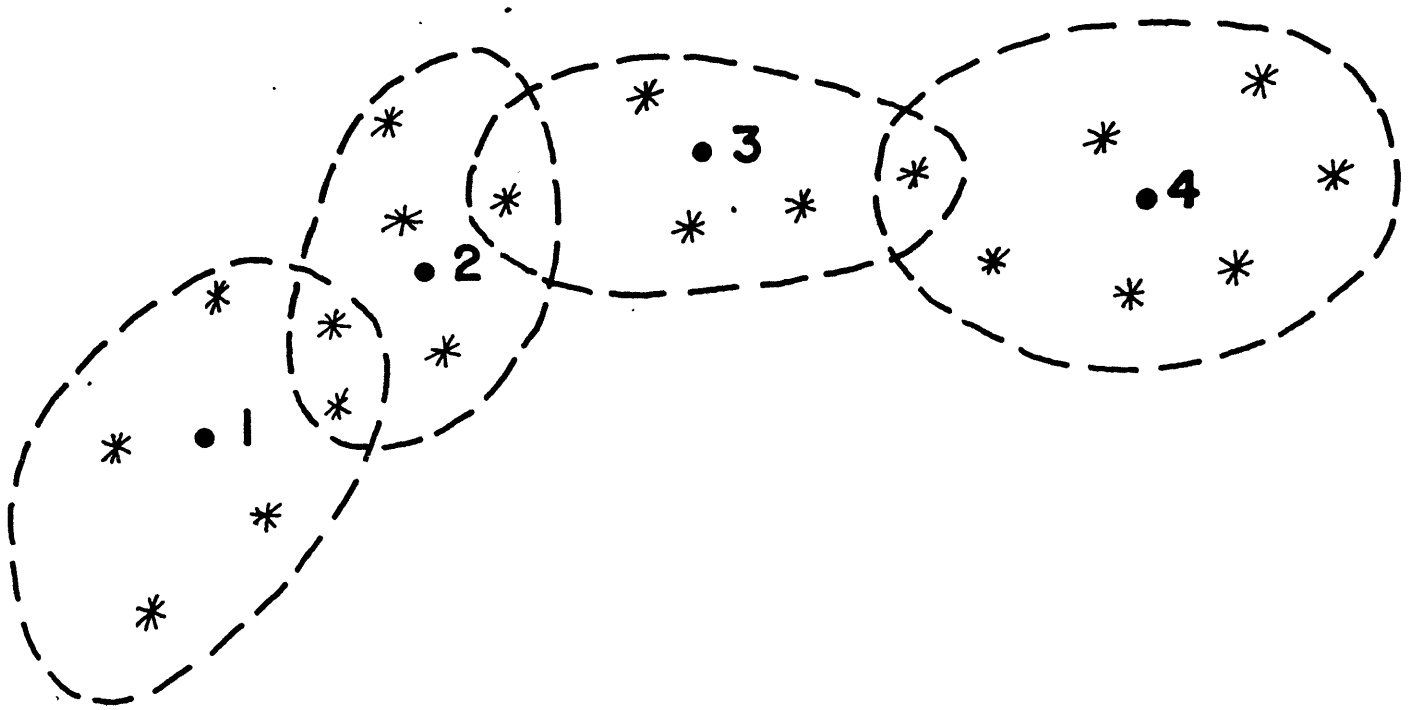

Fig. 2-2.2: Reference point movement by overlapping source regions.

result once $\hat{H}_{ik}$ and $\hat{\phi}_{ik}$ have converged, implying that the addition of new events and the revision of pooled events will cause little change in these estimates.

After full development, we move to a new reference point in another source region, and thus the supply of new events is endless. The movement takes place by a small jump from the initial reference point along the world-wide seismic belts. As shown in Figure 2-2.2, the next reference point is located in a source region with some overlap of the previous region. In this manner, reference point No. 2 and onward will always have the necessary reference events with which to start the iteration.

3. JOINT USE OF PHASE AND AMPLITUDE

The source spectrum isolated in Equation 2-1.5 is comprised of two factors: A^s, the amplitude spectral density of the surface wave excitation and the factor, $e^{-i\phi^s}$, involving the focal phase, ϕ^s. There are numerous studies of surface waves in the literature where amplitude or phase was used to study the seismic source. Relatively few studies (Press et al., 1961; Ben-Menahem and Toksoz, 1962, 1963a, 1963b; Brune and Pomeroy, 1963; Aki, 1964) have made use of both simultaneously, and to my knowledge, none have combined the two in the form of complex spectra. The usefulness of forming complex source spectra, i.e., real and imaginary parts of the surface wave source spectrum, will become evident in Section 4 of this chapter. In this section, we discuss the advantages of having both amplitude and focal phase to study the

seismic source.

The widespread use of surface waves to study the seismic source was given great impetus with the development of the normal mode theories for excitation in layered medium (Haskell, 1963; Harkrider, 1964; Ben-Menahem and Harkrider, 1964; Saito, 1967). Theoretical calculations for a point force system, such as the double-couple buried in a layered medium, demonstrated that there is significant variation of amplitude and focal phase radiation patterns of earthquakes with changes in the focal mechanism. It also became evident that neither the amplitude nor the focal phase of the surface wave radiation alone could determine the complete set of source parameters. For example, the sense of fault-slip motion at the source cannot be recovered from the observation of amplitudes alone. It has become common practice to supplement the observations of amplitude with a P-wave solution in order to resolve this ambiguity. Some surface wave methods, such as the method to determine source depth (Tsai and Aki, 1970), require additional data in the form of a P-wave solution.

Unfortunately, this additional data is not available for small events. Using teleseismic WWSSN data, the event generally must have a magnitude greater than 5.5 to determine a P-wave solution. Very often the source is too small to be studied using P-waves, but may excite surface waves with better signal to noise ratio. The study of small intra-plate earthquakes may be cited for their difficulty to obtain reliable P-wave fault plane solutions. Yet many of these events are efficient sources of surface

wave generation.

Early surface wave studies made extensive use of focal phase through the phase equalization method (Aki, 1960a-d; Brune et al., 1960; Brune and Pomeroy, 1962). Studies by Aki (1960a) had called upon the azimuthal dependence in the focal phase of Love waves to distinguish between single-couple and double-couple source models. In later studies (Aki, 1960b,c), Rayleigh wave phase was used to determine the direction of slip motion at the earthquake source. Brune and Pomeroy (1962) investigated focal phase of explosions and earthquakes which showed that the azimuthal pattern of focal phase for earthquakes is in general more complicated than that of explosions. More recently, studies by Weidner (1972) and Weidner and Aki (1973) revitalized interest in the focal phase as a sensitive indicator of the source depth.

The sensitivity of the focal phase of surface waves to the orientation of the double-couple force system is demonstrated for three types of faulting in Figure 2-3.1. This calculation applies to Rayleigh waves from a point source with step-function time dependence, and $h/\lambda \rightarrow 0$ where h is the source depth and λ the wavelength. The focal phase discriminates between all three mechanisms provided there is adequate sampling of the radiation pattern. One reliable estimate of the focal phase plus the amplitude pattern would also resolve between the mechanisms.

The study of a small intra-plate earthquake in Southeastern Missouri provides us with a good example for this discussion. The earthquake, located on the map in Figure 2-3.2, has a body

wave magnitude of 5.2 which is too small for a reliable P-wave first motion study. The P-wave solution in Figure 2-3.3 is proposed by Mitchell (1973) to support the conclusion that the event was primarily dip-slip normal faulting. In my opinion, the P-waves may suggest normal faulting but the number of uncertain and inconsistent observations reflects the weakness of this suggestion.

The main reason to avoid focal phase measurements has been the lack of accurate, regionalized phase velocities with which to remove the propagation phase delay. The Missouri earthquake is adequately covered by WWSSN stations with short travel paths over a very homogeneous structure. In addition, there are numerous measurments of regionalized surface wave phase velocities for North America (Ewing and Press, 1959; McEvilly, 1964; Biswas and Knopoff, 1974). Thus, it was feasible to study the focal phase of the surface waves to resolve the ambiguity of the slip vector of the Missouri earthquake.

Table 2-3.1 gives the regionalized phase velocities used to isolate the focal phase delay by Equation 2-1.4 where ϕ^E is replaced by the phase obtained from Fourier transform of the surface waves, corrected for instrumental response (Hagiwara, 1958). The numerical results are given in Table 2-3.2 and plotted in Figure 2-3.4. Error bars shown through the data points in this figure were estimated from three possible error sources: (1) observational errors due to noise, (2) errors in the phase velocity data and (3) errors caused by source finiteness and uncertainty

in epicenter location and origin time (Patton, 1976). The error bar is the square root of the sum of the variances of the three error sources. Small errors at Madison (MDS) and Atlanta (ATL) reflect their short epicentral distances and good signal to noise ratios.

The horizontal dotted lines labeled ϕ_N and ϕ_T in Figure 2-3.4, indicate the focal phase values predicted on the basis of the simple dip-slip normal and thrust faulting source models shown in Figure 2-3.1. At long period where the assumption $h/\lambda \rightarrow 0$ is valid, the observations at ATL, DAL and MDS favor the normal faulting hypothesis for the Missouri event. The details of most of the observations in Figure 2-3.4 can be explained by a second calculation based on normal mode theory of surface wave excitation in a layered medium (Saito, 1967). The medium is the Gutenberg earth model, as adopted by Tsai and Aki (1970) and the source is taken to be a point double-couple, behaving as a step-function in time. For source depths confined to the crust, a source model was found which minimized the differences between observed values and calculated values of focal phase. The search for parameters of the model was taken over depth, slip angle, dip angle and strike of the fault plane. The fault planes of this source model are also shown on the stereographic net in Figure 2-3.3. The mechanism is dip-slip on a normal fault at a depth of 6km.

The discrepancies between observed and calculated phase are probably due to noise in the seismogram (both ambient noise and

TABLE 2-3.1: RAYLEIGH WAVE PHASE VELOCITIES USED IN TABLE 2-3.2.

STATION	PHASE VELOCITY (KM/SEC) AT 50, 40, 33, 20 SEC
ATL	4.0, 3.96, 3.82, 3.50
BOZ	4.0, 3.96, 3.78, 3.44
DAL	4.0, 3.96, 3.80, 3.50
LUB	4.0, 3.96, 3.82, 3.55
MDS	4.0, 3.96, 3.80, 3.50
RCD	4.0, 3.96, 3.81, 3.50

TABLE 2-3.2: RESULTS OF CALCULATING FOCAL PHASE OF RAYLEIGH WAVES FROM THE MISSOURI EARTHQUAKE

STATION	X(KM)	ω(HZ)	ϕ_O	ωt	$\frac{\omega X}{C}$	ϕ_F
ATL, Atlanta, Georgia	755.0	.02	.53	1.74	3.77	.50
		.025	.05	2.18	4.76	.47
		.0333	.08	2.91	6.60	.39
		.05	.71	4.36	10.79	.28
BOZ, Bozeman, Montana	1933.9	.02	.17	10.93	9.67	.53
		.025	.59	13.69	12.20	.09
		.0333	.53	18.24	17.08	.69
		.05	.65	27.36	28.11	.90
DAL, Dallas, Texas	747.3	.02	.43	2.88	3.74	.58
		.025	.47	3.60	4.72	.35
		.0333	.02	4.81	6.56	.27
		.05	.62	7.21	10.68	.15
LUB, Lubbock, Texas	1084.2	.02	.67	5.34	5.42	.59
		.025	.40	6.67	6.84	.23
		.0333	.09	8.90	9.46	.53
		.05	.78	13.34	15.27	.86
MDS, Madison, Wisconsin	650.9	.02	.31	2.40	3.25	.45
		.025	.59	3.00	4.11	.48
		.0333	.23	3.99	5.71	.51
		.05	.79	5.99	9.30	.49
RCD, Rapid City, S. Dakota	1259.3	.02	.70	5.35	6.30	.76
		.025	.77	6.69	7.91	.51
		.0333	.57	8.92	11.01	.49
		.05	.01	13.39	17.64	.76

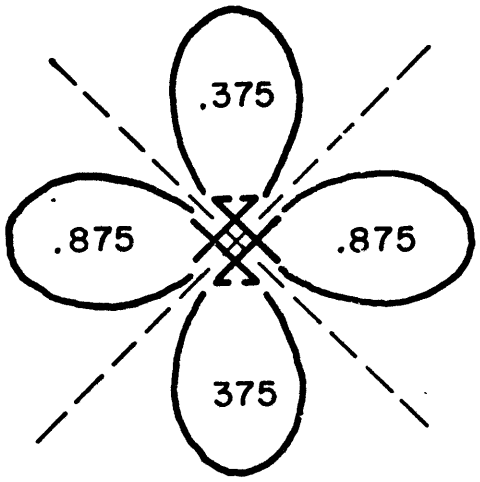

VERTICAL STRIKE-SLIP FAULT

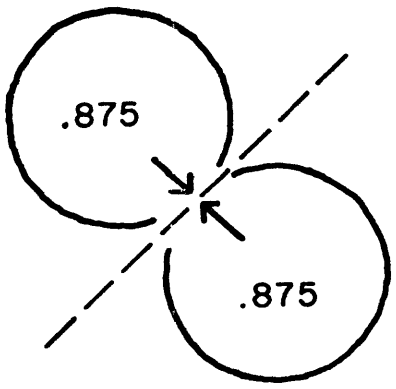

THRUST FAULT

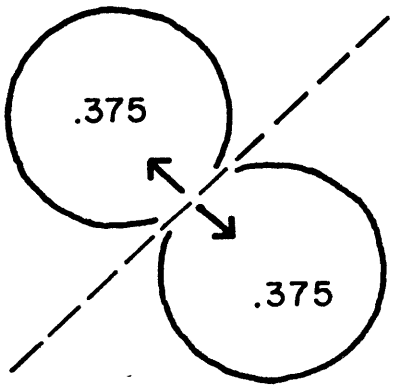

NORMAL FAULT

Fig. 2-3.1: Rayleigh wave source effects for three types of faults in a homogeneous half-space. The solid lines represent the amplitude radiation and numerical values refer to source phase delay. Dashed lines show fault traces. Dip slip faulting occurs on 45° planes. See text for details of the calculation.

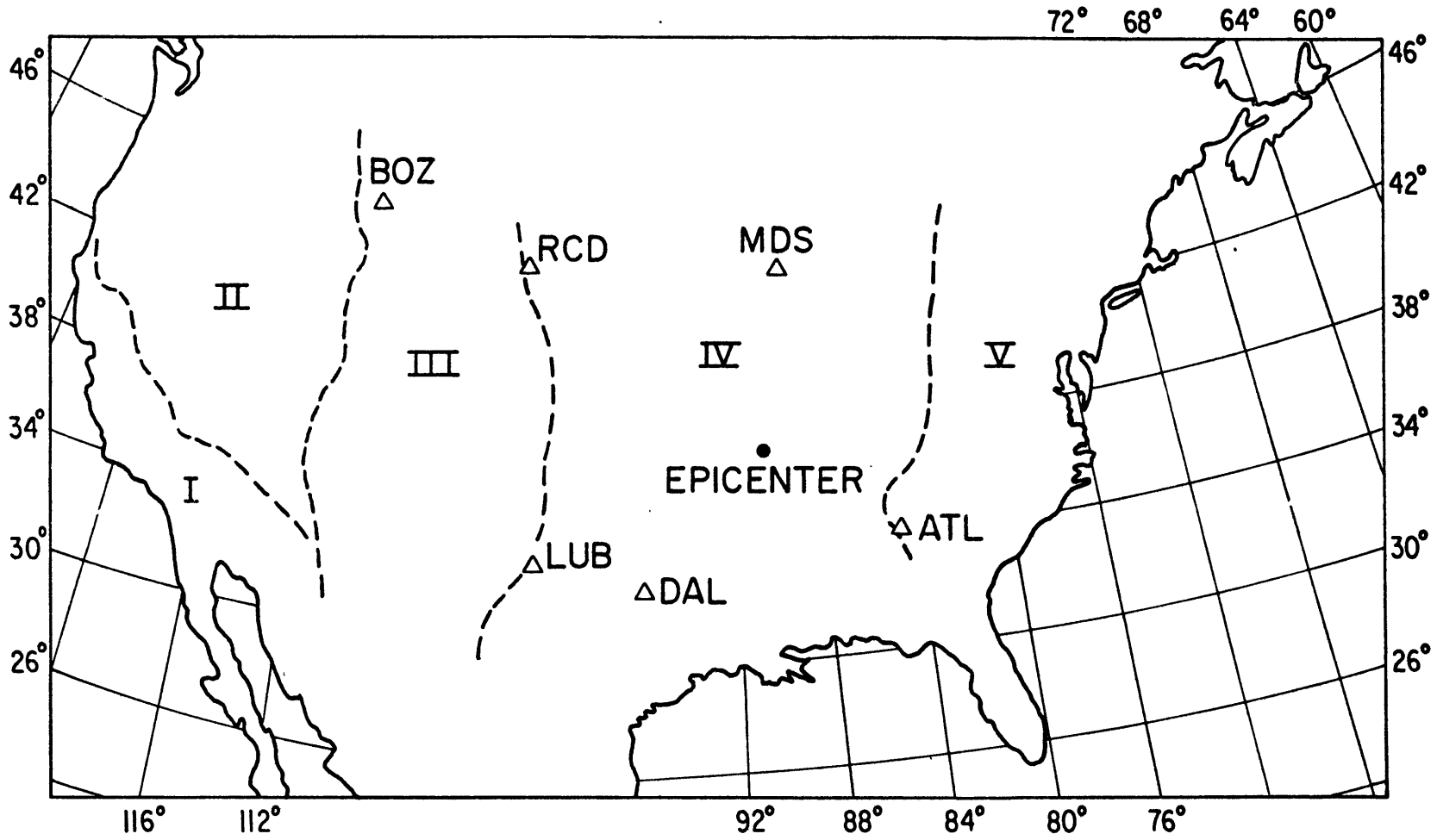

Fig. 2-3.2: Regionalized map of the United States based on the study of phase velocities and crustal structure by Ewing and Press (1959). Regions III, IV and V, for example, represent three provinces, namely Rocky Mountains, Interior Plains, and Appalachian Mountains, respectively.

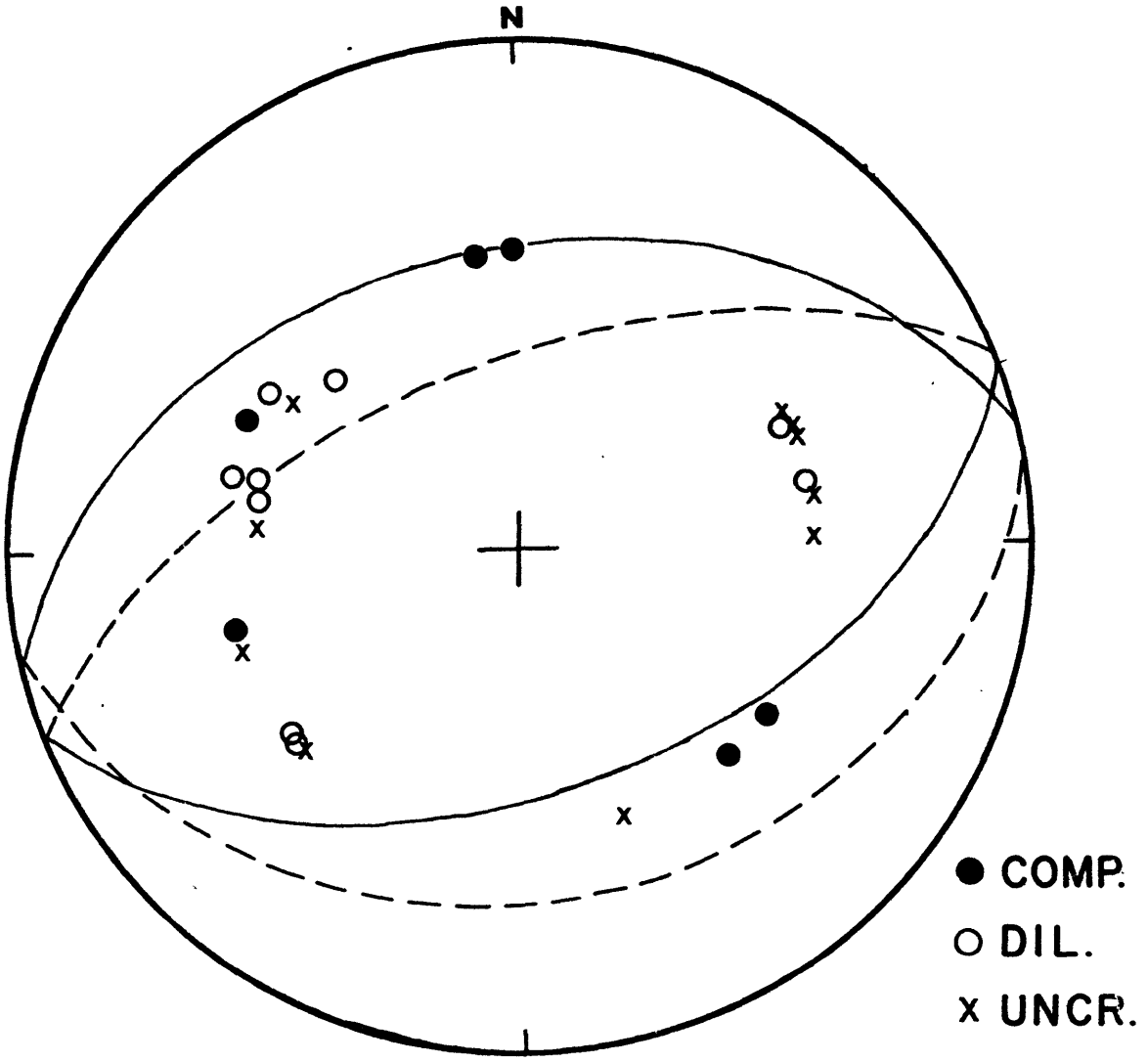

Fig. 2-3.3: Stereographic projection of P-wave first motions for the southeastern Missouri earthquake (after Mitchell, 1973). Solid lines indicate fault plane geometry determined by Mitchell from amplitude radiation patterns of Rayleigh waves Dashed lines are fault planes determined from the source phase measurements.

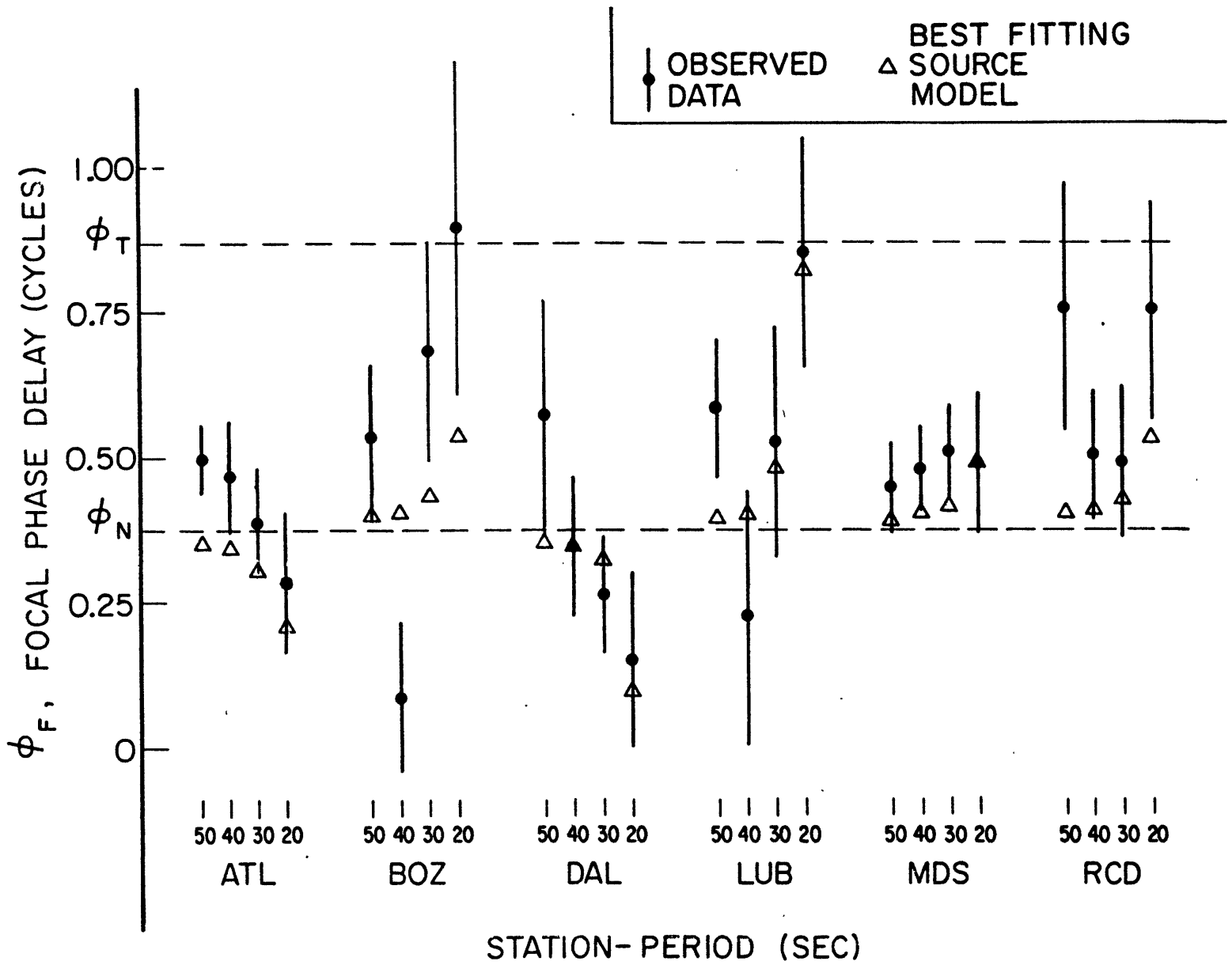

Fig. 2-3.4: Source phase spectra of Rayleigh waves from the Missouri earthquake. Dashed lines represent constant phase spectra and radiation pattern for thrust (ϕ_T) and normal (ϕ_N) faults, as given in Figure 2-3.1. Best fitting source model is described in the text.

propagation interference) or perhaps due to errors in the phase velocity data.

4. LINEAR INVERSION FOR THE SEISMIC MOMENT TENSOR

Our purpose in this section is to invert the observations of complex source spectra obtained in Equation 2-1.5 to recover source parameters. The linear inversion for the seismic moment tensor (Gilbert, 1970) will be the focus of our attention. Gilbert showed the linear relationship between the amplitude of free oscillations and the seismic moment tensor. The first application of the linear inversion was carried out by Dziewonski and Gilbert (1974) on free oscillation datasets for two deep shocks in South America. Extensions of this method to other datasets have been proposed by a number of investigators (Buland and Gilbert, 1976; McCowan, 1976; Mendiguren, 1977).

The extension to surface waves by Buland and McCowan calls for linear inversion in the time domain, while Mendiguren proposes frequency domain inversion. Mendiguren's is based on surface wave excitation formulae derived by Saito (1967). For a vertically heterogeneous medium the vertical component fundamental mode Rayleigh wave spectrum due to a point source may be expressed in terms of a linear superposition of six elements of the moment tensor:

$$u(r,\theta,\omega) = \frac{Y_1(0)}{4CUI_1}\sqrt{\frac{2}{\pi kr}}\, e^{-i(\frac{\omega r}{C} - \frac{3\pi}{4})} \cdot$$

$$\left\{(M_{xx} + M_{yy})\frac{kY_3(h)}{2} - M_{zz}\frac{Y_2(h)+\lambda(h)kY_3(h)}{\lambda(h)+2\mu(h)}\right.$$

$$- (M_{yy} - M_{xx})\frac{kY_3(h)\cos 2\theta}{2} + M_{xy}kY_3(h)\sin 2\theta \qquad (2\text{-}4.1)$$

$$\left. - iM_{xz}\frac{Y_4(h)\cos\theta}{\mu(h)} - iM_{yz}\frac{Y_4(h)\sin\theta}{\mu(h)}\right\}$$

where the moment components, M_{ij}, are given in Cartesian coordinates with origin at the source and the x-, y-, and z-axes pointing east, north, and up respectively. The Y_i's are stress-motion eigenfunctions where Y_1 and Y_3 refer to the vertical and horizontal components of displacement, respectively, and Y_2 and Y_4 to the vertical and horizontal components of traction acting on the x-y plane. These eigenfunctions satisfy the equations of motion, free surface and radiation conditions given in Saito (1967). All four are real functions of frequency, ω, and depth, h, and are normalized at each frequency such that $Y_1(0)=1$. The Lame' constants, $\mu(h)$ and $\lambda(h)$, are real functions of depth only. The kinetic energy of the surface wave is $\omega^2 I_1$, and k, C, and U refer to wave number, phase velocity, and group velocity respectively. The position of the receiver is expressed in polar coordinates where r is the horizontal distance from the source and θ is its azimuth measured counter-clockwise from east. For a source with a step function time dependence, there is an additional factor of

$1/i\omega$ outside the brackets, where i is the $\sqrt{-1}$. In this case all moment components are regarded real variables. The complex quantity inside the brackets, which will be referred to as S, represents source effects involving four moments, M_{xx}, M_{yy}, M_{zz}, M_{xy}, entering on the real part and two moments, M_{xz}, M_{yz} on the imaginary part.

At a specified frequency and source depth, S shall depend only on moment and azimuth such that

$$\begin{aligned} \mathrm{Re}\{S\} = (M_{xx}+M_{yy})G_1 + M_{zz}G_2' - (M_{yy}-M_{xx})G_1 \cos 2\theta \\ + 2M_{xy}G_1 \sin 2\theta \end{aligned} \qquad (2\text{-}4.2)$$

and

$$\mathrm{Im}\{S\} = M_{xz}G_3 \cos\theta + M_{yz}G_3 \sin\theta$$

where the G_i's are real functions of frequency and depth. The real and imaginary parts of S are simple sinusoidal functions of the azimuth with their amplitude proportional to the moment components. Determination of the moments in each part requires adequate sampling in azimuth. At a single frequency, it is apparent that we cannot determine both the components $M_{xx} + M_{yy}$ and M_{zz} separately, because they both have isotropic dependence in azimuth. Even with data over a range of frequencies, the resolu-

tion of these two components is not possible if the data consists of only the fundamental mode Rayleigh waves (Mendiguren and Aki, 1978). In the absence of higher mode data to resolve them, it will be necessary to apply the constraint, $M_{xx} + M_{yy} + M_{zz} = 0$, which forces models of the source to be free of volume change.

The behavior of S with frequency and source depth is determined by the functions, G_i. These functions multiplied by the factor, $\frac{\sqrt{k}}{U\omega^2 I_1}$, are the response of the assumed layered medium to a point source with a step time dependence and moment, M_{ij}. The sensitivity of the response to changes in source depth and moment is, of course, very important. Assuming the Gutenberg earth model, (for layer parameters, see Table 2-4.1) we have plotted in Figure 2-4.1 the responses over the frequency range .015-.05 Hz and for source depths in the crust. This figure shows that the resolution of source depth using fundamental mode Rayleigh waves is best for shallow events. Furthermore, the greatest sensitivity to source depths in the upper crust occurs in the high frequency portion of the surface wave spectrum. All surface wave methods to determine focal depths of shallow events (e.g. Tsai and Aki, 1970; Weidner and Aki, 1973) have relied on these two important characteristics. In working with complex source spectra, we shall decompose our data into real and imaginary parts. As can be seen in Figure 2-4.1, the responses that enter on the real part change polarity at frequencies depending on the focal depth. This behavior is not duplicated by the responses appearing on the imaginary part. Because of this change in polarity

the real part has better resolving power of the source depth than the imaginary part.

The behavior of responses on the imaginary part of S is such that resolution of M_{xz} or M_{yz} will be better at high frequencies than at low frequencies, regardless of source depth. On the other hand, resolution of moments on the real part depends on the depth of the source. At depths near mid-crust ($\sim$15 km), the resolution will be better at low frequencies. At greater depths in the crust, the resolution improves for the high frequencies.

INVERSION PROCEDURE. Our observations consists of complex source spectra obtained in Equation 2-1.5, where A^s_{ik} is the amplitude at the frequency ω_k in the azimuth of the i^{th} station at a great-circle distance $\bar{X}_i$ from the source. (The subscript 1 has been dropped to simplify notation.) Assuming the geometrical spreading factor for a laterally homogeneous spherical earth, this amplitude is reduced to the distance independent quantity, S, defined in Equation 2-4.2. The phase delay, ϕ^s_{ik}, will be reduced to the phase of S by removing the phase shift, $-3\pi/4$, coming from the asymptotic expansion of the Hankel function, and the phase delay, $\pi/2$, introduced by the slip time function, in this case assumed to be a step function. The real part, α_{ik} and the imaginary part, β_{ik}, of this reduced spectrum is related to the model in Equation 4.2 as follows:

$$\alpha_{ik} = M_{zz}[G_{2k}(h)-G_{1k}(h)] - (M_{yy}-M_{xx})G_{1k}(h) \cos 2\theta_i + 2M_{xy}G_{1k}(h) \sin 2\theta_i + \varepsilon^{\alpha}_{ik}$$

and

(2-4.3)

$$\beta_{ik} = M_{xz}G_{3k}(h) \cos \theta_i + M_{yz}G_{3k}(h) \sin \theta_i + \varepsilon^{\beta}_{ik}$$

where we have constrained $M_{xx} + M_{yy} + M_{zz} = 0$ and where ε^{α} and ε^{β} are error terms. The inverse problem may be posed as follows: given m observations of α_{ik} and β_{ik} for frequencies $\omega_L < \omega < \omega_H$ and for stations distributed around the source, what estimates of the moment components and the source depth will minimize the errors, ε^{α} and ε^{β}.

The source depth, which is the only non-linear source parameter that remains in this model, must be determined by repetitive application of the linear inversion. We shall assume several trial depths at which to carry out the inversion. At each trial depth, a sum of squared residuals will be computed by the following formula

$$\varepsilon^2 = \sum_{i,k} (\varepsilon^{\alpha^2}_{ik} + \varepsilon^{\beta^2}_{ik}) \qquad (2\text{-}4.4)$$

The depth which minimizes this residual will be chosen as the source depth. The moment tensor is immediately known from the

TABLE 2-4.1: LAYER PARAMETERS OF THE GUTENBERG EARTH MODEL

Depth, km	ρ, g/cm^3	α, km/sec	β, km/sec
0-19	2.74	6.14	3.55
19-38	3.00	6.58	3.80
38-50	3.32	8.20	4.65
50-60	3.34	8.17	4.62
60-70	3.35	8.14	4.57
70-80	3.36	8.10	4.51
80-90	3.37	8.07	4.46
90-100	3.38	8.02	4.41
100-125	3.39	7.93	4.37
125-150	3.41	7.85	4.35
150-175	3.43	7.89	4.36
175-200	3.46	7.98	4.38
200-225	3.48	8.10	4.42
225-250	3.50	8.21	4.46
250-300	3.53	8.38	4.54
300-350	3.58	8.62	4.68
350-400	3.62	8.87	4.85
400-450	3.69	9.15	5.04
450-500	3.82	9.45	5.21
500-600	4.01	9.88	5.45
600-700	4.21	10.30	5.76
700-800	4.40	10.71	6.03
800-900	4.56	11.10	6.23
900-1000	4.63	11.35	6.32

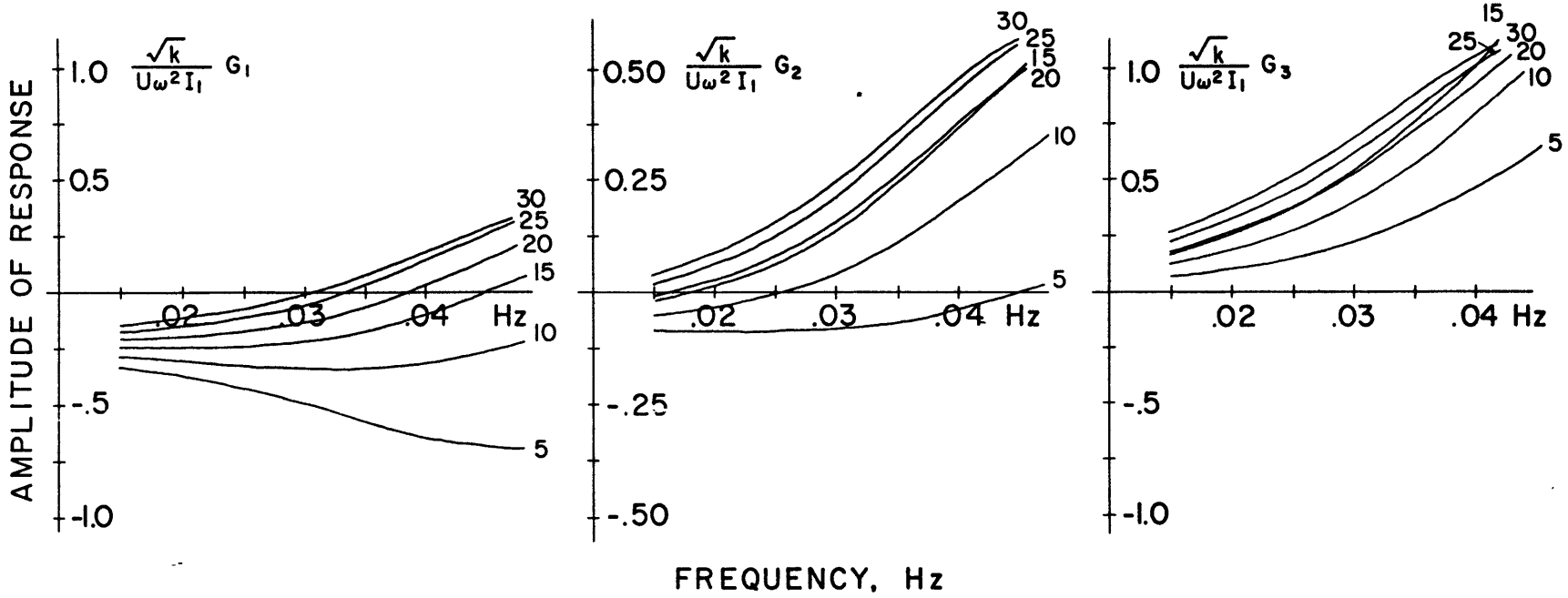

Fig. 2-4.1: Fundamental mode Rayleigh wave responses for six focal depths (km) in the Gutenberg earth model. Responses G_1 and G_2 enter on the real part of the complex source spectrum and G_3 on the imaginary part as defined in Equation 2-4.2.

linear inversions carried out at this chosen depth.

This completes the description of the approach taken to obtain the focal depth and to invert for the seismic moment tensor. Appendix A gives a detailed account of the techniques used to implement the least squares inversion.

5. ERROR MINIMIZATION IN COMPLEX SPECTRA

This section concerns the problem of making statistical estimates of source and propagation parameters from observed seismograms that contain noise. Specifically, we wish to obtain methods for estimating (1) H_{ik} and ϕ_{ik} from observed and calculated spectra discussed in Section 2.1 and (2) source parameters from observed complex spectra, $A^s_{ik}e^{-i\phi^s_{ik}}$ obtained in Equation 2-1.5. Based on their statistical properties, the noise contaminants are divided into two broad categories - background and signal-generated noise. The following discussion analyzes each noise source separately to arrive at the appropriate methods.

BACKGROUND NOISE. The background noise on the seismograph record may be assumed to be a Gaussian process. Consider the record, $f_{ji}(t)$, at the i^{th} receiver due to the j^{th} event to consist of signal, $s_{ji}(t)$, and noise, $n_{ji}(t)$. Dropping the receiver subscript for the sake of convenience, the Fourier transform of $f_j(t)$ can be separated into real (cosine transform) and imaginary (sine transform) parts:

$$cf_j(\omega) = \int f_j(t) \cos \omega t dt = \int [s_j(t)+n_j(t)] \cos \omega t dt = cs_j(\omega) + cn_j(\omega)$$

$$sf_j(\omega) = \int f_j(t) \sin \omega t dt = \int [s_j(t)+n_j(t)] \sin \omega t dt = ss_j(\omega) + sn_j(\omega) \quad (2\text{-}5.1)$$

We shall assume that for a given ω_k, each of the transforms of the noise, cn_{jk} and sn_{jk}, follow a Gaussian distribution with zero mean and variance $z\sigma_k^2$.

As described in Section 2.1, the propagation medium is parameterized by the transfer function $H(\omega)e^{i\phi(\omega)}$. Let $S_j(t)$ be the input signal to the medium. Its cosine and sine transforms, $cS_j(\omega)$ and $sS_j(\omega)$, are related to the output signal transform, $cs_j(\omega) + i\, ss_j(\omega)$, through the transfer function by the equation

$$cs_j(\omega) + iss_j(\omega) = H(\omega)e^{i\phi(\omega)}[cS_j(\omega) + isS_j(\omega)] \quad (2\text{-}5.2)$$

Our knowledge of the input is not free of error, however, and what we observe is $F_j(t)$ having cosine and sine transforms, $cF_j(\omega)$ and $sF_j(\omega)$. We can write

$$\begin{aligned} cF_j(\omega) &= cS_j(\omega) + cN_j(\omega) \\ sF_j(\omega) &= sS_j(\omega) + sN_j(\omega) \end{aligned} \quad (2\text{-}5.3)$$

where $cN_j(\omega)$ and $sN_j(\omega)$ are Fourier transforms of the noise at the input. At a given ω_k we assume each of these noise transforms follow a Gaussian distribution with zero mean and variance σ_k^2.

Dropping the subscript k for compact notation, $cF_j - cS_j$ and $sF_j - sS_j$ will follow a Gaussian distribution with zero mean and variance σ^2, and $cf_j - cs_j$ and $sf_j - ss_j$ will follow a Gaussian distribution with zero mean and variance $z\sigma^2$. Since they are statistically independent, the joint probability density function is the product of the individual density functions. The likelihood function can be written as follows

$$\text{Log } L = -M \text{ Log}(2\pi\sigma^2) - M \text{ Log } (2\pi\sigma^2 z)$$

$$- \sum_{j=1}^{M} \frac{(cF_j - cS_j)^2 + (sF_j - sS_j)^2}{2\sigma^2}$$

$$- \sum_{j=1}^{M} \frac{(\bar{c}f_k - cs_j)^2 + (sf_j - ss_j)^2}{2\sigma^2 z} \qquad (2\text{-}5.4)$$

Following the approach taken by Pisarenko (1970), we shall find expressions for H and ϕ that maximize the likelihood function. Estimates of H and ϕ based on this formulation are referred to as maximum likelihood estimates (MLE). First, the output signal is written in terms of the transfer function and the input signal

$$cs_j = cS_jH \cos\phi - sS_jH \sin\phi$$

$$ss_j = sS_jH \cos\phi + cS_jH \sin\phi \qquad (2\text{-}5.5)$$

These expression are substituted into 2-5.4 for cs_j and ss_j. Then, holding H, ϕ and σ^2 fixed, it is possible to find formulas for cS_j and sS_j in terms of the outputs which maximize the likelihood function

$$\hat{cS}_j = \frac{zcF_j + cf_jH \cos\phi + sf_jH \sin\phi}{z + H^2}$$

and (2-5.6)

$$\hat{sS}_j = \frac{zsF_j - cf_jH \sin\phi + sf_jH \cos\phi}{z + H^2}$$

Substituting expressions $\hat{cS}_j$ and $\hat{sS}_j$ for cS_j and sS_j into the likelihood function, and maximizing this function with respect to H and ϕ, the MLE for H and ϕ are obtained as follows

$$\hat{H} = \frac{V - zU^2}{2(W^2+X^2)^{1/2}} + \sqrt{\frac{(V-zU)^2}{4(W^2+X^2)} + z}$$

and (2-5.7)

$$\hat{\phi} = \tan^{-1}\left(\frac{X}{W}\right)$$

where

$$U = \frac{1}{M} \sum_{j=1}^{M} (cF_j^2+sF_j^2), \qquad V = \frac{1}{M} \sum_{j=1}^{M} (cf_j^2+sf_j^2)$$

$$W = \frac{1}{M} \sum_{j=1}^{M} (cF_j cf_j+sF_j sf_j), \quad X = \frac{1}{M} \sum_{j=1}^{M} (cF_j sf_j-sF_j cf_j)$$

As shown by Pisarenko, these estimators are consistent, asymptotically unbiased, and asymptotically normal under the condition that $U < C$ as $M \to \infty$, where C is a constant. Furthermore, expressions for the variances of these estimates may be obtained

$$VAR\{\hat{H}\} = \frac{(H^2+z)R + 2z}{MR^2}$$

and (2-5.8)

$$VAR\{\hat{\phi}\} = \frac{(H^2+z)R + 2z}{MH^2R^2}$$

where R equals U/σ^2.

A simple interpretation of $\hat{H}$ and $\hat{\phi}$ can be made when the input and output are expressed in polar coordinates:

$$cF(\omega) + i\, sF(\omega) = A(\omega)e^{i\Lambda(\omega)}$$

and (2-5.9)

$$cf(\omega) + i\, sf(\omega) = a(\omega)\, e^{i\lambda(\omega)}$$

If $\theta = \lambda - \Lambda$, then Equation 2-5.7 becomes

$$\tan \hat{\phi} = \frac{\Sigma a_j A_j \sin \theta_j}{\Sigma a_j A_j \cos \theta_j} \qquad (2\text{-}5.10)$$

which means that $\hat{\phi}$ is simply the phase angle of the vector sum of $a_j A_j e^{i\theta_j}$. This is shown schematically in Figure 2-5.1. If there is no noise at the output, i.e., z=0, then the expression for $\hat{H}$ in polar coordinates reduces to

$$\hat{H} = \frac{\Sigma a_j^2}{\Sigma a_j A_j \cos(\theta_j - \hat{\phi})} = \frac{\Sigma (a_j A_j)\left(\frac{a_j}{A_j}\right)}{D} \qquad (2\text{-}5.11)$$

The denominator, D, is the length of the vector sum of $a_j A_j e^{i\theta_j}$. As in the case of $\hat{\phi}$, the weighting is proportional to the product of the output and input amplitudes, $a_j A_j$. When noise is present, $z \neq 0$, a correction is added to account for the fact that the noise will perturb the amplitude, a_j. This interpretation was first noted by Lowes (1970).

Turning to the problem of estimating source parameters, the linear inversion on observations of complex spectra to obtain estimates of the moment tensor elements also implies that an addi-

tive Gaussian error is the noise contaminant. Under these conditions, the two separate linear least squares inversions, one on the real and the other on the imaginary part, as described in Section 2.4, will give maximum likelihood estimates of the moment tensor elements.

SIGNAL GENERATED NOISE. Signal generated noise arises from a variety of interference phenomena, including contamination by body waves and higher mode Rayleigh waves, focusing and defocusing, and multipath interference. Pilant and Knopoff (1964) investigated the interference between two identical waveforms with different amplitudes and arrival times expressed by

$$f(t) = S(t) + bS(t-\Delta t) \qquad (2\text{-}5.12)$$

where S(t) is the waveform, b is an amplitude factor, Δt is a time shift, and f(t) is the observed seismogram. Transforming to the frequency domain, Equation 2-5.12 becomes

$$f(\omega) = S(\omega)[1 + be^{i\omega\Delta t}] \qquad (2\text{-}5.13)$$

and thus the signal generated noise, $bS(\omega)e^{i\omega\Delta t}$ is proportional to the signal, $S(\omega)$. Similarly, the fluctuation generated by focusing is proportional to signal amplitude. In general, we may write the effect of interference and focusing as

$$f(\omega) = S(\omega)\ [1 + \varepsilon] \tag{2-5.14}$$

Taking the logarithm of the above equation, we obtain

$$\ln a(\omega) + i\phi(\omega) = \ln A(\omega) + i\Phi(\omega) + \ln(1+\varepsilon) \tag{2-5.15}$$

Assuming small ε, the following relationships can be written

$$\begin{aligned} \ln a(\omega) &= \ln A(\omega) + \mathrm{Re}\{\varepsilon\} \\ \phi(\omega) &= \Phi(\omega) + \mathrm{Im}\{\varepsilon\} \end{aligned} \tag{2-5.16}$$

where $a(\omega) = |f(\omega)|$, $A(\omega) = |S(\omega)|$ and $\phi(\omega)$ and $\Phi(\omega)$ are phase spectra of $f(\omega)$ and $S(\omega)$, respectively.

Thus, when the noise is primarily signal-generated, as in the case of focusing and multipath interference, log amplitudes and phase will have additive noise instead of the real and imaginary parts of the complex spectrum. Consequently, the statistical estimate should be based on minimization of the following error

$$E = \sum_{j=1}^{M} E_j^2 = \sum_{j=1}^{M} \{ (\ln a_j - \ln A_j)^2 + (\phi_j - \Phi_j)^2 \} \tag{2-5.17}$$

where the subscript j refers to the j^{th} event. In regard to estimating propagation parameters, H and ϕ, this error minimization

leads to the formulae

$$\text{Ln } \hat{H} = \frac{1}{M} \sum_{j=1}^{M} \ln H_j$$

and (2-5.18)

$$\hat{\phi} = \frac{1}{M} \sum_{j=1}^{M} \phi_j$$

where M is the number of events observed at the i^{th} station, and the frequency dependence of these parameters is understood. Expressions for variances on each of these estimates are also straight-forward,

$$\text{VAR}\{\ln \hat{H}\} = \frac{1}{M-1} \sum_{j=1}^{M} (\ln H_j - \ln \hat{H})^2$$

and (2-5.19)

$$\text{VAR } \{\hat{\phi}\} = \frac{1}{M-1} \sum_{j=1}^{M} (\phi_j - \hat{\phi})^2$$

These expressions for $\hat{\text{LnH}}$ and $\hat{\phi}$ given above are MLE when LnH_j and ϕ_j follow the Gaussian distribution.

With signal-generated noise present, the estimation of source parameters from complex spectra, $A^s_{ik} e^{i\phi^s_{ik}}$ is based on minimizing the following error expression

$$E = \sum_{i,k} [(\ln A^s_{ik} - \ln M_o S_{ik})^2 + (\phi^s_{ik} - \phi^F_{ik})^2] \qquad (2\text{-}5.20)$$

where M_0 is the seismic moment, S_{ik} is the source amplitude, computed for a unit moment double-couple, and ϕ^F_{ik} is the computed focal phase. It is understood that

$$S_{ik} = S(h,s,d,\theta'_i,\omega_k)$$

$$\phi^F_{ik} = \phi^F(h,s,d,\theta'_i,\omega_k) \qquad (2\text{-}5.21)$$

where h is the source depth, s is the slip angle, d is the dip angle, θ'_i is the azimuth of the station relative to strike of the fault, θ^F, i.e.,

$$\theta'_i = \theta^F - \theta_i \qquad (2\text{-}5.22)$$

θ_i being the station azimuth measured clockwise from north. Unfortunately, the log amplitude and phase are not linearly related to the source parameters. Furthermore, a linearization scheme would encounter difficulties because of the nature of the logarithm and arctangent. The minimization of the quantity E requires a systematic search through parameter space as was done in the method of Weidner and Aki (1973). The moment, M_o, is estimated by minimizing the error in amplitude for the trial mechanism, i.e.,

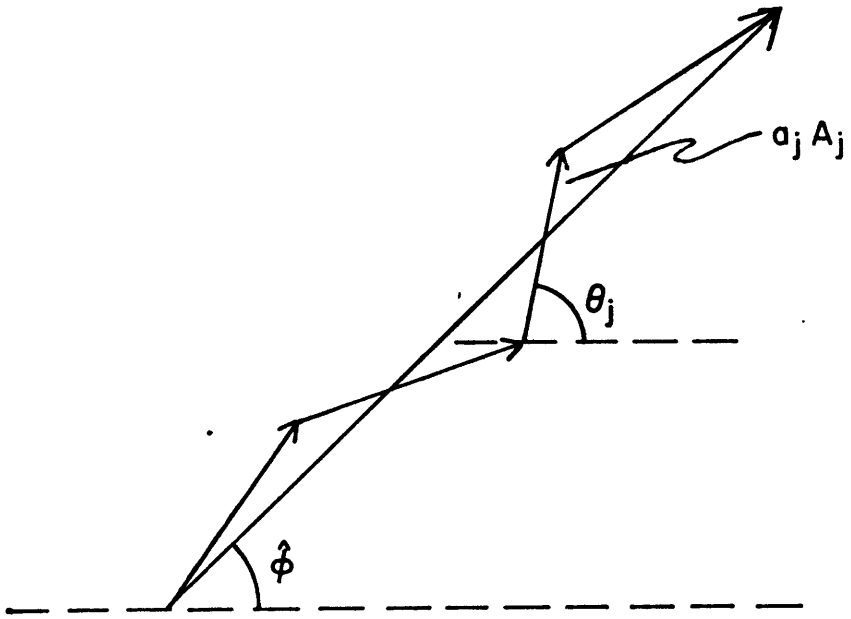

Fig. 2-5.1: Interpretation of the maximum likelihood estimate of ϕ given by Lowes (1970).

$$\min E^A = \sum_{i,k} (\ln A^S_{ik} - \ln M_o S'_{ik})^2 \qquad (2\text{-}5.23)$$

where S'_{ik} is the trial amplitude. If there is a total of M observations, then we compute the estimate, $\hat{M}_o$, as follows:

$$\ln\hat{M}_o = \frac{1}{M} \sum_{i,k} (\ln A^S_{ik} - \ln S'_{ik}) \qquad (2\text{-}5.24)$$

6. SUMMARY

The reference point equalization scheme allows the separation of source and propagation effects provided reference events are available. Initialization supplys the reference event(s) on which to base the initial estimates of the propagation parameters. The iteration that follows refines the estimates as the pool of reference events grows. A reference point jump occurs along the seismic belts by defining a new source region that overlaps the old. In this manner, reference events are always available to start the iteration, and the supply of new events is endless.

In source mechanism studies, common practice has been to supplement the observations of surface wave amplitudes with auxiliary data in the form of P-wave fault plane solutions. When the magnitude of the source is less than 5.5, this auxiliary data is usually unreliable due to poor signal to noise ratio. The amplitude and phase of surface waves supply complementary and, as we

have seen, consistent information about the source. We can supplant the use of P-waves to determine the direction of fault slip by measuring the focal phase if regional phase velocities are known. We demonstrated this for the southeastern Missouri earthquake and confirmed that its mechanism is dip-slip normal faulting.

If the source is assumed to be a point in space having step-function time dependence, the fundamental mode Rayleigh wave complex spectrum is a linear function of the medium response and six moment tensor elements, four elements appearing on the real part and two on the imaginary part. Determination of the moments in each part requires adequate sampling in azimuth. Plotting the medium response functions gives insight into the sensitivity of the spectrum to changes in the tensor elements and focal depth. The real part of the spectrum is more sensitive to changes in the focal depth of crustal events than the imaginary part. Since the spectrum is non-linearly related to the depth, it is necessary to carry out repeated applications of the linear inversion at trial depths. The depth which minimizes the residual obtained from the linear inversion is chosen to be the focal depth.

Noise on the seismogram can be divided into two broad categories - background noise and signal-generated noise. It was shown that background noise introduces additive errors into the complex spectra and signal-generated noise introduces multiplicative errors. The methods for estimating source and propagational parameters in the presence of these errors were based on minimi-

zation of the appropriate error expression. In the case of background noise, error minimization involves the real and imaginary parts of the complex spectrum. In the case of signal-generated noise, the minimization involves the logarithm of amplitude and phase. Expressions were obtained for maximum likelihood estimates of the propagation parameters in both cases. The linear inversion method yields MLE of the seismic moment tensor elements when background noise is the contaminant. Unfortunately, the log amplitude and phase are non-linearly related to the source parameters, and a method of trial and error search is the only resort when estimating the source parameters in the presence of signal-generated noise.

CHAPTER III

DATA AND ERROR ANALYSIS

We have selected our first reference point in Central Asia. There are two reasons for this choice: a) the location in mid-continent has excellent coverage by the World-Wide Seismographic Station Network (WWSSN) with epicentral distances not unreasonably long, and b) the seismicity of this part of Central Asia is very high and there are numerous active faults in this region (Shirokova, 1974; Molnar and Tapponnier, 1975) for selecting the next reference point. The data required by our analysis consists of epicentral data on the earthquakes in the source region, digitized seismograms over the time window for surface waves, and body wave data in the form of P-wave fault-plane solutions, the latter required for the initialization. We present this data in Section 3.1 and describe the preliminary data processing.

In the previous chapter, we discussed two important sources of noise on the seismogram. These noise sources were seen to cause additive and multiplicative errors on the complex spectra. Through a series of numerical experiments using synthetic data, we demonstrate the effects of these errors on the recovery of source parameters via the moment tensor inversion method. The analysis is divided into two parts. In Section 3-2 we analyze the synthetic data contaminated with random multiplicative or additive errors. In Section 3-3, we extend the analysis to possible sources of systematic errors, such as those in the auxiliary

data and in the assumptions underlying our data analysis.

1. DATA

The source region selected for this study is located in Central Asia, north of the Pamir thrust zone. As shown by the map centered at the reference point (Figure 3-1.1), this location has excellent coverage by approximately 50 stations of the WWSS Network. The wavepaths cover most of the landforms represented on the Eurasian continent. The average path length is approximately 4800km of which a large fraction is in the continental interior.

EARTHQUAKE EPICENTRAL DATA. Table 3-1.1 gives the epicentral data reported by the International Seismological Center (ISC) for nine events located within 100-150km of the reference point. Using Equation 2-1.1, our reference point is determined from the average of the epicentral coordinates of all nine events (39.58N, 73.55E). Estimates of the standard error on location and origin time reported by ISC are also given in Table 3-1.1. Events 7-9 are among the larger aftershocks triggered by the mainshock (1h 13m 55s, m_b=6.2) on August 11, 1974. All of the events produced clear, unclipped recordings of the direct surface waves on the majority of the WWSS stations shown in Figure 3-1.1.

SOURCE REGION STRUCTURE. The expression for surface wave excitation given in Section 2-4 requires that the medium response be known. Since we do not have apriori knowledge of the medium response for Eurasia, our approach will be to assume an earth

model based on auxililary data and to calculate the medium response for this model. Refinements to this initial model may be added as our knowledge of the earth structure in Eurasia improves.

Section 2-1 discusses the method to remove the medium response between the reference point and stations in the network. The model of the earth's structure assumed in this study should embody the average characteristics of the crust and upper mantle appropriate to the source region. In their survey of crustal sections taken throughout U.S.S.R., Belyaevsky et al. (1973) found crustal thicknesses as great as 65-70km under the Pamir Mountains south of the source region. Along a profile between the Tien Shan, just north of the reference point, and the Pamir Mountains (Kosminskaya et al., 1964), the crust was interpreted to have two layers, each 30km thick, the upper and lower layers having P-wave velocities of 5.5 and 6.5 km/sec, respectively. This profile is incorporated into the model for the source region structure given in Table 3-1.2. The crust is overlain by a sedimentary layer based on results of Arkhangel'skaya et al. (1969), Molnar et al. (1973), and Chen and Molnar (1975). The upper mantle structure is assumed to be the same as the Gutenberg earth model given in Table 2-4.1. Using a flat earth approximation, we computed tne phase velocity dispersion curve and medium response shown in Table 3-1.3 and Figure 3-1.2, respectively. This dispersion curve agrees well with observed phase velocities in the source region (Savarensky et al., 1969) and will be used in

the calculation of ϕ^E using Equation 2-1.3.

P-WAVE FAULT PLANE SOLUTIONS. Body wave data in the form of P-wave solutions is required in the initialization step in Section 4.1. Two of the four solutions (Events 1 and 3) shown in Figure 3-1.3 were obtained by Molnar et al. (1973). These authors and Molnar and Tapponier (1975) have interpreted geology, fault-plane solutions and active faults to infer that the regional stress has the maximum compressive axis close to horizontal in the north-south direction, presumably due to a northward converging Indian subcontinent. Further discussion of the details of the tectonic regime in this area are deferred until Chapter 5.

SURFACE WAVE DATA. The surface wave data set was obtained from the vertical component seismograms of the WWSS network shown in Figure 3-1.1. A time window (t_1-t_2) that contained the fundamental mode Rayleigh wave was determined for each record. The time of the start of the window, t_1, was estimated assuming a group velocity of 4.2km/sec. The end of the window, t_2, corresponded in most cases to velocities in the range of 2.0-2.6km/sec. However, the over-riding consideration in choosing the length of the window was that it include the entire wave train of surface waves recognized on individual records. This insured minimal distortion due to window effects on the Fourier analysis. The records were digitized manually over the time windows at a sampling rate which varied from one point every 1.1sec to one every 1.4sec, depending on whether the printed record was from 35mm chip or

roll and on the drum speed of the original recording. The digitization was checked by overlaying a plot of the digital time series on the original record.

DIGITAL PROCESSING. The digital time series were detrended, Fourier transformed, and corrected for instrumental response using formulas of Hagiwara (1958) and the instrumental constants supplied on each record by the WWSSN.

In addition, all records were filtered using the time variable filter technique (Landisman et al., 1969). This involved two processing steps. First, group velocities were obtained by the moving window analysis. The output of this analysis gives a two dimensional plot (velocity versus period) of the energy contained in a windowed portion of the time series. The position and length of the cosine-squared window, applied to the time series, depends on the velocity and period to be analyzed. In our case, the length was always set to four times the period. The arrival of the group or wave packet is inferred from the energy contours drawn on the resultant plot. The second step filters the seismogram by passing only those wave packets with group velocities that correspond to the fundamental mode Rayleigh wave. Weidner (1972) found that this filtering technique reduces noise without distorting the phase of the original record. The present author confirmed this by overlaying the filtered record on the original. Its effect on the amplitude spectrum can be seen from examples in Figure 3-1.4.

NOISE. On many records background noise of the same length as the signal window was digitized before and after the arrival of the signal. The noise time series were detrended, Fourier transformed, and corrected for instrumental response in the same manner as the signals. The background noise levels in the frequency range .025-.05Hz were found to be well below signal levels on most records. The data analysis was restricted to a frequency range in which signal levels are at least a factor of two greater than background noise.

Signal generated noise caused by body wave and higher mode interference, focusing of the primary waves, and multipath interference poses a more serious problem in the data analysis than background noises as will be seen in the next section. Strong excitation of higher modes is common for crustal earthquakes in Central Asia (Forsyth, 1976). Propagation of higher modes in Eurasia (Crampin, 1966) is characterized by very efficient transmission across the stable platform of northern Asia and poor transmission through tectonic provinces in the south. For most records that showed contamination by higher modes or body waves, time variable filtering was able to remove the contaminant since their frequency content and arrival times were outside of the windows determined for the fundamental mode. The effects of focusing and multipathing are expected to be more serious. Focusing and defocusing is the result of refraction of surface waves due to lateral variations in velocity along the wavepath (McGarr, 1969). Studies by Capon (1970) and Bungum and Capon

(1974) concluded that the major cause of multipathing is lateral reflections of waves off continental margins, mountain chains, and mid-ocean ridges. Thus, the type of interference will depend on the frequency range and on the nature of the wavepath between the source and receiver. On the Eurasian continent, for example, no multipathing is observed at Norsar for 40sec Rayleigh waves originating from the Lop Nor nuclear test site, 2000km west of our reference point (Bungham and Capon, 1974). The observations of 20sec Rayleigh waves from Lop Nor showed evidence of multipathing but the results of their analysis may have been affected by the occurence of an interferring earthquake. Figure 3-1.5 shows examples of waveforms used in this study and the results of the moving window analysis on these waveforms. While waveforms observed at northern European stations show little interference, waveforms recorded by stations east and west of the reference point are complex. The contrast is strongest for stations across tectonic provinces of China and the European stations lying north of the Russian platform. Complications enhanced by source effects (e.g. a station lying near a node in the radiation pattern) were minimized by selecting only lobe stations in these examples. Multipath arrivals, well separated from the primary arrival, as in the case of HKC in Figure 3-1.5, were eliminated by the time variable filtering. Considering the lengths of the wavepaths (Aki et al., 1972) and the complexities due to the noise sources discussed above, we were forced to restrict our data analysis to periods longer than 25 seconds.

TABLE 3-1.1: EPICENTRAL DATA FROM ISC

EVENT	DATE mo/dy/yr	ORIGIN TIME hr:mn:sc	ΔO.T. (sec)	LAT (^{o}N)	ΔLAT (^{o})	LONG (^{o}E)	ΔLONG (^{o})	DEPTH (km)	m_b
1	5/11/67	14:50:57	±1.80	39.33	±.028	73.74	±.031	2	5.5
2	8/28/69	03:58:36.7	± .20	39.07	±.032	73.61	±.042	22	5.2
3	9/14/69	16:15:25.6	± .57	39.70	±.022	74.80	±.025	38	5.5
4	7/24/71	11:43:39.3	± .40	39.47	±.019	73.18	±.024	36	5.5
5	10/28/71	13:30:56.4	± .92	41.88	±.020	72.35	±.023	15	5.4
6	11/12/72	17:56:52.9	± .25	38.33	±.016	73.17	±.017	111	5.9
7	8/11/74	20:05:30.9	± .30	39.44	±.014	73.67	±.016	41	5.7
8	8/11/74	21:21:37.1	± .85	39.46	±.018	73.62	±.020	26	5.8
9	8/27/74	12:56:01.0	± .92	39.52	±.021	73.82	±.024	19	5.7

TABLE 3-1.2: LAYER PARAMETERS OF THE PAMIR EARTH MODEL

Depth, km	ρ, g/cm^3	α, km/sec	β, km/sec
0-4	2.41	4.41	2.55
4-30	2.66	5.50	3.18
30-60	2.90	6.50	3.76
60-80	3.36	8.10	4.51
80-90	3.37	8.07	4.46
90-100	3.38	8.02	4.41
100-125	3.39	7.93	4.37
125-150	3.41	7.85	4.35
150-175	3.43	7.89	4.36
175-200	3.46	7.98	4.38
200-225	3.48	8.10	4.42
225-250	3.50	8.21	4.46
250-300	3.53	8.38	4.54
300-350	3.58	8.62	4.68
350-400	3.62	8.87	4.85
400-450	3.69	9.15	5.04
450-500	3.82	9.45	5.21
500-600	4.01	9.88	5.45
600-700	4.21	10.30	5.76
700-800	4.40	10.71	6.03
800-900	4.56	11.10	6.23
900-1000	4.63	11.35	6.32

TABLE 3-1.3: RAYLEIGH WAVE PHASE VELOCITY OF THE PAMIR EARTH MODEL

T sec	C km/sec	T sec	C km/sec
98	3.934	58	3.765
96	3.927	56	3.750
94	3.919	54	3.734
92	3.912	52	3.716
90	3.905	50	3.696
88	3.898	48	3.673
86	3.891	46	3.647
84	3.884	44	3.618
82	3.876	42	3.584
80	3.869	40	3.545
78	3.862	38	3.503
76	3.854	36	3.455
74	3.846	34	3.403
72	3.838	32	3.349
70	3.829	30	3.290
68	3.820	28	3.232
66	3.810	26	3.173
64	3.800	24	3.116
62	3.790	22	3.061
60	3.777	20	3.009

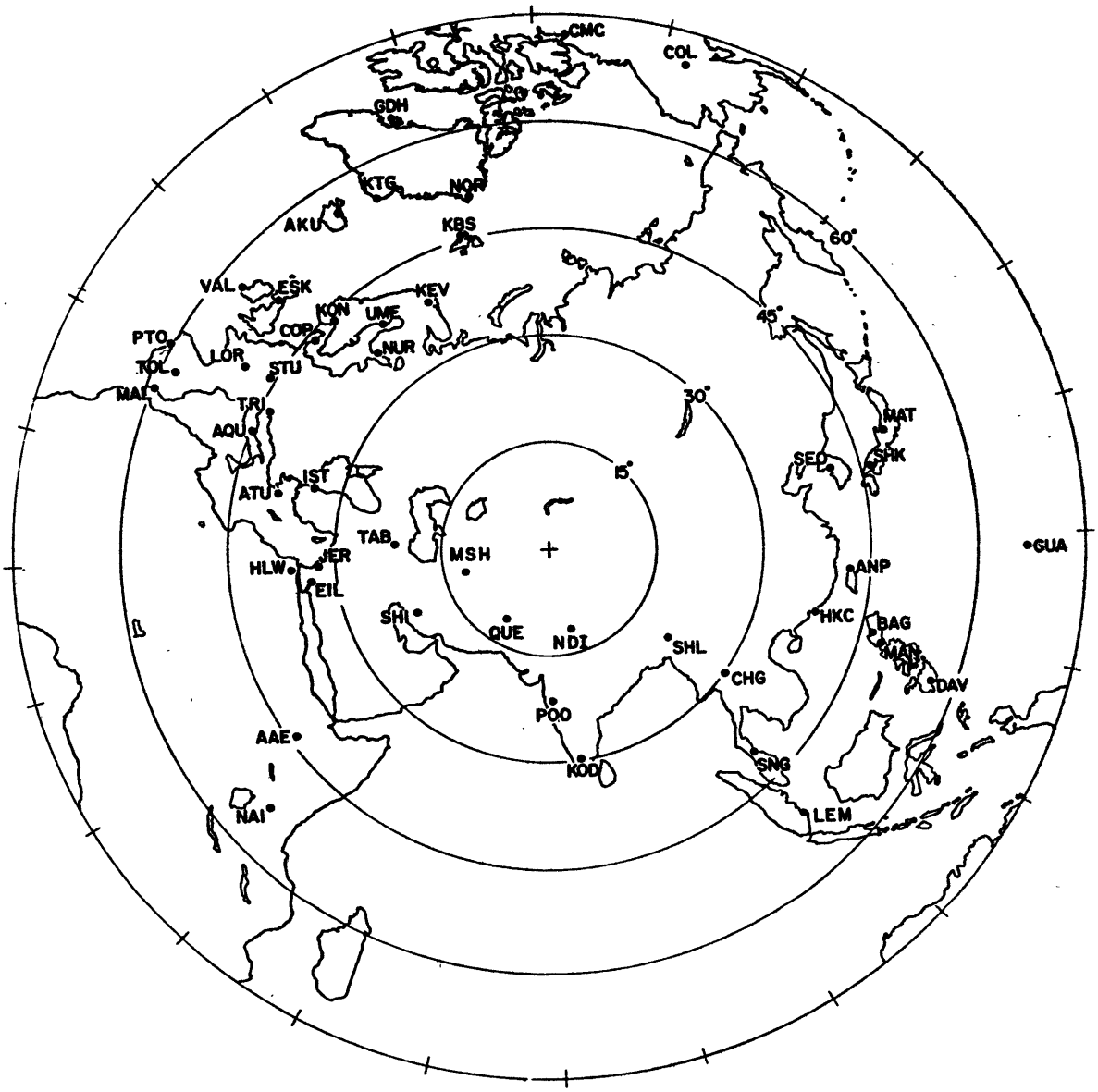

Fig.3-1.1: Azimuthal equadistance projection of Eurasia centered on the reference point in the Pamir Mountains. All stations used in this study are shown on this map.

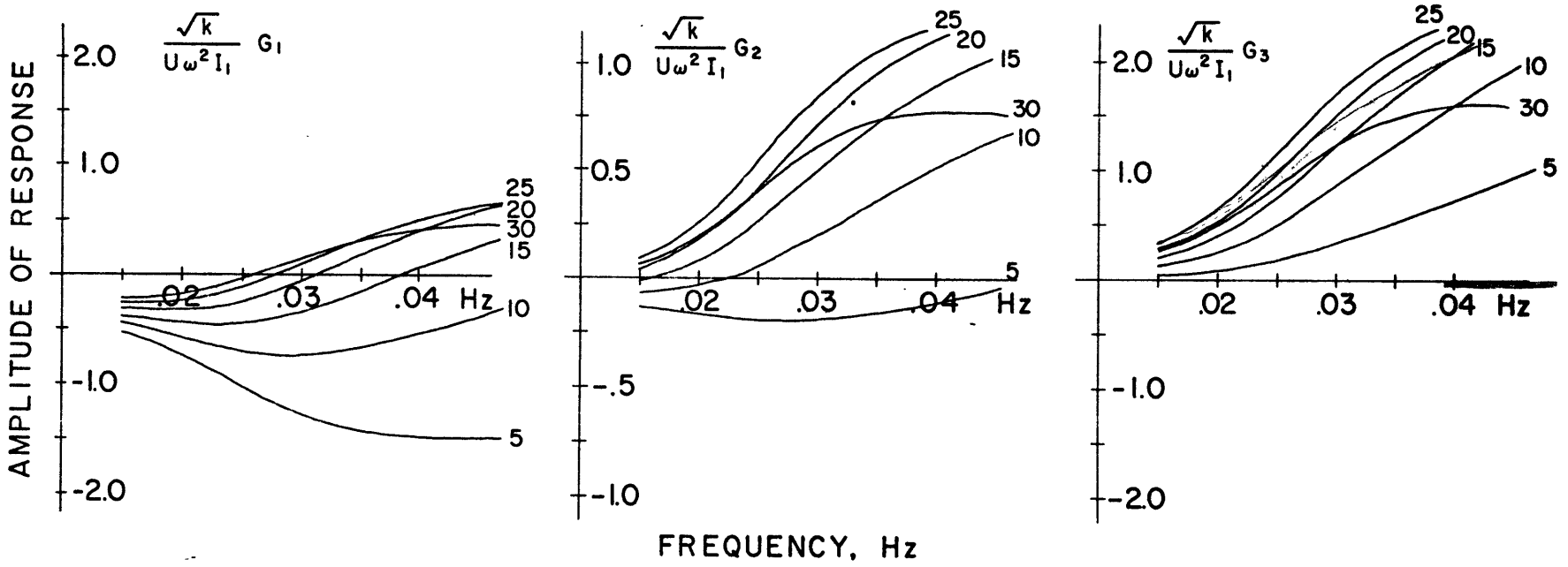

Fig. 3-1.2: Fundamental mode Rayleigh wave responses for six focal depths (km) in the Pamir earth model. Relative amplitudes of responses may be compared with those of the Gutenberg model in Figure 2-4.1.

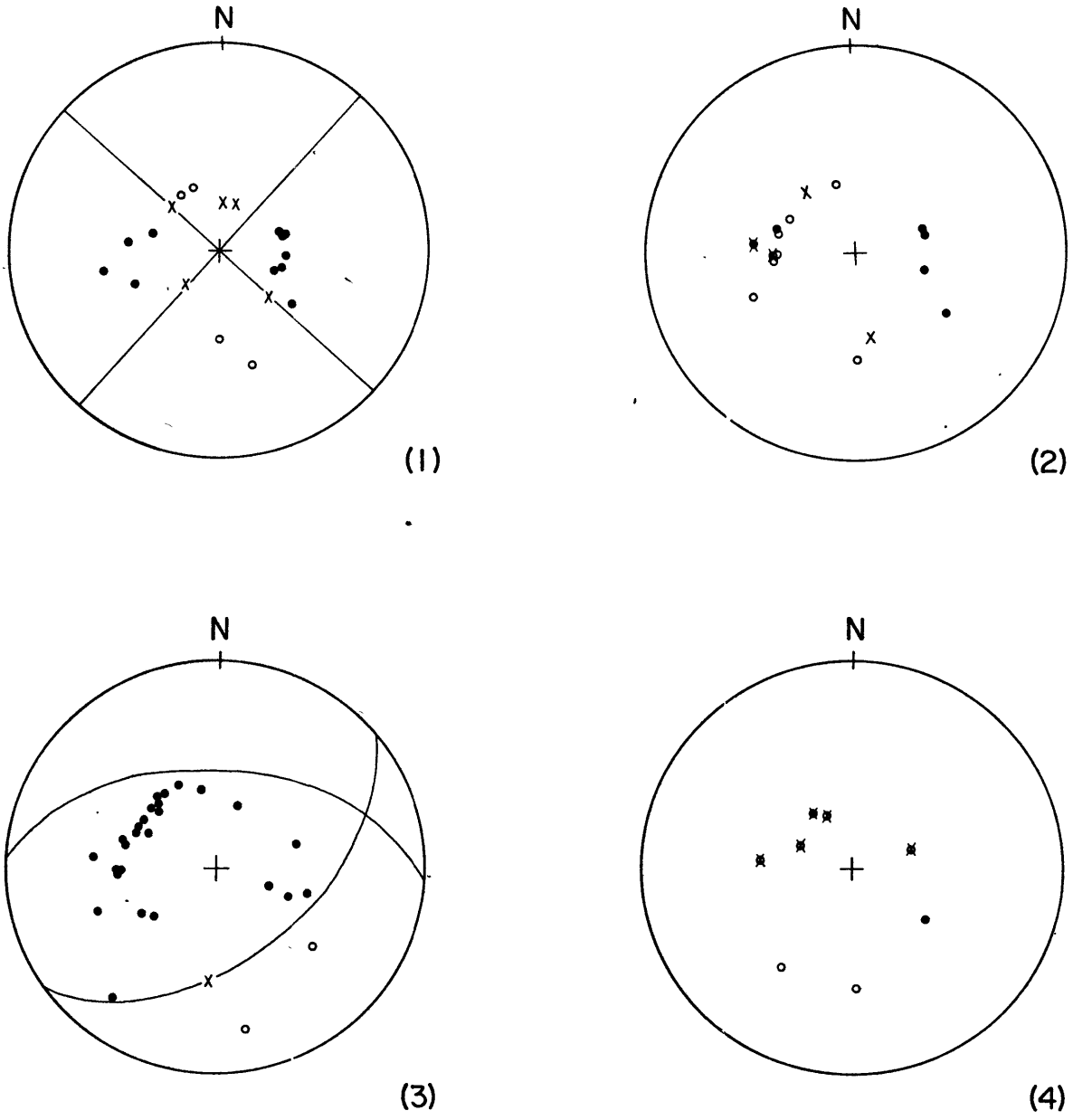

Fig. 3-1.3: P-wave first motions plotted on a stereographic net: ● compression, o dilation, x no P-wave, ✖ uncertain compression, ✖ uncertain dilation. Fault plane solutions for events 1 and 3 were obtained by Molnar et al. (1973).

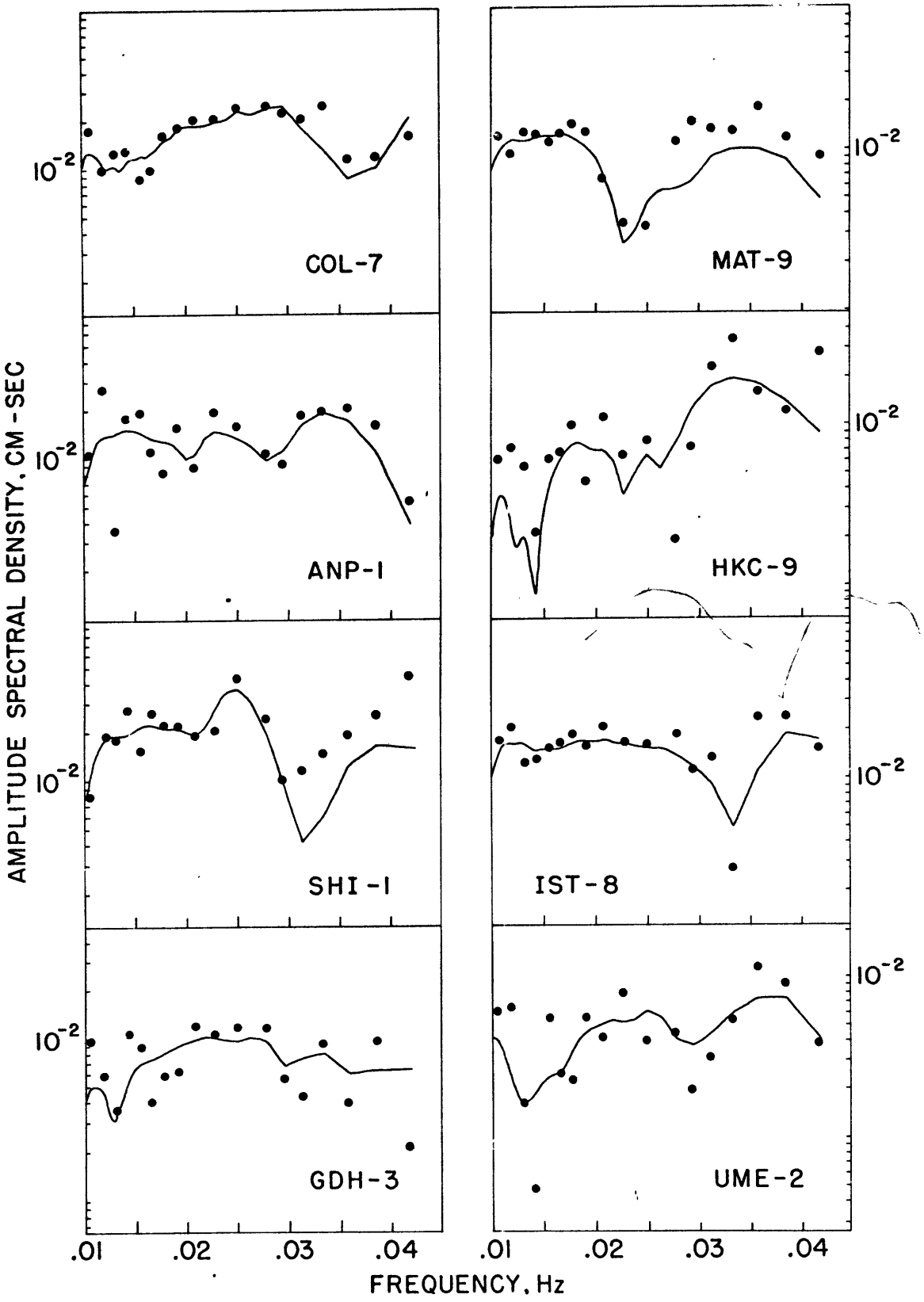

Fig. 3-1.4: Amplitude spectra before (dots) and after (line) applying the time variable filter.

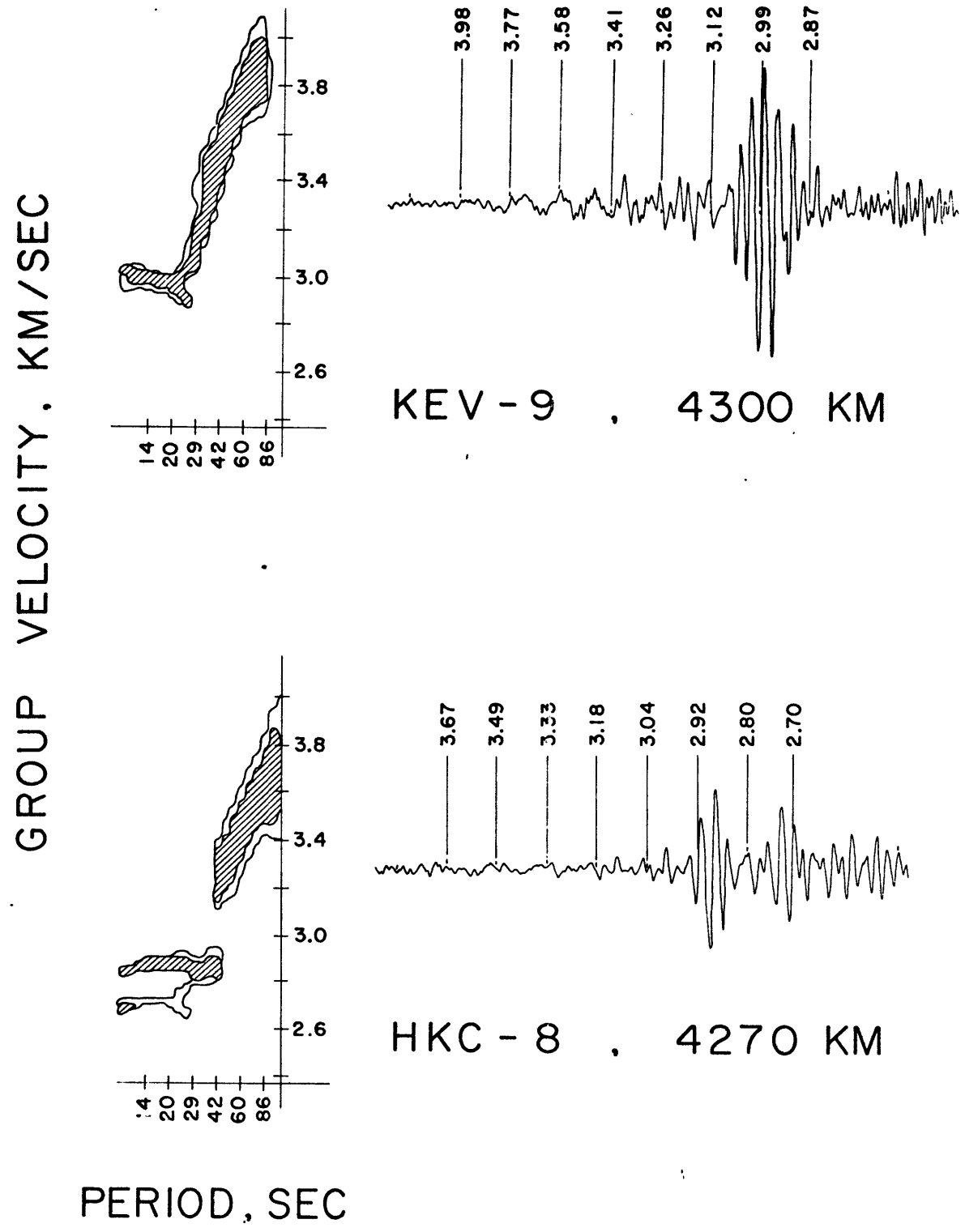

Fig. 3-1.5a: Waveforms and the results of the moving window analysis. Values of group velocity are shown at minute marks along the waveforms. Energy contours are shown at 4 and 8db down from the maximum computed for each period.

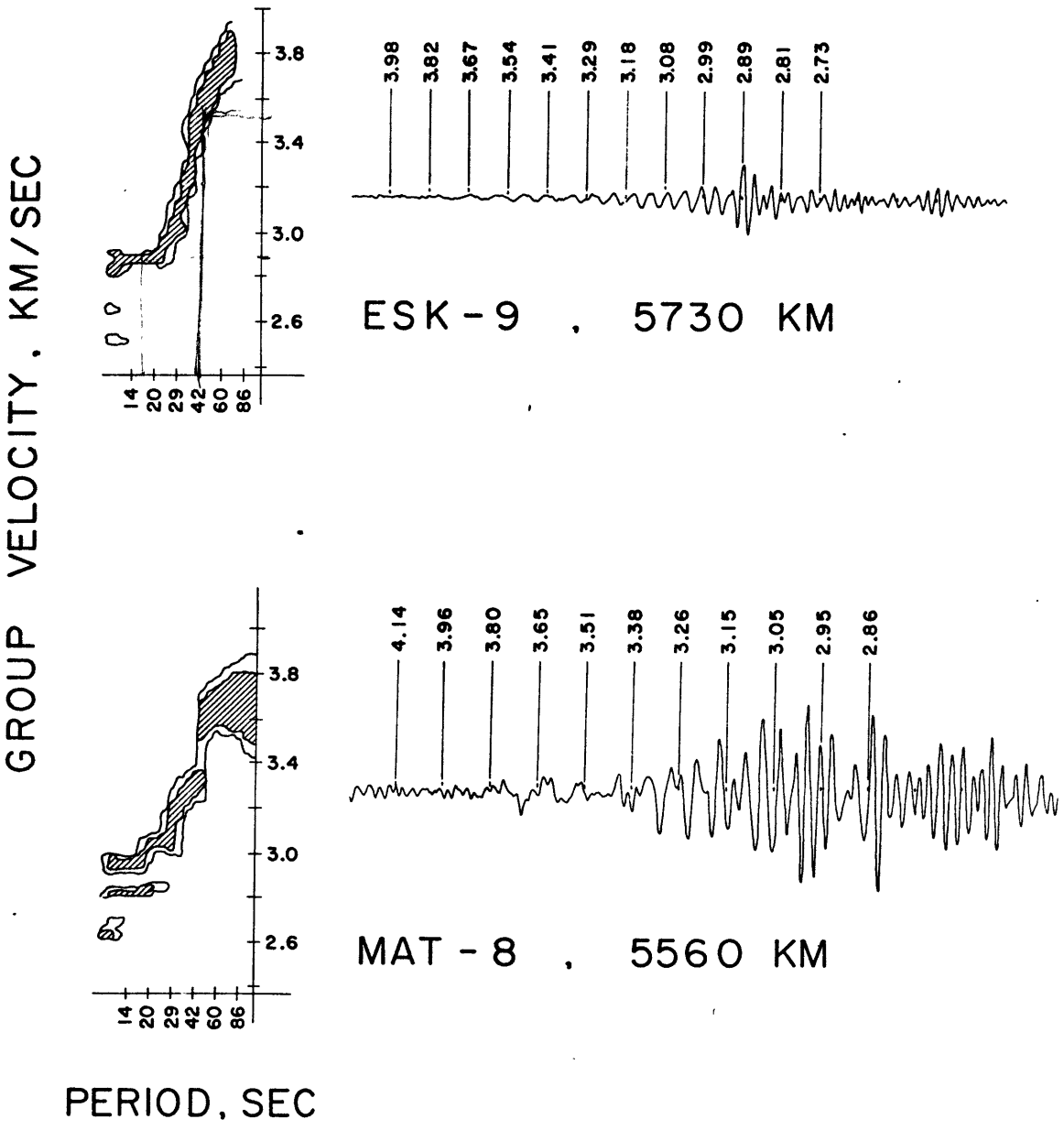

Fig. 3-1.5b: See caption of Figure 3-1.5a.

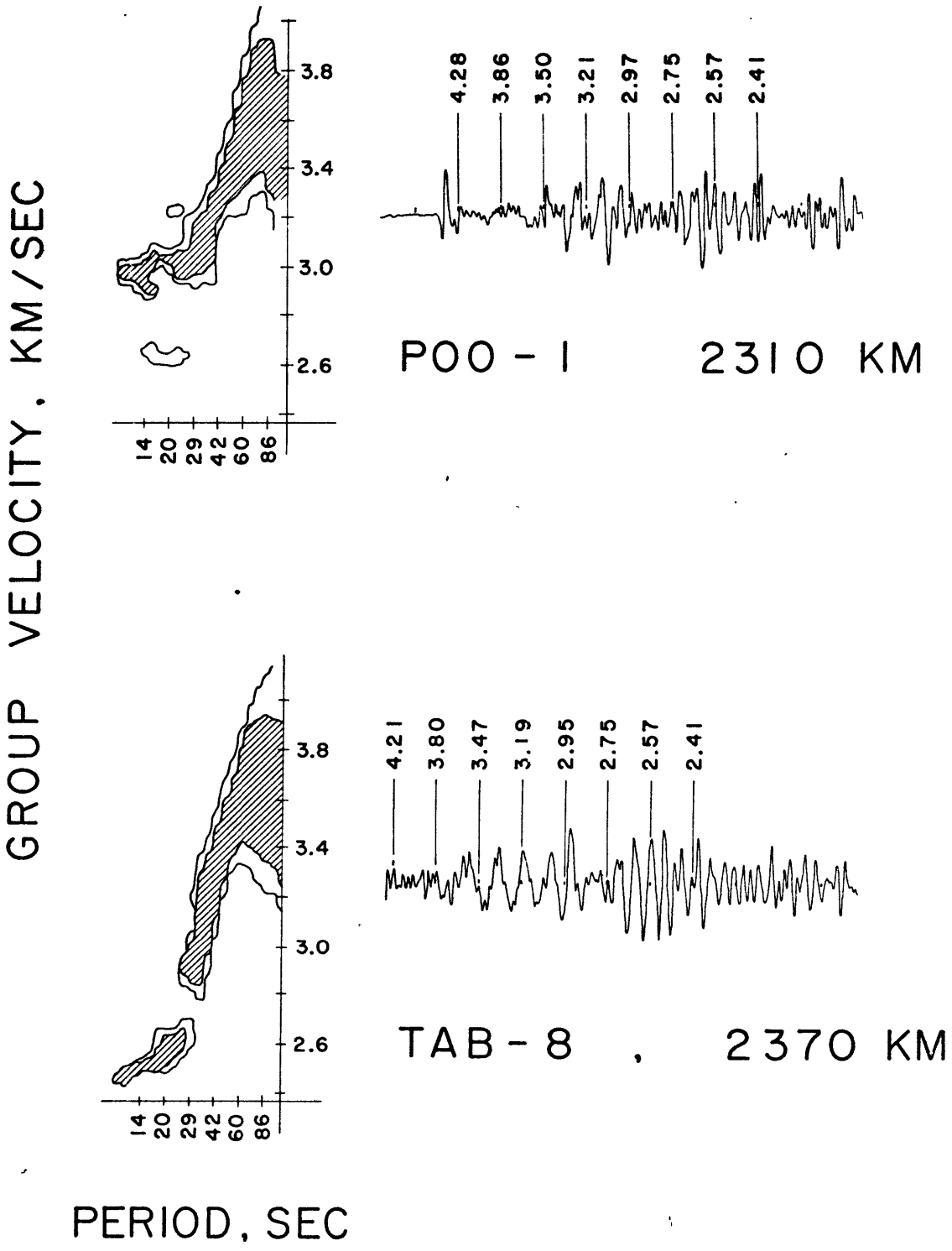

Fig. 3-1.5c: See caption of Figure 3-1.5a.

2. NUMERICAL EXPERIMENTS FOR ERROR ANALYSIS

Section 2-5 addressed the problem of estimating source parameters from complex spectra contaminated by noise in the seismogram. It is important that the effects on the linear inversion of moment tensor due to noise and other sources of error are known. In the following "cause and effect" analysis, synthetic data will be contaminated with noise to demonstrate its effect on the linear inversion.

The synthetic data in the form of amplitude and phase spectra are constructed for twenty stations of the WWSS Network surrounding Eurasia shown in Figure 3-1.1. Table 3-2.1 lists the stations and the source parameters of a theoretical source located at the reference point determined in Section 3-1. The double-couple source has its fault-plane geometry defined by conventions of Tsai and Aki (1970) or equivalently by the moment tensor expressed in east-, north- and up coordinates in Table 3-2.1. The time history of each element in the tensor is a step-function. Using the Gutenberg continental earth model, the fundamental mode Rayleigh wave spectrum is computed at six frequencies over the range .015-.04Hz (1/60, 1/50, 1/40, 1/34, 1/30, 1/26Hz). The amplitude spectra are equalized to a common distance of 4000km.

AMBIENT NOISE. As described in Section 2-5, the linear inversion is appropriate when the signal is contaminated by an additive

background noise. This will be illustrated by adding the noise spectra, collected for the noise analysis in Section 3-1, to the real and imaginary parts of the synthetic spectra using Equation 2-5.1.

Table 3-2.2 gives S/N ratios at various periods averaged over all stations for three cases of different noise levels. The noise amplitudes in cases 2 and 3 are 5 and 25 times larger, respectively, than the amplitudes obtained from the observed noise spectra. The results of the linear inversion which are given in the east-, north-, up-coordinates and in the principal axes coordinate frame are shown in Table 3-2.3. The source depth that minimized the sum of squared residuals, in each case, was the starting depth, 10km. Twelve out of fifteen estimates of the moment tensor elements are within the standard error of the true values as expected.

MULTIPLICATIVE NOISE. As shown in Section 2-5, the effects of focusing, defocusing, and interference cause fluctuations in the amplitude which are proportional to the signal amplitude. If perturbations in the phase spectrum may be neglected as in the case of focusing, multiplicative noise can be simulated by introducing random magnification errors b_i as follows

$$A'_{ik} = b_i A_{ik} \qquad (3\text{-}2.1$$

where A_{ik} is the synthetic amplitude at station i and frequency

k. If an equal number of stations are amplified as are attenuated, the mean of log amplitude over all stations will be left unchanged. The arithmetic mean will over-estimate the true value because this type of noise skews the amplitude distribution.

To see the effect of this noise on the moment tensor inversion six cases are presented in Table 3-2.4. Cases 4-6 have magnification errors of 2 or 0.5 occurring with equal probability. The differences between cases arise from the random permutation of magnifications. Cases 7-9 have magnification errors of either 5 or 0.2.

Table 3-2.5 shows the results of the inversion for these six cases, and, as expected, the tensor elements have been significantly over-estimated. This bias is stronger in cases 7-9 because of the larger magnification errors.

Multiplicative errors are likely to be stronger at high frequencies. In the following analysis, cases 7-9 were modified so that the magnification error became frequency dependent. For low frequencies (1/60, 1/50, 1/40Hz) no magnification error was introduced ($b_{ik}=0$). At high frequencies (1/34, 1/30, 1/26Hz), the errors were the same as those shown in Table 3-2.4. The results of the inversion on cases 7' 8' and 9' are compared with the results of cases 7-9 in Table 3-2.6. The only change appears to be some reduction in the bias of the seismic moment. Note that moment elements which appear on the imaginary part of Equation 2-4.1, namely M_{xz} and M_{yz}, are not changed because they are controlled by data at high frequencies.

Cases 10-12, are examples of multiplicative noise having strong azimuthal dependence, which simulates scattering along preferential azimuths. The network of twenty stations was divided in half. Magnification errors, given in Table 3-2.7, were applied to the stations lying east-west of the source. The remaining stations were not contaminated with noise. This azimuthal pattern is suggested from what we observed in the moving window analysis (Section 3-1). The results of the inversion are given in Table 3-2.8. In addition to biasing the moment, the results indicate a systematic departure of the source mechanism away from a double-couple to a three-couple system.

MULTIPLICATIVE NOISE CAUSED BY PHASE ERRORS. The effect of phase errors introduced into the synthetic spectra are examined in cases 13-21. Amplitude errors have not been introduced into any of the nine cases. The random phase error $\Delta\phi$ is assumed to follow a boxcar distribution at all frequencies and stations. Cases 13-15 allow $\Delta\phi$ to vary from -.125 to .125 cycles, cases 16-18 from -.25 to .25 and cases 19-21 from -.5 to .5 cycles. The last three cases imply complete loss of phase coherency.

The results of the inversion are given in Table 3-2.9. The requirement of phase coherency in this analysis is apparent from the results of cases 19-21. It can be seen in cases 13-18 that the loss of phase coherency leads to a bias that underestimates the moment components without seriously affecting the geometrical property of the tensor (i.e. orientation of principal axes). The

reason for this effect is illustrated in Figure 3-2.1, where Im{S} at 40 seconds is plotted as a function of azimuth. The comparison of the least squares fit between cases with $|\Delta\phi| \leq .125$ and one with $|\Delta\phi| \leq .25$ shows that a greater phase fluctuation tends to make the data points scatter more evenly over positive and negative values, and the fitted curve lies closer to the zero axis.

COMBINED EFFECTS OF AMPLITUDE AND PHASE ERRORS. On the basis of the results given above, the combined effects on the linear inversion due to amplitude fluctuations and phase incoherency is expected to be complicated. In cases 22-27, the amplitude fluctuations are the same as in case 8. In cases 22-24, random phase errors with $|\Delta\phi| \leq .125$ cycles (boxcar distribution) are added to the synthetic phase data. The remaining three cases have $|\Delta\phi| \leq .250$ cycles added. Results of the inversion given in Table 3-2.10 demonstrate the competing effects caused by amplitude and phase errors. Comparing these with the results of case 8, we observed that cases 22-24 have slightly smaller moment components. Increasing the phase error, as we have done in cases 25-27, reduces the moment components significantly. It is apparent that the overestimation of seismic moment due to amplitude fluctuation is considerably reduced by increases in the range of phase errors. The geometric property of the moment tensor also shows greater variability with larger phase errors as seen from the results of these cases.

In summary, when phase coherency prevails as in focusing and defocusing, the amplitude fluctuations will lead to over-estimating the seismic moment (cases 22-24). Phase incoherency which may be introduced by multipathing, will cause the moment to be under-estimated as shown in cases 13-18. The combined errors may introduce less systematic bias but can be expected to increase the uncertainty of the result obtained from the linear inversion.

MULTIPLICATIVE ERRORS FROM THE PATH CORRECTION. In this study, we shall obtain the complex source spectrum, $A^s_{lik}e^{-i\phi^s_{lik}}$, by removing path effects using Equation 2-1.5. The source of error has been assumed to be noises on the seismogram, which are introduced into the calculation of $A^s e^{-i\phi^s}$ through the observed spectrum, $A^o_{lik}e^{-i\phi^o_{lik}}$. Another potential source of error in this calculation is the path correction itself. Since the path correction, $H_{ik}e^{-i\phi_{ik}}$, is a multiplicative factor on the observed spectrum, errors in the estimates of H_{ik} and ϕ_{ik} will enter multiplicatively on the complex source spectrum. Thus, we expect errors in $A^s e^{-i\phi^s}$ proportional to the signal amplitude, regardless of the nature of noises on the seismogram. If the errors in the estimates of H_{ik} and ϕ_{ik} are small, this source of multiplicative error in $A^s e^{-i\phi^s}$ will be second order to seismogram noises and should not have a significant effect on the results of the inversion.

TABLE 3-2.1: SOURCE PARAMETERS AND STATIONS IN THE NUMERICAL ANALYSIS OF ERRORS

SOURCE PARAMETERS:

DEPTH = 10km

SLIP = 170°

DIP = 120°

STRIKE = N30°E

MOMENT = 6 x 10^{24} dyne-cm

-OR-

M_{xx} = 5.11 x 10^{24} dyne-cm

M_{xy} = 2.17 "

M_{yy} = -4.21 "

M_{xz} = 1.03 "

M_{yz} = 2.82 "

M_{zz} = - .90 "

STATIONS:

COL	17° +	JER	269°
MAT	71°	IST	288°
ANP	94°	TRI	299°
HKC	104°	STU	304°
DAV	110°	VAL	313°
CHG	125°	KON	319°
SNG	136°	NUR	322°
KOD	172°	KEV	336°
AAE	236°	GDH	342°
SHI	248°	KBS	346°

+ azimuth measured clockwise from north

TABLE 3-2.2: AMPLITUDE SIGNAL TO NOISE RATIOS IN CASES 1-3

CASE \ PERIOD	60sec	50sec	40sec	34sec	30sec	26sec
1	10	20	25	50	75	75
2	2	4	5	10	25	25
3	0	1	1	2	5	5

TABLE 3-2.3: RESULTS OF THE INVERSION FOR CASES WITH ADDITIVE NOISE

	TRUE	CASE 1	CASE 2	CASE 3
$\Sigma\epsilon_i^2$		.0554	.0628	.282
h = 5km		.0028	.0104	.235
10km	X	.0015	.0094	.235
15km		.0040	.0117	.237
20km			.0194	.245
	$\times 10^{24}$	$\times 10^{24}$	$\times 10^{24}$	$\times 10^{24}$
M_{zz}	- .90*	- .82 ± .06	- .5 ± .3	1.1 ± 1.5
$M_{yy} - M_{xx}$	-9.31	-9.30 ± .06	-9.2 ± .3	-8.8 ± 1.5
M_{xy}	2.17	2.14 ± .04	2.0 ± .2	1.4 ± .9
M_{xz}	1.03	1.02 ± .03	1.0 ± .2	.7 ± .8
M_{yz}	2.82	2.82 ± .04	2.8 ± .2	2.8 ± 1.0
λ_1	6.0	5.94 ± .04	5.7 ± .2	4.5 ± 1.1
λ_2	0.0	0.06 ± .06	.3 ± .3	1.6 ± 1.4
λ_3	-6.0	-6.00 ± .05	-6.0 ± .2	-6.2 ± 1.2
e_1	-106° 14° +	-106° 15°	-106° 15°	-105° 22°
e_2	-221° 59°	-221° 59°	-224° 59°	-238° 59°
e_3	-8° 27°	-8° 27°	-8° 26°	-6° 20°

* Moments in dyne-cm

\+ Orientation of principal axes given by azimuth in degrees from north (positive : clockwise) and dip angle from horizontal plane.

TABLE 3-2.4: MAGNIFICATION ERRORS INTRODUCED ON EACH STATION IN CASES 4-9

STATION \ CASE	4	5	6	7	8	9
AAE	0.5	2.0	0.5	0.2	5.0	0.2
ANP	0.5	2.0	2.0	5.0	5.0	5.0
CHG	2.0	2.0	0.5	5.0	5.0	5.0
COL	0.5	0.5	0.5	5.0	5.0	5.0
DAV	2.0	0.5	0.5	0.2	5.0	5.0
GDH	0.5	0.5	2.0	0.2	0.2	0.2
HKC	2.0	2.0	2.0	5.0	5.0	5.0
IST	2.0	0.5	0.5	0.2	5.0	5.0
JER	0.5	0.5	0.5	0.2	5.0	5.0
KBS	2.0	2.0	2.0	0.2	5.0	0.2
KEV	2.0	0.5	2.0	0.2	5.0	5.0
KOD	0.5	0.5	2.0	0.2	0.2	5.0
KON	0.5	0.5	0.5	5.0	0.2	0.2
MAT	2.0	0.5	2.0	0.2	0.2	5.0
NUR	2.0	2.0	0.5	5.0	0.2	0.2
SHI	2.0	2.0	2.0	0.2	0.2	0.2
SNG	0.5	2.0	2.0	5.0	0.2	0.2
STU	0.5	0.5	2.0	5.0	0.2	0.2
TRI	2.0	2.0	0.5	5.0	0.2	0.2
VAL	0.5	2.0	0.5	5.0	0.2	0.2

TABLE 3-2.5: RESULTS OF INVERSION ON CASES WITH MAGNIFICATION ERRORS

	TRUE	CASE 4	CASE 5	CASE 6	CASE 7	CASE 8	CASE 9
$\Sigma\varepsilon_i^2$		.114	.104	.153	.358	.726	.762
h = 5km		.032	.030	.030	.234	.296	.275
10km	X	.030	.029	.027	.233	.284	.260
15km		.036	.035	.032	.236	.304	.281
20km		.048	.046	.051	.250	.364	.354
	$\times 10^{24}$	$\times 10^{24}$	$\times 10^{24}$	$\times 10^{24}$	$\times 10^{24}$	$\times 10^{24}$	$\times 10^{24}$
M_{zz}	-0.90	$-2.0 \pm .8$	$-2.6 \pm .8$	$-5.5 \pm .7$	0.6 ± 2.2	-3.1 ± 2.4	-2.6 ± 2.3
$M_{yy} - M_{xx}$	-9.31	$-11.7 \pm .8$	$-9.8 \pm .8$	$-14.5 \pm .7$	-13.2 ± 2.2	-29.1 ± 2.4	-32.4 ± 2.2
M_{xy}	2.17	$2.8 \pm .5$	$3.5 \pm .5$	$3.2 \pm .4$	2.0 ± 1.3	2.2 ± 1.5	1.4 ± 1.4
M_{xz}	1.03	$1.1 \pm .2$	$1.2 \pm .2$	$1.5 \pm .2$	$0.3 \pm .5$	$3.8 \pm .6$	$3.6 \pm .6$
M_{yz}	2.82	$3.0 \pm .2$	$3.1 \pm .2$	$3.9 \pm .2$	$5.1 \pm .6$	$7.3 \pm .7$	$6.9 \pm .7$
λ_1	6.0	$7.8 \pm .6$	$7.8 \pm .6$	$8.8 \pm .5$	6.8 ± 1.7	17.3 ± 1.7	18.3 ± 1.6
λ_2	0.0	$-0.8 \pm .6$	$-1.2 \pm .6$	$0.4 \pm .7$	2.8 ± 1.8	-0.4 ± 1.9	-0.3 ± 1.9
λ_3	-6.0	$-7.0 \pm .5$	$-6.6 \pm .5$	$-9.2 \pm .5$	-9.6 ± 1.4	-16.9 ± 1.5	-18.0 ± 1.5
e_1	-106° 14°	-105° 11°	-110° 12°	-105° 15°	-103° 13°	-97° 13°	-95° 11°
e_2	-221° 59°	-213° 58°	-216° 52°	-226° 62°	-217° 60°	-210° 59°	-208° 63°
e_3	-8° 27°	-9° 29°	-12° 35°	-9° 23°	-7° 26°	0° 28°	0° 24°

TABLE 3-2.6: RESULTS OF INVERSION ON CASES WITH FREQUENCY DEPENDENT MAGNIFICATION ERRORS

	TRUE $\times 10^{24}$	CASE 7 $\times 10^{24}$	CASE 7' $\times 10^{24}$	CASE 8 $\times 10^{24}$	CASE 8' $\times 10^{24}$	CASE 9 $\times 10^{24}$	CASE 9' $\times 10^{24}$
M_{zz}	-0.90	0.6 ± 2.2	- 0.4 ± 1.6	- 3.1 ± 2.4	- 0.4 ± 2.1	- 2.6 ± 2.3	0.1 ± 2.1
$M_{yy} - M_{xx}$	-9.31	-13.2 ± 2.2	-11.2 ± 1.6	-29.1 ± 2.4	-20.3 ± 2.0	-32.4 ± 2.2	-22.1 ± 2.0
M_{xy}	2.17	2.0 ± 1.3	2.4 ± 1.0	2.2 ± 1.5	1.7 ± 1.2	1.4 ± 1.4	1.2 ± 1.2
M_{xz}	1.03	0.3 ± .5	0.4 ± .5	3.8 ± .6	3.6 ± .6	3.3 ± .6	3.3 ± .6
M_{yz}	2.82	5.1 ± .6	4.8 ± .6	7.3 ± .7	6.7 ± .7	6.9 ± .7	6.4 ± .7
λ_1	6.0	6.8 ± 1.7	6.6 ± 1.1	17.3 ± 1.7	12.0 ± 1.4	18.3 ± 1.6	12.3 ± 1.4
λ_2	0.0	2.8 ± 1.8	1.9 ± 1.3	- 0.4 ± 1.9	1.4 ± 1.6	- 0.3 ± 1.9	1.7 ± 1.7
λ_3	-6.0	-9.6 ± 1.4	-8.5 ± 1.1	-16.9 ± 1.5	-13.4 ± 1.4	-18.0 ± 1.5	-14.0 ± 1.4
e_1	-106° 14°	-103° 13°	-107° 14°	-97° 13°	-101° 20°	-95° 11°	-98° 19°
e_2	-221° 59°	-217° 60°	-219° 56°	-210° 59°	-223° 55°	-208° 63°	-222° 58°
e_3	-8° 27°	-7° 26°	-9° 30°	0° 28°	0° 27°	0° 24°	1° 25°

TABLE 3-2.7: MAGNIFICATION ERRORS INTRODUCED ON SELECTED STATIONS IN CASES 10-12

STATION \ CASE	10	11	12
AAE	0.2	5.0	5.0
ANP	0.2	0.2	5.0
CHG	0.2	0.2	0.2
DAV	0.2	5.0	0.2
HKC	5.0	5.0	0.2
IST	0.2	5.0	5.0
JER	5.0	5.0	5.0
MAT	5.0	0.2	0.2
SHI	5.0	0.2	0.2
TRI	5.0	0.2	5.0

TABLE 3-2.8: RESULTS OF INVERSION ON CASES WITH AZIMUTHAL BIAS IN MAGNIFICATION ERRORS

	TRUE	CASE 10	CASE 11	CASE 12
$\Sigma\epsilon_i^2$		.461	.347	.367
h = 5km		.172	.161	.170
10km	X	.178	.160	.170
15km		.227	.183	.196
20km		.259	.204	.218
	$\times 10^{24}$	$\times 10^{24}$	$\times 10^{24}$	$\times 10^{24}$
M_{zz}	- .90	- 9.1 ± 2.1	- 5.9 ± 2.0	- 6.4 ± 2.0
$M_{yy} - M_{xx}$	-9.31	-19.5 ± 2.0	-17.6 ± 1.9	-17.5 ± 2.0
M_{xy}	2.17	6.2 ± 1.2	2.8 ± 1.2	3.7 ± 1.2
M_{xz}	1.03	3.0 ± .4	2.4 ± .3	2.4 ± .4
M_{yz}	2.82	4.3 ± .4	3.8 ± .4	4.0 ± .4
λ_1	6.0	16.8 ± 1.5	12.6 ± 1.4	13.2 ± 1.4
λ_2	0.0	- 4.9 ± 1.3	- 3.0 ± 1.3	- 3.2 ± 1.3
λ_3	-6.0	-11.9 ± 1.6	- 9.7 ± 1.3	-10.0 ± 1.3
e_1	-106° 14°	-108° 9°	-101° 9°	-103° 9°
e_2	-221° 59°	-203° 33°	-200° 43°	-202° 41°
e_3	-8° 27°	-4° 56°	-1° 45°	-3° 47°

TABLE 3-2.9: RESULTS OF INVERSION ON CASES WITH PHASE ERRORS

	TRUE	CASE 13	CASE 14	CASE 15	CASE 16	CASE 17	CASE 18	CASE 19	CASE 20	CASE 21
$\Sigma\varepsilon_i^2$		.055	.055	.055	.055	.055	.055	.055	.055	.055
h = 5km		.011	.011	.011	.031	.029	.031	.054	.054	.054
10km	X	.010	.010	.010	.031	.028	.030	.054	.055	.054
15km		.011	.011	.013	.032	.028	.031	.053	.055	.054
20km		.017	.017	.020	.047	.030	.035	.053	.055	.054
	$\times 10^{24}$	$\times 10^{24}$	$\times 10^{24}$	$\times 10^{24}$	$\times 10^{24}$	$\times 10^{24}$	$\times 10^{24}$	$\times 10^{24}$	$\times 10^{24}$	$\times 10^{24}$
M_{zz}	-0.90	-0.58 ± .30	-0.96 ± .28	-1.05 ± .27	-0.5 ± .6	-0.8 ± .5	-1.1 ± .6	0.4 ± .8	0.6 ± .9	-0.6 ± .9
$M_{yy} - M_{xx}$	-9.31	-8.27 ± .30	-8.03 ± .27	-8.26 ± .26	-7.0 ± .5	-5.8 ± .5	-6.0 ± .6	0.0 ± .8	0.3 ± .9	-1.0 ± .9
M_{xy}	2.17	1.83 ± .18	2.05 ± .16	2.12 ± .16	1.4 ± .3	1.3 ± .3	2.2 ± .4	-0.4 ± .5	-0.4 ± .5	0.3 ± .5
M_{xz}	1.03	0.92 ± .18	1.04 ± .18	0.93 ± .18	0.5 ± .3	0.7 ± .3	0.7 ± .3	0.2 ± .4	-0.4 ± .4	0.1 ± .4
M_{yz}	2.82	2.70 ± .22	2.79 ± .21	2.54 ± .22	1.3 ± .4	2.5 ± .3	1.5 ± .3	0.9 ± .4	0.0 ± .4	0.7 ± .4
λ_1	6.0	5.2 ± .2	5.4 ± .2	5.5 ± .2	4.2 ± .4	3.9 ± .4	4.5 ± .4			
λ_2	0.0	0.3 ± .3	0.0 ± .3	-0.2 ± .3	-0.2 ± .6	0.4 ± .5	-0.8 ± .5			
λ_3	-6.0	-5.5 ± .2	-5.4 ± .2	-5.4 ± .2	-3.9 ± .4	-4.3 ± .4	-3.8 ± .4			
e_1	-106° 14°	-106° 16°	-108° 16°	-107° 14°	-102° 9°	-108° 17°	-110° 12°			
e_2	-221° 59°	-222° 58°	-221° 55°	-220° 58°	-216° 68°	-220° 51°	-223° 62°			
e_3	-8° 27°	-8° 27°	-8° 31°	-9° 28°	-9° 20°	-6° 34°	-14° 25°			

TABLE 3-2.10: RESULTS OF INVERSION ON CASES WITH PHASE ERRORS AND WITH MAGNIFICATION ERRORS (CASE 8)

	CASE 8	CASE 22	CASE 23	CASE 24	CASE 25	CASE 26	CASE 27
$\Sigma\varepsilon_i^2$	.726	.726	.727	.726	.727	.727	.727
h = 5km	.296	.368	.374	.380	.562	.542	.583
10km	.284	.365	.360	.374	.551	.544	.580
15km	.304	.401	.369	.397	.545	.554	.564
20km	.364	.475	.416	.448	.559	.583	.551
	$\times 10^{24}$	$\times 10^{24}$	$\times 10^{24}$	$\times 10^{24}$	$\times 10^{24}$	$\times 10^{24}$	$\times 10^{24}$
M_{zz}	-3.1 ± 2.4	-4.2 ± 2.6	-2.6 ± 2.4	-3.6 ± 2.5	-0.8 ± 2.5	-2.0 ± 2.7	-3.1 ± 2.6
$M_{yy} - M_{xx}$	-29.1 ± 2.4	-27.3 ± 2.6	-26.1 ± 2.4	-26.0 ± 2.4	-18.0 ± 2.4	-19.2 ± 2.7	-13.8 ± 2.6
M_{xy}	2.2 ± 1.5	2.9 ± 1.6	2.1 ± 1.5	2.7 ± 1.5	0.7 ± 1.5	2.8 ± 1.6	1.6 ± 1.6
M_{xz}	3.8 ± 0.6	2.7 ± 0.8	4.3 ± 0.8	2.5 ± 0.9	3.6 ± 1.2	1.8 ± 1.2	2.8 ± 1.2
M_{yz}	7.3 ± 0.7	5.0 ± 0.9	6.6 ± 1.0	6.2 ± 1.0	4.6 ± 1.4	3.8 ± 1.3	5.7 ± 1.4
λ_1	17.3 ± 1.7	16.5 ± 1.8	15.8 ± 1.7	15.6 ± 1.7	10.8 ± 1.7	11.4 ± 1.9	9.7 ± 1.8
λ_2	-0.4 ± 1.9	-2.4 ± 2.2	-0.7 ± 2.0	-0.9 ± 2.1	0.0 ± 2.2	-0.9 ± 2.4	0.3 ± 2.1
λ_3	-16.9 ± 1.5	-14.2 ± 1.7	-15.2 ± 1.6	-14.7 ± 1.7	-10.8 ± 1.8	-10.5 ± 1.9	-10.1 ± 2.0
e_1	-97° 13°	-97° 9°	-98° 16°	-98° 10°	-97° 22°	-100° 10°	-103° 17°
e_2	-210° 59°	-205° 62°	-214° 57°	-205° 59°	-220° 57°	-212° 65°	-211° 45°
e_3	0° 28°	-3° 26°	0° 28°	-3° 29°	3° 26°	-6° 23°	2° 40°

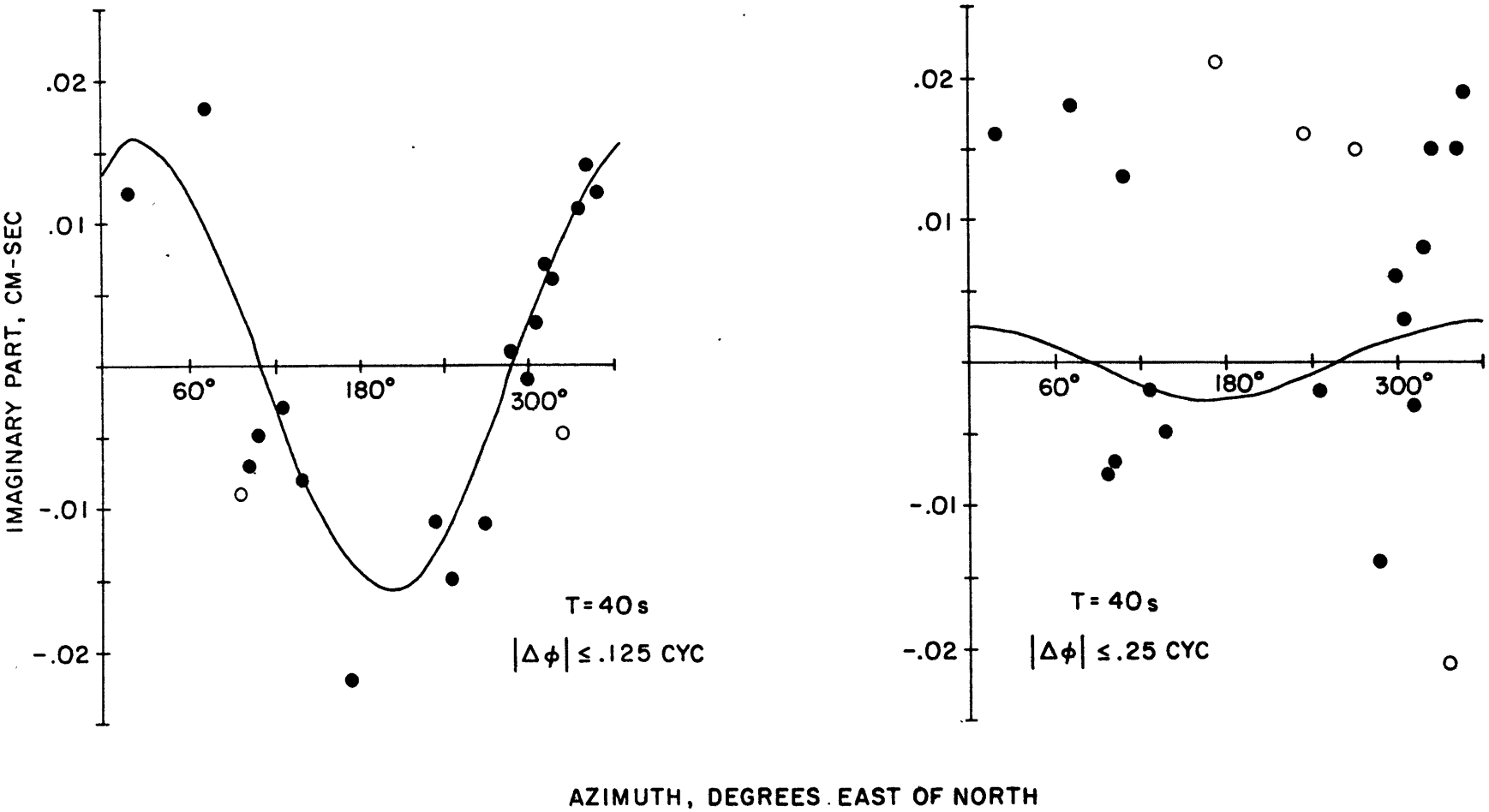

Fig. 3-2.1: Least squares fit to the data on the imaginary part for two cases having phase errors. On the left phase errors are less than .125cyc; on the right less than .25cyc. The number of bad points (o) increases with the size of phase errors.

3. ERRORS IN THE AUXILIARY DATA AND ASSUMPTIONS

For the remainder of this chapter we will study the effects on the linear inversion due to systematic errors caused by uncertainties in the epicentral data and in our assumptions about the source and medium models.

ERRORS IN EPICENTRAL DATA. Mislocation of the source will introduce an error in the calculation of the initial phase which depends on both frequency and azimuth. The difference between the observed phase delay for the true epicenter ϕ_i^o and the phase delay for the assumed epicenter ϕ'^o_i at the i^{th} station is

$$\phi_i^o - \phi'^o_i = \frac{\omega b \cos\gamma_i}{C} \qquad (3\text{-}3.1)$$

where ω is frequency, C is phase velocity, γ_i is the azimuth of the i^{th} station measured from the line connecting the mislocated epicenter to the true epicenter, and b is the distance between the mislocated epicenter and the true epicenter. Table 3-3.1 shows the results of the linear inversion on synthetic spectra with a location error of 15km in a direction N45^{o}W of the true epicenter. The location error appears to bias the estimate of source depth. In Figure 3-3.1 the synthetic amplitude data, which is unaffected by the location error, and the calculated amplitudes based on the source parameters obtained in Table 3-3.1 are plotted as a function of azimuth. Although the differences are small in this example, it illustrates that epicentral loca-

tion errors may cause a lack of fit between observed and calculated amplitudes.

An origin time error, Δt, will result in phase shifts equal to $\omega\Delta t$ on all stations. In the following examples, we introduced a 2sec and 5sec origin time error into the synthetic source spectra with the results of the inversion given in Table 3-3.2. The estimates of the moment elements, M_{xz} and M_{yz}, which appear on the imaginary part of Equation 2-4.2, are affected more by these errors than elements on the real part. This is due to the fact that the real part of the complex source spectrum, S, happens to be much larger than the imaginary part for the particular source geometry examined in our analysis. Let $\Delta\phi$ be the phase error introduced into S so that we have $Se^{i\Delta\phi}$ instead of S. Then, for small $\Delta\phi$, the real part is $Re\{S\} - \Delta\phi Im\{S\}$ and the imaginary part is $Im\{S\} + \Delta\phi Re\{S\}$. If $Re\{S\}$ is an order of magnitude larger than the imaginary part, the error, $\Delta\phi Re\{S\}$, will be comparable to $Im\{S\}$ and will cause strong effects on the estimates of M_{xz} and M_{yz}.

Considering the typical errors in epicentral data reported by ISC, another case was computed to illustrate the combined effect of an 8km epicentral mislocation and a 2sec origin time error. The results of the linear inversion are given in Table 3-3.3.

ERRORS IN THE SOURCE MODEL. The earthquake is assumed to be a point source with a step-function time dependence. This section

considers the possibility of errors in these assumptions and their effects on the linear inversion.

Finiteness of the source will affect both amplitude and phase spectrum of surface waves. Ben-Menahem (1961) found the finiteness factor on the amplitude spectrum for a propagating rupture to be

$$\left|\frac{\sin x_i}{x_i}\right| , \quad x_i = \frac{\omega L}{2} \left(\frac{1}{V} - \frac{\cos \gamma_i}{C}\right) \qquad (3\text{-}3.2)$$

where L is fault length, V is rupture velocity, C is phase velocity, γ_i is azimuth of the station measured from the direction of rupture propagation, and ω is frequency. The effect is negligible for wavelengths much longer than the fault dimensions. Considering the shortest period in our analysis and the size of the events to be studied, the finiteness effects on amplitude are quite small as a simple calculation shows. Assuming L=15km, V=3km/sec, C=3.2km/sec, the finiteness factor on the amplitude of 26sec waves in the direction where maximum effect occurs, γ=180, is .79, i.e. the amplitude of the finite source about 20% less than the point source amplitude.

The phase delay caused by finiteness of a propagating rupture may be written as follows (Ben-Menahem,1961)

$$\phi_i = \frac{\omega L}{2} \left(\frac{1}{V} - \frac{\cos \gamma_i}{C}\right) \qquad (3\text{-}3.3)$$

which is the same as X in the expression above for the amplitude

finiteness factor. The first term is independent of azimuth and has the same effect on the phase spectrum as an equivalent origin time error. The other term is equivalent to an epicentral mislocation error. Therefore, the effects of finiteness on the linear inversion are expected to be similar to those caused by origin time and epicentral mislocation errors. For the above assumed fault length and rupture velocity, the equivalent origin time and mislocation errors are 2.5sec and 7.5km, respectively. Based on results given in Table 3-3.3, we may conclude that finiteness errors in the initial phase will not cause serious effects on the estimates of the moment tensor elements.

We have assumed that each moment tensor element behaves as a step-function in time. In light of the evidence summarized by Aki (1967, 1972) and Chouet et al. (1977), the step-function assumption is valid for periods longer than 20sec when the magnitude of the source is six or less.

ERRORS IN THE MEDIUM MODEL. The earth structure assumed in Section 3-1 should be regarded as an approximation to the actual source region structure. With present computational abilities, we are restricted to plane-layered earth models. There could be large differences between our assumed model and the best plane-layered model representing the response of the true medium. The purpose of this section is to see what effects differences in the assumed earth structure would have on recovering source parameters.

The model used to calculate the synthetic spectra was a standard continental earth model (for layer parameters, see Table 2-4.1). The Pamir model (see Table 3-1.2) is considerably different from the standard model. The ideal plane-layered model representing the excitation of surface waves in Central Asia may well be bracketed by these two models. Therefore, it is of interest to investigate the effect of inverting the synthetic, error-free spectra using the Pamir model. The results are shown in Table 3-3.4. Neither source depth nor the geometric property of the moment tensor is biased by the differences in these earth models. This is consistent with previous results from focal depth and focal mechanism studies based on amplitude (Tsai and Aki, 1970; Mendiguren, 1971) and from studies based on initial phase delay (Weidner, 1972; Frez and Schwab, 1976). It is noteworthy that the seismic moment obtained in Table 3-3.4 is reduced by a factor of two. This may be regarded as an upper limit on the possible bias in the estimate of moment due to uncertainties in the assumed earth model.

The error in ϕ^E (Equation 2-1.3) due to an error in the phase velocity curve of Pamir model will be equal to the phase delay, $\omega(\bar{X}_i - X_{ji})/C$, times the fractional error in phase velocity. The phase delay is largest at short period (26sec) and equals 1.2 cycles for a distance of 100km. Based on comparisons with observed phase velocities in the Pamir Mountains (Savarensky et al., 1969), the error in the calculated velocity is likely to be less than 2-3% and certainly less than 5%. A 5% error represents

TABLE 3-3.1: RESULTS OF INVERSION WHEN EPICENTER IS MISLOCATED 15KM N45°W OF THE TRUE EPICENTER

	TRUE	$\Sigma\epsilon_i^2$
h = 2.5km		.0560
5.0km		.0110
7.5km		.0096
10.0km		.0089
12.5km	X	.0086
15.0km		.0082
17.5km		.0064
20.0km		.0050
25.0km		.0043
30.0km		.0069
35.0km		.0120
40.0km		.0130
		.0150

FOCAL DEPTH		20km	10km
	$\times 10^{24}$	$\times 10^{24}$	$\times 10^{24}$
M_{zz}	-0.90	$1.4 \pm .1$	$-1.4 \pm .4$
$M_{yy} - M_{xx}$	-9.31	$-13.2 \pm .3$	$-5.4 \pm .4$
M_{xy}	2.17	$1.8 \pm .1$	$1.0 \pm .2$
M_{xz}	1.03	$1.7 \pm .1$	$2.1 \pm .1$
M_{yz}	2.82	$3.3 \pm .1$	$4.1 \pm .1$
λ_1	6.0	$7.0 \pm .2$	$5.2 \pm .3$
λ_2	0.0	$1.5 \pm .1$	$0.7 \pm .3$
λ_3	-6.0	$-8.5 \pm .2$	$-5.9 \pm .3$
e_1	-106° 14°	-102° 23°	-116° 29°
e_2	-221° 59°	-241° 60°	-226° 32°
e_3	-80° 27°	-5° 18°	6° 44°

TABLE 3-3.2: RESULTS OF INVERSION WHEN ORIGIN TIME IS IN ERROR BY 2 AND 5 SECONDS

	TRUE	2 SEC	5 SEC
$\Sigma\epsilon_i^2$		.0560	.0550
h = 2.5km		.0084	.0317
5.0km		.0075	.0309
7.5km		.0068	.0302
10.0km	X	.0065	.0295
12.5km		.0071	.0291
15.0km		.0091	.0296
17.5km		.0123	.0310
20.0km		.0177	.0337
h		10km	10km
	$\times 10^{24}$	$\times 10^{24}$	$\times 10^{24}$
M_{zz}	-0.90	$-0.8 \pm .3$	$-0.5 \pm .5$
$M_{yy} - M_{xx}$	-9.31	$-9.3 \pm .2$	$-7.2 \pm .5$
M_{xy}	2.17	$2.3 \pm .2$	$2.0 \pm .3$
M_{xz}	1.03	$0.8 \pm .1$	$0.3 \pm .3$
M_{yz}	2.82	$2.0 \pm .2$	$0.0 \pm .3$
λ_1	6.0	$5.9 \pm .2$	$4.3 \pm .4$
λ_2	0.0	$-0.4 \pm .3$	$-0.5 \pm .5$
λ_3	-6.0	$-5.5 \pm .2$	$-3.8 \pm .4$
e_1	-106^o 14^o	-105^o 11^o	-105^o 3^o
e_2	-221^o 59^o	-221^o 66^o	-305^o 86^o
e_3	-8^o 27^o	-11^o 21^o	-195^o 1^o

TABLE 3-3.3: RESULTS OF INVERSION WHEN EPICENTER AND ORIGIN TIME ARE IN ERROR BY 8KM N45°W AND 2 SECONDS, RESPECTIVELY

	TRUE	
$\Sigma\varepsilon_i^2$		
h = 5km		.0560
10km	X	.0098
15km		.0080
20km		.0085
		.0127
	$\times 10^{24}$	$\times 10^{24}$
M_{zz}	-0.90	$-0.92 \pm .3$
$M_{yy} - M_{xx}$	-9.31	$-7.90 \pm .3$
M_{xy}	2.17	$1.90 \pm .2$
M_{xz}	1.03	$1.40 \pm .1$
M_{yz}	2.82	$3.10 \pm .1$
λ_1	6.0	$5.6 \pm .2$
λ_2	0.0	$0.1 \pm .2$
λ_3	-6.0	$-5.6 \pm .2$
e_1	-106° 14°	-109° 20°
e_2	-221° 59°	-225° 51°
e_3	-8° 27°	-6° 32°

TABLE 3-3.4: RESULTS OF THE INVERSION WHEN THE ASSUMED EARTH MODEL IS ERRONEOUS

	TRUE	
$\Sigma\epsilon_i^2$		.0560
h = 2.5km		.0044
5.0km		.0029
7.5km		.0013
10.0km	X	.0005
12.5km		.0024
45.0km		.0095
17.5km		.0230
20.0km		.0360
	$\times 10^{24}$	$\times 10^{24}$
M_{zz}	-0.90	$-0.48 \pm .06$
$M_{yy} - M_{xx}$	-9.31	$-4.73 \pm .05$
M_{xy}	2.17	$1.05 \pm .03$
M_{xz}	1.03	$0.50 \pm .01$
M_{yz}	2.82	$1.35 \pm .01$
λ_1	6.0	$3.01 \pm .04$
λ_2	0.0	$-0.04 \pm .05$
λ_3	-6.0	$-2.95 \pm .04$
e_1	-106° 14°	-105° 13°
e_2	-221° 59°	-219° 59°
e_3	-8° 27°	-8° 27°

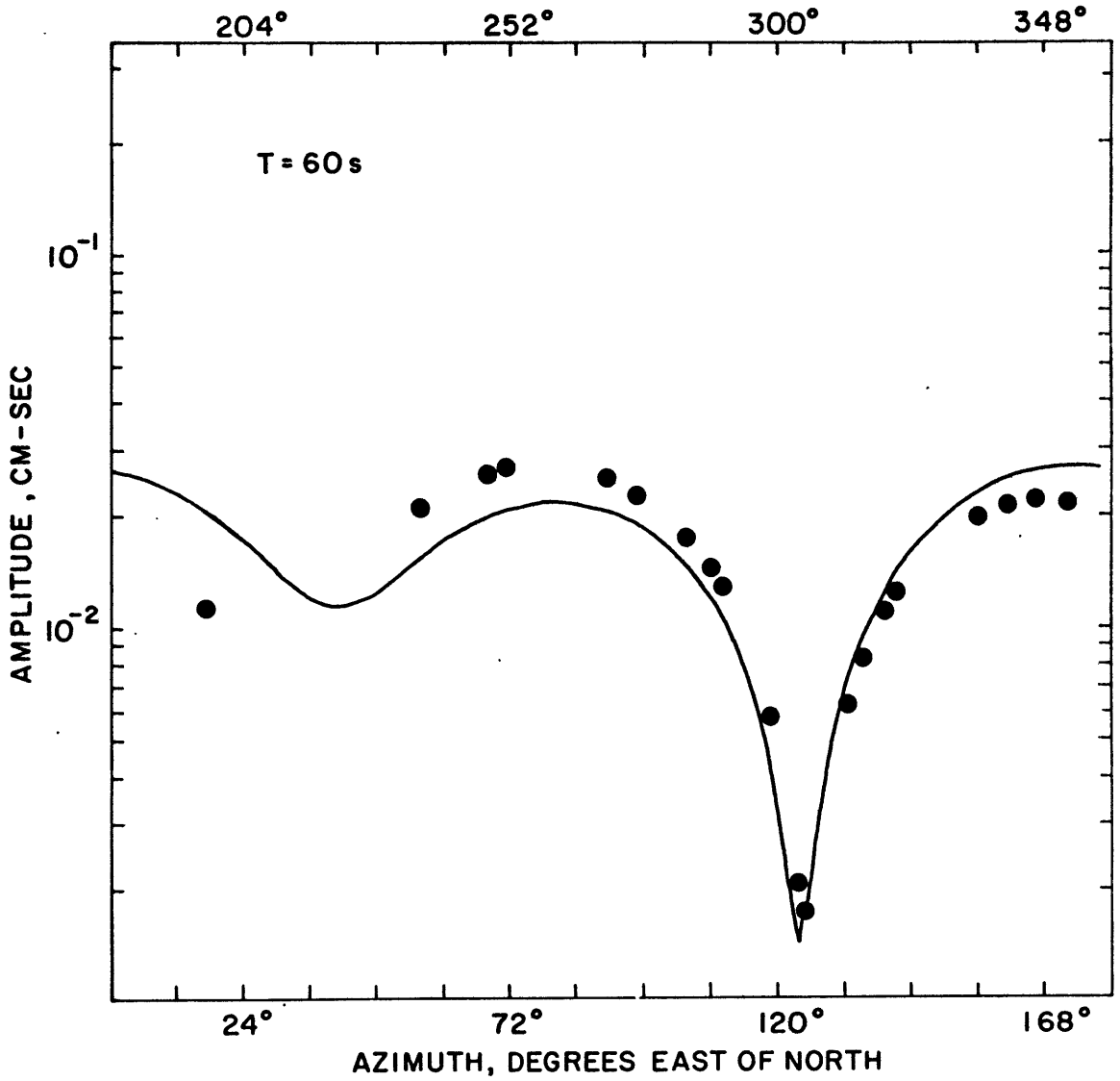

Fig. 3-3.1: Bias in the computed amplitude pattern from the linear inversion due to systematic errors in the phase data. In this case, errors are caused by a 15km epicentral location error.

at most an error of .06 cycles in the calculation of ϕ^E at the shortest analyzed period. Thus, errors in ϕ^E due to the assumed source region phase velocity will not be large enough for concern.

4. SUMMARY

Approximately two hundred and fifty seismograms from fifty WWSSN stations were digitized over the time window of the surface wave arrivals. These surface waves originated from earthquakes in a source region in Central Asia north of the Pamir thrust zone.

The amplitude of background noise on most seismograms was high enough to limit the analysis to periods less than 70 seconds. Signal complexity due to adverse propagation effects limits the analysis to periods longer than 25 seconds. There was an indication that the signal complexity has regional variation.

The presence of random additive errors in the complex spectra due to background noise does not pose difficulties for recovering reliable source parameters via the moment tensor inversion method. This is not true of multiplicative errors caused by signal-generated noise. Amplitude fluctuations leads to significant over-estimation of the moment tensor elements when phase is coherent, as is the case for focusing and defocusing. Phase incoherency caused by multipathing leads to significant underestimation of the moment elements. The combined errors result in

less systematic biases, however the uncertainty of the estimates is greater.

In our analysis of errors in the epicentral data, a mislocation of 15km was seen to bias the estimate of the focal depth obtained from the minimum in the residuals of repeated moment tensor inversions. Origin time errors as large as 5 seconds did not seriously affect the estimate of focal depth, but did affect the estimates of some of the tensor elements.

Regarding the assumption of a point source, we argue that amplitude errors are too small for concern based on expected fault dimensions for the size of events in our analysis. Possible phase errors due to this assumption are the same as those introduced by an equivalent mislocation and origin time error. Again based on expected fault dimensions, the phase errors should not be large enough to seriously affect the estimates of source parameters.

Large differences in the assumed source region structure do not affect the estimate of the source depth nor the geometric property of the moment tensor. The phase velocity of our assumed structure may be in error by as much as 5% of the true source region dispersion curve. Nevertheless, the error in ϕ^E due to erroneous phase velocities will not be large enough for concern.

CHAPTER IV

RESULTS OF ANALYSIS

This chapter presents the results of the analysis in three parts: 1) the initialization of our iterative method, 2) the iteration itself, and 3) the final estimates of propagation parameters.

Section 4-1 concerns the initialization step using the earthquake pair method of Weidner and Aki (1973). We successfully implemented this method to obtain our first reference events and initial estimates of the propagation parameters.

Section 4-2 is an "in-depth" analysis of the results from the iteration, particularly the results relating to source effects and the impact of errors. We evaluate the possibility of bias in the results of the linear inversion due to random amplitude and phase errors by comparing them with the outputs of the logarithmic fitting described in Section 2-5. This leads to some modification of the straight least squares inversion method. An analysis of the residuals obtained from the inversions as a function of trial depth turns up an unexpected result: we find that the residuals have two minima, leaving the focal depth determination in doubt. Factors causing this result are discussed and we show ways that the ambiguity in the depth may be resolved. Next, we investigate the systematic errors arising from the epicentral data reported by the ISC. Having exhausted the possibilities of serious errors from all sources, we present the results of the

linear inversions on all the events in our chosen source region. The section concludes with a detailed analysis of the residuals.

Final estimates of the propagation parameters, H_{ik} and ϕ_{ik}, are converted into attenuation coefficients and phase velocities for presentation in Section 4-3. Estimates of the errors in these measurements are made. Section 2-5 showed two methods to calculate the propagation parameters depending on the statistical properties of noise on the seismogram. By comparing the results of calculating H_{ik} two ways, we answer some questions about the nature of noises on the seismogram. Finally, a look at the azimuthal changes of the path parameters around the reference point gives qualitatively an insight of the regional variations of path effects and their correlation with land forms on the Eurasian continent.

1. INITIALIZATION

As described in Section 2-2, the method of Weidner and Aki (1973) requires two earthquakes having different P-wave solutions. By virtue of their proximity, the spectral ratios between these earthquakes will cancel the propagation effects to a given station and retain the effects of source differences. Events 1 and 3 in Table 3-1.1 were chosen for this analysis. The observed spectral ratios for a few stations are shown in Figure 4-1.1. In this section we present the results of the analysis.

Following Weidner and Aki, residuals are defined by

$$\sigma_{\phi}^{2} = \frac{\Sigma W_{ik}(\Delta\phi^{o}_{1-3,ik} - \Delta\phi^{T}_{1-3,ik})^{2}}{\Sigma W_{ik}}$$

for phase data and by (4-1.1)

$$\sigma_{A}^{2} = \frac{\Sigma W_{ik}(\ln(A^{o}_{1ik}/A^{o}_{3ik}) - \ln(A^{T}_{1ik}/A^{T}_{3ik}))^{2}}{\Sigma W_{ik}}$$

for amplitude data, where the superscripts o and T refer to observed and theoretical quantities, respectively, and W_{ik} is the weight. The remaining symbols have been defined in Chapter 2. The weight on each phase observation is equal to the average of the observed amplitudes, $\frac{A^{o}_{1ik} + A^{o}_{3ik}}{2}$. In the case of the amplitude residual, the weight is computed from the average of theoretical amplitudes, $\frac{A^{T}_{1ik} + A^{T}_{3ik}}{2}$, in order to minimize the contribution from stations lying in the node of the radiation pattern.

A trial and error search of parameter space is carried out to find the depth and mechanism of each event that minimizes the residuals. The search does not cover the entire 8-dimensional space as constraints are imposed by the P-wave solutions. Figure 4-1.2, shows plots of the residuals versus source parameters in the vicinity of the point in parameter space giving a minimum in the residuals. The curves in each box in this figure were obtained by holding all of the parameters fixed at the values which gave a minimum and varying the parameter specified for the box. The solutions based on amplitude and phase residuals agree well.

The resultant match of theoretical to observed quantities is shown in Figure 4-1.1.

The solution in Figure 4-1.2 is located at the absolute minimum in the residuals, and no distinct local minima were found that suggested other possible mechanisms Weidner (1972) found that the amplitude residual at depths of 50-60km was about equal if not smaller than the residual at shallow depths for the Mid-Atlantic Ridge earthquakes. The phase residual was large for the deep focus solution however and thus resolved the ambiguity. In our search over the range of 0-55km, we do not see this ambiguity in the amplitude residual. Indeed, the search converged directly to the solution shown above. Some indication of the good definition of this minimum is given by the slices of parameter space shown in each box in Figure 4-1.2.

SEISMIC MOMENTS. In fitting amplitude ratios, the analysis above gives an estimate of the ratio of the seismic moments between events 1 and 3. Rather than assume an initial Q-model for Eurasia and risk introducing a bias that would remain in later Q-models, the moments and attenuation coefficients were estimated simultaneously by the method of Tsai and Aki(1969).

The observed amplitudes for a given frequency were corrected for the radiation pattern corresponding to the source parameters obtained above and for geometric spreading. The resultant amplitudes were plotted on a log scale as a function of distance from the source. The slope of this plot is proportional to the at-

TABLE 4-1.1: SOURCE PARAMETERS OF EVENTS 1 AND 3 OBTAINED FROM EARTHQUAKE PAIR METHOD OF WEIDNER AND AKI

	EVENT 1	EVENT 3
FOCAL DEPTH:	5km	5km
SLIP ANGLE:	40°	110°
DIP ANGLE:	100°	105°
FAULT STRIKE:	215°	295°
SEISMIC MOMENT:	4×10^{24} dyne-cm	4×10^{24} dyne-cm
	OR	
	$\times 10^{24}$ dyne-cm	$\times 10^{24}$ dyne-cm
M_{xx}:	2.2	0.7
M_{xy}:	1.4	0.1
M_{yy}:	-3.1	-2.6
M_{xz}:	-2.3	1.7
M_{yz}:	1.0	2.8
M_{zz}:	0.9	1.9

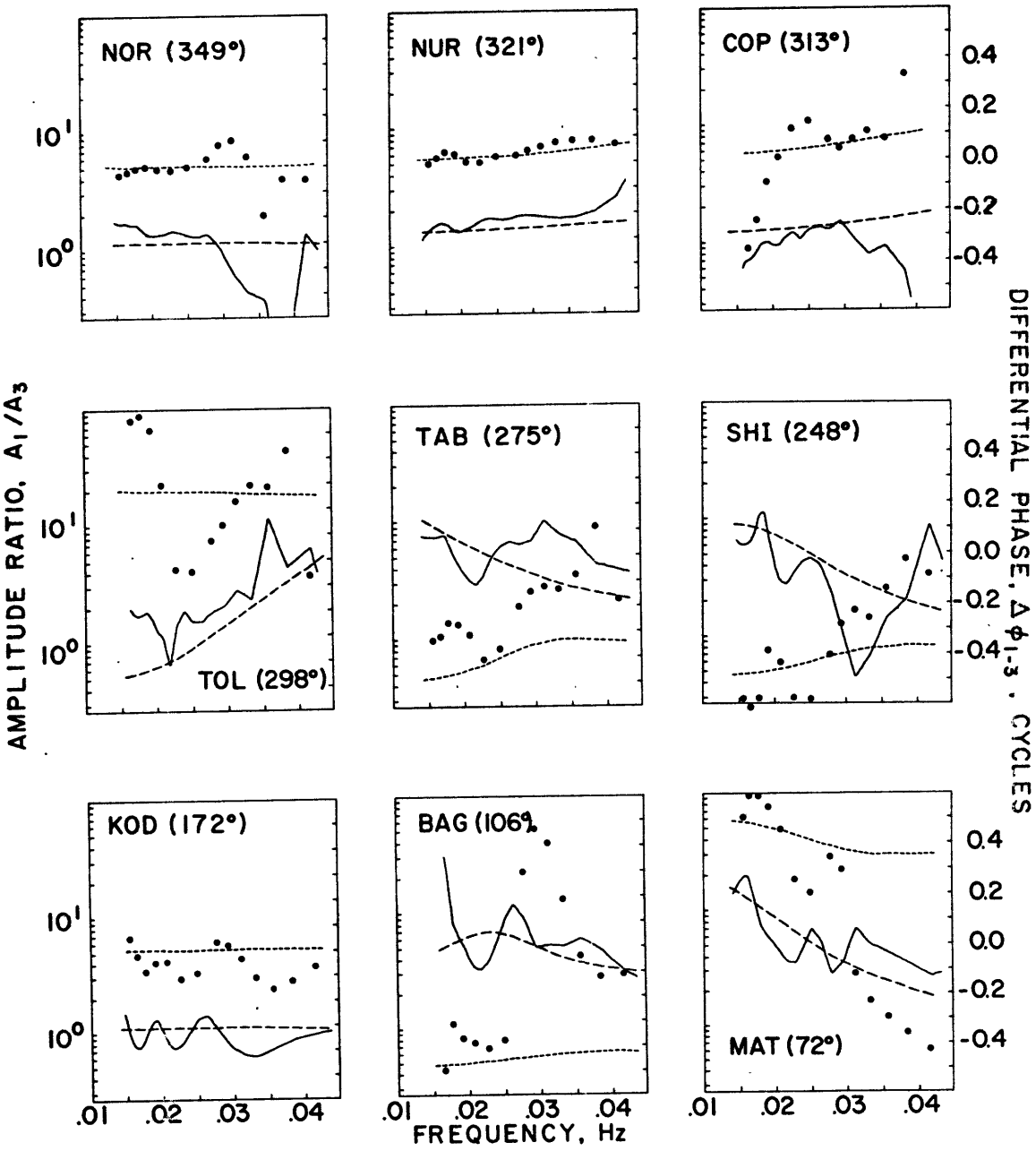

Fig.4-1.1: Examples of observed amplitude ratios (——) and differential phase (●) at nine stations. Theoretical counterparts (— — —and-----, respectively) are based on source parameters minimizing σ_A^2 and σ_ϕ^2.

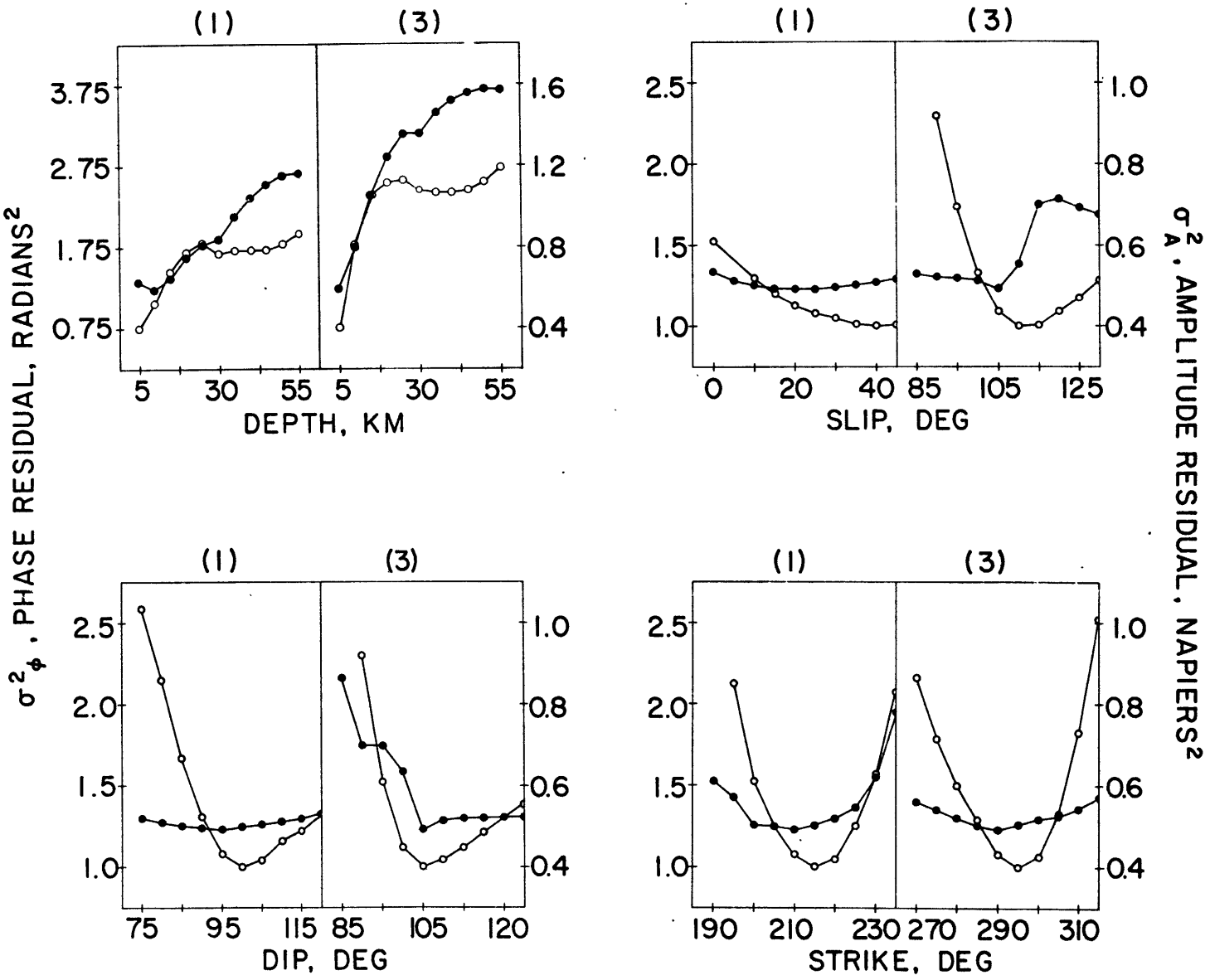

Fig. 4-1.2: Amplitude (—o—) and phase (—●—) residuals, as defined in Equation 4-1.1, plotted against trial source parameters of earthquakes 1 and 3. The residual curve in each box is obtained by varying the parameter of the box while holding all others fixed at their minima.

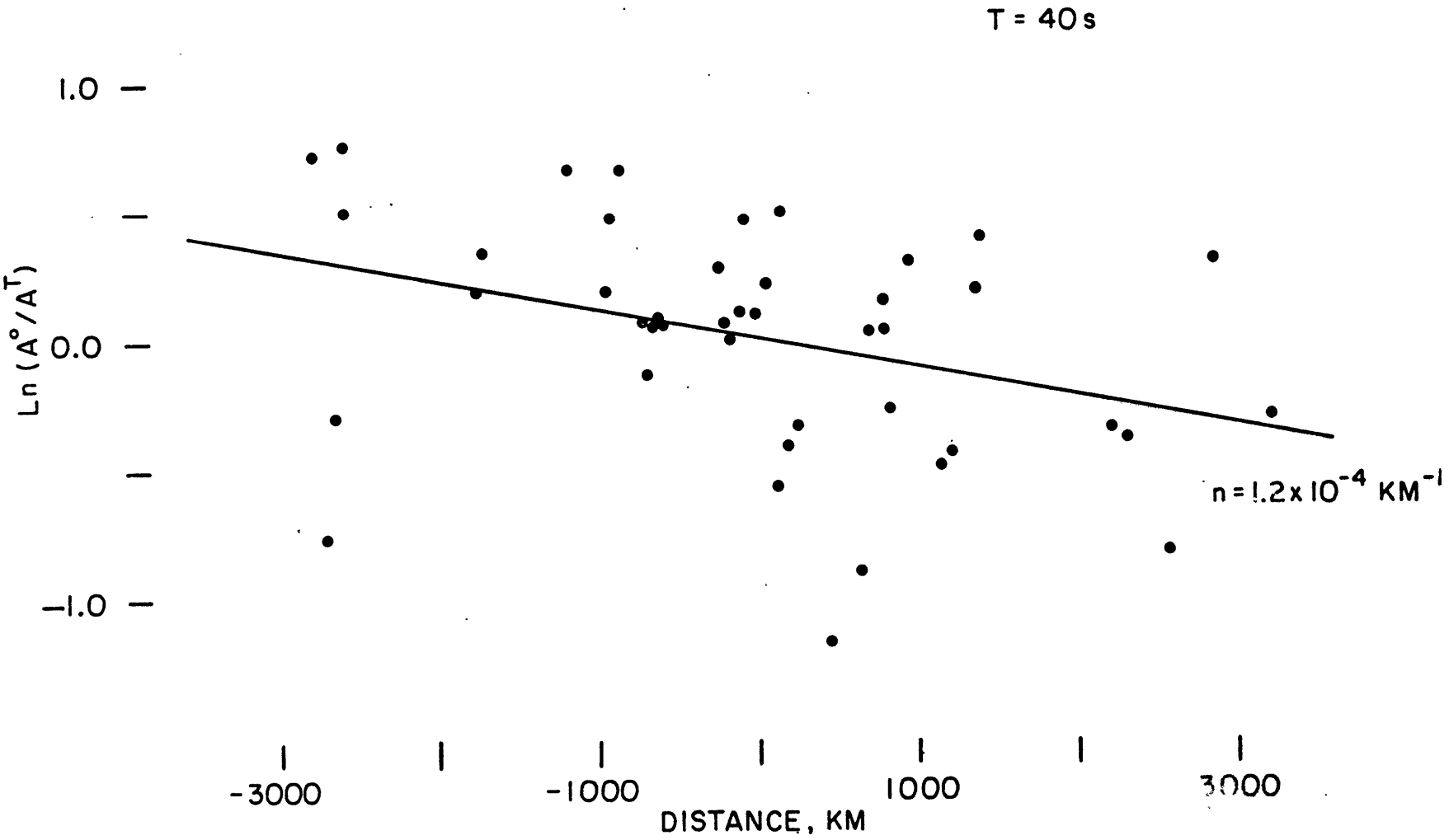

Fig. 4-1.3: Amplitude decay with distance of 40sec period Rayleigh waves. The slope of the line gives an estimate of average attenuation coefficient, n, for Rayleigh waves in Eurasia.

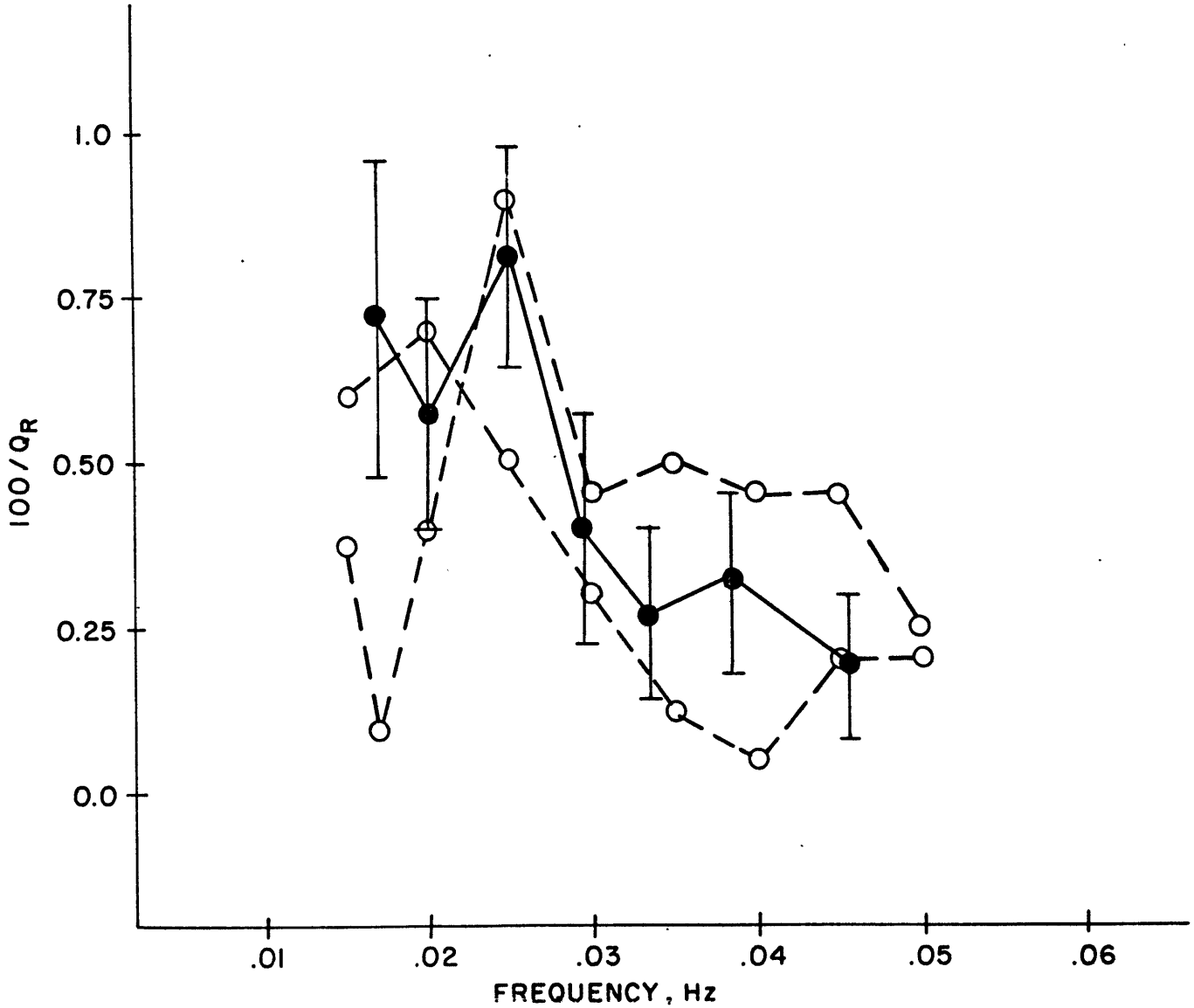

Fig. 4-1.4: Observed Q of Rayleigh waves in Eurasia from this study (—●—) and from Burton's (1974) (—o—). Error bar represents one standard deviation in the estimate of attenuation from the least squares fit of the amplitude delay. Datasets of events 1-4 were combined to make these estimates.

tenuation coefficient of the seismic waves while the intercept gives an estimate of the moment. Figure 4-1.3 shows an example of this plot for 40sec period waves. The datasets from events 1 and 3 have been reduced to one plot by removing the means, $\overline{\ln A}$ and $\bar{r}$, from each dataset. The least squares estimates of attenuation, shown in Figure 4-1.4, are representative of the Eurasian continent sampled by ray paths between the reference point and the surrounding station network.

For comparison, we have also plotted in Figure 4-1.4 other measurements of Q for Eurasia (Burton, 1974). Our Q agrees well with Burton's measurements which are for Rayleigh waves from nuclear explosions at Lop Nor. One feature of these measurements is a rapid increase in Q across the frequency range .025-.033Hz. This would signal a clear transition from lithosphere to asthenosphere for Eurasia if it were not for the uncertain results at lower frequencies. We defer further discussion of these results until our analysis of regional attenuation characteristics in Chapter 5.

The source parameters for events 1 and 3 determined by this analysis are summarized in Table 4-1.1.

2. ITERATION

Once initialized, our method follows the iterative cycle described in Chapter 2. We estimate the path transfer functions for those stations that recorded reference events 1 and 3. At

long periods ($T \geq 40s$) the estimates of H and ϕ are calculated using Equation 2-5.7 based on Gaussian random errors in the complex spectrum. At short periods the estimates are calculated using Equation 2-5.18. This choice of 40sec period is not arbitrary, as the results of various preliminary analyses including the moving window analysis, checks of the signal to ambient noise ratio, the smoothness of the observed spectra and others indicated that noise sources other than ambient background noise were important for periods less than 40sec.

All nine events in Table 3-1.1 were introduced one by one (not necessarily in numerical order) into the iterative cycle. The estimates of H and ϕ and the source parameters of events 1 and 3 were subsequently revised in this process. As an example, the results of a detailed analysis of event 9 are given below.

COMPARISON OF LINEAR INVERSION AND $\ln A + i\phi$ FITTING. Figures 4-2.1a and 1b show radiation patterns of the source amplitude, A^s, and source phase, ϕ^s, respectively, for event 9. The amplitude radiation pattern is plotted on log scale over 180^o by making use of its two-fold symmetry. Phase is plotted in radians over 360^o of azimuth. Only the data shown in these figures were included in the analysis. In Figures 4-2.2a and 2b we have plotted the real and imaginary parts which correspond to α_{ik} and β_{ik} as defined in Section 2-4. The radiation patterns of the real part in Figure 2a show the expected azimuthal dependence, namely $\sin 2\theta$. The imaginary part in Figure 2b show the expected $\sin\theta$

dependence. The lines appearing in these figures are the results of the following analysis.

A least squares inversion for the moment tensor was applied to all data at eight trial focal depths over the range 0-32km. The plot of the residuals, as defined in Equation 2-4.4, versus the depth is shown in Figure 4-2.3. The inversion at 12km focal depth gave the estimates of the moment tensor elements in Table 4-2.1. The radiation patterns based on these estimates are shown in Figures 4-2.1 and 4-2.2.

The analysis was repeated a second time excluding a few data points marked by open circles in Figures 4-2.1 and 4-2.2. These points are "anamolous" on the display of the imaginary part but not on the plot of the real part. The results of the inversion at 12km depth are given in Table 4-2.1 and are also plotted in the figures. As may be expected, the biggest difference between these results and the results of the first inversion is seen on the imaginary part, where the estimates of M_{xz} and M_{yz} are about a factor of two apart.

Using $\ln A^s$ and ϕ^s of all data, the source parameters were determined by the trial and error search method described in Section 2-5 and which we shall call logarithmic fitting in our discussion. The results of the linear inversion were helpful to narrow the search to the following region of parameter space:

RANGE	INTERVAL
$6 \leq h \leq 24$km	3km
$-65^{\circ} \leq s \leq 25^{\circ}$	15°
$-15^{\circ} \leq d \leq 75^{\circ}$	15°
$195^{\circ} \leq \theta^{F} \leq 235^{\circ}$	15°

making approximately 1700 permutations of source parameters. We searched all 1700 possible sets of source parameters for the one having the smallest residual which, as defined by Equation 2-5.20 is the sum of the amplitude variance, σ^2_A, measured in Napier^2, and the phase variance, σ^2_ϕ, in radian^2. Figure 4-2.4 shows contour plots of the residuals for several cross-sections of parameter space through the minimum (marked by +). The source parameters at the minimum residual are h=12km, $s=-5^{\circ}$, $d=60^{\circ}$, $\theta^F=205^{\circ}$ and $M_o=5.2\times10^{24}$cm-sec or equivalently by the moment tensor given in Table 4-2.1. The radiation patterns based on this model are shown in Figures 4-2.1 and 4-2.2.

The agreement between the results from the logarithmic fit and the results of the linear inversion is very good. We note that the biggest differences between the calculated radiation patterns occur where the station coverage is poorest. At short periods the logarithmic fit favors the result obtained from the linear inversion on the dataset which excluded the erratic data points. Apparently, these points did not affect the results of the trial and error method because their influence is unnoticed in the logarithmic residual space.

The erratic data points excluded in the above analysis are anomalous outliers which do not seem to belong to the representative error distribution. The results of the above experiments demonstrate a distinct advantage of a robust method, such as the logarithmic fit, over the least squares inversion when outliers are present. We discuss robust methods applicable to the linear inversion in Appendix A. As an example, we show in Figure 4-2.5 the imaginary part with the results from applying straight least squares and the robust method described in Appendix A. The robust method is a weighted least squares where weights are automatically assigned to the data points, thus avoiding the subjectivity of winnowing out erratic data points. The fitted curves in Figure 4-2.5 are obtained for each period separately. They demonstrate significant improvement of the robust inversion over the least squares (60, 50, 40, 34 and 26s) as well as its limitations (30s) when the erratic data points are apparently very influential. The result obtained from the robust inversion is also given on Table 4-2.1 and compares well with the results of the logarithmic fit.

RESIDUALS AS A FUNCTION OF FOCAL DEPTH. We have recomputed the residuals of the inversion based on the robust method over a wide range of depths in Figure 4-2.6. The residual curve shows a clear minimum at about 15km. The depth is only slightly changed from the depth giving a minimum from least squares inversions shown in Figure 4-2.3. The residuals in Figure 4-2.6 are about

six or seven times smaller than the least squares residuals, a consequence of the weighting function, $\rho(\xi)$, adopted in the robust method. Apparently, only the level not the shape of the residual curve as a function of depth was affected by the erratic data points. A remarkable feature of this curve is the occurrence of another minimum centered at about 90km. The residual at this minimum is only slightly larger than the residual at 15km. In Figure 4-2.6 we also show a break-down of the total residual into contributions from separate inversions on the real and imaginary parts. The major characteristics of the total residual are determined by the residuals from the real part. The imaginary part shows far less sensitivity to the focal depth than the real part, as expected from the discussion in Section 2-4.

We plot the medium responses (see Section 2.4 also Figures 2-4.1 and 3-1.2) as a function of frequency for focal depths of 10, 15, 80 and 100km in Figure 4-2.7. Based on the results in Table 4-2.1, the main ingredient of the real part is $\frac{\sqrt{k}}{U\omega^2 I_1} G_1$, which has similar behavior across frequency for both shallow and deep foci. Consequently, if the response at 12km matches the data well, we expect that it must also match well at 80-100km. On the other hand, the response, $\frac{\sqrt{k}}{U\omega^2 I_1} G_3$, is quite different for shallow and deep foci. Based on the behavior of this response for shallow focus, the amplitude of the imaginary part is about a factor of 10 greater at high frequency than at low frequency. For deep focus, the amplitude of the response is at least a factor of 2 smaller at high frequency than at low frequencies.

Therefore, it is surprising that the residuals from the imaginary part do not show much preference between shallow and deep foci.

The results of the inversion at 12, 80, 90 and 100km are given in Table 4-2.2. The curve fit for the imaginary part based on these results is shown in Figure 4-2.8. The calculated amplitudes for 12km match the observations better than the amplitudes for 80km at the short periods (30, 26s). On the other hand, the amplitudes for 80km match the observations better at long periods (60, 50, 40s). These characteristics of the fit (or lack of fit) plus the fact that more weight was placed on the long period observations (see Appendix A) are reasons why there is little difference between the magnitude of the residuals for the shallow and deep focus solutions.

Despite the apparent ambiguity surrounding both solutions, we do find strong evidence supporting a focus of 12km. The amplitude and phase radiation patterns based on the results in Table 4-2.2 are plotted in Figure 4-2.9. As may be expected the greatest differences in the calculated patterns are seen at short periods. Comparing these patterns to the observed amplitudes, we can reject unequivocally the solutions for 90 and 100km, but perhaps not for 80km.

More evidence supporting a focus of 12km comes from re-examining the amplitudes on the imaginary part. We may enhance the characteristics of the observed imaginary part by calculating an RMS amplitude at each period. This amplitude may be compared period by period with the amplitude based on the deep and shallow

focus solutions. In this manner we avoid the details of the curve fitting in Figure 4-2.8 and discriminate only on the basis of the dependence of the amplitudes on frequency. Table 4-2.3 gives the normalized RMS values as a function of period for the observed amplitudes at 12km and 80km. The observed RMS amplitude increases about a factor of two from 40 to 26sec. This is consistent with a shallow focus. The deep focus predicts a factor of two decrease in the range of 40 to 26sec.

The final evidence supporting the shallow focal depth comes from auxiliary data. We plot long-period P-wave first motions (observed by this author) on a stereographic net for comparison with the fault planes and expected motions based on the solutions at 12 and 80km. As seen in Table 4-2.2, the solutions have principal stress directions rotated about 90° in such a way that the shallow focus has maximum compressive stress aligned nearly N-S and the deep focus has E-W alignment. Very different first motion patterns are expected for these solutions. Clearly the observed pattern of P-wave first motions is incompatible with the pattern of the deep focus solution.

Having established that the focus is shallow, we may consider further the results of the curve fitting in Figure 4-2.8. There is evidence of a lack of fit between the calculated amplitudes, which are systematically low at long periods, and the observed amplitudes. This is responsible for a residual on the imaginary part that is about twice as large as its counterpart on the real part. We discuss two possibilities of the cause of

failing to match the observations: 1) a shortcoming in our model of the amplitude excitation and 2) a bias in the observations.

The lack of fit may be an indication that the calculated response functions based on the Pamir earth model are inadequate. We explored this possibility in Figure 4-2.11 by plotting the response, $\frac{\sqrt{k}}{U\omega^2 I_1} G_3$, as a function of frequency for the Pamir and Gutenberg earth models. Their responses at 10km and 15km have been plotted so that the amplitudes at high frequency (>.03Hz) agree within 10%. In this manner, we can examine the differences in the responses at low frequencies. As seen in this figure, the amplitudes of the Gutenberg response are generally larger than amplitudes of the Pamir response. At the lowest frequency, .015Hz, the Gutenberg response for h=10km has about twice the amplitude of the Pamir response. Thus, our observations at long periods would show better agreement with the Gutenberg earth model. Nevertheless, this may be rather weak evidence that the response of the Gutenberg model is closer to the true response of Eurasia, as an analysis of the errors in our observations shows. If $\Delta\phi$ is the error in the source phase, the error in the imaginary part due to small $\Delta\phi$ will be $\mathrm{Re}\{S\}\Delta\phi$, where Re{ } means taking the real part. If the real part is larger than the imaginary part by a factor of two, a $\Delta\phi$ of 0.5 radians will cause an error in the imaginary part of the same magnitude as Im{S} itself. The residual in the phase, σ_ϕ, from the logarithmic fitting is about 0.9 radians. At long periods, the RMS error in ϕ^S may be as small as 0.5 radians. As seen in Table 4-2.3, the RMS

amplitudes of the real part are 2 to 3 times greater than that of the imaginary part. Therefore, the differences between observed and calculated amplitudes in Figure 4-2.8 are not significantly larger than those we expect from phase errors alone. Amplitude errors may also be important, particularly for stations near a node in the amplitude radiation. If $\Delta\phi$ is only 0.25 radians and the amplitude error is a factor of two, the resultant error in the imaginary part is again the same magnitude as the imaginary part. Considering that the amplitude residual, σ_A, from the logarithmic fit is about 0.6, an amplitude error of a factor of 2 at a station close to the node is reasonable.

In summary, the lack of fit which resulted in high residuals on the imaginary part for shallow foci is probably not caused by the medium model used to calculate the response functions in the fit. The differences between observed and calculated amplitudes are not significantly larger than possible errors in the imaginary part caused by uncertainties in A^s and ϕ^s. A more plausible explanation is that the observed imaginary part at long period is biased high due to small amplitude and phase errors, particularly at stations lying close to the node. Another possible source of bias in the observations is taken up in the following discussion.

SYSTEMATIC ERRORS: LOCATION AND ORIGIN TIME. Both of these potential sources of error were investigated in the numerical experiments in Chapter 3. It was shown that a location error of 15km

can cause a bias in the estimate of the focal depth obtained from the residuals of the linear inversion as a function of trial depth. This is not only true of the linear inversion but also of any surface wave method to determine depth relying on the measurement of the focal phase. Since the linear inversion and the trial and error search involved both amplitude and focal phase measurements, the bias may be less than the case in which only focal phase is involved because the epicentral errors do not affect the amplitude measurement. Nevertheless, the source parameters giving a minimum residual will sacrifice the quality of the amplitude fit to match the erroneous observations of focal phase, as was seen in Figure 3-3.1. In the linear inversion, sources of random phase errors (such as interference) may also cause a poor fit to the amplitudes. However, we can exclude the possibility of random phase errors if it appears that the logarithmic fit has also failed to match the amplitudes. There is some indication that this is the case in Figure 4-2.1a when we compare the results of the linear inversion and the logarithmic fit to the observed amplitudes particularly at 34, 30 and 26sec. The amplitudes in Europe and Scandinavia are generally higher than the calculated curves, as are amplitudes at some stations across China. We explore the possibility of mislocation in the following analysis.

It is noteworthy that a mislocation may account for the behavior of the observed imaginary part in Figure 4-2.8. We plot in Figure 4-2.12 the radiation pattern of the imaginary part at

60 and 26sec for the case examined in the numerical experiments (Section 3-3) of a 15km location error. The true imaginary part is drawn as a line for comparison with the perturbed amplitudes (dots). The perturbations on the 60sec plot resemble, both in size and sign, the differences between observed and calculated imaginary part in Figure 4-2.8.

We may draw some inferences about the direction of a possible mislocation from the observed focal phase patterns in Figure 4-2.1b. Calling attention to long period (60, 50, 40s) it is seen that the focal phase at azimuths around 72^{o} and 264^{o} are advanced and delayed, respectively, relative to the calculated curves. At 40sec, for example, the difference between observed and calculated is approximately 0.7 radians which is larger than the RMS $\Delta\phi$ of 0.5 radians calculated from the observations at European and Scandinavian stations (azimuths > 312^{o}) in this plot. If the observed focal phase is advanced relative to true phase, this implies that the correction by the propagation phase, $\hat{\phi}_{ik}$, is greater than it would have been for the true epicenter. Assuming our phase velocity is correct, this means that the epicentral distance from the assumed epicenter, X_{ji}, is longer than the actual epicentral distance. If the observed focal phase is delayed relative to the true, then our assumed distance is too short. The most we can say on the basis of the differences between observed and calculated focal phase in Figure 4-2.1b is that the true epicenter may lie east of the one reported by ISC.

We moved the epicenter to the east by 15km. The linear

inversion on the dataset with the new location was applied at trial depths from 0-50km, and the residuals plotted as a function of the depth are shown in Figure 4-2.13. The minimum in the residual curve occurs at 10km. We give the results of the inversion at 10km in Table 4-2.4 and show in Figures 4-2.14a and 4-2.14b the calculated amplitude and phase radiation patterns. For comparison, we also plot the calculated radiation patterns based on the results of the inversion at 10 and 15km before relocation.

At long periods, all of the calculated amplitude patterns are very similar except along azimuths where station coverage is poor. The agreement between observed and calculated amplitudes is excellent. At short periods, the differences between the calculated patterns are large enough to show that the solution having a focal depth of 15km does not match the observations as well as the other two solutions. Both solutions having 10km focal depths predict higher amplitudes for Europe, Scandinavia and China in agreement with the observations at 34 and 30sec. The radiation patterns based on the solution after relocation shows the best agreement with the observations. One interesting detail in the observations is the very low amplitudes at long period for station COL (az=17^{o}). The amplitude of the Rayleigh wave in this azimuth is very sensitive to changes in the dip angle of fault plane #2 in Figure 4-2.10. Both the observed amplitudes at COL and the P-wave polarities in Figure 4-2.10 favor a steeper dip angle for fault plane #2 than calculated on the basis of results

prior to relocation. The radiation patterns after relocation show a better developed node for azimuths near COL than either solution before relocation. Indeed, the dip angle of fault plane #2 after relocation is steep enough to resolve three inconsistent P-wave polarities in Figure 4-2.10.

Unfortunately, we do not gain further support for this relocation attempt from an independent study. Many of the aftershocks following the August 11 mainshock have been relocated using P-waves (Jackson and Molnar, private communication). The output of their analysis gave new locations and depths relative to a chosen master event. Their results show small changes (<10km) in the epicentral location from the ISC reportings of all large aftershocks, including our event 9.

Turning to origin time errors, we may assume that they are mainly a function of errors in the focal depth and not the epicentral coordinates determined by the ISC. Indeed, a serious error in origin time much larger than the estimated standard errors in Table 3-1.1, may result from an erroneous focal depth in the ISC computation. This is due to the fact that in epicentral determinations using body wave travel times the origin time and focal depth are strongly coupled and that the resolution of both parameters is usually very poor unless one of them is constrained independently. On these grounds we put little trust in the accuracy of the ISC reporting of both depth and origin time for most of the events in Table 3-1.1 (Event 6 is an exception because depth phases were used as a constraint.) The focal depth deter-

mined in our analysis is reliable, and may be used to revise the origin time using a correction calculated from the difference between ISC focal depth and the surface wave estimate.

The two focal depths, the ISC's and the estimate from surface waves, are expected to differ purely on methodological grounds. The body wave determination uses the travel times of onset of P-waves generated at the initial rupture of the fault surface. The long period surface waves are generated from the entire ruptured fault surface. Since the earthquake source is treated as a point in the earth, the focal depth obtained in our analysis corresponds approximately to the center of the ruptured fault surface. Thus, we may attribute a difference in the two estimates of focal depth to the finiteness of the fault.

For the range of magnitude of events in Table 3-1.1, the difference due to fault length is probably not greater than 10km. The focal depth reported by ISC for event 9 is 19km, which is only 9km deeper than the focal depth favored by surface waves, within the range attributable to source dimension. On the other hand event 7 has an ISC focal depth of 41km which is roughly 30km deeper than the estimate based on surface waves (Table 4-2.5). If the ISC focal depth of event 7 is in error by 20km, we may expect an origin time error of 20km/v, where v is the medium P-wave velocity, or approximately 3sec. A 2sec correction to the origin time leads to significant improvement of the imaginary part of the complex spectrum as seen by comparing Figures B-7.b and B-7.b' in Appendix B. Figure B-7b shows the observed amplitude radia-

tion of the imaginary part and the curve fit at each period for the origin time reported by ISC. The results of these fits show a peculiar behavior as a function of frequency, articularly between 40 and 34sec where it is apparent that the moments, M_{xz} and M_{yz}, must change sign. This inconsistency between the moments at long and short period on the imaginary part is resolved almost completely by a 2sec correction as seen in Figure B-7.b' . The curve fits show better consistency across the frequency band and indeed compare well with calculated amplitudes of imaginary part based on the results of the inversion in Table 4-2.5.

We revised the origin time of all events in Table 3-1.1 where it appeared that the discrepancy between the ISC and surface wave depth was too great to be attributed to fault finiteness alone. The results of the inversion of all events are reported in the next section.

RESULTS FOR ALL EVENTS: DEPTHS AND SEISMIC MOMENT TENSORS. We show the residuals as a function of trial depth for all remaining events in Figure 4-2.15. The inversions were carried out by the robust method described in Appendix A. The moment tensors for the focal depth at the minimum in these residual curves are given in Table 4-2.5. Appendix B contains the plots of the real and imaginary data for all events along with the calculated amplitudes based on the solutions in Table 4-2.5, for comparison.

All residual curves in Figure 4-2.15 show a minimum in the upper 15km. With the exception of event 6, these minima are

clear determinations of the focal depth. The residual curve of event 6 appears to have an absolute minimum at depths greater than 100km. The local minimum at shallow focus for this event is caused by similar effects that gave a local minimum at great depths for event 9 as discussed above.

In regard to the shape of the residual curves in the vicinity of the minimum, we note the following generalization: shallow events with broad minima, such as 1, 2 and 9, have strike-slip mechanisms, whereas dip-slip events such as 3 and 7 have sharp minima. Weidner (1972) found this to be true of the minima in σ_ϕ^2, the residual from the analysis of differential phase. The reason that shallow focus dip-slip events have stronger depth signatures than strike-slip may be understood by comparing medium responses $\frac{\sqrt{k}}{U\omega^2 I_1} G_1$ and $\frac{\sqrt{k}}{U\omega^2 I_1} G_2$ in Figure 3-1.2. The latter response, which is excited by the moment element, M_{zz}, changes character more rapidly at shallow foci (0-15km) than G_1 does. This means that in the frequency range (.02-.04Hz) the Rayleigh wave complex spectrum is very sensitive to the depth of focus near the surface when it is made up of large component of M_{zz}, as in the case of dip-slip mechanisms.

On the basis of the residuals in Figure 4-2.15, the focal depths of dip-slip events are not deeper than 10-15km below the surface. Strike-slip events are certainly not deeper than 20km and appear to range from 5-20km, perhaps slightly deeper than dip-slip events in general.

Qualitatively, the curve fit of the calculated amplitudes to

the observed on the real and imaginary parts, as given in the figures in Appendix B, is similar to what was seen for event 9. Our best fit as measured by reduction of the variance of the observed amplitudes was at long period on the real part. The poorest fit was often seen at long periods on the imaginary part. As shown above, this is due to the fact that small errors in amplitude and/or phase were magnified on the imaginary part when the real part was much larger. This was also true of the real part, as seen in the case of event 6.

As was done for event 9, we checked the results of the linear inversions in the vicinity of the minimum in the residuals by plotting the calculated curves on the radiation patterns of $\ln A^S$ and ϕ^S. We show the results of these checks and of other computations in Figures 4-2.16 through 4-2.23. The following is a discussion of these results.

First, there are some general comments. The source parameters at the minimum of the residual curve did not always show the best match on $\ln A^S$ and ϕ^S plots among the neighboring source models (e.g. events 1, 2, 5, 6 and 9). This is best seen on the plots of $\ln A^S$. Events 1 and 5 show slightly better fits at trial depths 2.5km from their minima. This small difference probably is an indication of the uncertainty in the estimate of focal depth due to random errors in the observations. The possibility of a bias in the estimate of the focal depth of event 9 has already been studied. Considerations of events 2 and 6 are given at further length below. The results of the inversions at 5 and 10km on the

plots of $\ln A^S$ for events 1 and 3 illustrates the better depth resolution of a shallow dip-slip event (3) than a strike-slip event (1).

The comparisons in events 3 and 7 show that the improvement resulting from the correction of the ISC reported origin times is rather small on the plots of $\ln A^S$. Because the ISC origin times cause only a small bias in the calculation of focal phase, the effect was seen most clearly on the plots of the imaginary part at long periods, as demonstrated in the case of event 7.

The following are some remarks about specific events.

EVENTS 2 AND 4: Both events were too small to obtain P-wave fault plane solutions. As seen in Figure 4-2.17, Figure 4-2.19 and Table 4-2.5 the mechanisms are clearly determined to be strike-slip and dip-slip, respectively, by both the linear inversion and trial and error logarithmic fit. In the case of event 2, the focal depths obtained by these two methods are 8km different. Although epicentral location errors may be a possible cause, the combination of a strike-slip mechanism and weaker signal strength from this small event adds greater uncertainty to the estimate of focal depth due to random errors. The results of event 4 clearly show that adequate sampling in azimuth is needed to determine confidently all fault plane parameters. Here the slip vector favored by both the linear inversion and logarithmic fit has a large component of dip-slip motion; however, due to poor azimuthal sampling, a sizeable strike-slip component is also

permissible.

EVENTS 7 AND 8: These events were separated by 1.5 hours and less than 10km in time and space. Yet, their source mechanisms are very different, as the radiation patterns in Figures 4-2.22 and 4-2.23 suggest. The focal depths of both are 7.5km. The linear inversion of event 7 gives primarily dip-slip motion on a thrust fault. For event 8, the linear inversion result is left-lateral strike-slip on a very shallow dipping fault plane (or dip-slip on a vertical plane). The direction of the principal axis in both mechanisms is aligned N-S, event 8's axis showing 30° greater dip from the horizontal plane than the event 7's. Events 7 and 8 and event 9, which occured sixteen days later, are among the larger shocks of an intense aftershock series following the August 11, 1974 mainshock.

Interestingly, both events 7 and 8 have large intermediate eigenvalues as seen in the results of the inversions on Table 4-2.5. As some results in Section 3-2 show (cases 7, 10-12), multiplicative errors can lead to large, significant departures from the double-couple force system. We checked the possibility that errors in our data were responsible for large intermediate eigenvalues by first running logarithmic fits on the datasets of event 7 and 8. The results are shown with the results of the linear inversion on the amplitude and phase plots of event 7 and 8. The similarity between these results for event 8 is very close. There is some indication that the frequency dependence of

the amplitudes is not as well matched by the logarithmic fit as it is by the linear inversion. In the case of event 7, the logarithmic fit shows largest discrepancies with the linear fit at high frequencies in the azimuths northeast and southwest of the source where station coverage is minimal. The linear fit shows some indication of a slightly better fit to the focal phase at high frequencies. Although it is tempting to conclude from the recovery of a large, apparently significant intermediate eigenvalue that there is a serious departure from the double-couple mechanism, as others (Randall and Knopoff, 1970, Dziewonski and Gilbert, 1974) have proposed, we find it difficult to establish this convincingly in the light of errors in our data and the closeness to the results of the double-couple models.

EVENT 6: The shape of its residual curve in Figure 4-2.15 indicates that its focal depth is greater than 100km. This is in agreement with the ISC reported source depth of 111km. On the amplitude plots in Figure 4-2.21 we show results of the linear inversion at trial depths of 60, 80 and 100km. The frequency content of the observed amplitudes are matched well by the 100km focus model except at the highest frequency where the calculated is too low. Deeper models will not improve this because the amplitude of the normal modes at these depths in the earth model and frequencies approach zero. Unless the high observed amplitudes can be accounted for by other means, we would have to conclude that this is a failing of the Pamir earth model assumed in

the calculation of the response functions for Central Asia. Although no attempt was made to improve the fit by changing the Pamir model, it should be possible to do so on the basis of the results of the interpretation of regionalized phase velocities in Chapter 5.

We give the final estimates of the focal depths and seismic moment tensors of all events in Table 4-2.6. The changes from Table 4-2.5 affect events 1, 2, 4, 5 and 9. In the case of events 1, 2, 5 and 9, the changes are made in connection with the initial estimates of the focal depth for reasons discussed above. There are several comments to make about these final source parameters. Comparison of the final parameters of events 1 and 3 with parameters obtained from the earthquake pair method in Table 4-1.1 is quite close. The depths show no change and the seismic moments are different by only about 25%. The estimate of the moment element, M_{xz}, shows the largest change among all elements for both events. In regard to the principal axes of all events, we call attention to the fact that the orientation of the P-axis, e_3, is very constant. The largest deviation from N-S alignment is 43^{o}W in the case of deep event 6. Among the shallow events, event 9's P-axis shows the largest deviation at 24^{o}W. The maximum deviation of the P-axis from horizontal is for events 6 and 8 at 43^{o}. Among shallow events, it is fair to conclude that P-axes are typically oriented N-S and horizontal. Further interpretation of the source parameters in light of the faulting and tectonics of this area is presented in Chapter 5.

ANALYSIS OF RESIDUALS. Before analyzing the residuals from the linear inversion, there are several conclusions to be drawn from the residuals, σ_A^2 and σ_ϕ^2, obtained in the initialization.

The major factors contributing to σ_A^2 are the ambient noise of the recording instrument and the amplitude error due to path effects not canceled by taking the ratio, such as focusing, defocusing, and multipathing that occurs near the source (Weidner, 1972). The sources of error contributing to in σ_ϕ^2 are the following: 1) uncertainties in the epicentral data, 2) finiteness of the source, 3) erroneous earth structure used to calculate $\Delta\phi^T$, and 4) noise contaminations (also Weidner, 1972). Based on the results of the error analysis in Chapter 3, errors due to source finiteness and erroneous earth structure are not serious enough over the frequency range and for the magnitudes of events in our analysis to contribute heavily to the residuals. The precautions to restrict the analysis to a frequency range having strong signal diminishes the importance of ambient noise. This leaves adverse propagation noise and errors in the epicentral data as the major contributors to the residuals, σ_A^2 and σ_ϕ^2. It is interesting that the experiment carried out by Weidner on Mid-Atlantic Ridge earthquakes gave residuals that were 2 to 3 times smaller than our residuals (σ_A^2: 0.2 vs. 0.4 Napier^2 and σ_ϕ^2: 0.4 vs. 1.2 radian^2). Both his study and this one were carried out under similar conditions with regard to distance between event pairs ($\sim$100km), magnitude of events, frequency range, and epicentral distances ($\bar{X}$: 4300km vs. 5000km). The major difference between

experiments is, of course, the tectonic setting. Although epicentral errors (in particular, origin time) may account for some differences in σ_ϕ^2, the large residuals in the present experiment are probably an indication that the waves are seeing greater differences in the propagation effects in the vicinity of our earthquake pair than waves did leaving the mid-ocean ridge. This is indirect evidence of more laterally heterogeneous crust and upper mantle structure in Central Asia than the oceanic crust and upper mantle across mid-ocean ridges.

Defining "heterogeneity quotients" to be $\sigma_A^2/\bar{X}$ and $\sigma_\phi^2/\bar{X}$, we can obtain a rough measure of increasing scatter in the amplitude and phase of Rayleigh waves per kilometer of propagation due to lateral heterogeneities along the path. For the oceans the heterogeneity quotients are approximately $.46 \times 10^{-4}$ Napier^2/km and $.93 \times 10^{-4}$ radian^2/km for amplitude and phase, respectively, of 20-50sec Rayleigh waves. For the continents, we obtain quotients of $.80 \times 10^{-4}$ Napier^2/km and 2.4×10^{-4} radian^2/km for 26-60sec Rayleigh waves.

The residuals from the linear inversion for 8 of the 9 events are summarized in Figure 4-2.24. Here we have plotted at four periods and for individual events the difference between the real parts, $Re_i^o - Re_i^T$, where o refers to observed quantity, T to theoretical and the i refers to the i^{th} station. The figure shows a "matrix" of histograms with the rows referring to events and the columns to periods. The events have been arranged in increasing order of moment with the top row being the smallest and

the bottom the largest event. Periods increase from right to left. Notice that scales change from column to column but not within a column. We summarize means and variances of these histograms in Table 4-2.7.

As a guide for the interpretation of these residuals, we show schematically several examples of noise contamination in Figure 4-2.25. In the diagrams of the complex plane, the true complex value (Re^T, Im^T) of which we have obtained an estimate by the linear inversion, is given by an arrow. The dots around the arrow head represent a hypothetical population from which the observation is drawn under the specific assumptions about the noise. For example, in the case of ambient background noise, the hypothetical population is a circular cluster around the arrow head, (see Figure (a)). On the real or imaginary parts, this noise may be modeled as a Gaussian random variable with zero mean and variance, σ^2. We draw the Gaussian density on the real axis of this figure to depict the population from which our observation of the real part, Re_i^o, is drawn. The statistics of this noise are independent of the signal amplitude and may also be considered independent of i and the event. Under these circumstances the residual, $Re_i^o - Re_i^T$ is a Gaussian random variable with a probability density, $N(0, \sigma^2)$.

In Figure (b), we depict cases when multiplicative noises contaminate the observations. By the shape of the hypothetical population, it may be seen that phase errors are too small to cause incoherency and that magnification errors have skewed the

distribution of observations. The two diagrams show that the population from which we draw Re_i^o may be skewed to the right or left, depending on the sign of Re_i^T. Assuming Re_i^T ranges continuously over equal positive and negative domains, and that the skewness does not change with i, the residual $Re_i^o - Re_i^T$, is a random variable drawn from a probability density ressembling that in Figure (c), which has mean zero and variance, $\sigma^2(A)$, the variance being a function of signal amplitude. The first assumption above is true when there is no preference in Re_i^T to positive or negative values which is dependant on the source mechanism. The second assumption is not strictly valid as the intensity of magnification errors will vary regionally. A failing of either assumption may add skewness to the density shown in (c).

Figure (d) shows a case where the population of observations has large amplitude and phase fluctuations around the true value. This occurs when the observations are contaminated with multiplicative errors affecting both the amplitude and the phase. The population that Re_i^o is drawn from is shown schematically in this figure. Assuming as we did for magnification errors above, the residual, $Re_i^o - Re_i^T$, is a random variable from a probability density resembling that in Figure (c), the important point being that variance is signal dependent.

Another case is when observations are contaminated with Gausian random noise, and a few observations are also affected by multiplicative noises. Under these circumstances, we expect the residuals to be drawn from a probability density resembling that

shown in Figure (e) where the sharp central peak is due to the Gaussian noise and the long tail due to multiplicative noises. In the parlance of statisticians, this kind of probability density is termed "leptokurtic" (Remington and Schork, 1970).

Two obvious trends seen in the matrix of histograms in Figure 4-2.24 are that variances increase along rows from left to right and in columns from top to bottom, i.e. variances increase with frequency and with seismic moment. Both trends are due to the presence of multiplicative errors in Re_i^o. The variances increase down the column because the signal amplitude increases approximately a factor of 10. On the other hand, signal amplitudes do not increase along rows because the source spectrum averaged over azimuth for most events is relatively flat across the frequency range considered here. This suggests that the increase of variance to the right may be due to higher contamination by signal generated noises on the seismogram at short periods and/or to larger errors in the path corrections at short period.

In general, the shapes of the histograms can be characterized by the density shown schematically in Figure 4-2.25e with the variance, $\sigma^2(A)$, controlling the extent to which individual histograms in Figure 4-2.24 appear leptokurtic. For example, histograms of the two smallest events are sharply peaked at all frequencies because multiplicative errors are small due to small signal amplitudes. Gaussian statistics are probably valid for the residuals of these events at all frequencies. Histograms for events 7, 3 and 1 (only at long periods for 1) are typically lep-

tokurtic due to the few observations affected by large multiplicative errors. We give the names of stations falling in the tails of these histograms on Figure 4-2.24. Histograms of larger events and for shorter periods have more populated tails, and several show evidence of skewness. In short, the leptokurtic character of histograms diminshes moving from the upper left hand corner to the lower right hand corner of the matrix.

It may be noted here that a robust method of inversion for the seismic moment tensor was required mainly because of a few observations at long period that show up in the tails of the residual distributions. Weighting across frequency by $1/S_k^2$ (see Appendix A) is justified because multiplicative errors controlled the size of S_k^2, the estimate of $\sigma_k^2(A)$.

The residuals of the inversions should also be compared with random errors that were introduced in the numerical experiments in Chapter 3. For example, in cases 4-6 and 7-9, we introduced magnification errors of a factor of 2 or .5 and 5 or .2, respectively, which in lnA are errors of $\pm$ 0.69 and $\pm$ 1.61 Napiers. The RMS amplitude error over our analyzed frequency band was found to be between 0.6 and 0.8 Napiers. The upper limit is probably a good figure for high frequencies. Cases 13-15 and 16-18 had RMS phase errors of .45 and .91 radians, respectively. These figures are to be compared with .57, .94 and 1.26 radians at periods 50, 34 and 26sec, respectively, in our data. In light of the results of the numerical experiments, the RMS multiplicative errors in our data are in the range where large bias in the

TABLE 4-2.1: RESULTS OF LINEAR INVERSIONS AND LOGARITHMIC FITTING APPLIED TO EVENT 9

METHOD	LINEAR LEAST SQUARES INVERSION ALL DATA	LINEAR LEAST SQUARES INVERSION SCREENED DATA	TRIAL & ERROR FIT, lnA+1ϕ ALL DATA	ROBUST INVERSION ALL DATA
FOCAL DEPTH	12km	12km	12km	12km
	$\times 10^{24}$	$\times 10^{24}$	$\times 10^{24}$	$\times 10^{24}$
M_{zz}	$-0.1 \pm .6$	$-0.3 \pm .5$	0.4	$0.4 \pm .3$
$M_{yy} - M_{xx}$	$-4.8 \pm .9$	$-4.8 \pm .8$	-6.6	$-4.8 \pm .3$
M_{xy}	$3.1 \pm .4$	$3.1 \pm .4$	3.0	$2.8 \pm .2$
M_{xz}	$0.3 \pm .2$	$0.9 \pm .2$	1.3	$0.8 \pm .1$
M_{yz}	$1.2 \pm .2$	$2.3 \pm .2$	2.2	$1.8 \pm .2$
λ_1	$4.1 \pm .5$	$4.8 \pm .5$	5.2	$4.1 \pm .2$
λ_2	$0.0 \pm .6$	$-0.3 \pm .4$	0.0	$0.2 \pm .3$
λ_3	$-4.1 \pm .5$	$-4.5 \pm .5$	-5.2	$-4.3 \pm .2$
e_1	-117° 11°	-121° 21°	-116° 24°	-118° 23°
e_2	-245° 72°	-248° 58°	-254° 60°	-258° 61°
e_3	-24° 14°	-21° 24°	-18° 19°	-21° 17°

TABLE 4-2.2: RESULTS OF LINEAR INVERSIONS AT TRIAL DEPTHS GIVING SMALL RESIDUALS

FOCAL DEPTH	12km	80km	90km	100km
	$\times 10^{24}$	$\times 10^{24}$	$\times 10^{24}$	$\times 10^{24}$
M_{zz}	$0.4 \pm .3$	-1.0 ± 1.0	-9.0 ± 0.4	-1.0 ± 0.4
$M_{yy} - M_{xx}$	$-4.8 \pm .3$	21.0 ± 2.0	20.0 ± 2.0	20.0 ± 2.0
M_{xy}	$2.8 \pm .2$	-10.0 ± 1.0	-10.0 ± 1.0	-10.0 ± 1.0
M_{xz}	$0.8 \pm .1$	1.6 ± 0.3	1.6 ± 0.3	1.7 ± 0.4
M_{yz}	$1.8 \pm .2$	2.9 ± 0.4	3.0 ± 0.4	3.1 ± 0.4
λ_1	$4.1 \pm .2$	15.7 ± 1.1	14.9 ± 1.1	14.9 ± 1.1
λ_2	$0.2 \pm .3$	-0.8 ± 1.0	-0.7 ± 0.4	-0.7 ± 0.4
λ_3	$-4.3 \pm .2$	-14.8 ± 1.1	-14.2 ± 1.1	-14.2 ± 1.1
e_1	-118° 23°	-202° 7°	-202° 8°	-202° 8°
e_2	-258° 61°	-79° 77°	-78° 76°	-79° 75°
e_3	-21° 17°	67° 11°	67° 11°	66° 12°

TABLE 4-2.3: RMS AMPLITUDES OF REAL AND IMAGINARY PARTS OF EVENT 9 - OBSERVED AND THEORETICAL

OBSERVED RMS AMPLITUDES, CM-SEC

PERIOD	REAL PART	IMAGINARY PART
60s	.021	.012
50	.031	.010
40	.033	.018
34	.032	.025
30	.034	.024
26	.039	.030

OBSERVED AND THEORETICAL RMS AMPLITUDES, NORMALIZED

PERIOD	IMAGINARY PART	10KM	80KM
60s	0.4	0.1	0.8
50	0.3	0.2	0.9
40	0.6	0.3	1.0
34	0.8	0.6	0.9
30	0.8	0.7	0.7
26	1.0	1.0	0.5

TABLE 4-2.4: RESULTS OF LINEAR INVERSIONS BEFORE AND AFTER RELOCATION OF EVENT 9

			RELOCATION
FOCAL DEPTH	10km	15km	10km
	$\times 10^{24}$	$\times 10^{24}$	$\times 10^{24}$
M_{zz}	$0.6 \pm .3$	$-0.2 \pm .2$	$0.8 \pm .2$
$M_{yy} - M_{xx}$	$-4.3 \pm .4$	$-5.4 \pm .3$	$-5.2 \pm .3$
M_{xy}	$2.3 \pm .2$	$3.5 \pm .2$	$2.3 \pm .2$
M_{xz}	$0.9 \pm .2$	$0.7 \pm .1$	$0.6 \pm .2$
M_{yz}	$2.1 \pm .2$	$1.6 \pm .2$	$0.8 \pm .2$
λ_1	$3.8 \pm .2$	$4.9 \pm .2$	$3.4 \pm .2$
λ_2	$0.3 \pm .3$	$-0.2 \pm .2$	$0.6 \pm .2$
λ_3	$-4.1 \pm .3$	$-4.7 \pm .2$	$-4.0 \pm .2$
e_1	-121° 30°	-118° 15°	-112° 19°
e_2	-260° 53°	-251° 69°	-270° 70°
e_3	-19° 20°	-24° 15°	-20° 7°

TABLE 4-2.5: FOCAL DEPTH AND SEISMIC MOMENT TENSOR GIVING SMALLEST RESIDUAL

EVENT	1	2	3	4	5	6	7	8	9
FOCAL DEPTH	7.5km	15km	5km	7.5km	10km	100km	7.5km	7.5km	15km
	$\times 10^{24}$	$\times 10^{24}$	$\times 10^{24}$	$\times 10^{23}$	$\times 10^{24}$	$\times 10^{25}$	$\times 10^{24}$	$\times 10^{24}$	$\times 10^{24}$
M_{zz}	$0.5 \pm .1$	$-0.21 \pm .07$	$1.5 \pm .1$	$4.1 \pm .6$	$1.2 \pm .1$	$-1.1 \pm .3$	$1.9 \pm .2$	$-1.1 \pm .3$	$-0.2 \pm .2$
$M_{yy} - M_{xx}$	$-5.3 \pm .1$	$-1.75 \pm .10$	$-2.3 \pm .1$	$-4.3 \pm .4$	$-1.2 \pm .1$	$1.3 \pm .6$	$-4.2 \pm .2$	$-5.0 \pm .4$	$-5.4 \pm .3$
M_{xy}	$1.2 \pm .1$	$0.33 \pm .06$	$-0.1 \pm .1$	$0.4 \pm .5$	$0.3 \pm .1$	$1.8 \pm .6$	$0.3 \pm .1$	$0.4 \pm .2$	$3.5 \pm .2$
M_{xz}	$0.6 \pm .2$	$-0.29 \pm .04$	$0.8 \pm .3$	$0.5 \pm .3$	$0.0 \pm .1$	$-0.1 \pm .2$	$0.2 \pm .2$	$2.0 \pm .4$	$0.7 \pm .1$
M_{yz}	$0.2 \pm .2$	$-0.30 \pm .05$	$2.8 \pm .4$	$2.0 \pm .4$	$1.1 \pm .1$	$1.3 \pm .3$	$1.3 \pm .3$	$6.0 \pm .5$	$1.6 \pm .2$
λ_1	$2.8 \pm .1$	$1.1 \pm .06$	$3.2 \pm .3$	$4.6 \pm .6$	$1.6 \pm .1$	$2.8 \pm .6$	$2.3 \pm .2$	$5.7 \pm .5$	$4.9 \pm .2$
λ_2	$0.3 \pm .1$	$-0.2 \pm .07$	$0.3 \pm .1$	$0.0 \pm .5$	$0.0 \pm .1$	$-0.6 \pm .3$	$1.1 \pm .2$	$2.0 \pm .4$	$-0.2 \pm .2$
λ_3	$-3.2 \pm .1$	$-0.9 \pm .06$	$-3.5 \pm .4$	$-4.6 \pm .5$	$-1.7 \pm .1$	$-2.2 \pm .4$	$-3.4 \pm .2$	$-7.7 \pm .5$	$-4.7 \pm .2$
e_1	-102° 15°	78° 15°	-154° 59°	-151° 75°	-171° 68°	-148° 15°	-135° 70°	-132° 39°	-118° 15°
e_2	278° 75°	-45° 65°	103° 8°	88° 8°	83° 6°	-252° 43°	90° 14°	119° 21°	-251° 69°
e_3	-12° 1°	-186° 20°	8° 30°	-3° 13°	-9° 21°	-43° 43°	-3° 14°	8° 43°	-24° 15°

TABLE 4-2.6: FINAL SOURCE PARAMETERS

	1	2	3	4	5	6	7	8	9
FOCAL DEPTH	5km	7km	5km	6km	7.5km	100km	7.5km	7.5km	10km
	$\times 10^{24}$	$\times 10^{24}$	$\times 10^{24}$	$\times 10^{23}$	$\times 10^{24}$	$\times 10^{25}$	$\times 10^{24}$	$\times 10^{24}$	$\times 10^{24}$
M_{zz}	$0.4 \pm .1$	0.06	$1.5 \pm .1$	5.0	$0.9 \pm .1$	$-1.1 \pm .3$	$1.9 \pm .2$	$-1.1 \pm .3$	$0.8 \pm .2$
$M_{yy} - M_{xx}$	$-4.6 \pm .1$	-1.38	$-2.3 \pm .1$	-5.8	$-1.1 \pm .1$	$1.3 \pm .6$	$-4.2 \pm .2$	$-5.0 \pm .4$	$-5.2 \pm .3$
M_{xy}	$1.0 \pm .1$	0.15	$-0.1 \pm .1$	-0.6	$0.2 \pm .1$	$1.8 \pm .6$	$0.3 \pm .1$	$0.4 \pm .2$	$2.3 \pm .2$
M_{xz}	$1.0 \pm .4$	-0.21	$0.8 \pm .3$	3.1	$0.0 \pm .1$	$-0.1 \pm .2$	$0.2 \pm .2$	$2.0 \pm .4$	$0.6 \pm .2$
M_{yz}	$0.5 \pm .4$	-0.07	$2.8 \pm .4$	6.6	$1.5 \pm .1$	$-1.3 \pm .3$	$1.3 \pm .3$	$6.0 \pm .5$	$0.8 \pm .2$
λ_1	$2.8 \pm .3$	0.74	$3.2 \pm .3$	9.0	$1.7 \pm .1$	$2.8 \pm .6$	$2.3 \pm .2$	$5.7 \pm .5$	$3.4 \pm .2$
λ_2	$-0.1 \pm .3$	0.00	$0.3 \pm .1$	0.0	$0.1 \pm .1$	$-0.6 \pm .3$	$1.1 \pm .2$	$2.0 \pm .4$	$0.6 \pm .2$
λ_3	$-2.7 \pm .1$	-0.74	$-3.5 \pm .4$	-9.0	$-1.8 \pm .1$	$-2.2 \pm .4$	$-3.4 \pm .2$	$-7.7 \pm .5$	$-4.0 \pm .2$
e_1	-103° 24°	82° 18°	-154° 59°	-142° 61°	-174° 61°	-148° 15°	-135° 70°	-132° 39°	-112° 19°
e_2	-268° 65°	-82° 72°	103° 8°	108° 10°	87° 5°	-252° 43°	90° 14°	119° 21°	-270° 70°
e_3	-11° 6°	174° 2°	8° 30°	13° 26°	-5° 29°	-43° 43°	-3° 14°	8° 43°	-20° 7°

TABLE 4-2.7: MEANS AND VARIANCES OF HISTOGRAMS IN FIGURE 4-2.24

(n = NUMBER OF SAMPLES)

	T = 50sec	T = 40sec	T = 34sec	T = 30sec
2	n = 22 x_2 = $.09 \times 10^{-2}$ σ^2 = $.13 \times 10^{-4}$	n = 24 x_2 = $.05 \times 10^{-2}$ σ^2 = $.36 \times 10^{-4}$	n = 24 x_2 = $.38 \times 10^{-2}$ σ^2 = 1.33×10^{-4}	n = 24 x_2 = $.35 \times 10^{-2}$ σ^2 = $.71 \times 10^{-4}$
5	16 .05 .08	22 -.14 .20	25 .03 .72	25 -.43 1.62
7	20 -.06 .19	24 .14 .63	24 -.19 2.93	22 -.02 3.14
3	23 -.04 .15	28 -.38 1.06	29 .42 3.95	29 .15 3.99
1	23 .07 .20	26 .34 1.33	27 .74 4.05	28 1.09 8.88
9	19 -.21 .35	21 -.13 .87	22 .08 4.97	22 .88 6.14
8	25 -.35 .95	24 .17 1.05	27 .39 6.95	26 1.0 11.5
6	16 -.77 11.3	14 -.80 15.7	15 .51 12.1	16 -.41 16.3

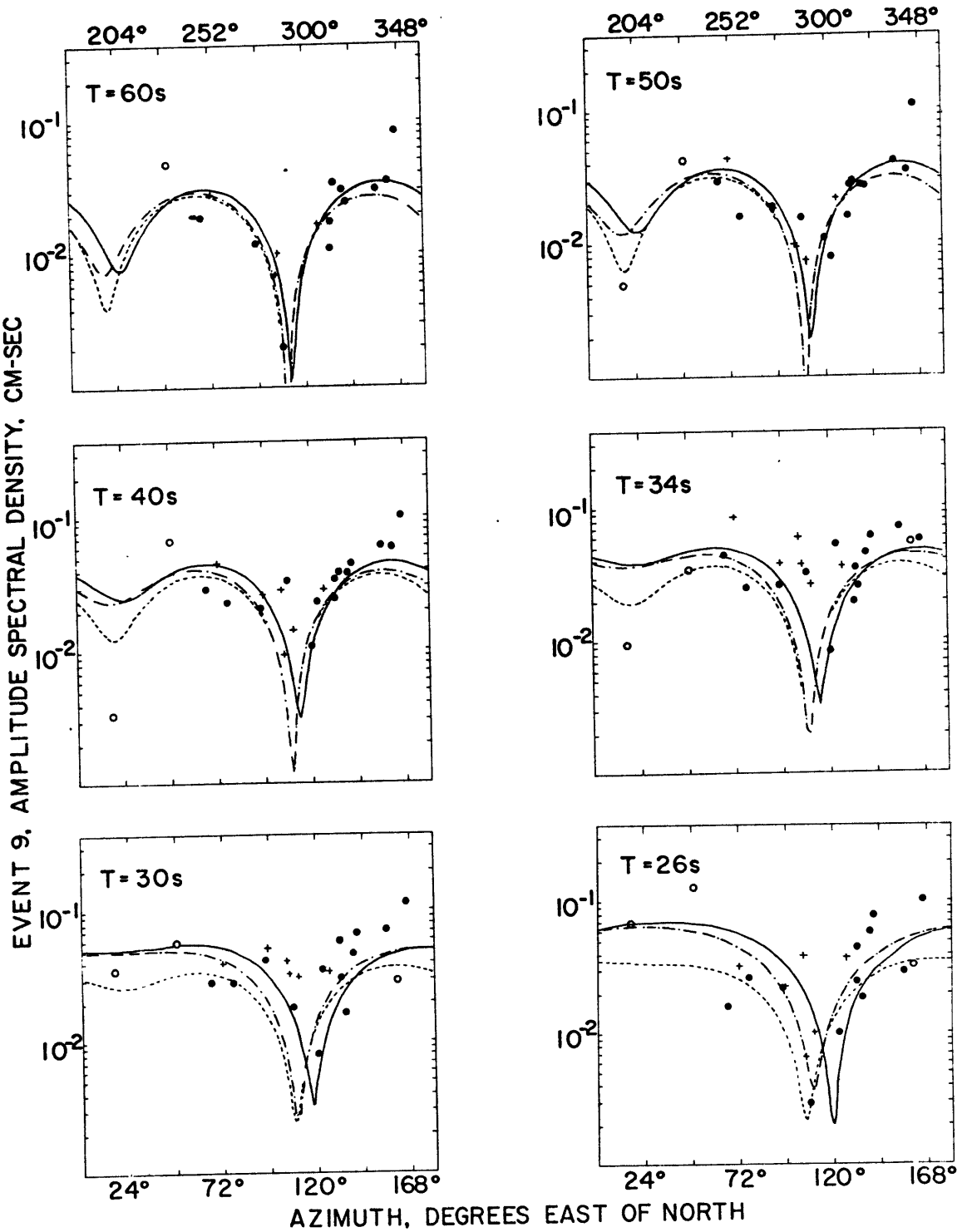

Fig. 4-2.1a: Amplitude radiation patterns of event 9. Two fold symmetry is reflected about N-S axes, showing stations east of north as (+) and west of north as (•). Screened data points are shown as (o). Shown are results of linear inversion on all data (-----), on screened data (———) and logarithmic fitting on all data (—·—·—·—).

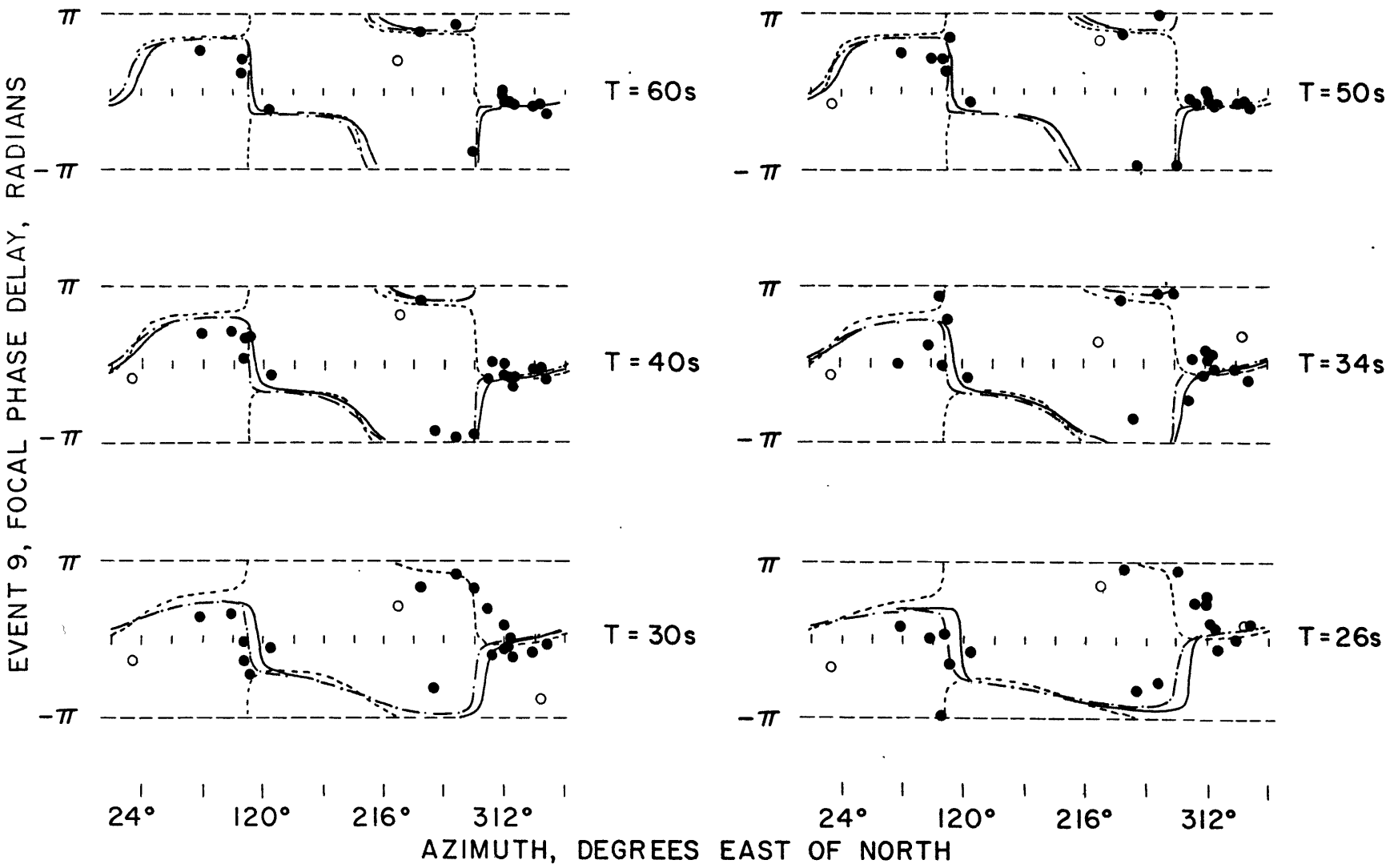

Fig. 4-2.1b: Focal phase radiation patterns of event 9. Screened data points are shown as (o). See caption of Figure 4-2.1a for definition of lines.

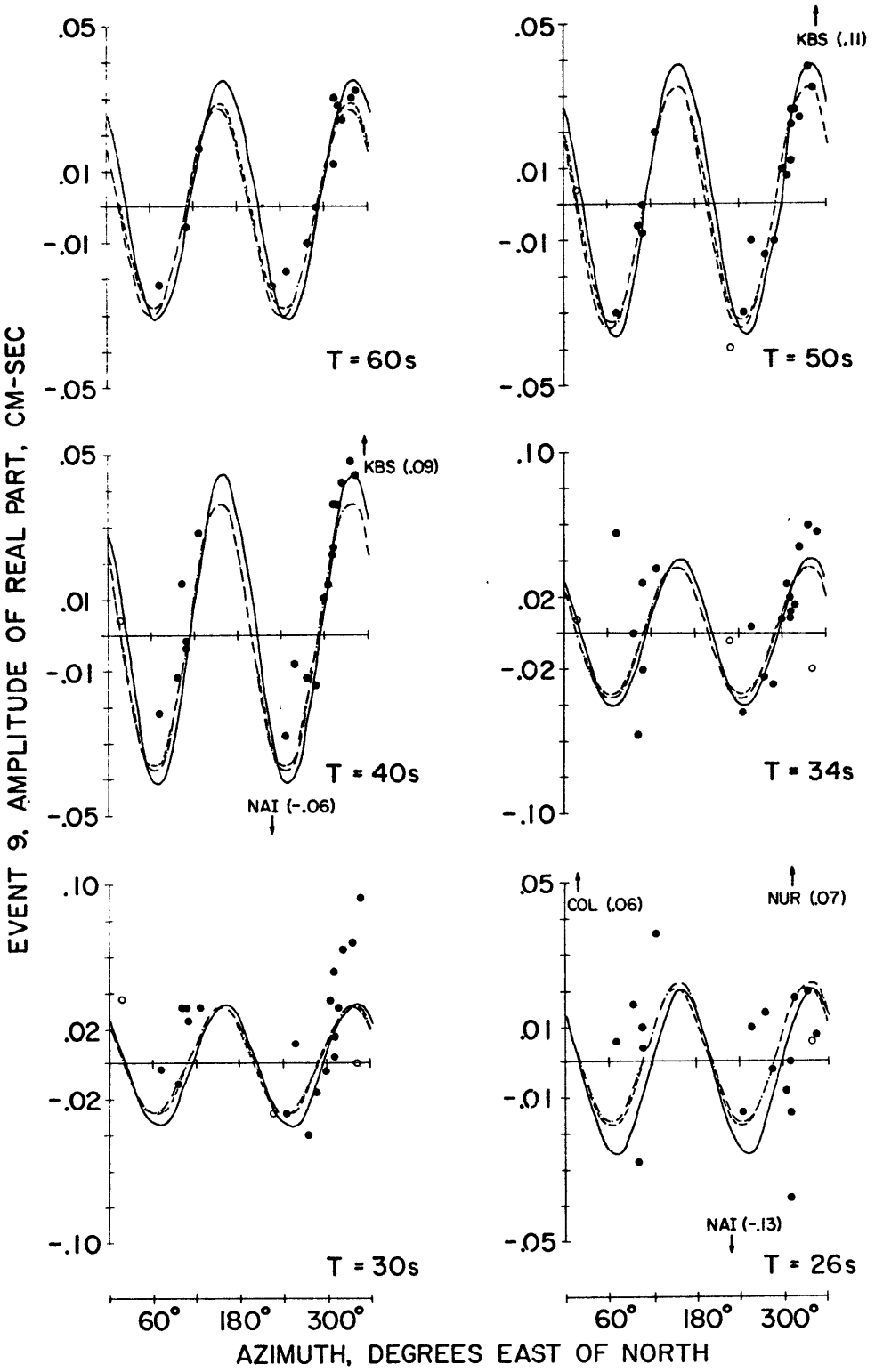

Fig. 4-2.2a: Radiation patterns of the real part of the complex source spectrum of event 9. Screened data points are shown as (o). See caption of Figure 4-2.1a for definition of lines.

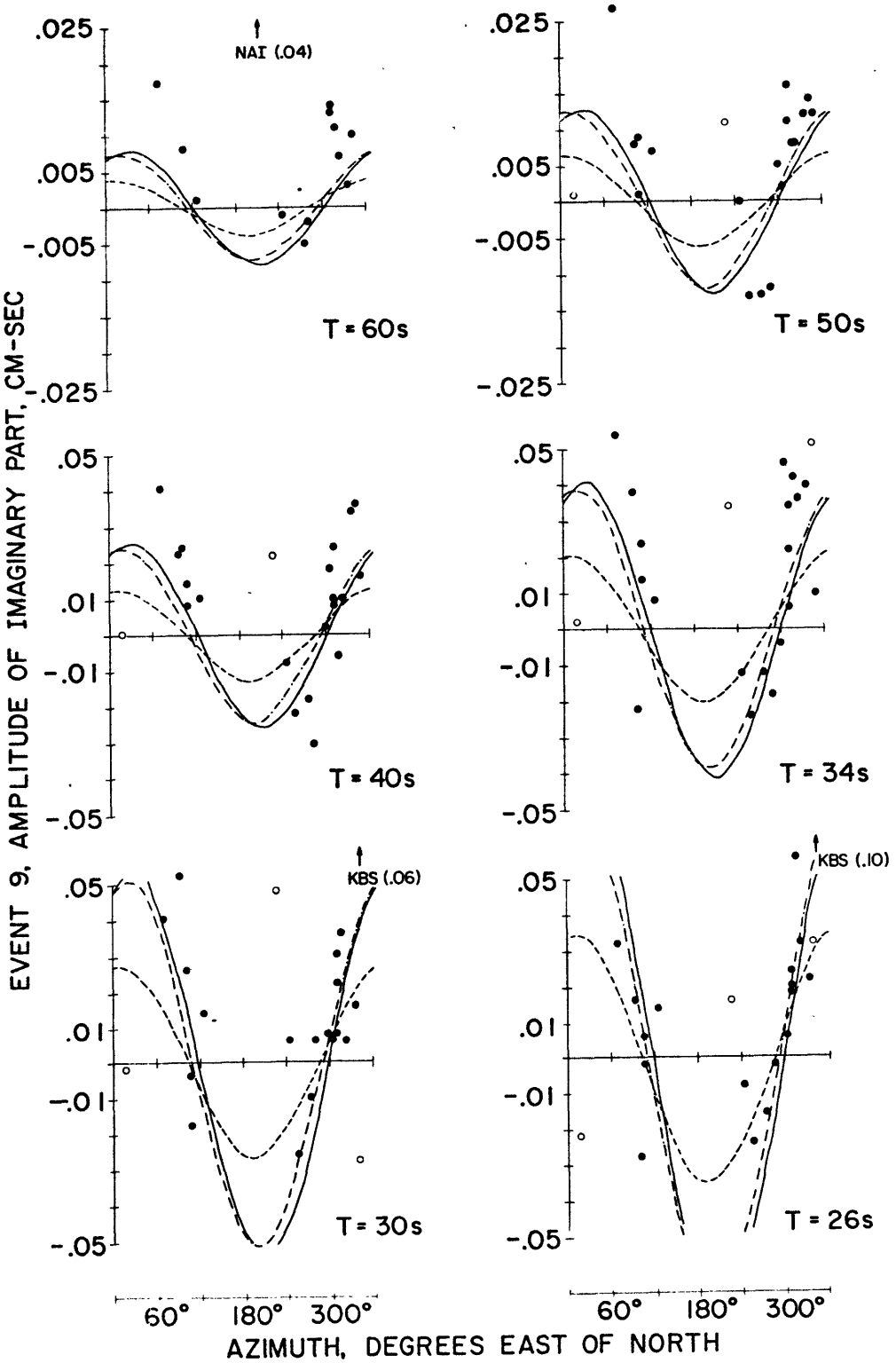

Fig. 4-2.2b: Radiation patterns of the imaginary part of the complex source spectrum of event 9. Screened data points are shown as (o). See caption of Figure 4-2.1a for definition of lines.

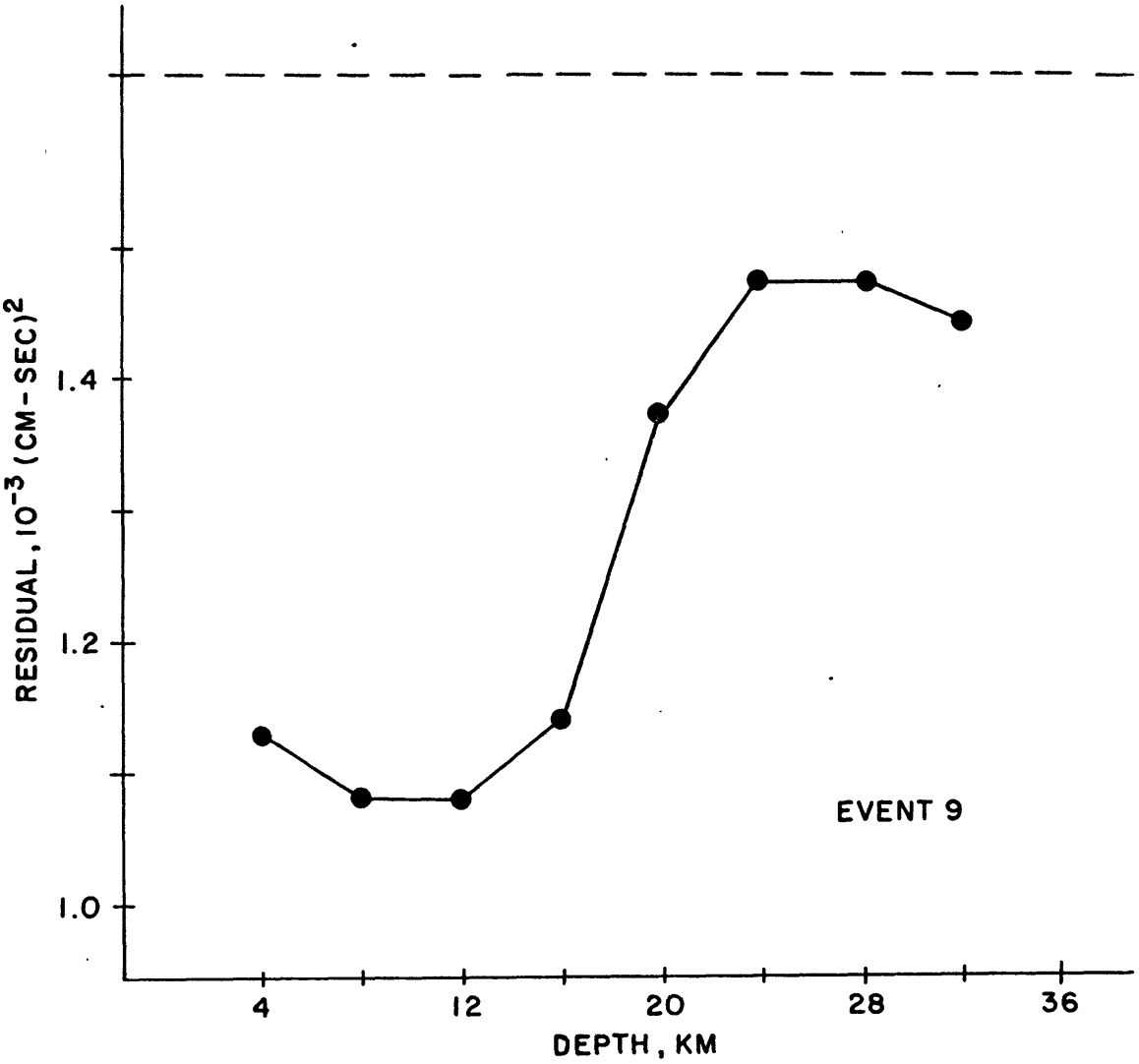

Fig. 4-2.3: Residual curve obtained from the repeated application of the straight least squares inversion method. The residual plotted here is ε^2 defined in Equation 2-4.4 divided by the number of degrees of freedom (i.e., N-5, where N is the number of data points). The horizontal line refers to the sum of squares of observed real and imaginary parts divided by the number of degrees of freedom.

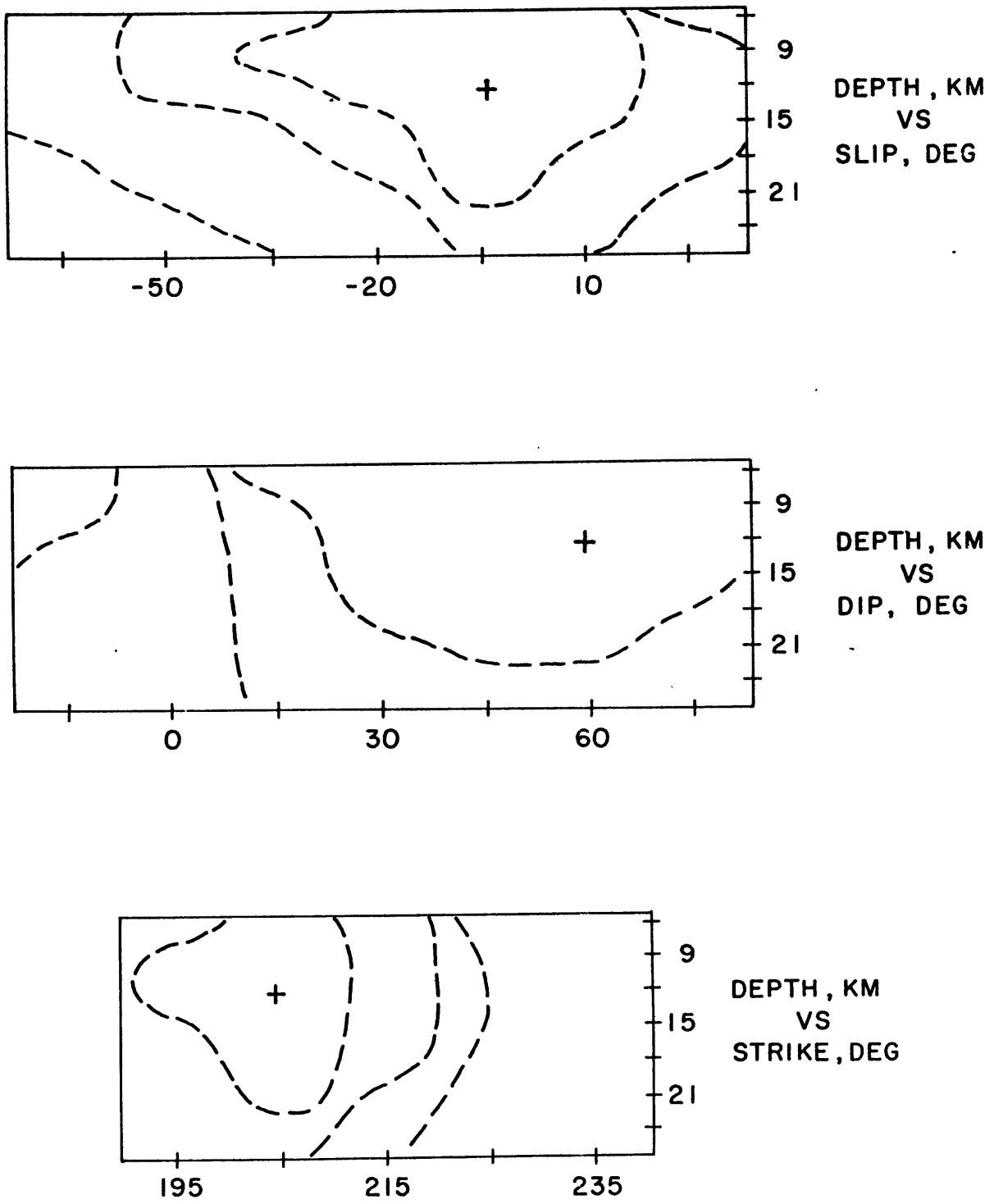

Fig. 4-2.4: Cross-sections of logarithmic residual space through the minimum (+). Dashed lines are contours of residuals 1.5, 2.0 and 3.0 times the value at the minimum.

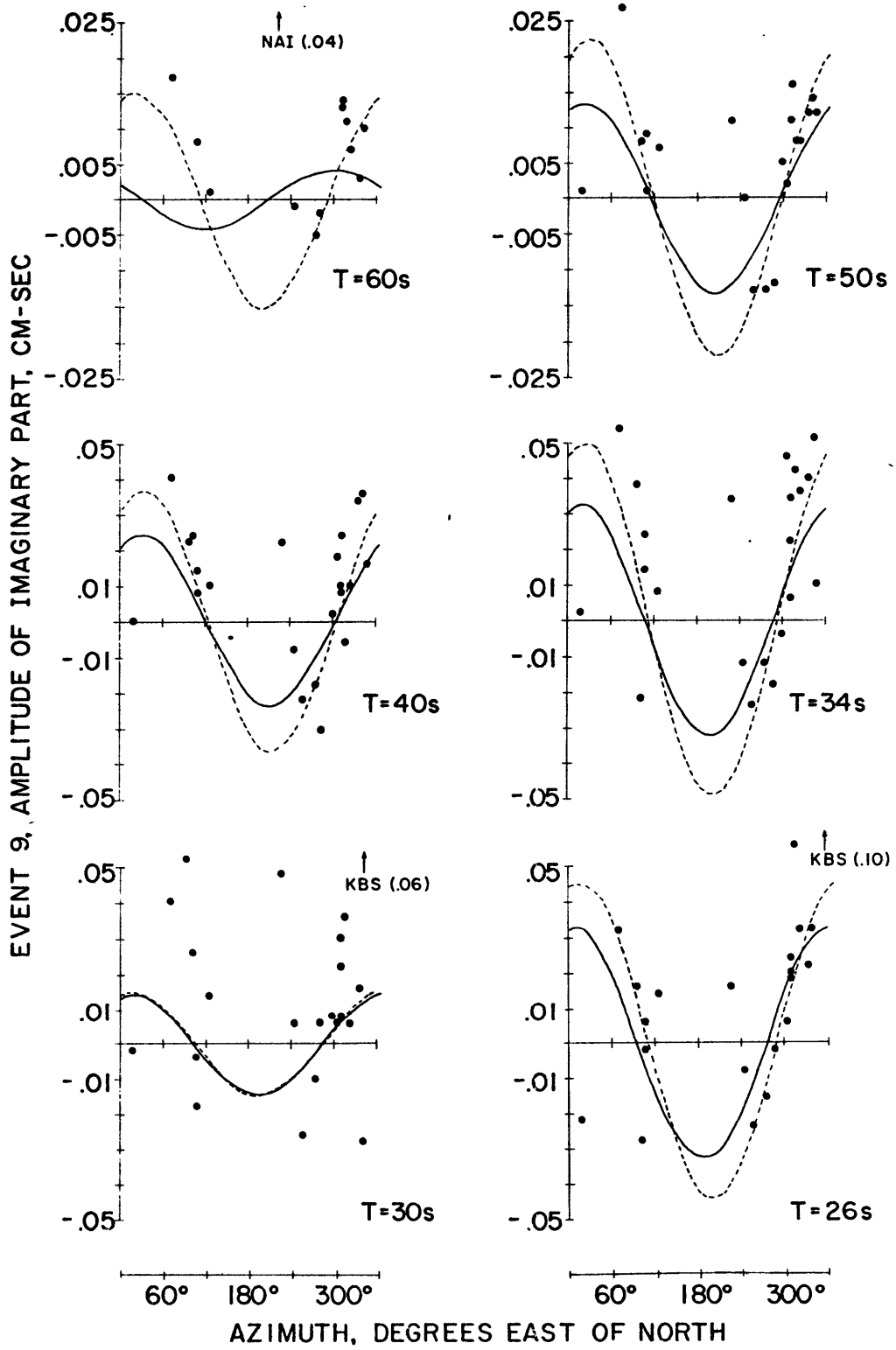

Fig. 4-2.5: Results of curve fitting using straight least squares (———) and the robust method (-----) involving weighted least squares. Curve fits performed just on the data in each plot (i.e., at a constant period).

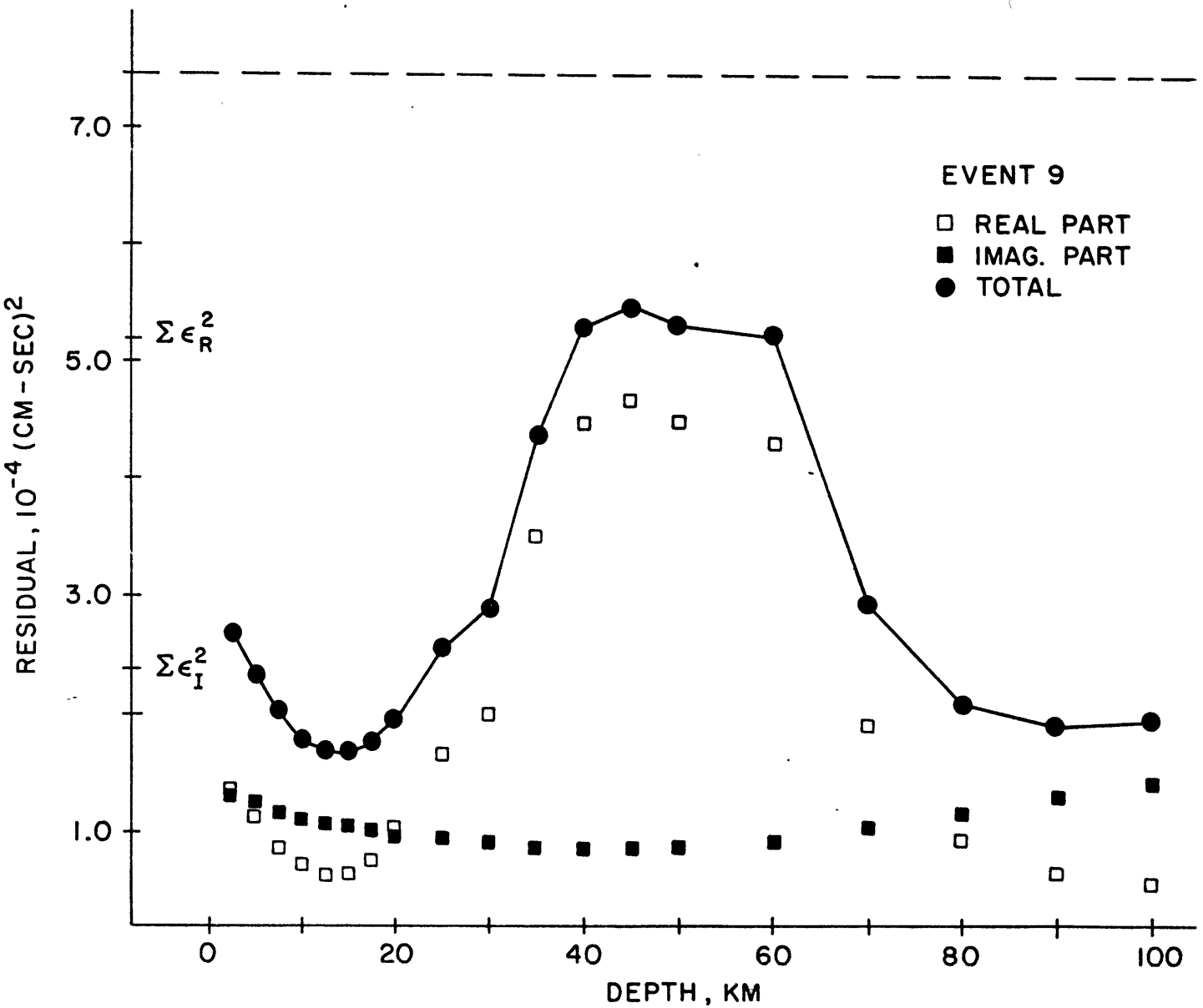

Fig. 4-2.6: Residual curve obtained from repeated application of the robust inversion method. As in Figure 4-2.3, residuals are normalized by the number of degrees of freedom.

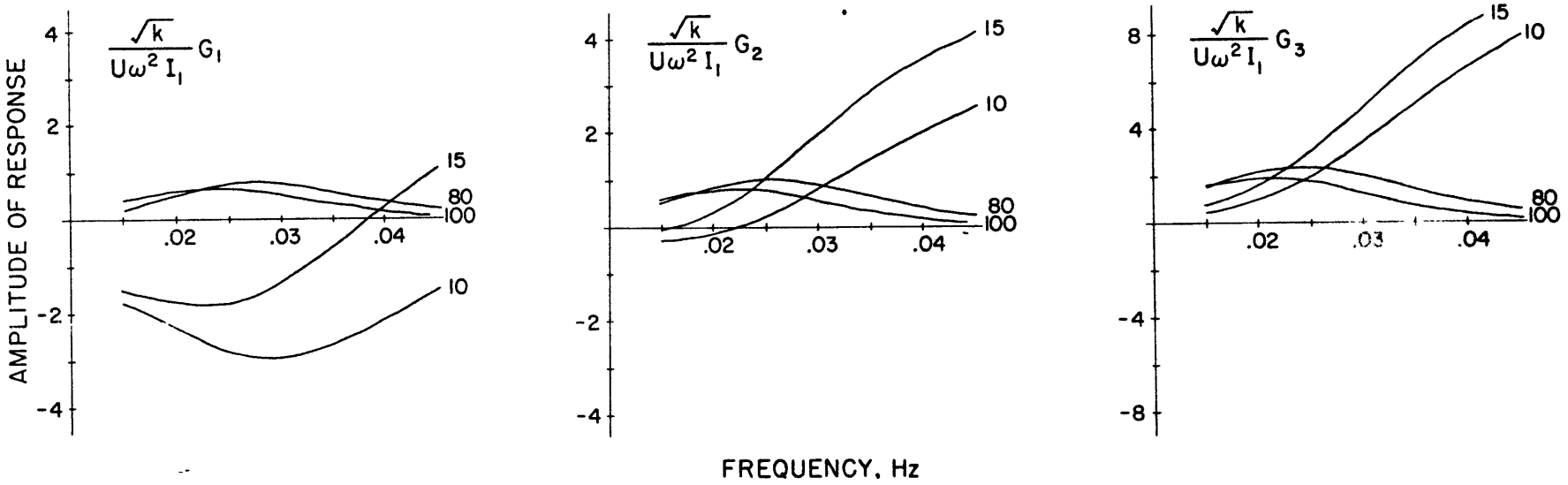

Fig. 4-2.7: Comparison of the fundamental mode Rayleigh wave responses of the Pamir earth model for shallow and deep foci.

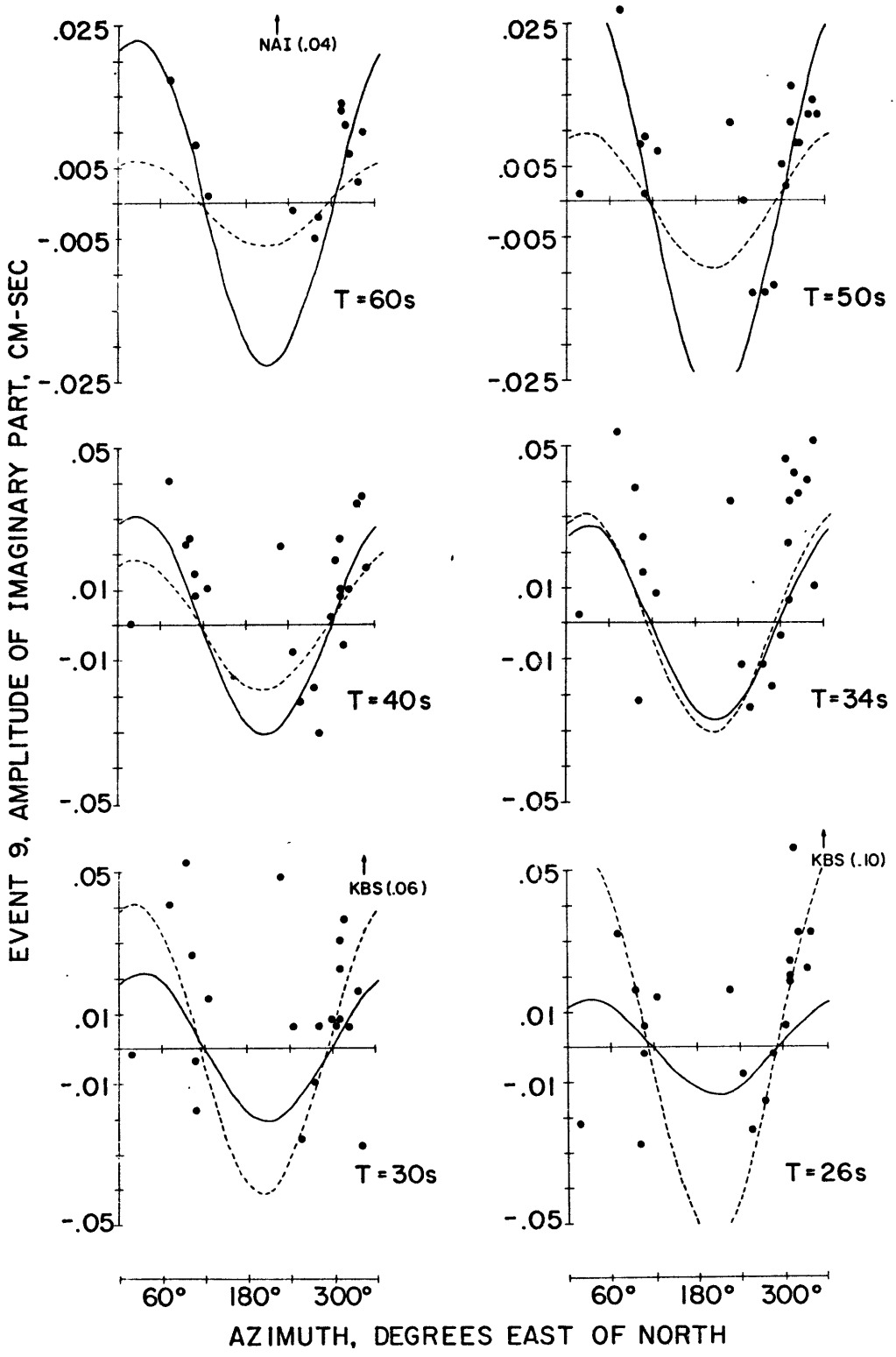

Fig. 4-2.8: Comparison of the observed imaginary part with the theoretical curves based on the results of the inversion at 12km (----) and at 80km (———) focal depth.

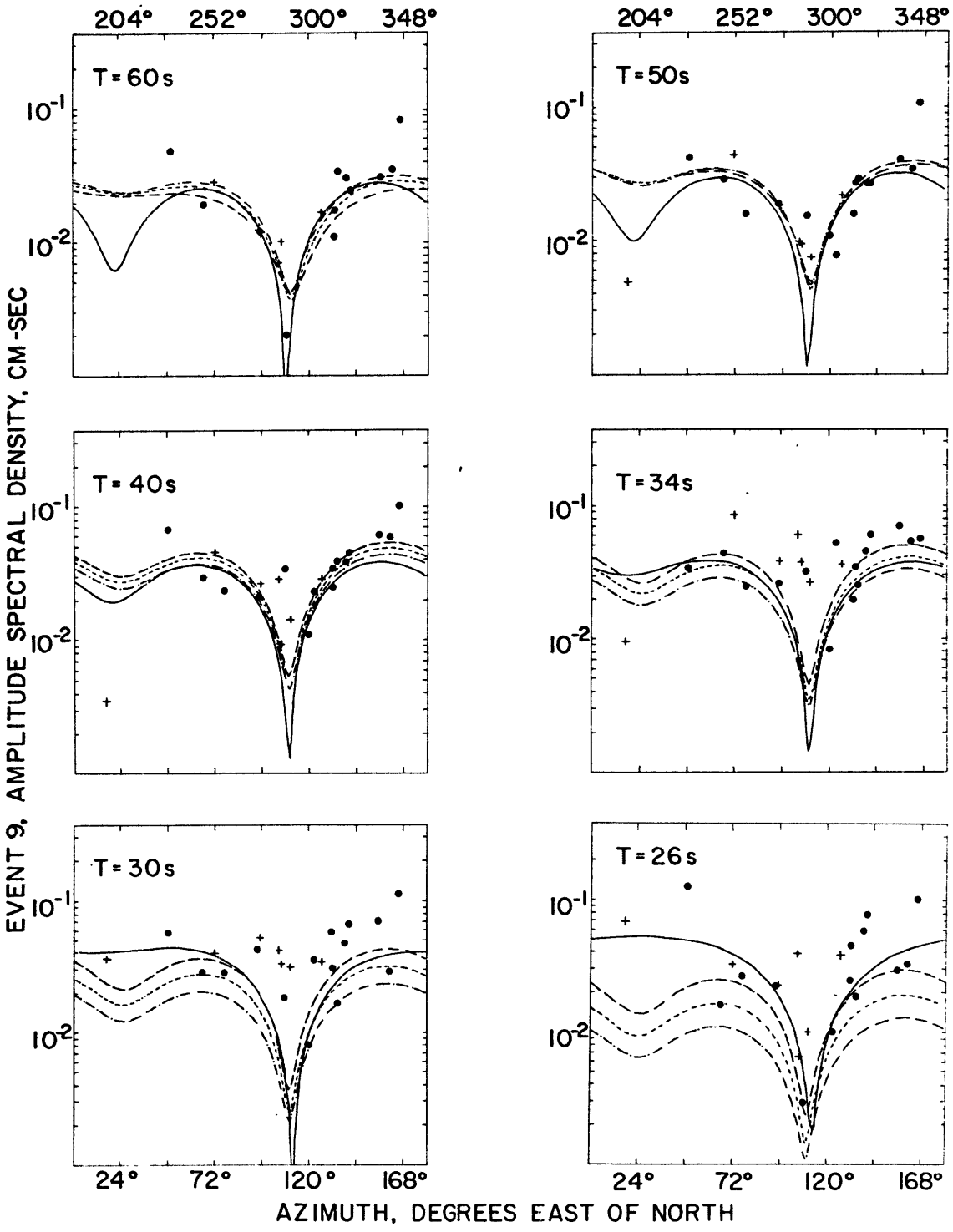

Fig. 4-2.9a: Comparison of the observed amplitude radiation patterns with the theoretical patterns based on results of the inversion at 12km (———), 80km (— —), 90km (- - - -) and 100km (—·—·) focal depth.

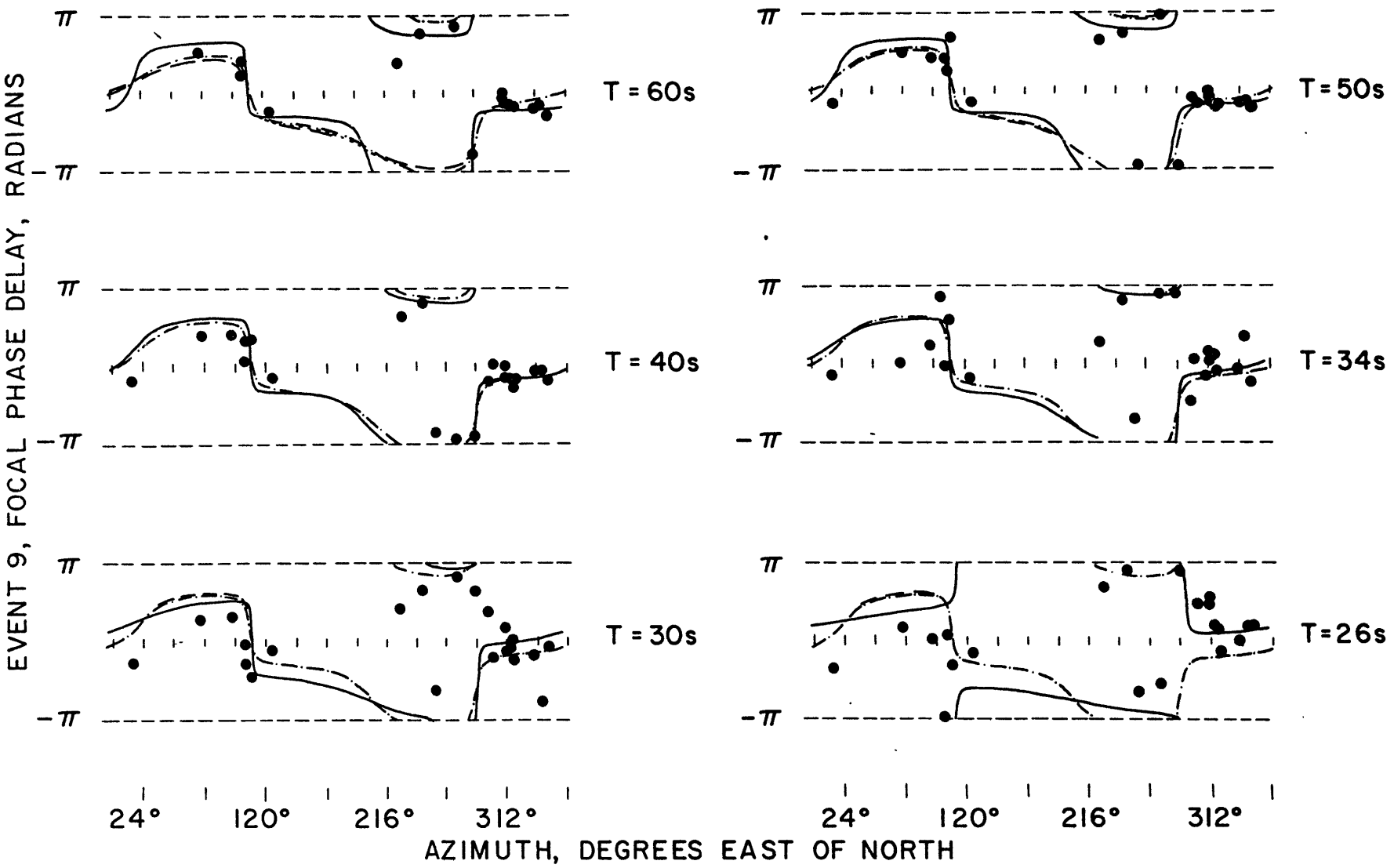

Fig. 4-2.9b: Comparison of the observed focal phase radiation patterns with the theoretical patterns for shallow and deep foci. See caption of Figure 4-2.9a for definition of lines.

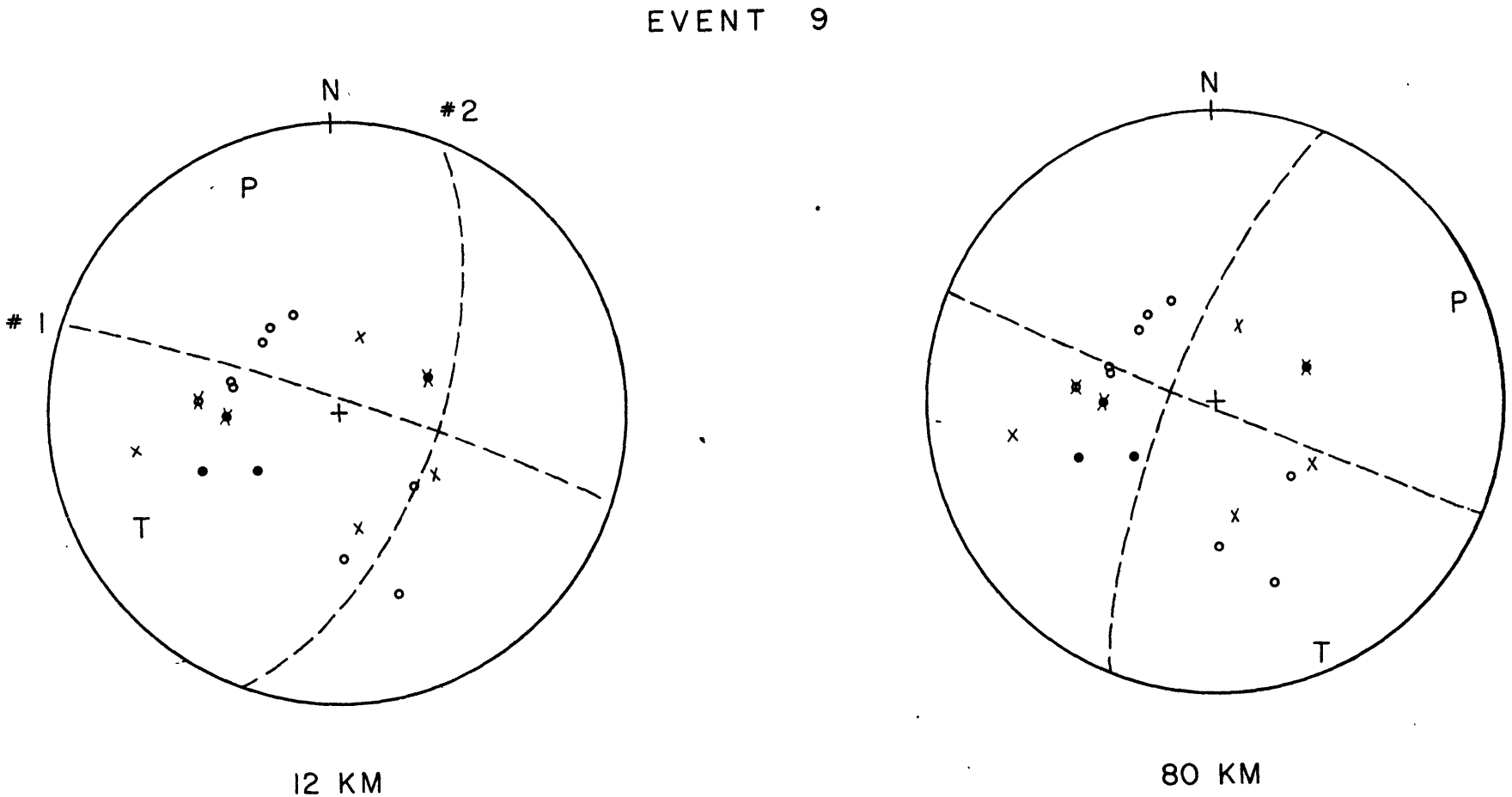

Fig. 4-2.10: P-wave first motions of event 9 plotted on a stereographic net; see caption of Figure 3-1.3 for definition of symbols. Shown with these observations are the fault planes and principal stress axes based on results of the inversion at shallow and deep foci.

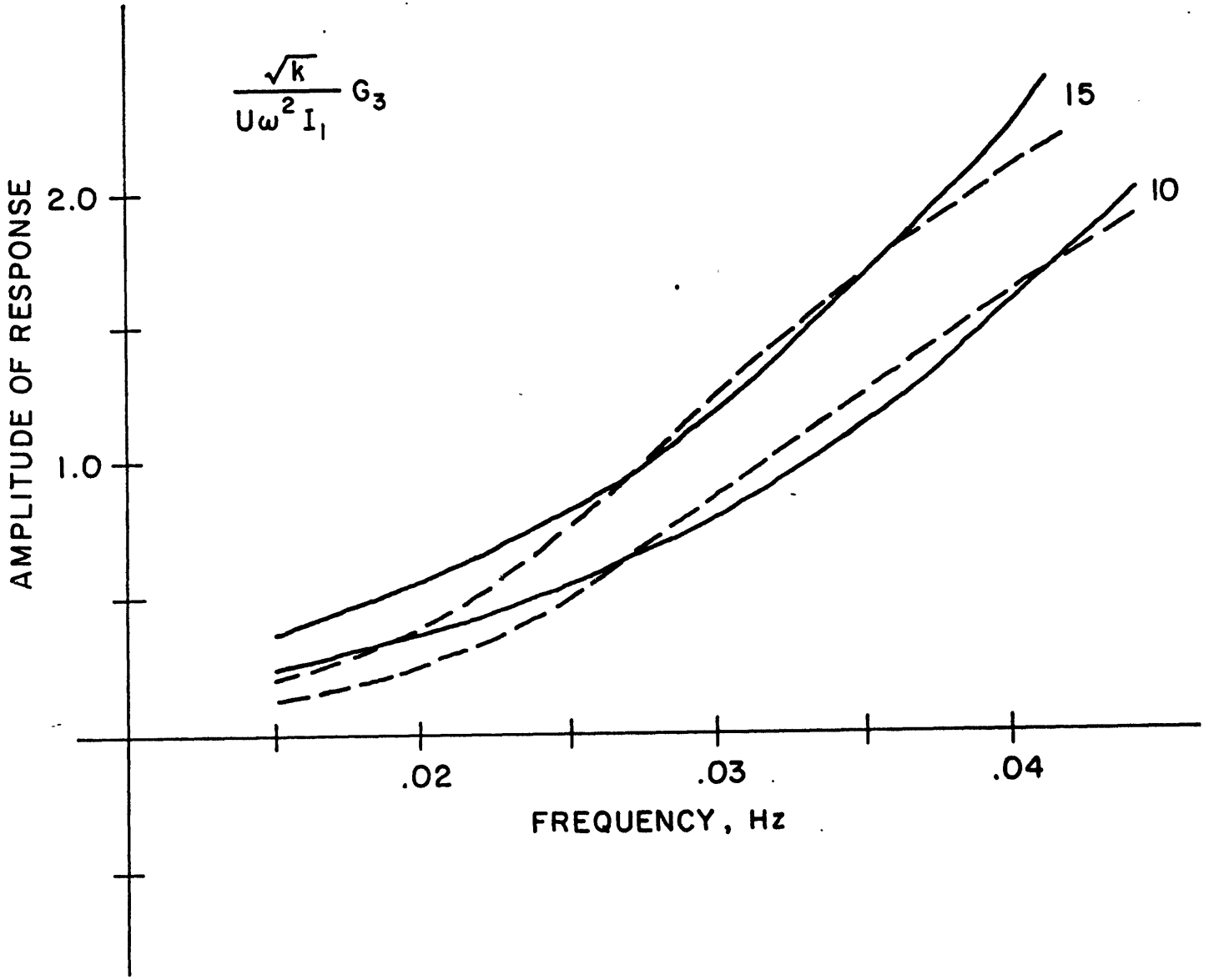

Fig. 4-2.11: Comparison between the fundamental mode Rayleigh response on the imaginary part for the Gutenberg earth model (———) and Pamir earth model (— — —). Numbers on the curves refer to focal depth, km.

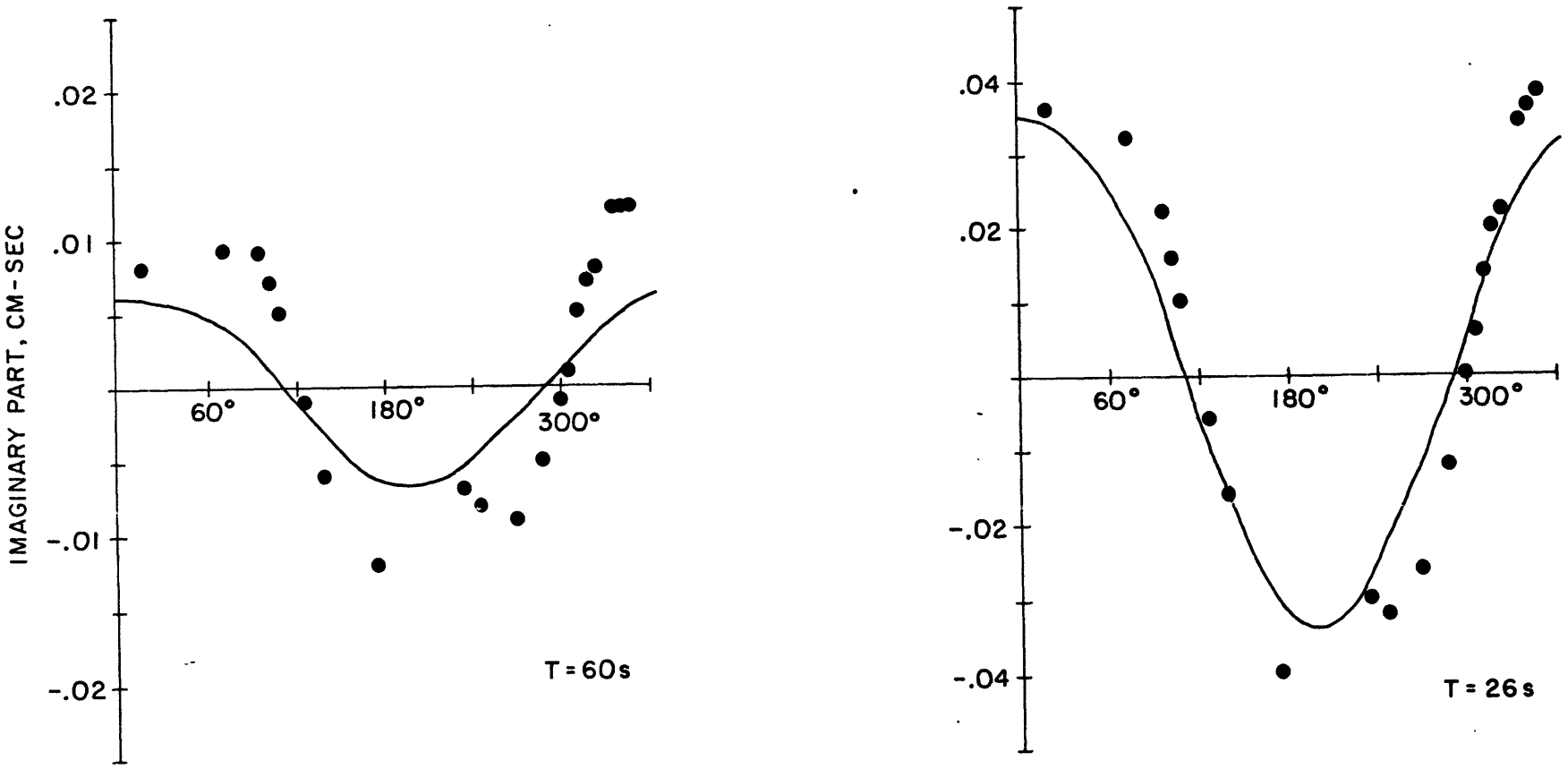

Fig. 4-2.12: Comparison of true (——) and perturbed (●) amplitudes on the imaginary part due to a 15km epicentral location error N45°W of the true epicenter. See Section 3-3 for details of the calculation involving synthetic data.

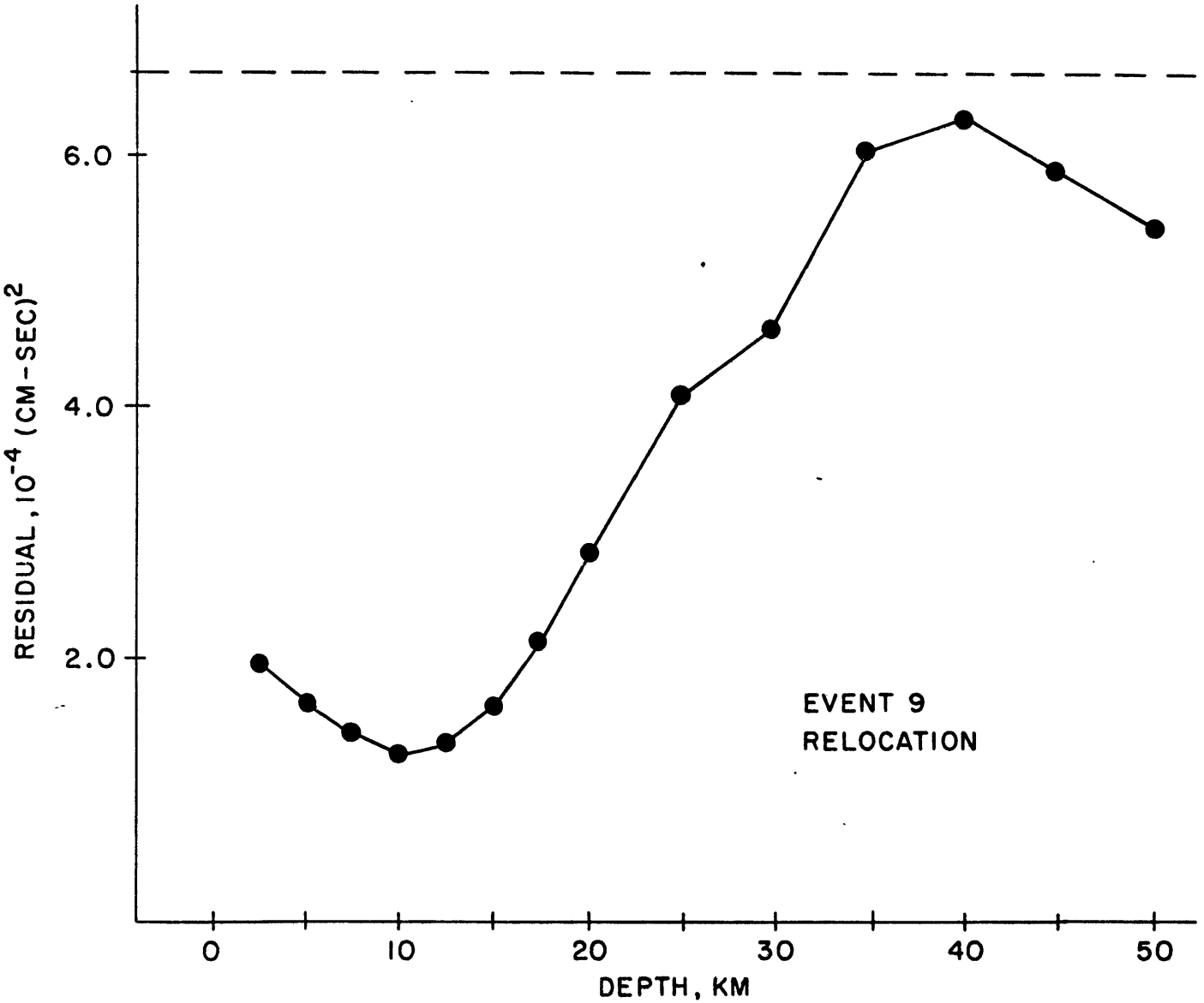

Fig. 4-2.13: Residual curve of event 9 after moving the location of its epicenter 15km to the east. Residuals are normalized as in Figure 4-2.6.

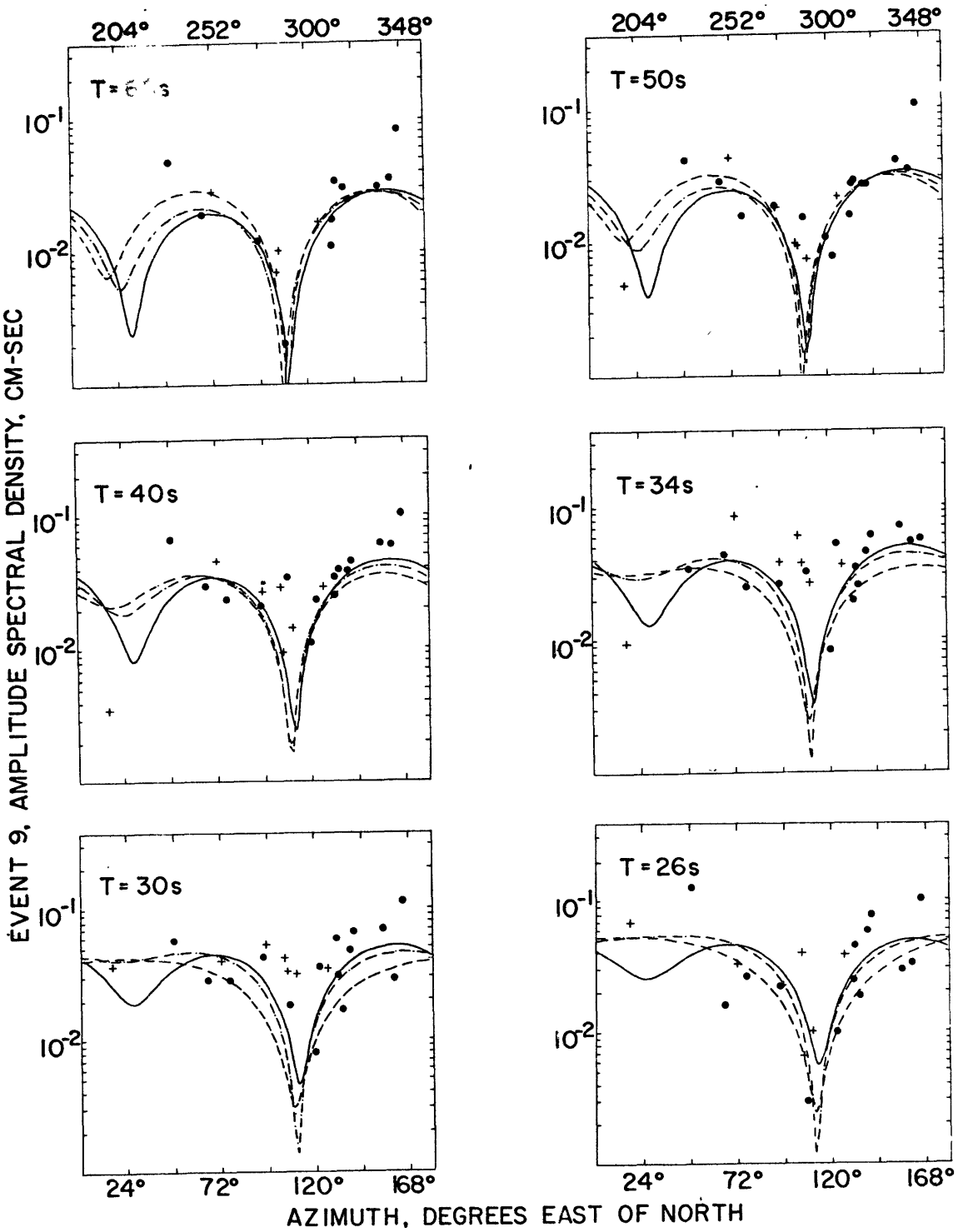

Fig. 4-2.14a: Comparison of the observed amplitude radiation patterns with the theoretical patterns based on the results of the inversion at focal depths of 10km (—·—·) and 15km (— — —) before relocation and 10km (———) after relocation.

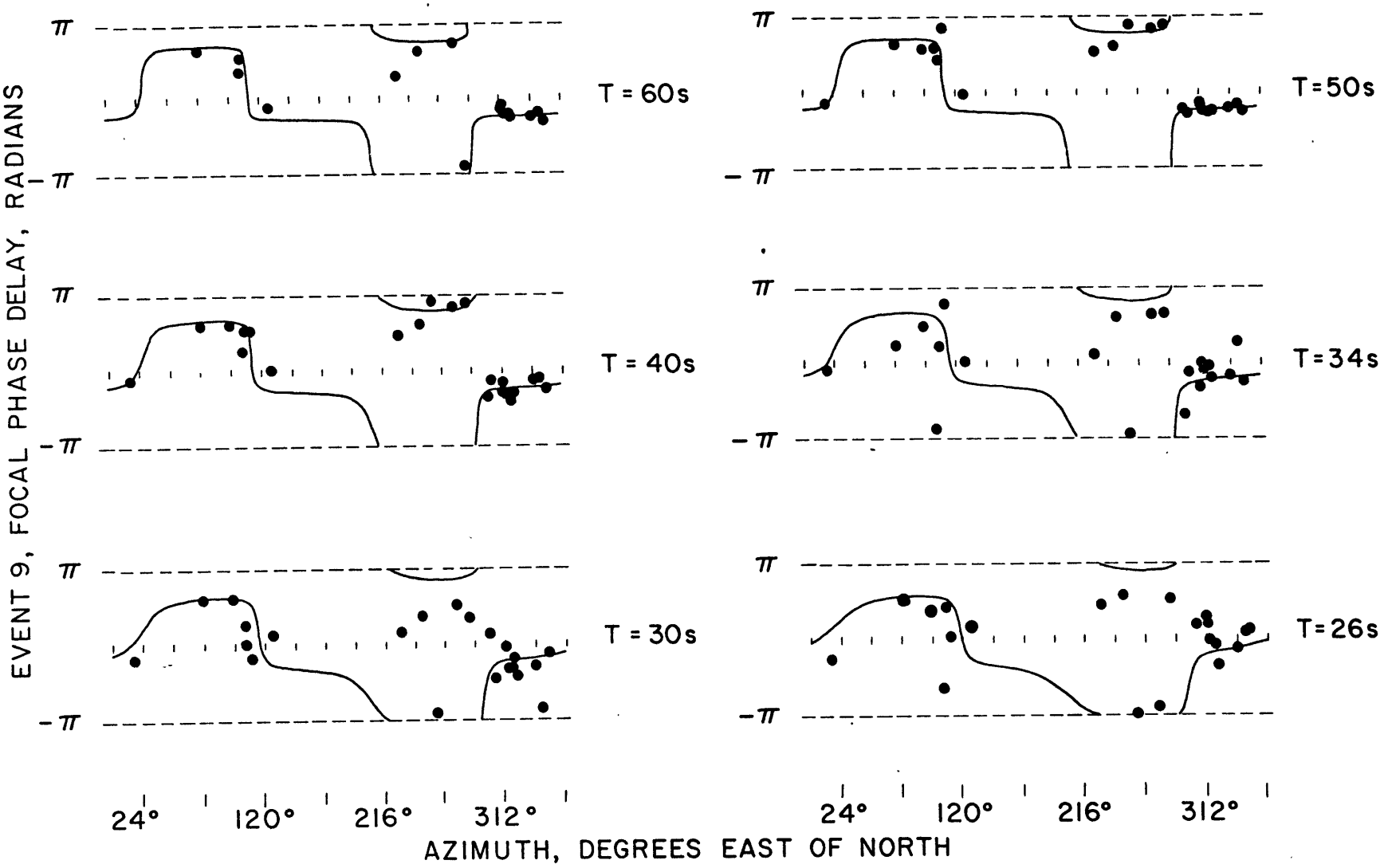

Fig. 4-2.14b: Comparison of the observed focal phase radiation pattern with the theoretical (———) based on the results of the inversion at 10km after the relocation.

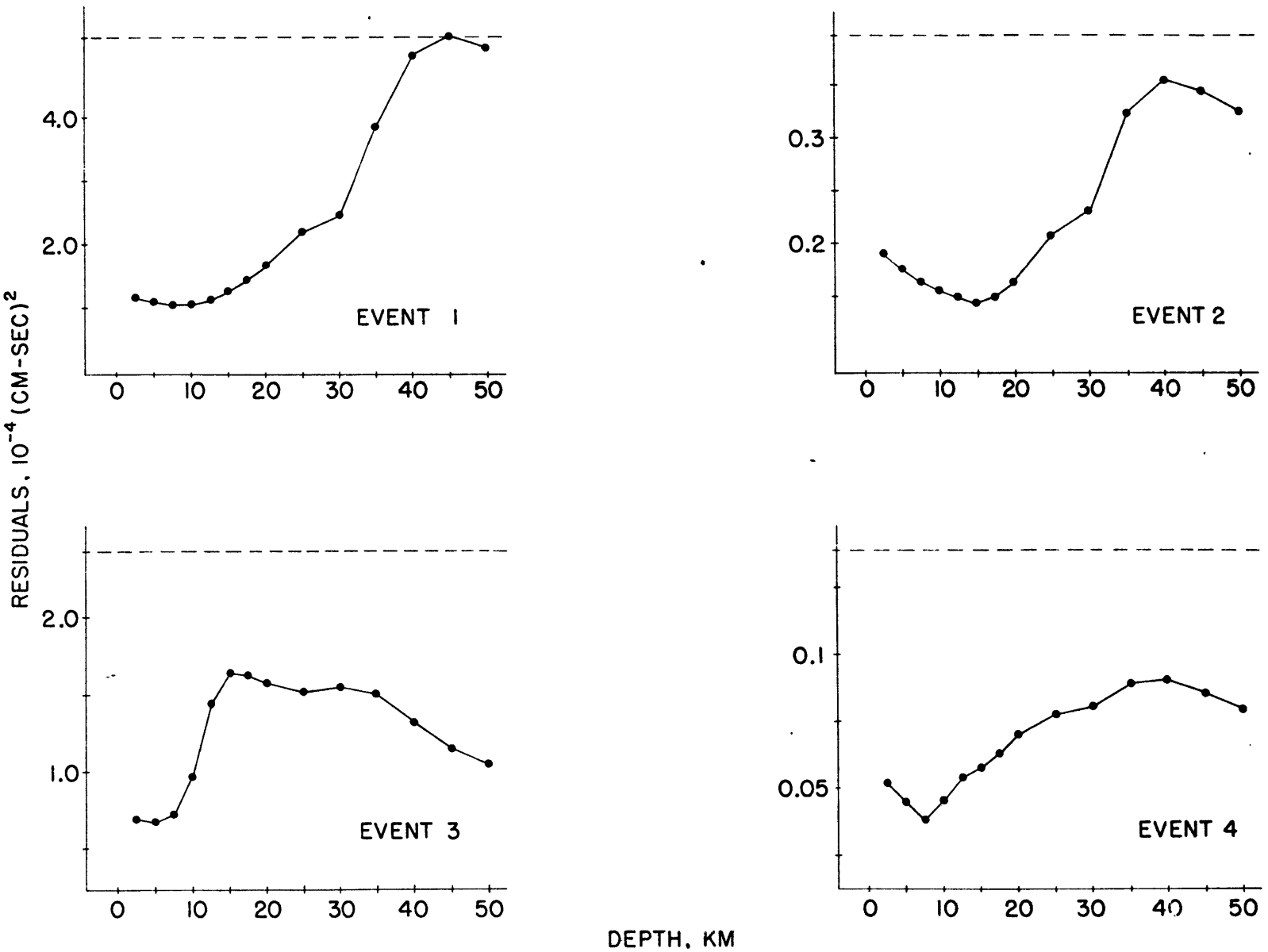

Fig. 4-2.15a: Residual curves for events 1-4. Residuals are normalized by the number of degrees of freedom.

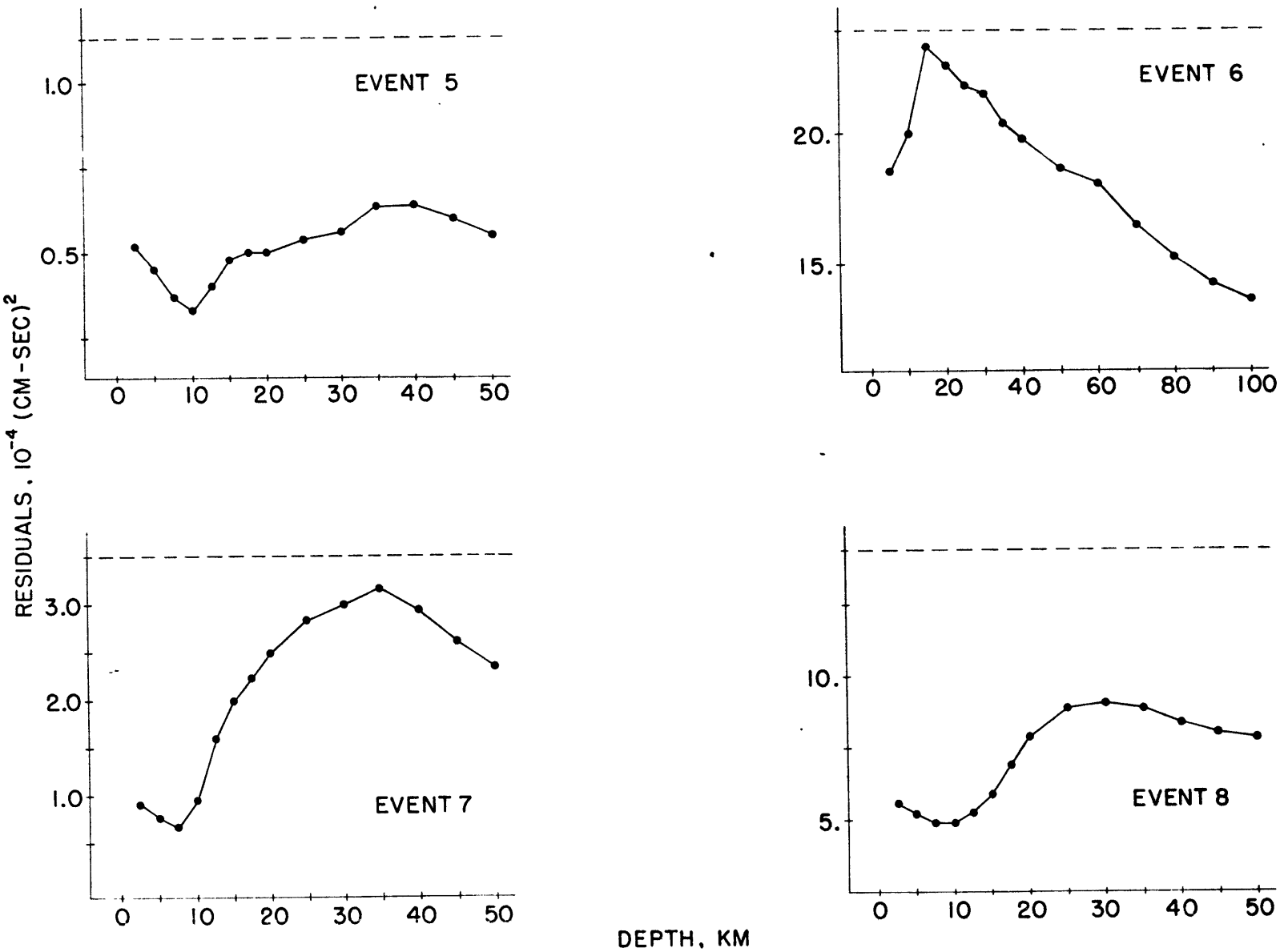

Fig. 4-2.15b: Residual curves for events 5-8. Residuals are normalized by the number of degrees of freedom.

Figures 4-2.16 - 4-2.23: All figures show comparisons of the observed amplitude and focal phase radiation patterns with their theoretical counterparts based on results of the linear moment tensor inversion or the trial and error logarithmic fit. Symbols for the data points are defined in the caption of Figure 4-2.1a. We give the definition of theoretical curves in the caption of each figure.

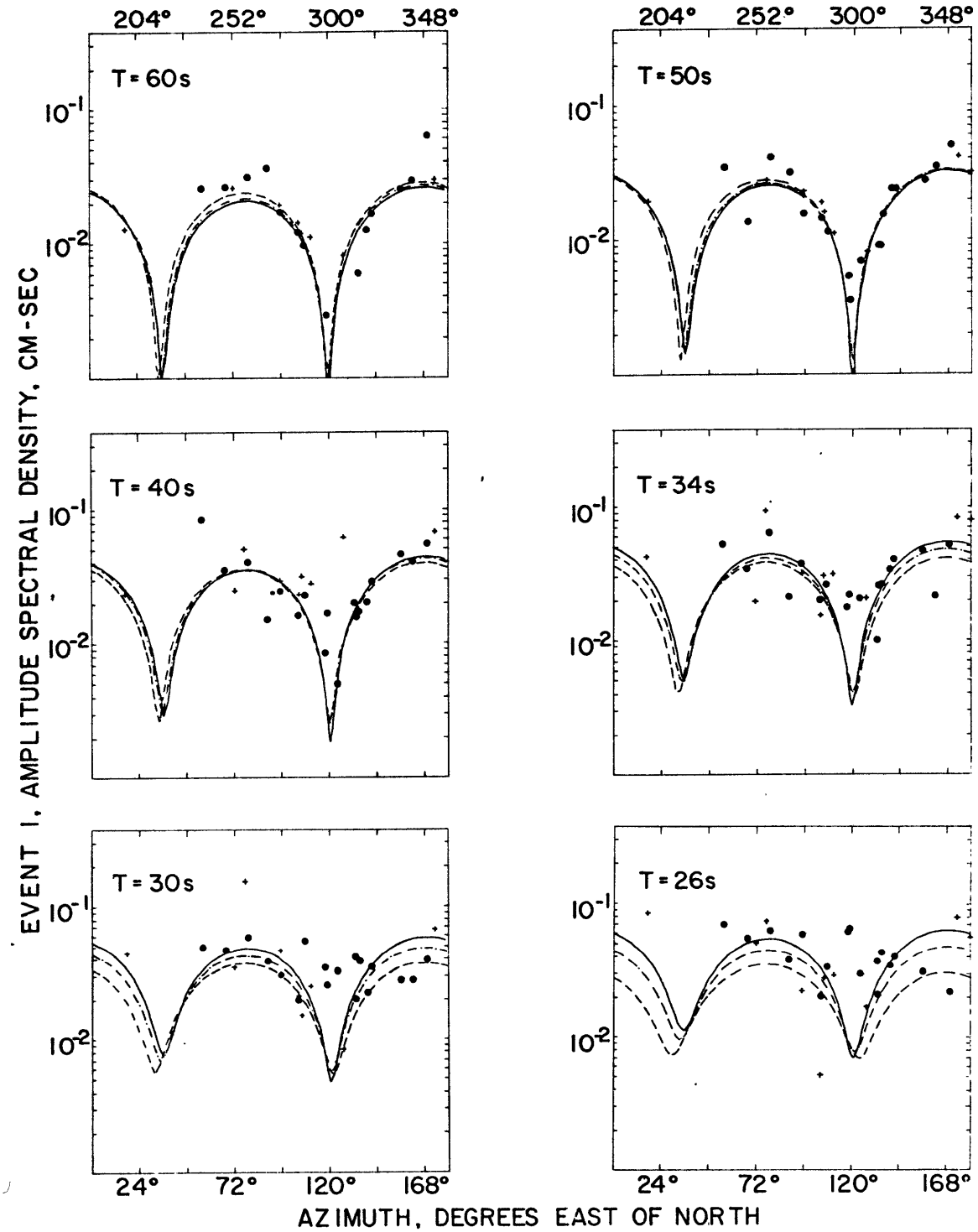

Fig. 4-2.16a: Results of the linear inversion at focal depths of 5km (———), 7.5km (—·—·) and 10km (— — —).

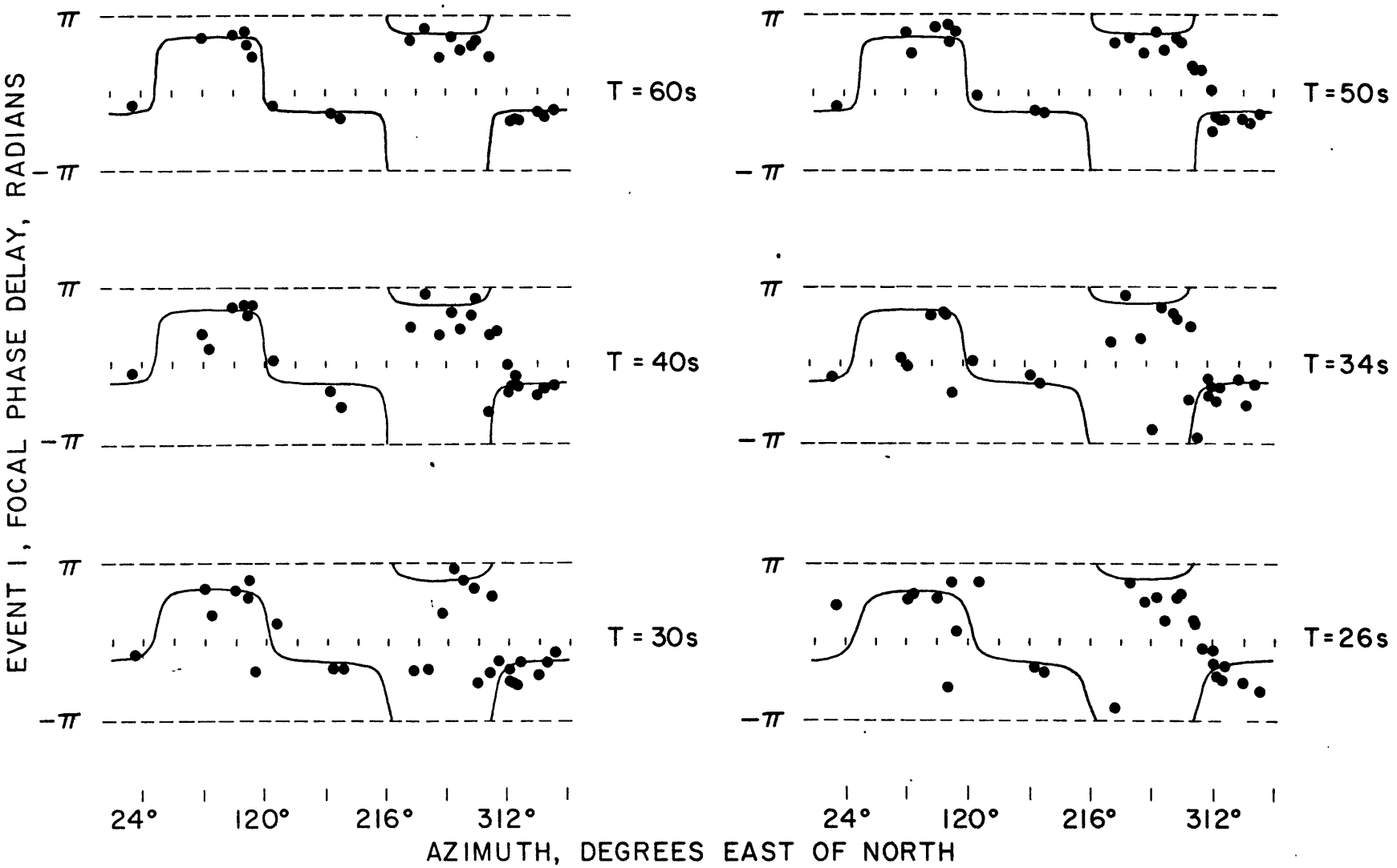

Fig. 4-2.16b: Results of the linear inversion at 5km (——) focal depth. Curves for 7.5km and 10km depths overlap drawn curve.

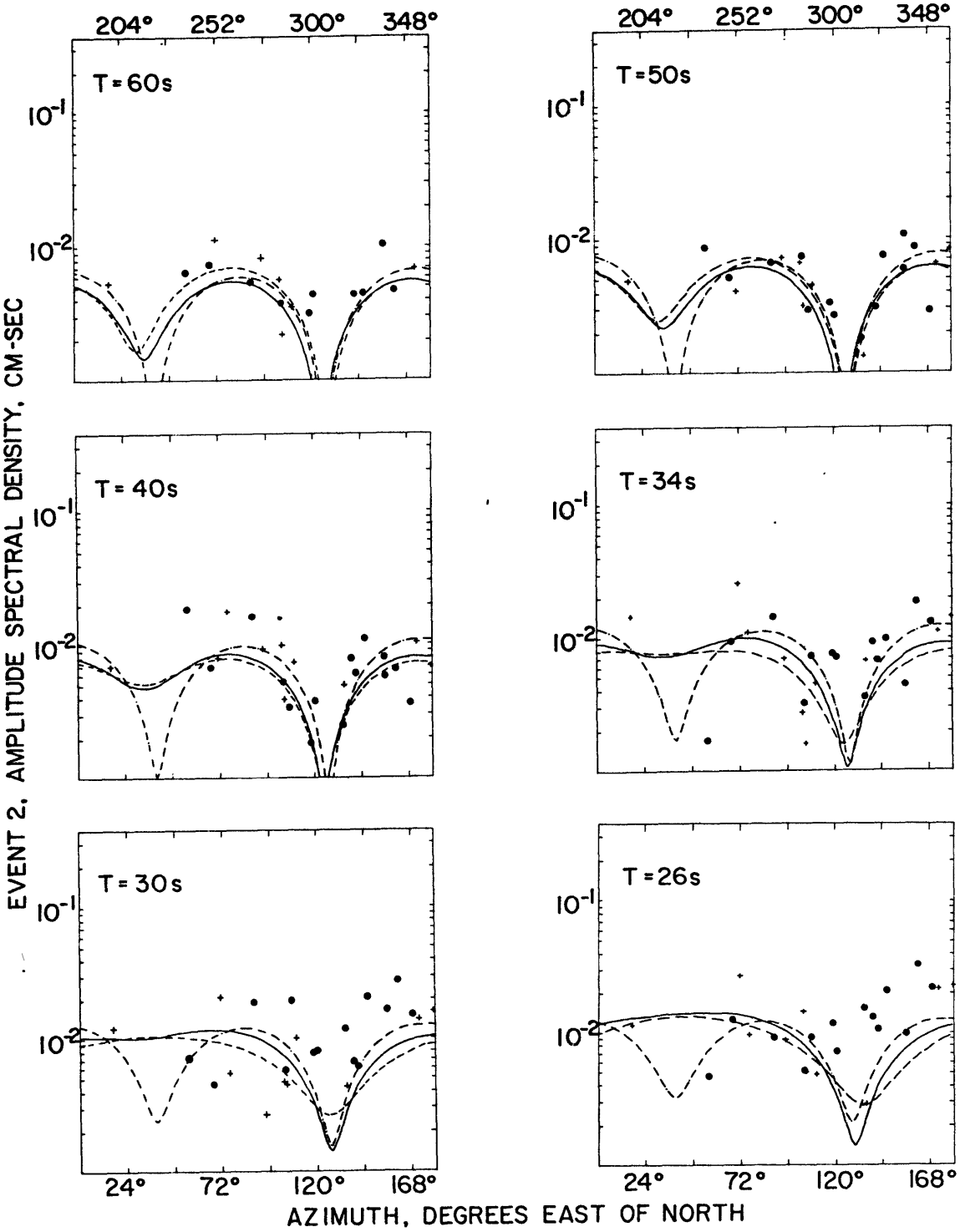

Fig. 4-2.17a: Results of the linear inversion at focal depths of 10km (———) and 15km (— — —); results of logarithmic fit (—·—·) at 7km focus.

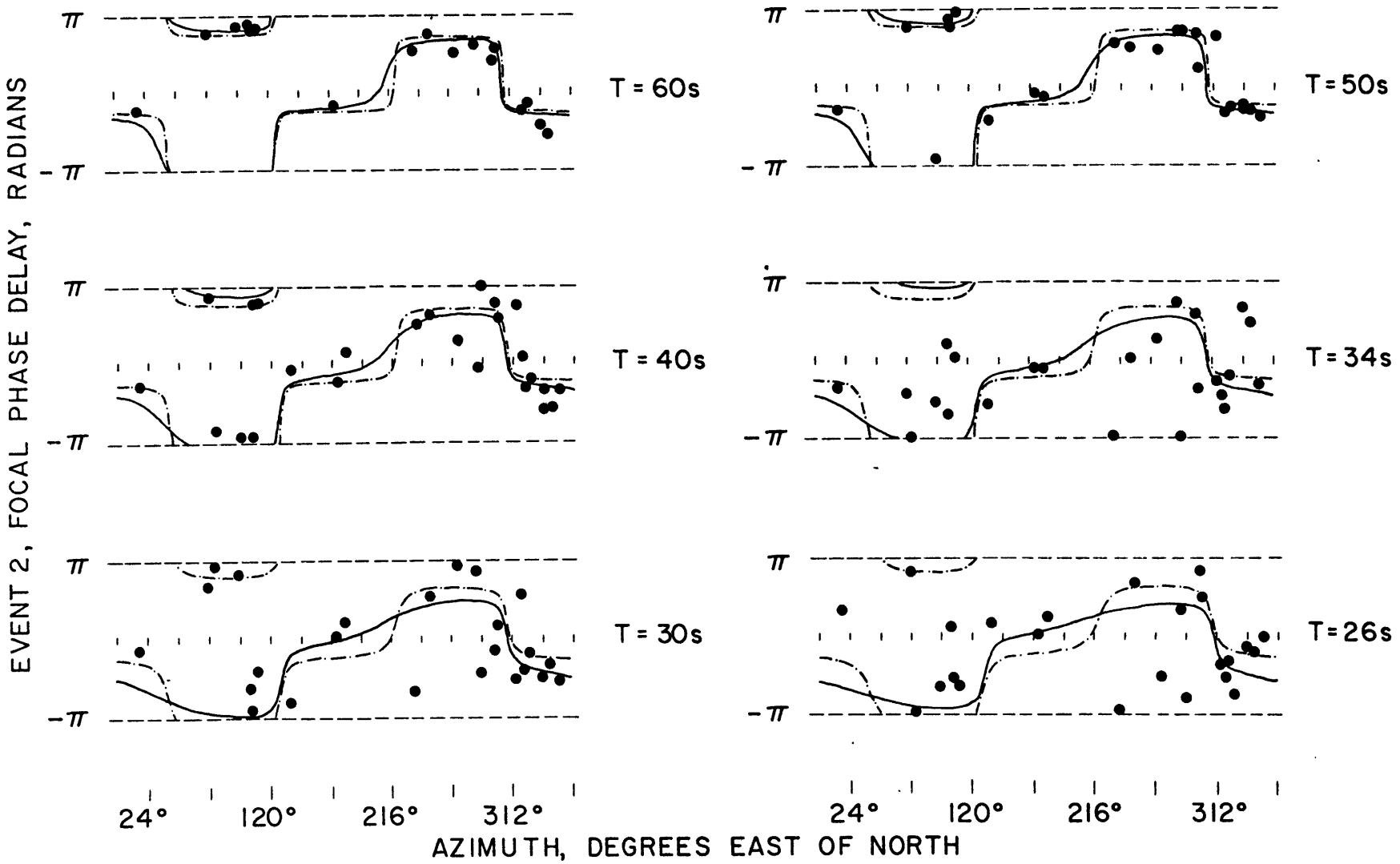

Fig. 4-2.17b: See caption of Figure 4-2.17a.

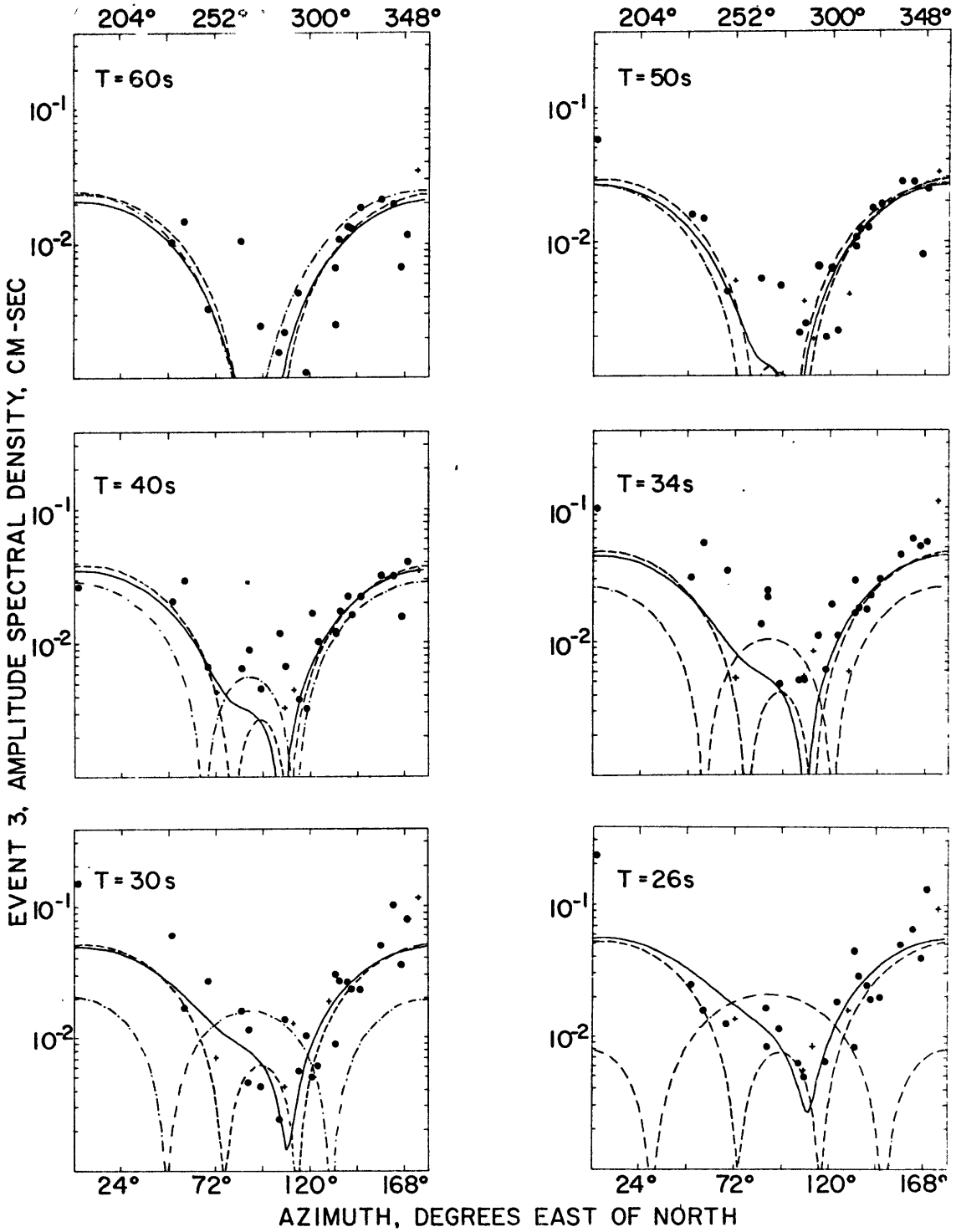

Fig. 4-2.18a: Results of the linear inversion at focal depths of 5km (———) and 10km (—·—·) with origin time revised by 4sec. Using only a 2sec correction, the result at 5km focal depth is shown by (— — —).

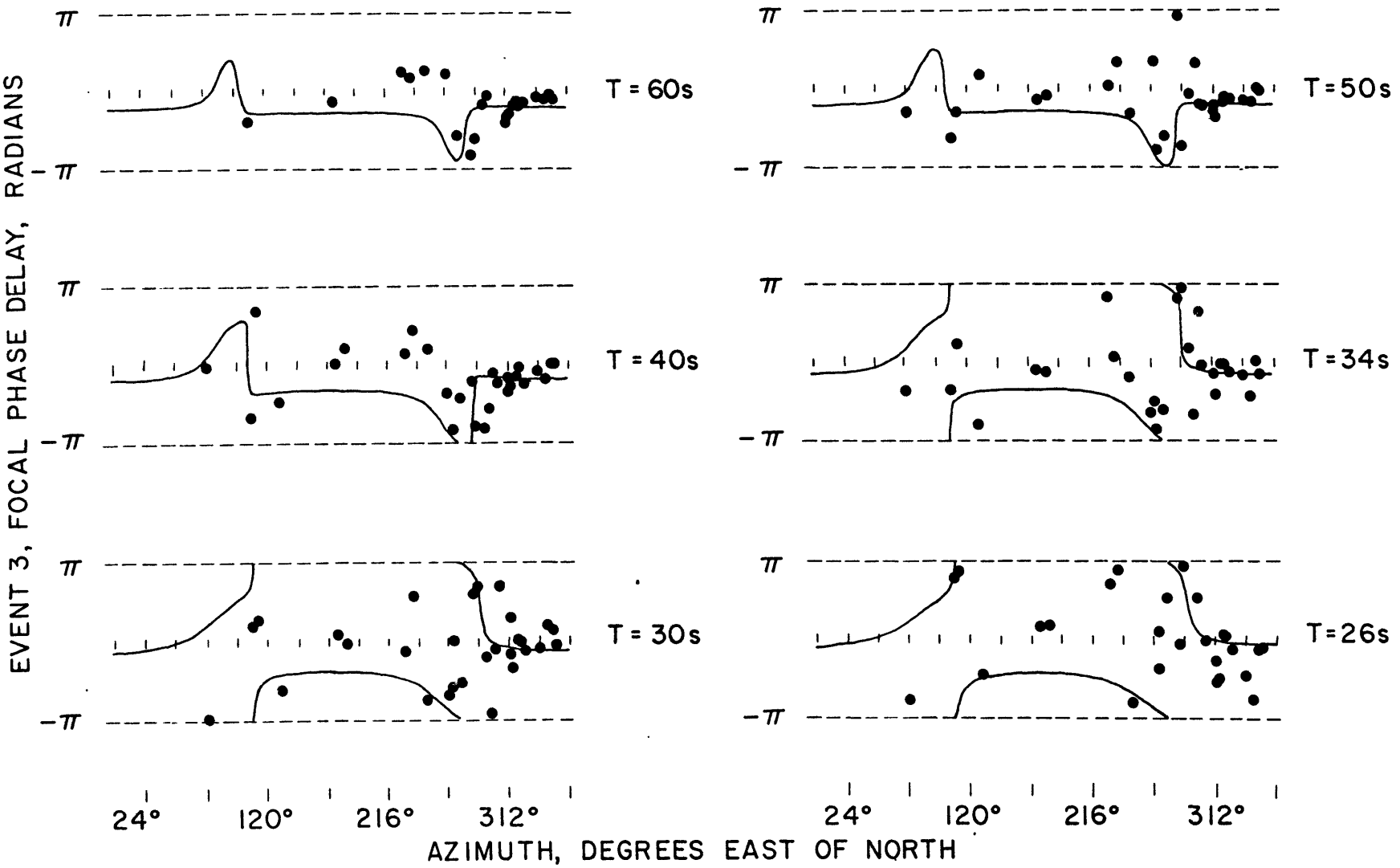

Fig. 4-2.18b: Result of the linear inversion at focal depth of 5km and a 4sec correction.

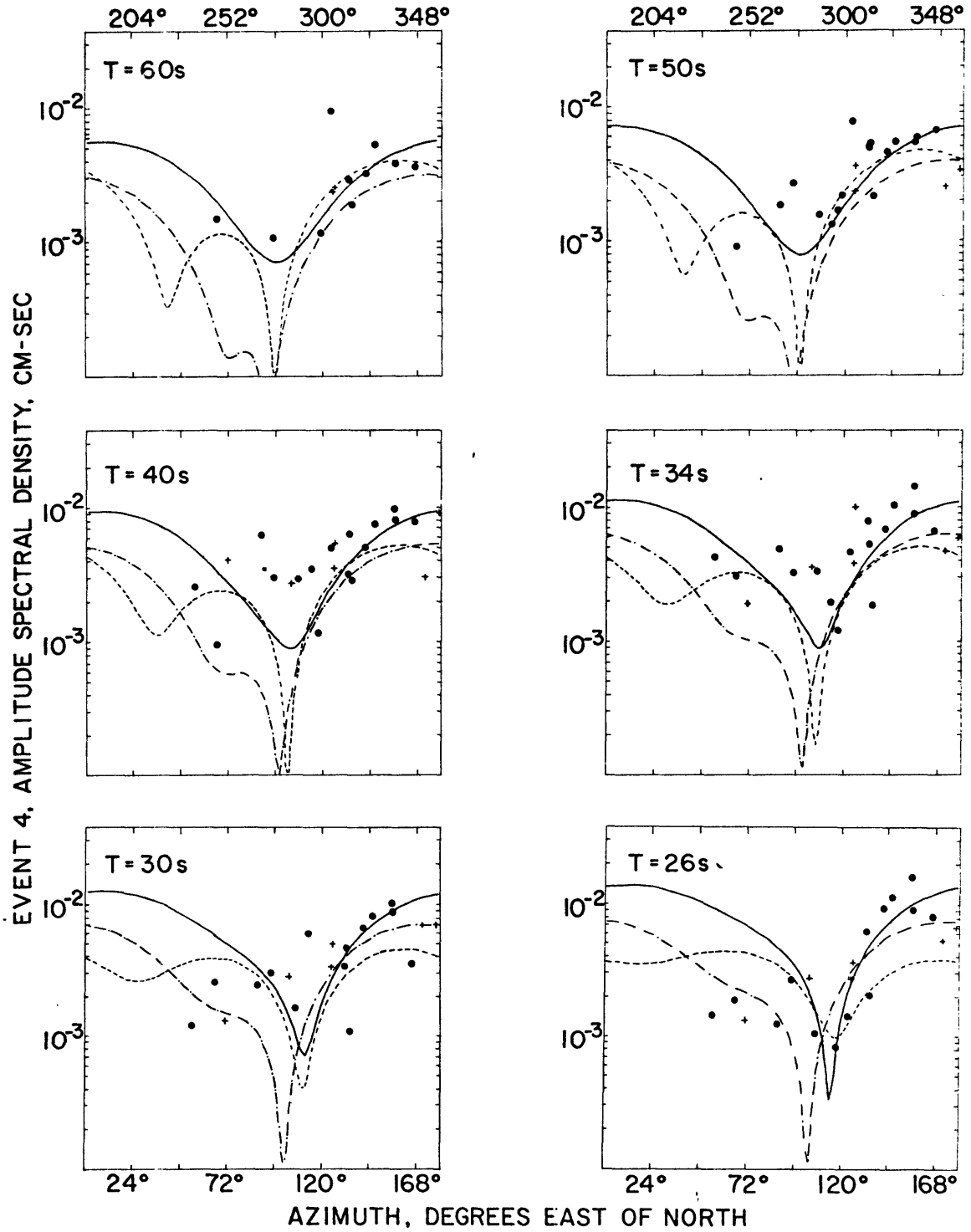

Fig. 4-2.19a: Results of the linear inversion at focal depths of 5km (—·—·) and 10km (— — —); results of logarithmic fit (———) at 6km focus.

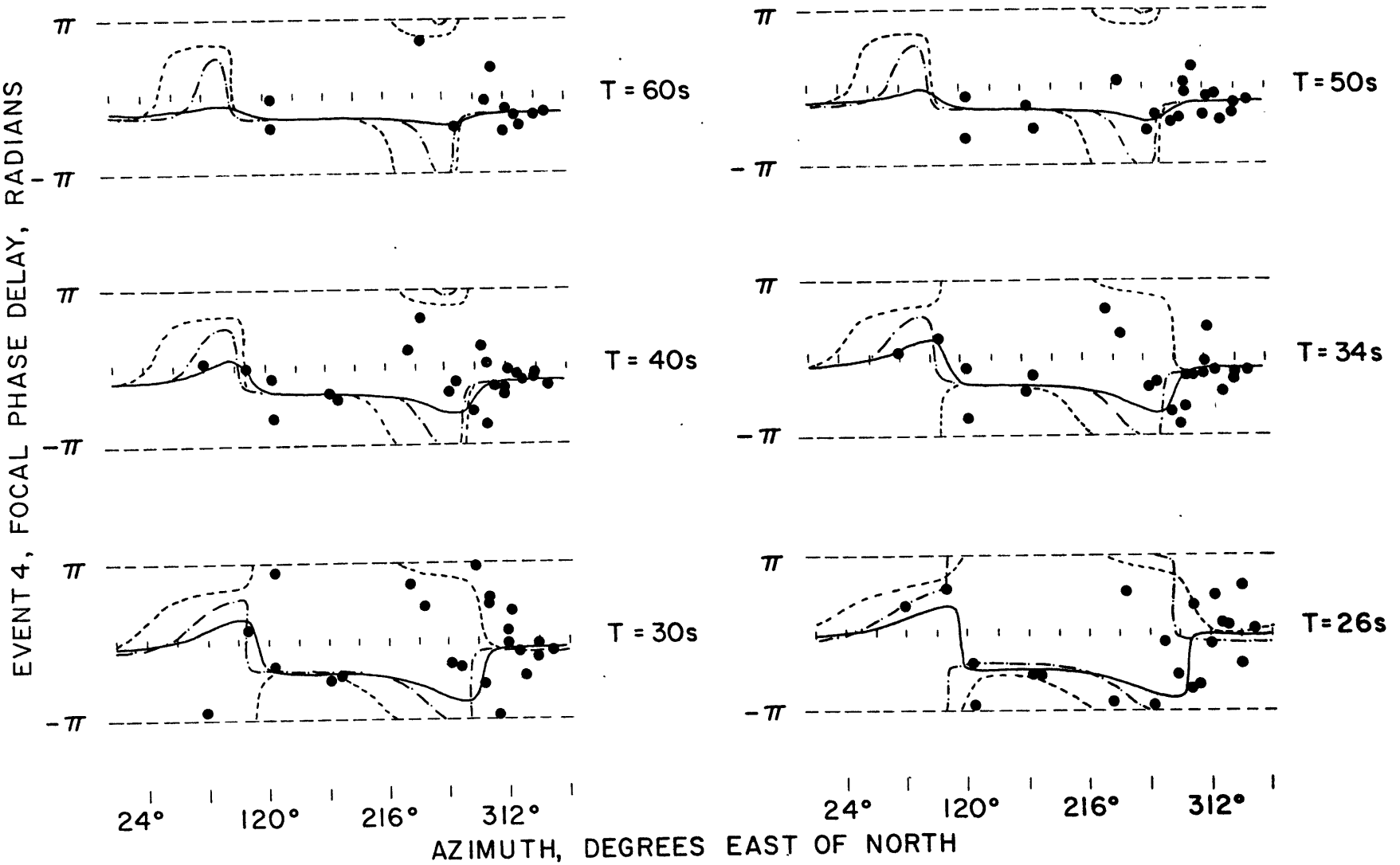

Fig. 4-2.19b: See caption of Figure 4-2.19a.

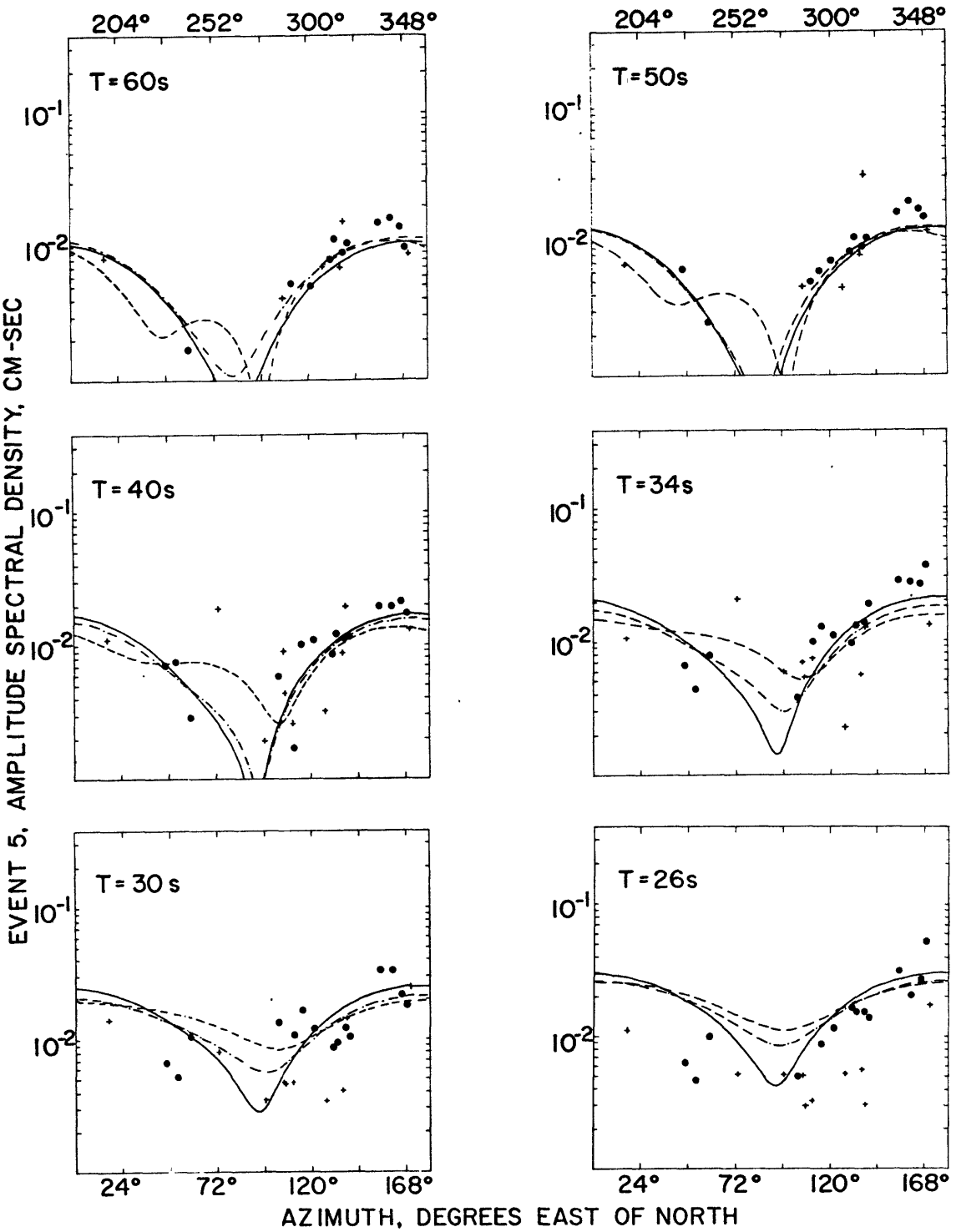

Fig. 4-2.20a: Results of the linear inversion at focal depths of 7.5km (———), 10km (—·—·) and 12.5km (— — —).

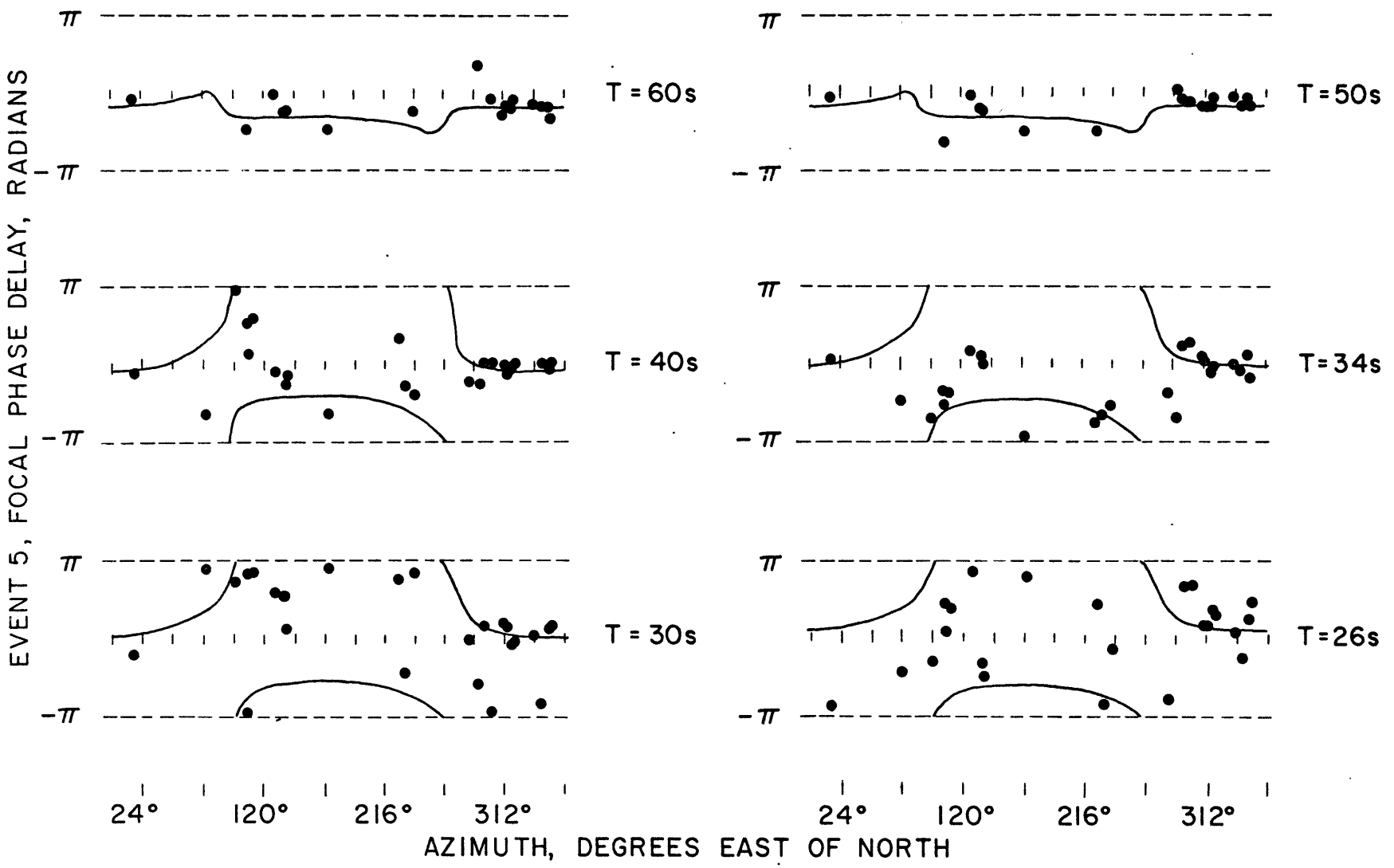

Fig. 4-2.20b: See caption of Figure 4-2.20a.

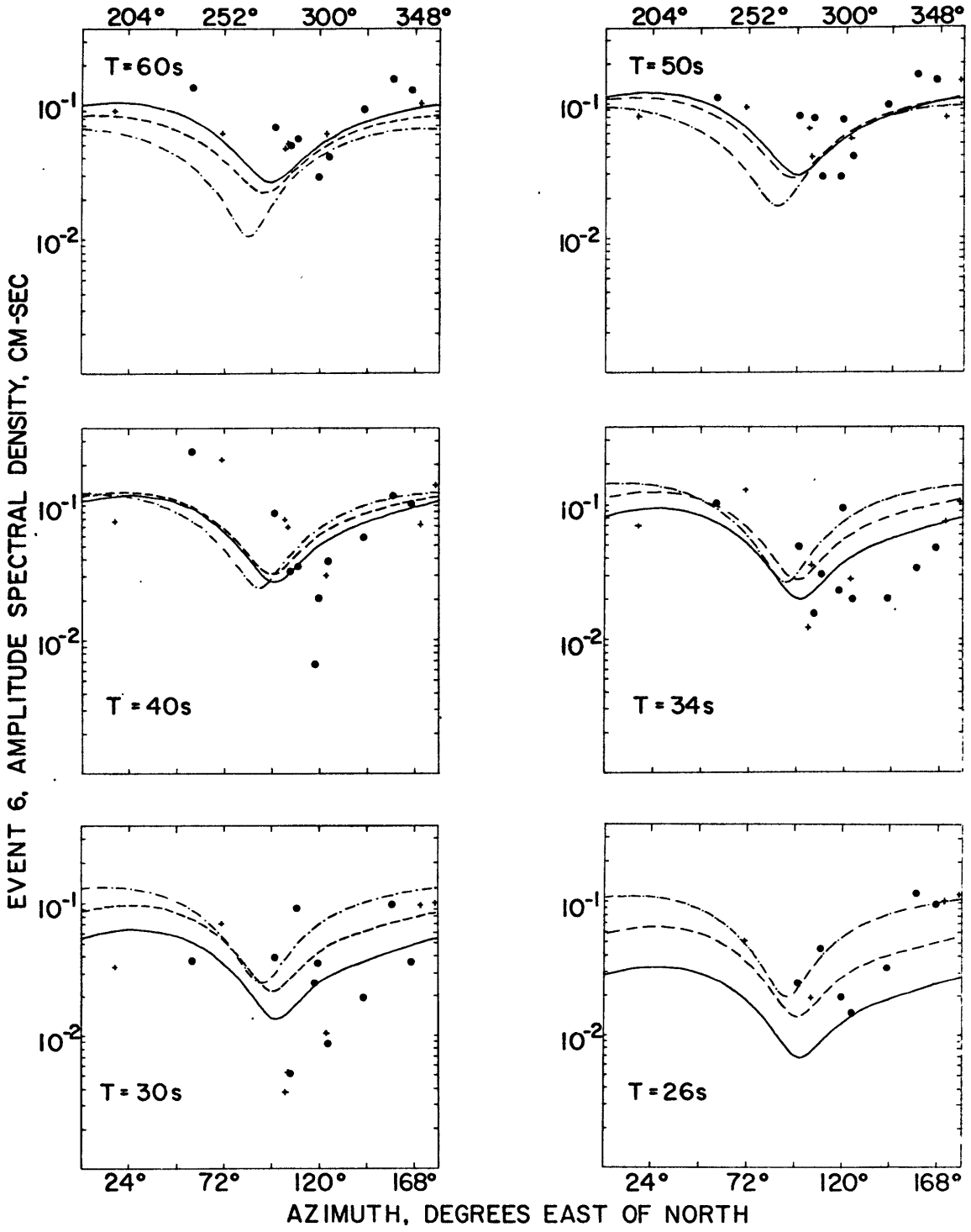

Fig. 4-2.21a: Results of the linear inversion at focal depths of 60km (—·—·), 80km (— — —) and 100km (———).

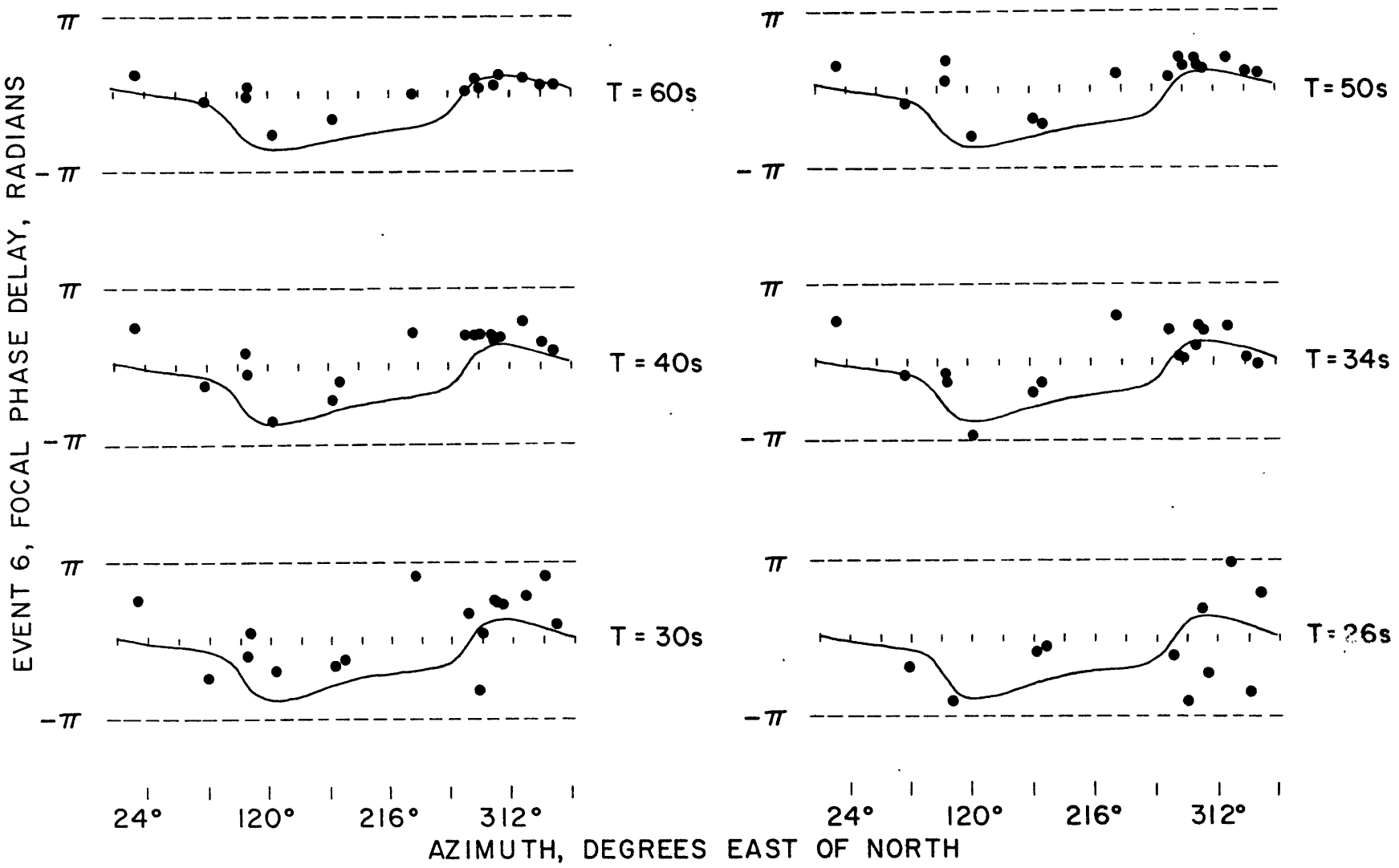

Fig. 4-2.21b: See caption of Figure 4-2.21a.

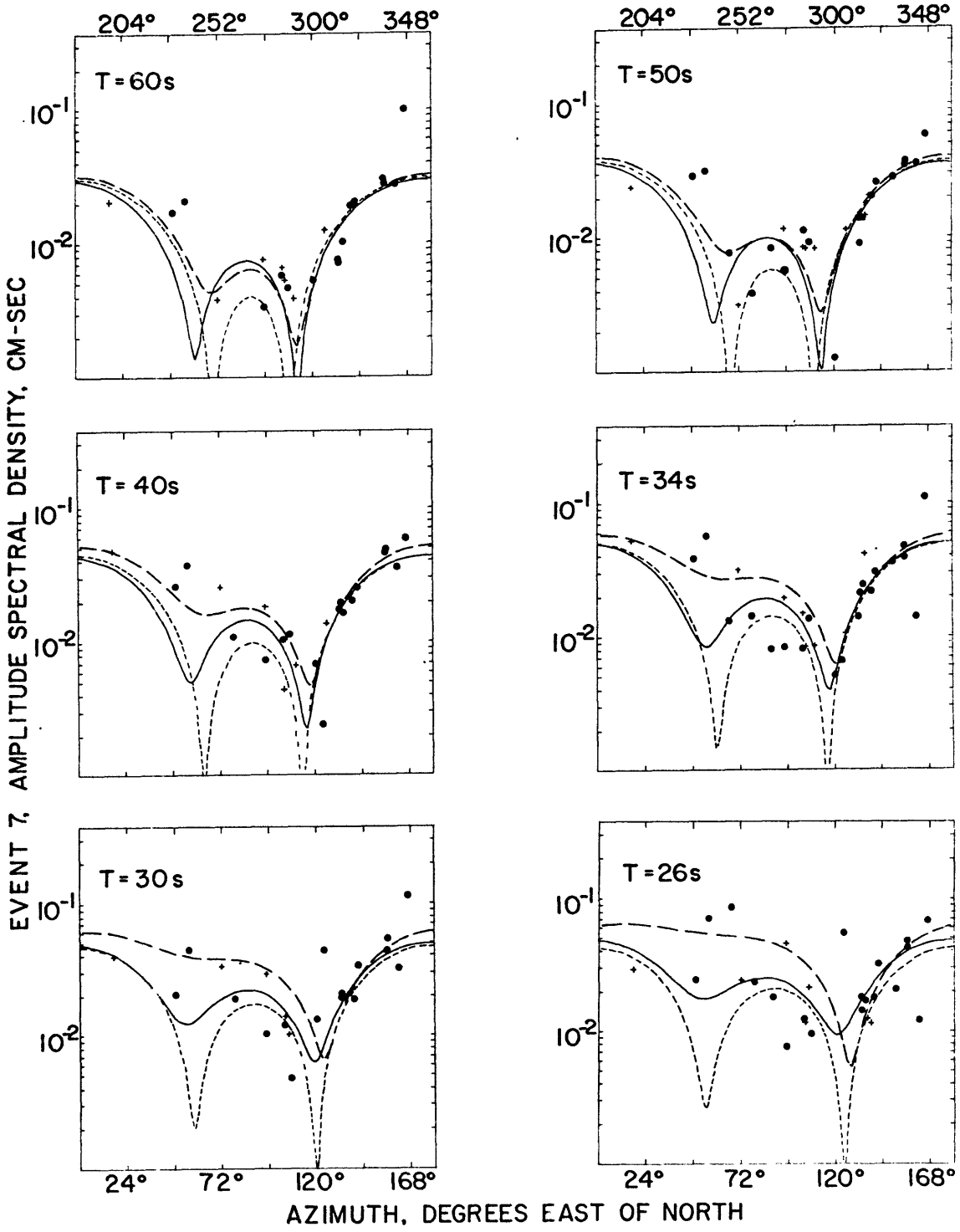

Fig. 4-2.22a: Results of the linear inversion at 7.5km focus with a 2sec origin time correction (———) and without (– – – –). Logarithmic fit (source parameters:h= 7.5km, s=-36°,d=34°, θ^F=240°, M_o=4.4x10^{24}) is shown by (— —).

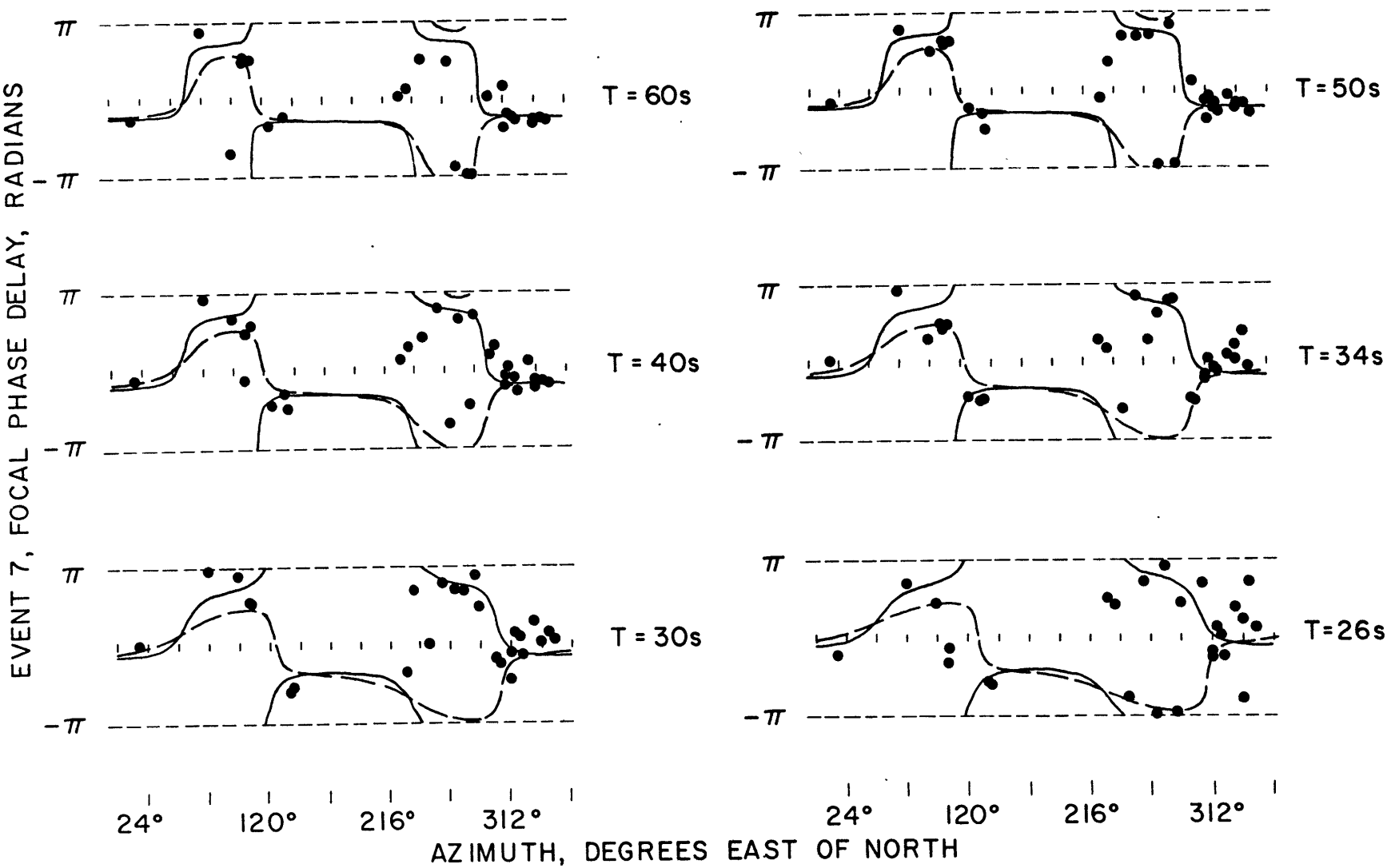

Fig. 4-2.22b: See caption of Figure 4-2.22a.

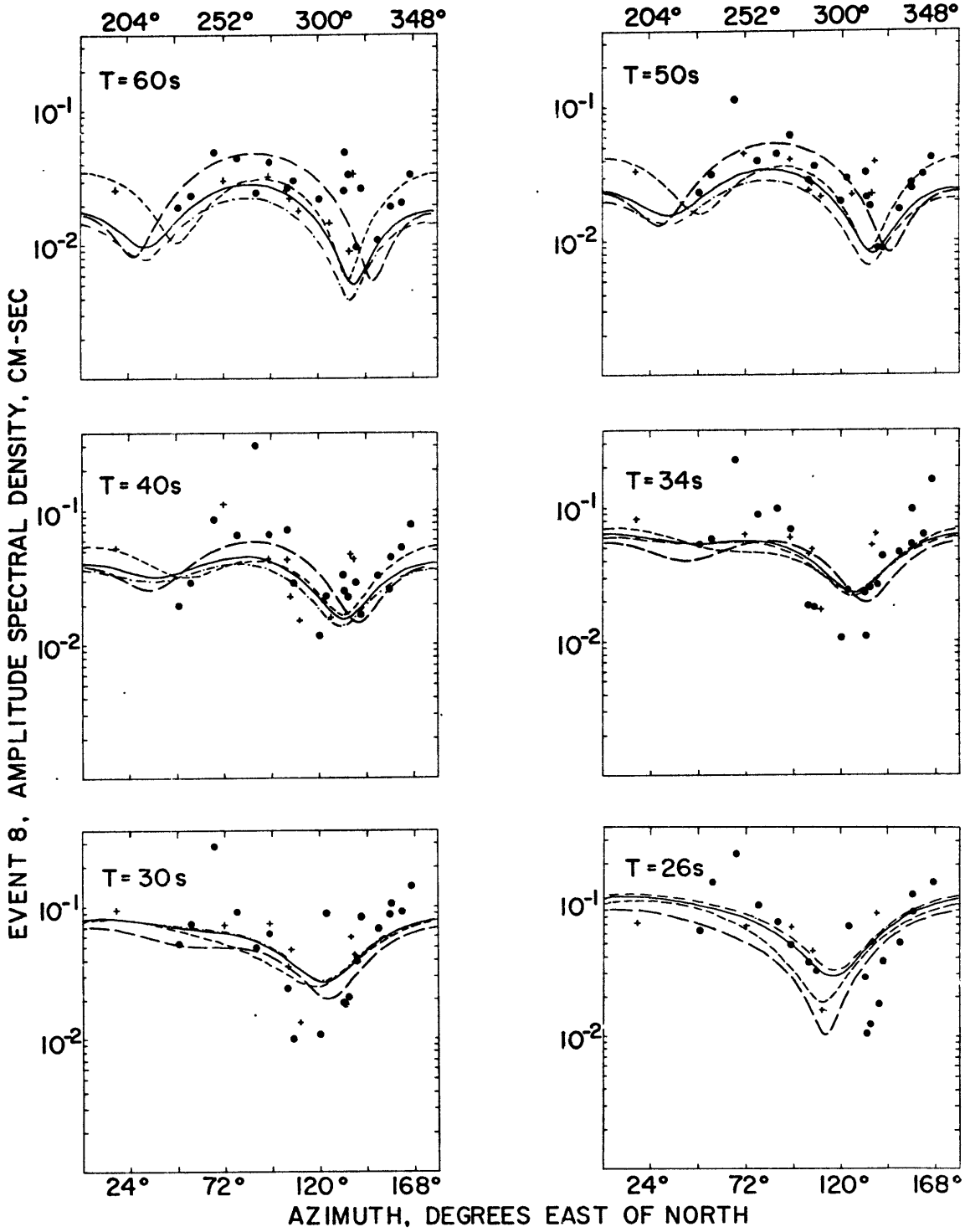

Fig. 4-2.23a: Results of the linear inversion at focal depths of 5km (—·—·), 7.5km (———), and 12.5km (– – – –). Logarithmic fit (source parameters: h=10.5km, s=36°, d=50°, θ_F=210°, M_o=6.1x10^{24}) is shown by (— —).

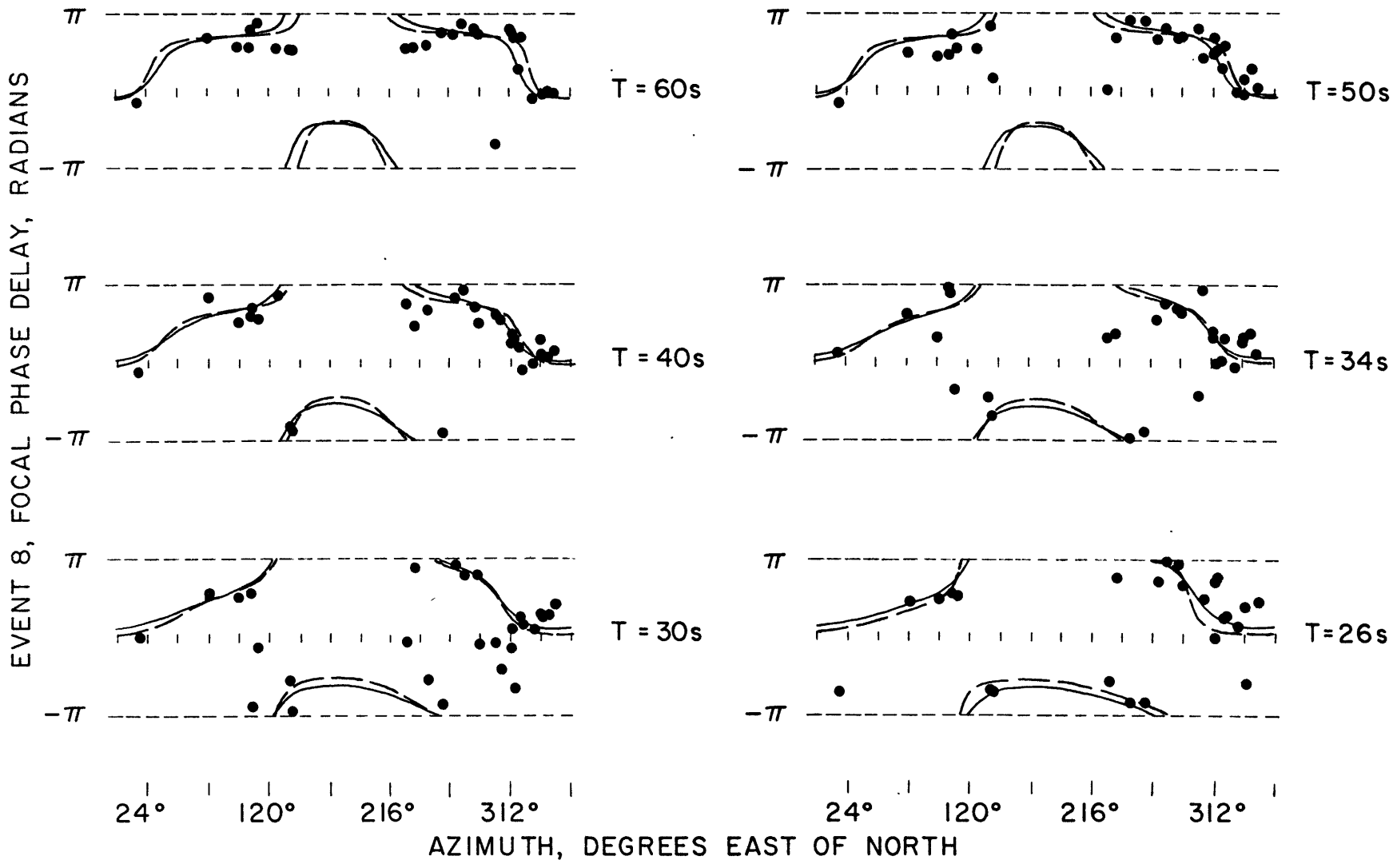

Fig. 4-2.23b: See caption of Figure 4-2.23a.

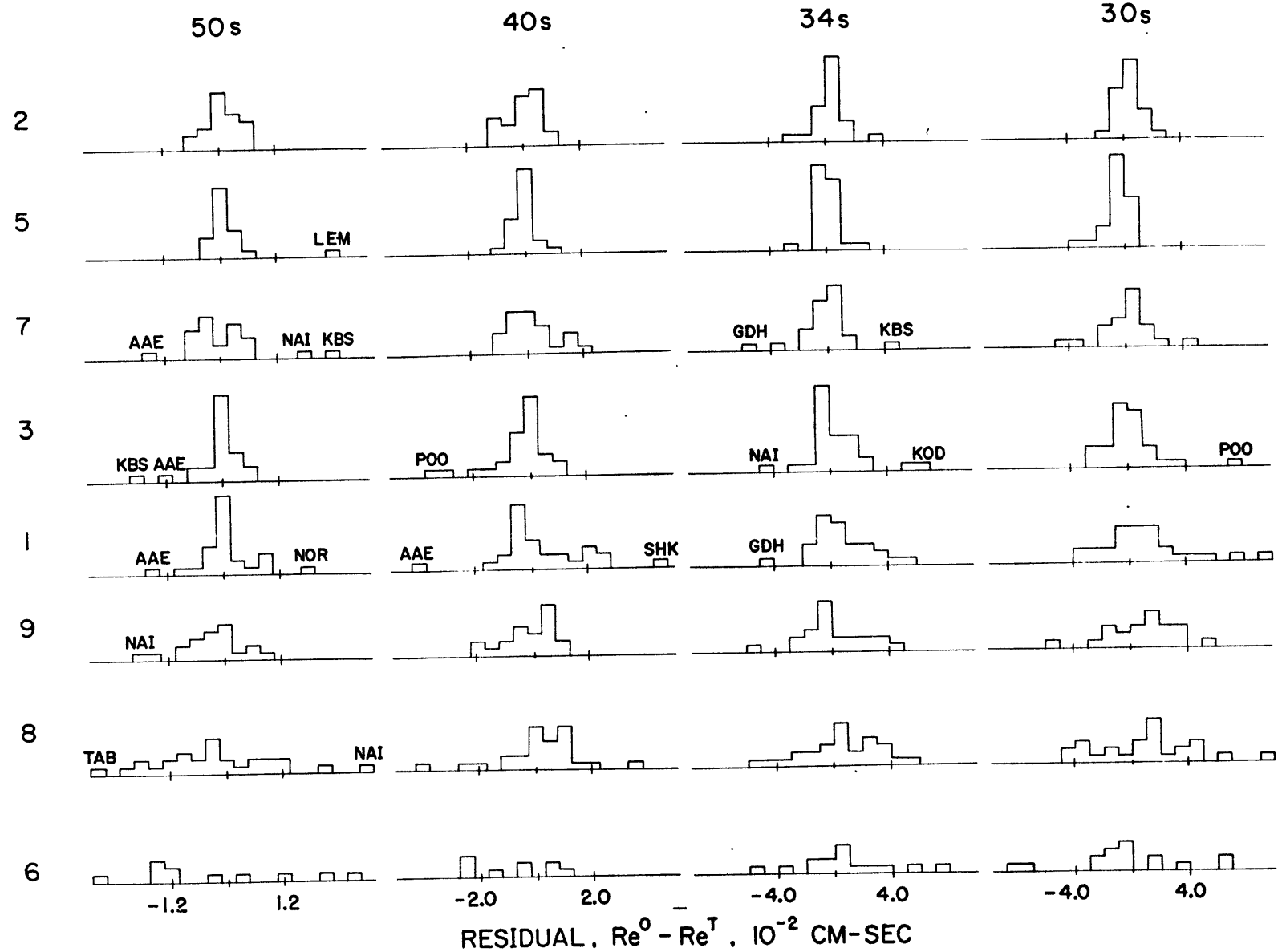

Fig. 4-2.24: Histograms of residuals on the real part of the complex source spectrum. Events are ordered in increasing seismic moment down the columns.

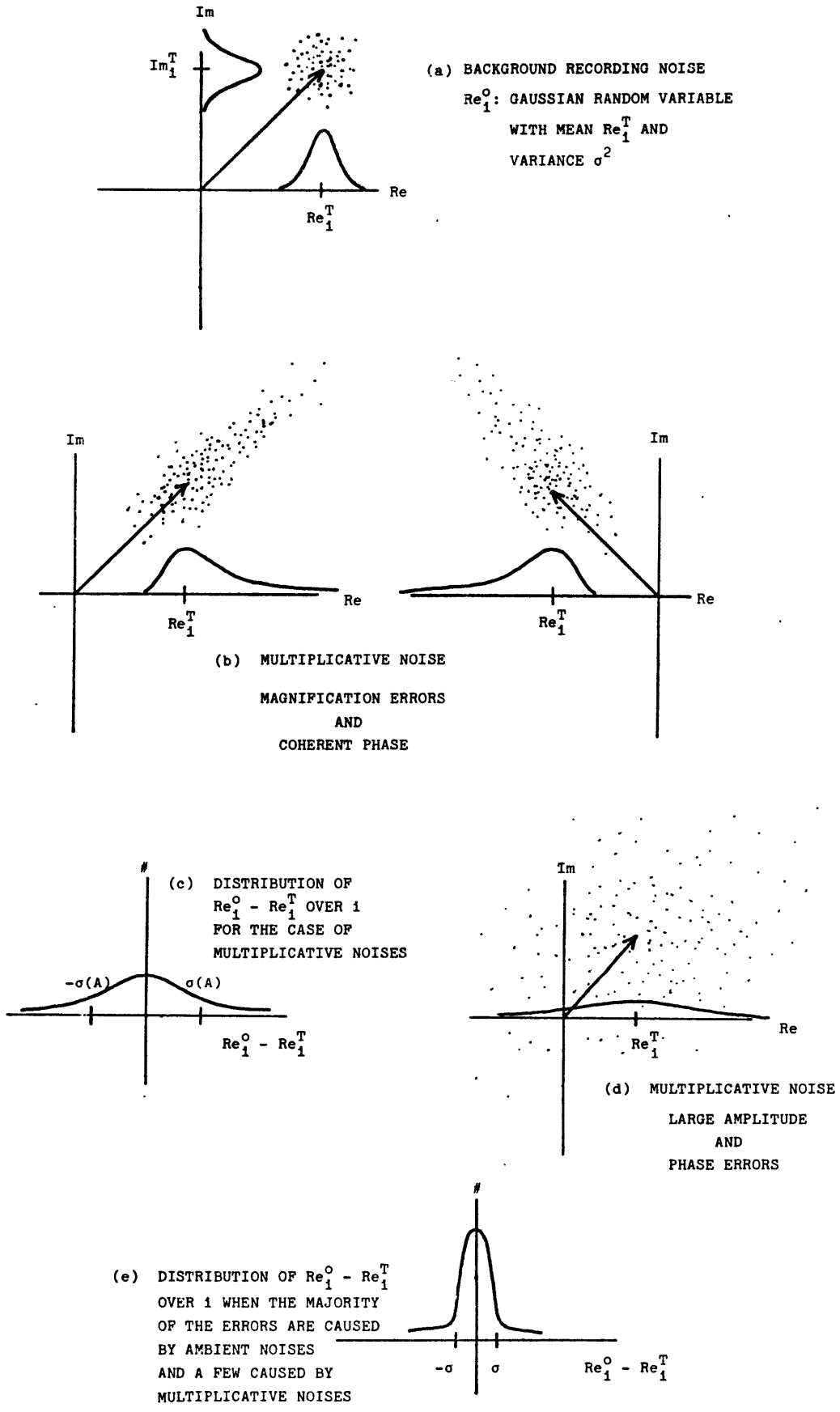

Fig. 4-2.25: Schematic distributions for the interpretation of the histograms in Figure 4-2.24.

estimates of moment is not a serious concern. This is consistent with our findings in the analysis of event 9. The RMS errors at short periods warn that estimation of the moment is more unreliable here. For shallow focus events, this will cause greatest difficulties in the estimation of moment elements on the imaginary part, as was seen in the analysis of event 9.

3. PROPAGATION PARAMETERS

The purpose of this section is to inspect final estimates of the propagation parameters, H_{ik} and ϕ_{ik}, and to ascertain possible random and systematic errors in these estimates. Quantitative analyses, such as regionalization of phase velocities and Q, is taken up in Chapter 5.

For purposes of displaying the path parameters, we converted the transfer functions into "apparent" phase velocities and attenuation coefficients. The word "apparent" is used in reference to the observations made over the total travel path from the reference point to the receiver. This distinguishes them from regional values, such as "pure path" phase velocities, which are the output of the regionalization and are useful for the interpretation of the medium properties. We calculate apparent phase velocities, $C_i(\omega_k)$, by the equation

$$C_i(\omega_k) = \frac{\omega_k}{K_k} = \frac{\omega_k \bar{X}_i}{\hat{\phi}_{ik}} \qquad (4\text{-}3.1)$$

where ω_k is frequency, K_{ik} is wave number, $\bar{X}_i$ is the distance from the reference point to the i^{th} receiver, and $\hat{\phi}_{ik}$ is an estimate of the propagation phase (total number of cycles including the order number). The apparent attenuation coefficient, $\eta_i(\omega_k)$, is computed as follows

$$\eta_i(\omega_k) = \frac{-\ln(\hat{H}_{ik})}{\bar{X}_i} \qquad (4\text{-}3.2)$$

where $\hat{H}_i(\omega_k)$ is an estimate of the amplitude transfer function defined in Equation 2-1.4. The apparent phase velocities and attenuation coefficients are shown in the figures given in Appendix C. On the plots of the attenuation coefficients, we show the results of two calculations, one obtained from an estimate of H_{ik} using Equation 2-5.7 (MLE) and the other using Equation 2-5.18 (LAV, i.e., log average). We discuss the results of these calculations below.

COMPARISON OF MLE AND LAV COMPUTATIONS OF H_{ik}. In the analysis of residuals from the linear inversions, multiplicative errors were detected at all frequencies. Unfortunately, the source of these errors was not identified in that analysis. For example, we anticipated multiplicative errors arising from the path

correction, because errors in $\hat{H}$ and $\hat{\phi}$ enter multiplicatively in the complex spectrum (Section 3-2). We also suspect that scattering of seismic waves due to lateral heterogenities may be important, perhaps for some paths more than others. We would like to be able to separate these sources of errors and study the more physically important of the two: seismic wave scattering. The importance of the calculations we are about to examine is that they are revealing about the nature of noises on the seismograms.

We must assume that the source parameters obtained from the linear inversions are correct in order to calculate the surface wave excitation, i.e. the input signals as we referred to them in Section 2-5. In light of the size of the computed amplitude and phase residuals from the inversions, this is a safe assumption. In making the MLE computation, the parameter, z, in Equation 2-5.7, defined in Section 2-5 as the ratio of the variance of the noise on the seismogram to the variance of noise in the input signal, was assumed to be 1.0 at all frequencies. This is an order of magnitude figure of a statistical parameter that, in our case, would be difficult to estimate precisely. However, it was found that a large change in z does not alter the MLE behavior on which we base our discussions below (see Figure 4-3.1).

Several plots of η versus frequency that are good examples of the results of calculating H_{ik} two ways are shown in Figure 4-3.1. We give error bars, representing one standard deviation in the calculation of LAV of H_{ik}, at three selected frequencies

(1/50, 1/34 and 1/26Hz). The estimates of n based on the MLE calculation are shown by open dots joined with straight lines in order to enhance the behavior of this estimate from one frequency to the next. For reasons given below, we believe that the behavior of the MLE, such as smoothness and variations from the LAV estimate, are indications about the statistical properties of noises on the seismogram.

We also use the standard error in the calculation of $\hat{\phi}_{ik}$, as computed in Equation 2-5.19, to assist us in this analysis. When interference occurs on the seismogram, phase errors are introduced into the signal spectrum. These errors can be very damaging in the MLE calculation. This is because large amplitude signals, which are weighted heavily in this calculation, suffer signal-generated noises more than small signals do on any common path. Large phase errors of course do not preclude the importance of ambient noise, especially in small signals. However, in that circumstance, the weighting in the MLE is appropriate to minimize the effects of these errors. When phase errors are small, there is still a possibility of a bias in the MLE due to large magnification errors. In this case, the MLE is expected to give a <u>low</u> estimate of the attenuation coefficient because the observed amplitude distribution is skewed to higher amplitude by the magnification errors.

Table 4-3.1 contains phase errors $\Delta\phi_{ik}$, propagation phase $\hat{\phi}_{ik}$, and fractional errors, $\Delta\phi_{ik}/\hat{\phi}_{ik}$, for many stations at three selected frequencies. We indicate dangerously large phase errors

($\Delta\phi \geq \pi/2$ radians) on the plots of attenuation coefficients in Appendix C and Figure 4-3.1 by connecting the MLE estimates with dashed lines.

In Figure 4-3.1 the MLE computed for GDH and UME are mildly variable at high frequencies. More eratic behavior is seen on plots of PTO, TRI, HKC and NAI. In general, suspicious behavior of the MLE often correlates well with the occurrence of large phase errors denoted on these plots. Our interpretation is that the noises over the frequency range where this occurs are predominantly signal generated in nature, such as multipathing interference. The station MSH shows a large spread of amplitudes, as the standard error on η indicates, and yet the phase error is small. Compared with the log average result, the MLE method underestimates η, as expected. Here, our interpretation is that magnification errors, perhaps due to focusing of seismic rays along azimuths to MSH, are causing the amplitude distribution to be skewed.

It is perhaps not as meaningful to try to interpret a multitude of details about the results of the two calculations as it is to look for trends among regional groups of stations. This can be done by examining the plots of η in Appendix C. The discussion below is a brief description of the trends that are most visible in eight regional station groups.

NORWEGIAN SEA GROUP (NOR, GDH, KTG, AKU): As mentioned above, the most distant station in this group, GDH, shows mild variabil-

ity in the MLE at frequencies >∿.03Hz. But half of the stations, KTG and AKU show no significant effects at all, and NOR is affected only at the highest frequencies, >.04Hz. Considering the long travel distances (see Table 4-3.1 for number of cycles in the propagation), this group of stations is remarkably free of any strong indications of interference. The same may be said for the station COL, which does not lie within any station grouping, but shares a similar type of path on the continent (stable and relatively homogeneous) as the Norwegian Sea Group.

SCANDINAVIAN GROUP (KBS, KEV, UME, NUR, KON, COP): The MLE of stations KEV and UME share suspicious behavior above .03Hz which may have more significance because of the stations' proximity. In general though, this group of stations appears to be free of interference up to frequencies as high as .0375Hz.

EUROPEAN GROUP (ESK, VAL, STU, PTO, TOL): The agreement between MLE and LAV gradually declines from northern to southern stations in Europe culminating in very eratic MLE estimates on PTO and TRI (see next group) at frequencies ∿.03Hz. Our interpretation is that scattering has intensified, presumably due to complexities of the travel paths through the Alpine foldbelts of southern and eastern Europe.

MEDITERRANEAN GROUP (TRI, AQU, IST, ATU): The trend of the European Group prevails for these stations surrounding the Mediterranean Sea. There is some indication of complexities even at

longer periods as we move further south (compare TRI and ATU for example).

MIDDLE EAST, IRAQ, AND IRANIAN GROUP (TAB, JER, MSH, SHI): These stations have short travel paths (<3500km). The error bars on η are very large, an indication of amplitude fluctuations both at high and low frequencies. The stations farther away from the source, JER and SHI, show phase errors too. If MSH ($\Delta \sim 1300$km) is a point where focusing occurs, as the analysis above suggests, interference phenomena can be expected at points greater distances away, as these two stations confirm. African stations, AAE and NAI, lying close to the same azimuth as SHI ($\Delta \sim 2200$km) but another 2000-3000km away, experience complexities which may be due in part to near-source (<2200km) effects in their propagation paths.

AFRICAN AND INDIAN GROUP (AAE, NAI, POO, KOD): AAE and NAI show large phase errors at frequencies as low as .02Hz. We might add that these stations were consistently anomalous on the plots of imaginary part because of phase errors. Indian stations have excellent agreement between MLE and LAV. Large magnification errors at high frequencies are apparent at POO.

BURMA AND INDONESIAN GROUP (SHL, CHG, SNG, LEM): Large magnification errors are clearly present at SHL, however, the MLE are not seriously biased. Larger phase errors at SHL than at MSH or TAB (see Table 4-3.1, 34s) can explain for less serious bias be-

cause phase errors offset magnification errors, as was seen in Section 3-2.

CHINA AND FAR EASTERN GROUP (BAG, HKC, ANP, SHK, MAT): HKC and ANP are an interesting contrast for two very close stations. The former has erratic MLE over much of the frequency range; the latter could pass for a Norwegian Sea or Scandinavian station. In general, it is difficult to characterize this group. Japanese stations, SHK and MAT, are interesting in that, despite phase errors, high frequency MLE and LAV show better agreement than at low frequency. At SHK, the discrepancy at low frequency is due to poor signal to noise ratio (recording noise) affecting the LAV estimate. Low signal strength for a few events (2, 4 and 5) is apparently the cause of large phase errors at high frequencies at station MAT.

In summary, it appears that erratic behavior of the MLE are often correlated with the occurrence of fluctuations in the phase spectra. We have interpreted this in light of the statistical properties of seismogram noises as evidence for scattering of seismic waves. Together with the LAV, a reasonable and consistent picture of propagation and recording noises is revealed by looking at trends within station groups. Overall the trends support our assumption at the start of the analysis that the principal noise source at frequencies lower than .025Hz is background recording noise. There are notable exceptions to this generalization in certain regional groups such as the Mediterranean, Mid-

dle Eastern, and African groups. Apparently due to its proximity to the source and the complexities of the travel paths, the Middle Eastern group shows the strongest evidences for focusing effects on seismic waves. The other two groups show signs of interference at long periods. This may be due to complexities in the propagation path west of the source region, perhaps in the first 1000-2000 kilometers as the observations at closer stations in the Middle Eastern Group support.

Estimates of the error in our phase velocity measurements may be obtained from the results in Table 4-3.1. The percentage error in the phase velocity equals 100 times the computed fractional error, $\Delta\phi_{ik}/\hat{\phi}_{ik}$, given in this table. For the station network, the average percentage errors in our measurements of phase velocity were 0.5%, 0.6% and 0.8% at 50, 34 and 26sec, respectively.

AZIMUTHAL VARIATIONS IN C_{ik} AND η_{ik}. Some indication of the regional variations of propagation characteristics in Eurasia may be obtained from the azimuthal variation of the apparent phase velocities and attenuation coefficients shown in Appendix C. The paths connecting the reference point to the surrounding station network cross many outstanding geologic land forms on the continent. In this section, we attempt to find some correlations between the measurements of propagation parameters on these paths and the various geologic and geographic provinces in Eurasia.

The subject of our discussions are three sets of plots in

Figure 4-3.2. Each plot shows our measurements of attenuation coefficients and phase velocities as a function of azimuth for periods 50, 34 and 26sec. Error bars on the attenuation coefficients are those computed in Appendix C from the LAV method. A scale showing 1% variation is given for reference on the plot of phase velocities. On the plot of attenuation coefficients, the horizontal line corresponds to the value of η obtained in Section 4-1 from the slope of the line that fits the decay of the log amplitudes plotted against epicentral distance. The values represent an average for the continent and are summarized in Figure 4-1.4. The horizontal line on the plot of the phase velocities corresponds to the value of phase velocity in the Gutenberg continental earth model given in Table 2-4.1.

Perhaps the most obvious result from Figure 4-3.2 is that the azimuthal variations of apparent attenuation and phase velocity increase with frequency. For example, the total percentage variation of phase velocity is 9%, 13% and 15% at 50, 34 and 26sec periods respectively. Paths with consistently the highest velocities in Eurasia are those crossing the Russian Platform and Norwegian Sea. The lowest velocities are measured on paths crossing the Tibetan Plateau and the Hindu Kush. The highest attenuation in Eurasia occurs at short periods on paths through the Middle East, Iraq and Iran. Stations in India showed high attenuation at short and long periods. The lowest apparent attenuation may be seen at short periods for paths through the Alpine forelands and foldbelt systems extending from Central Europe

through the Adriatic and including the Alpide foldbelts, the Crimea and the Caucasus. Anomalously low apparent attenuation is measured at long periods for paths crossing the Tibetan Plateau, Indonesia and southern China.

Azimuthally, from left to right across the plot, the phase velocities at long period drop steadily from the paths on the Russian Platform, the Alpine forelands and Central European paths, and the southern European paths through Alpine-Alpide foldbelt systems. This trend appears to "bottom out" on paths crossing the Middle East, Iraq and Iran. Indian Shield paths have the highest velocities in southern Asia. For paths east of the reference point, the variation of velocities at long period as well as at short period is controlled by the percentage of the path in the Tibetan Plateau. Paths across northern China show the highest velocities of all eastern paths.

At short period, all but two paths show apparent velocities below the average continental velocities represented by the Gutenberg earth model. The velocities over paths interior to the continent on the Russian Platform around 60° of azimuth show little variation. This includes many southern paths through the tectonic Alpine-Alpide foldbelts. A rapid transition is apparent at 285° azimuth near the stations IST and ATU. To the right of this transition, paths through the Middle East, Iraq and Iran show little variation in velocity again.

Apparent attenuation at long period shows little variation about the mean value, especially for western paths. Eastern

paths show variation in inverse relationship to the phase velocities: for Tibetan paths we see low velocities and high Q and for northern China we see high velocities and low Q. South of the reference point, Indian stations also show high phase velocities and low Q. At long period only three western paths deviate significantly from the mean attenuation. One path crosses the Norwegian Sea to station KTG. The other two paths cross the Russian Platform to adjacent stations in Scandinavia, NUR and KON.

For periods 34 and 26sec, we have connected the attenuation coefficients for paths that cross the Norwegian Sea separately from the other measurements. Except for high apparent attenuation at two stations in Scnadinavia, KEV and UME, all paths interior to the continent crossing the Russian Platform, Alpine forelands and foldbelt systems show lower attenuation than the Norwegian Sea paths. Nevertheless, attenuation on the continental paths south of the reference point is even higher than that observed at stations across the Norwegian Sea. Most southern paths regardless of the type of landform shows much higher attenuation than the mean value at high frequencies. There are evidences of extremely rapid variations of apparent attenuation on paths to stations in Burma and Indonesia. The measurements of attenuation coefficients on three paths through northern China are remarkably constant over the frequency range.

TABLE 4-3.1: RMS ERROR, $\Delta\phi$, AND FRACTIONAL ERROR OF THE PROPAGATION PHASE, ϕ (CYCLES)

	50s			34s			26s		
	$\Delta\phi$	ϕ	$\Delta\phi/\phi$	$\Delta\phi$	ϕ	$\Delta\phi/\phi$	$\Delta\phi$	ϕ	$\Delta\phi/\phi$
NOR	.05	28.1	.002	.05	43.0	.001	.48	58.7	.008
KBS	.05	25.5	.002	.06	38.9	.002	.17	53.6	.003
GDH	.07	35.7	.002	.24	54.4	.004	1.20	74.5	.016
KEV	.04	21.4	.002	.04	32.9	.001	.30	45.2	.007
KTG	.05	30.4	.002	.21	46.0	.005	.78	62.6	.012
AKU	.05	30.6	.002	.08	46.5	.002	.09	63.3	.001
UME	.10	21.3	.005	.15	32.8	.005	.25	44.9	.006
NUR	.08	20.1	.004	.09	30.9	.003	.14	42.6	.003
KON	.03	24.0	.001	.07	36.9	.002	.07	50.7	.001
ESK	.21	28.3	.007	.13	43.3	.003	.46	59.4	.008
COD	.07	23.5	.003	.05	36.0	.001	.15	49.5	.003
VAL	.03	31.3	.001	.05	47.9	.001	.43	65.4	.007
STU	.38	25.4	.015	.28	38.8	.007	.46	53.2	.009
PTO	.12	33.8	.004	.28	51.3	.005	.72	70.5	.010
TRI	.16	24.2	.007	.19	37.0	.005	.50	50.7	.010
TOL	.16	32.4	.005	.33	49.3	.007	.45	66.9	.007
AQU	.04	24.8	.002	.27	37.6	.007	.57	51.5	.011
IST	.14	19.2	.007	.29	29.1	.010	.56	40.5	.014
ATU	.23	22.4	.010	.49	34.6	.014	.48	47.6	.010
TAB	.09	12.2	.007	.13	18.8	.007	.20	26.2	.008
JER	.06	18.4	.003	.16	28.3	.006	.70	39.2	.018
MSH	.08	6.6	.012	.15	10.4	.014	.16	14.4	.011
SHI	.06	11.6	.005	.18	18.1	.010	.16	24.9	.006
AAE	.25	25.2	.010	.29	38.4	.008	.45	52.8	.009
NAI	.26	30.3	.009	.71	46.2	.015	.67	62.8	.011
POO	.03	11.6	.003	.06	17.8	.003	.13	24.4	.005
KOD	.07	16.4	.004	.12	25.2	.005	.19	34.4	.006
LEM	.24	32.4	.007	.12	49.6	.002	.04	67.5	.001
SNG	.09	23.5	.004	.17	36.1	.005	.36	49.1	.007
SHL	.09	12.6	.007	.20	20.3	.010	.14	27.8	.005
CHG	.09	17.8	.005	.16	28.3	.006	.42	39.2	.011
BAG	.22	27.2	.008	.27	42.9	.006	.28	58.7	.005
HKC	.13	22.6	.006	.33	35.9	.009	.66	49.3	.013
ANP	.07	24.5	.003	.14	37.9	.004	.15	52.1	.003
SHK	.04	26.4	.002	.28	40.6	.007	.41	55.6	.007
MAT	.06	28.6	.002	.33	43.7	.008	.57	59.6	.010
COL	.07	39.7	.002	.11	60.4	.002	.26	82.1	.003

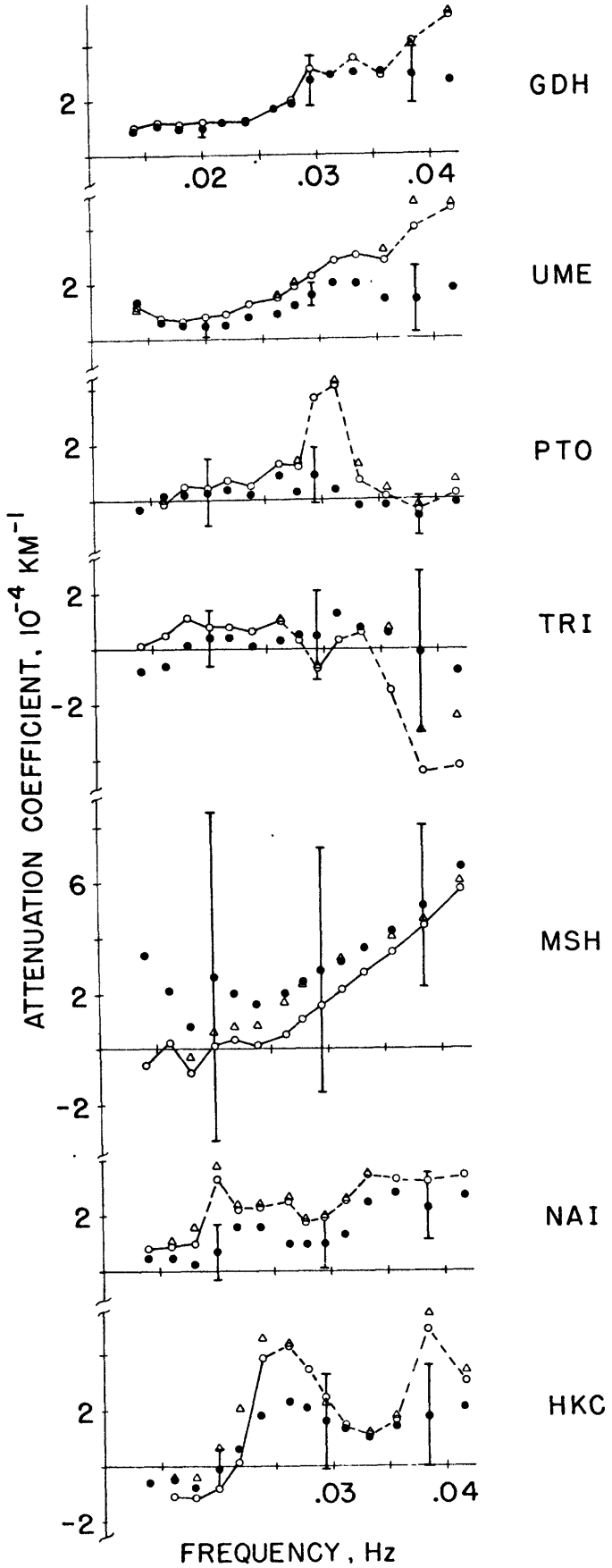

Fig. 4-3.1: Attenuation coefficients based on the results of calculating H_{1k} two different ways. LAV are shown by (●) with bars representing one standard deviation in this estimate. MLE are shown by (o) for z=1.0 and by (Λ) for z=5.0. See text for definition of lines.

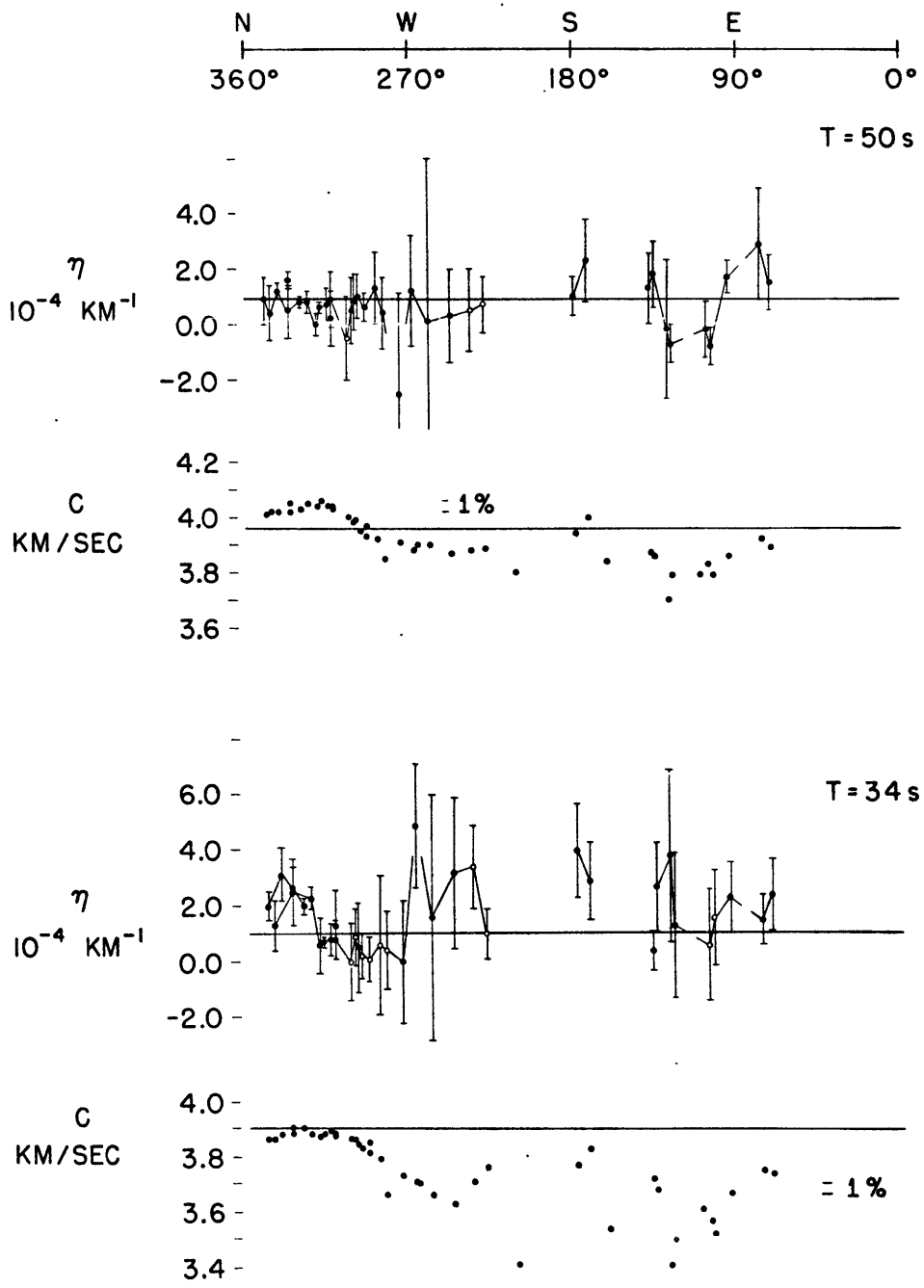
N
W
S
E
360°
270°
180°
90°
0°
T = 50 s
η
10⁻⁴ KM⁻¹
4.0
2.0
0.0
-2.0
C
KM / SEC
4.2
4.0
3.8
3.6
= 1%
T = 34 s
η
10⁻⁴ KM⁻¹
6.0
4.0
2.0
0.0
-2.0
C
KM/SEC
4.0
3.8
3.6
3.4
= 1%

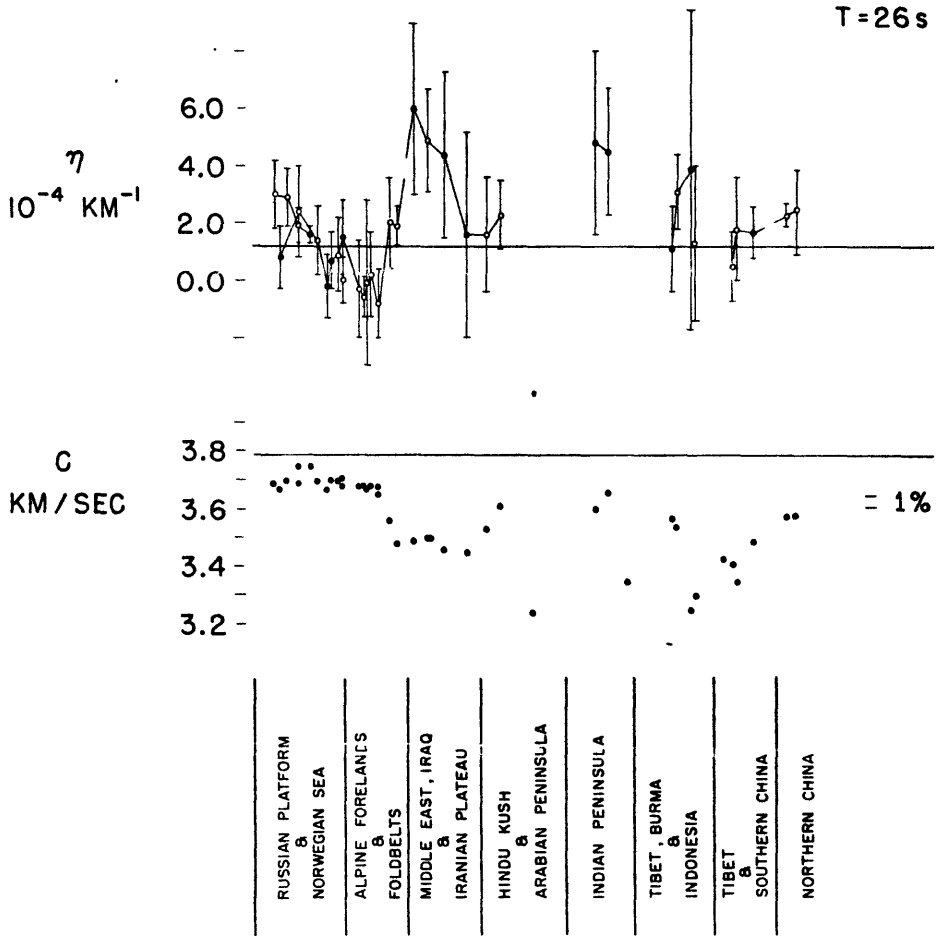

Fig. 4-3.2: Plots of attenuation coefficient and phase velocity against azimuth of the station. Error bars represent one standard deviation in the LAV estimate. Open circles show stations with RMS phase errors larger than $\pi/2$.

4. SUMMARY

We successfully applied the method of Weidner and Aki (1973) to obtain focal depths and revised fault plane parameters of a pair of earthquakes in the vicinity of the reference point. This enabled us to calculate initial estimates of the path transfer functions needed to start the iteration. The interation went smoothly, resulting in the determination of source parameters for nine events and the accumulation of a large quantity of refined propagation data.

The results of the least squares moment tensor inversion agreed well with the source parameters determined from the logarithmic fit when precautions were taken to remove bad data points. A modification of the straight least squares inversion was proposed to make the inversion insensitive to the presence of bad data points. This robust method, involving weighted least squares, is not as fast as the straight least squares approach; however, it still represents a significant saving in computer time over the trial and error fitting.

The residuals obtained from the repeated application of the moment tensor inversion over trial focal depths showed two minima; one minima occurred at depths less than 20km and the other at depths greater than 70 or 80km. The values of the residuals at these minima were often close enough to cast doubt on the determination of focal depth. The ambiguity is due to a combination of factors, one of which is the similarity of the response,

$\frac{\sqrt{k}}{U\omega^2 I_1} G_1$, at shallow and deep focus over the frequency range of this study. We were able to resolve the ambiguity by examining the behavior of the RMS amplitudes on the imaginary part and by comparing the geometry of the moment tensor obtained for shallow and deep focus inversions with the observed P-wave polarities.

For the earthquakes in our source region, we found no evidence of serious bias in the source parameters due to epicenter mislocation. Origin time errors were large enough to bias the estimates of moment tensor elements of a few events. Fortunately, we can avoid this bias by revising the origin time using the focal depth determined from surface waves as a constraint.

Having exhausted the possibility of any sources of serious errors, the source parameters of all events are found to be remarkably consistent as focal depths of all shallow events are between 5-15km and principal compressive stress axes are oriented north-south close to the horizontal plane. The inversion generally gives three-couple force systems having a significant non-zero intermediate component. This may be expected on the basis of the results of numerical experiments modelling the effects of noise contamination (Chapter 3). Comparisons of source effects of the double couple source models and the three-couple models are very close. Therefore, in the light of errors in our data it can not be established convincingly that the results of the linear inversion are caused by departures of the source from the double couple model.

Comparing the residuals obtained by Weidner (1972) with

ours, there is indication of more laterally heterogeneous crust and upper mantle in Central Asia than in the oceans near the rifts. We computed heterogenity quotients of .46 vs .80 x 10^{-4}Napier^2/km and .93 vs 2.4 x 10^{-4}radian^2/km for ocean versus continents as a measure of the increasing scatter in amplitude and phase of 20-60sec Rayleigh waves due to lateral heterogenities.

The presence of mulitplicative errors in our data is the factor controlling the behavior of the residuals from the linear inversion. This explains why variances of the residuals increase with the seismic moment of the event (i.e., scales with surface wave amplitude) and with frequency. Multiplicative errors are also responsible for the bad data points that required the implementation of the robust inversion.

Comparison of the attenuation coefficients computed using MLE and LAV methods is revealing about the nature of noises contaminating the seismogram. Characteristics of the propagation and recording noises are clearly visible in the regional groups of stations. The results of analysis shows that the principal source of noise at frequencies less than .025Hz is backgroud recording noise. There is suggestion that troublesome phase perturbations at African and Mediterranean stations were caused by complexities in the propagation over the first 1000-2000km of the paths west of the reference point.

Apparent phase velocities show strong azimuthal variation that is well correlated with geologic and geographic features on

the Eurasian continent. The lowest apparent velocities in Eurasia are on paths over Tibet and the Hindu Kush. The highest apparent velocities are measured over paths on the northern platforms. The differences in these velocities is 9% at 50sec, 13% at 34sec and 15% at 26sec. Apparent attenuation at 50sec period shows relatively minor azimuthal variation compared to the attenuation at the short period (26sec). At the short period attenuation over continental paths south of the reference point is higher than it is on paths crossing the mid-Atlantic Ridge in the Norwegian Sea. Northern paths confined mainly to the platforms have lower attenuation at short period than either Norwegian Sea paths or southern paths.

Some features of the propagation data are difficult to reconcile. For most northern and northwestern paths on the continent we see high velocities and high Q which is consistent with expected correlations between these data. However, on southern and eastern paths there are many observations showing the opposite correlation, i.e., low velocity and high Q or high velocity and low Q. Our interpretations in the next chapter will address these features and the question of lateral variation of velocity and Q on the Eurasian continent.

CHAPTER V

INTERPRETATION

A considerable amount of propagation data has been accrued in Chapter 4. This data consists of phase velocities and attenuation coefficients of Rayleigh waves for more than 40 Eurasian paths. In addition, an interesting variety of focal mechanisms in a small source region has been obtained from the moment tensor inversions. The purpose of this chapter is to interpret this data in terms of the structure and tectonics of Eurasia.

In Section 5-1, we interpret the orientation of the stress field inferred from the focal mechanisms in terms of the north-south convergence of the Indian and Eurasian plates and a network of intersecting strike-slip and dip-slip fault systems. In regard to the magnitude of shear-stress in the plates, we find that apparent stress levels in the source region are roughly 2 to 3 times greater than average levels reported in other tectonic settings.

Section 5-2 deals with regional variation of phase velocities. Using auxiliary data in the form of crustal thicknesses and topography, we propose a regionalization model with six provinces. The range of phase velocities between these provinces is great: in the Plateau province, for example, velocities are 20%

slower than velocities on the Indian Shield at 26sec period, and 5% slower at long period (90sec).

Our interpretation of the regionalized phase velocities is given in Section 5-3. Lateral variation of crustal thicknesses alone cannot explain the observed regional phase velocities. Profound diffences must exist in the upper mantle structures. For example, we find that the lid under the Indian Shield, is ∿80km thick, comparable to that of the Canadian Shield. The Platform province is found to have a crust ∿70km thick if shear velocities are high (∿3.75km/sec) in the lower crust. Our proposed upper mantle structure under this province is quite similar to James' (1971) for the Andes mountain regions.

We discuss factors affecting surface wave amplitudes in Section 5-4. Horizontal refraction of surface waves is considered as well as intrinsic Q of the medium. We find indications of very different Q structures under stable and tectonic provinces. In fact, the Q structure under tectonic provinces in Eurasia inferred from our models, appears to be quite different from other tectonic regions, e.g., western United States.

1. TECTONICS OF THE SOURCE REGION AND RELATED SUBJECTS

The geometries of the seismic moment tensors obtained in Chapter 4 showed a very consistent result: among shallow events, the principal compressive stress axis is aligned north-south very close to the horizontal plane. Azimuths of the P-axes ranged

from 20° west of north to 13° east of north and the dip angle from -2° to 43° off the horizontal plane. This characteristic of the stress field is in agreement with the interpretation that present tectonic activity in Central Asia is due to the north-south convergence of the Eurasian and Indian plates (Dewey and Bird, 1970; Molnar et al., 1973; Molnar and Tapponnier, 1975).

In Figure 5-1.1, we show a map of faults in Central Asia from the study of Shirokova (1974). The Talasso-Fergana fault (a) and the northwestern extension of the Karakoram fault (b) are large right lateral strike-slip fault systems (Shirokova, 1974; Molnar and Tapponnier, 1975). The Talasso-Fergana fault diagonally intersects the Tien Shan mountain range and is shown on this map terminating at the junction of a major east-west lineament (c). This lineament, the Hissar-Kokshaal fault, is a series of steep dipping faults running along the southern foothills of the Tien Shan (Shirokova, 1974). The Pamir mountains lie immediately south of this fault and west of the Kanakoram anticlinorium. The fault trace of the northern section of the Kanakoram fault is apparently buried in folds of the Pamir mountains.

By the location of epicenters on this map, it may be seen that events 3 and 4 and the large aftershocks 7, 8 and 9 that followed the August 11, 1974 mainshock lie very close to the Hissar-Kokshaal fault. Events 1 and 2 and deep event 6 lie further south away from mapped fault traces. Finally, event 5 lies very close to the Talasso-Fergana fault.

Shirokova (1974) concludes that compressive stresses are

oriented on a horizontal plane across the Hissar-Kokshaal fault with tensile stresses nearly vertical. This is consistent with the geometry of the moment tensors obtained for events 3, 4 and 7. By plotting fault planes it is found that all of these events have a steep plane dipping northward. If this plane is the actual fault plane as suggested by Shirokova's description of the Hissar-Kokshaal fault, then motion is reverse faulting of the northern block over the Pamir mountains in the south. Other studies (Molnar et al., 1973; Ni, 1978) cite evidence for the Pamirs over thrusting the Tien Shan mountains on the northern block. In that case, reverse faulting occurs on a very shallow southward dipping ($<30^{o}$) fault plane.

South of the Hissar-Kokshaal fault, the strike-slip mechanisms of events 1 and 2 are evidence for a northward extension of the Karakoram fault into the Pamirs. Strike-slip event 9, lying further north of events 1 and 2, suggests that the Karakoram fault may in fact intersect the Hissar-Kokshaal fault. Alternatively, there may be a series of strike-slip faults in the Pamirs. Calling plane #1 of event 9 the fault plane (see Figure 4-2.10), the locations of events 1 and 2 and similar alignments of their fault planes suggest an enechelon series of right lateral strike-slip faults, perhaps buried in the highly folded Pamir mountain belt. Considering the fact that all shallow focus events were confined to a narrow depth range, 5-15km, the interaction between strike-slip enechelon faults and the Hissar-Kokshaal fault may be quite complicated, as seen by the focal

mechanism of event 8. This event, occurring about 1.5 hours after thrust event 7, was caused either by (a) normal faulting on a vertical plane aligned with the enechelon faults or (b) strike-slip faulting on a shallow plane transverse to the enechelon faults.

The focal mechanism of event 5 is an indication of enechelon faulting along the Talasso-Fergana fault. In this case enechelon reverse faults may be relieving stress on this strike-slip fault in the Tien Shan.

Event 6 occurring more than 100km in the Pamir Foredeep is evidence that the stress field changes at depth. Interestingly, the tensile stress axis is oriented nearly horizontal only 30^{o} east of north. We may interpret the stress field at depth in terms of the buoyancy of the continental crust causing the P-axis to become more vertical, or in terms of drag forces opposing the northward movement of the upper portion of the lithosphere over the lower causing the T-axis to be horizontal in the north-south direction.

APPARENT STRESS. There is considerable interest in the magnitude of shear stress in the lithosphere. Richardson and Solomon (1977) have found that apparent stress which is a measure of the average shear stress on the fault plane before and after an earthquake does not show significant differences in magnitude in different tectonic settings. Their survey of apparent stress measurements included earthquakes occurring on mid-ocean ridges,

transform faults, in subduction zones, and in the middle of plates. From mid-plate earthquakes, it was concluded that both apparent stress and stress drops are consistent with magnitudes of shear stress differences in the lithosphere of about 100 bars. This does not preclude possible high stress areas in the lithosphere. In the environment of continent-continent collision, compressive stress may be as large as 1 kilobar (Bird,1976). Indeed, observations of large amplitude, high frequency S_n phases recorded at Garm from intermediate depth earthquakes about 200km away in the Pamir-Hindu Kush region could be evidence of very high stress drops of the order of kilobars (Khalturin et al., 1977).

Apparent stress is defined as the product of the average shear stress before and after faulting, $\bar{\sigma}$, and the seismic efficiency factor, η. It may be measured from seismic observations using the formula by Aki (1966):

$$\eta\bar{\sigma} = \mu \frac{E_s}{M_o} \qquad (5\text{-}1.1)$$

where μ is the shear modulus, E_s is the radiated seismic energy and M_o is the seismic moment. The radiated seismic energy may be estimated from the formula of Gutenberg and Richter (1956):

$$\log_{10} E_s = 5.8 + 2.4\, m_b \qquad (5\text{-}1.2)$$

where m_b is the body wave magnitude. Although this formula yields only a rough estimate of E_s, it should suffice for compar-

ing relative differences in the apparent stress levels within a population of seismic events (Richardson and Solomon, 1977).

In this case we compare the apparent stress of our nine events, computed in Table 5-1.1 using m_b reported by ISC to estimate radiated seismic energy, with the data set compiled by Richardson and Solomon (see their Figure 3). As may be seen in Table 5-1.1, the apparent stress levels of all nine events lies in the range 0.8-3.3 bars. The median value is 1.1 bars which may be compared with the value of $\sim$0.4 bars reported by Richardson and Solomon for other tectonic settings. These measurements for shallow focus earthquakes in the Pamirs suggest that apparent stress levels in continent-continent collision zones are greater, perhaps a factor of 2 or 3, than levels in other tectonic settings.

TECTONIC STRESS RELEASE vs. EXPLOSION. It is of interest to know whether the inversion method used in Chapter 4 could aid in the problem of discrimination between earthquakes and nuclear explosions. In particular, questions may arise concerning the effect of imposing the constraint that $M_{ii}=0$, which is applicable to the earthquake source but not to the explosive source.

In the following experiment designed to test this effect, we computed synthetic spectra at the twenty stations of the WWSSN network used in Chapter 3 (see Table 3-2.1). The Rayleigh wave complex spectra were computed for an explosive source ($M_{xx}=M_{yy}=M_{zz}=1\times10^{25}$dynes-cm) buried 1km deep and having step

TABLE 5-1.1: CALCULATION OF APPARENT STRESS LEVELS FOR EARTHQUAKES IN CENTRAL ASIA

EVENT NO.	m_b	E_s dynes-cm	M_o dynes-cm	$\eta\bar{\sigma}$ bars
1	5.5	1.0×10^{19}	2.8×10^{24}	1.1
2	5.2	1.9×10^{18}	7.4×10^{23}	0.8
3	5.5	1.0×10^{19}	3.5×10^{24}	0.9
4	5.5	1.0×10^{19}	9.0×10^{23}	3.3
5	5.4	5.8×10^{18}	1.8×10^{24}	1.0
6	5.9	9.1×10^{19}	2.8×10^{25}	1.0
7	5.7	3.0×10^{19}	3.4×10^{24}	2.6
8	5.8	5.2×10^{19}	7.7×10^{24}	2.0
9	5.7	3.0×10^{19}	4.0×10^{24}	2.2

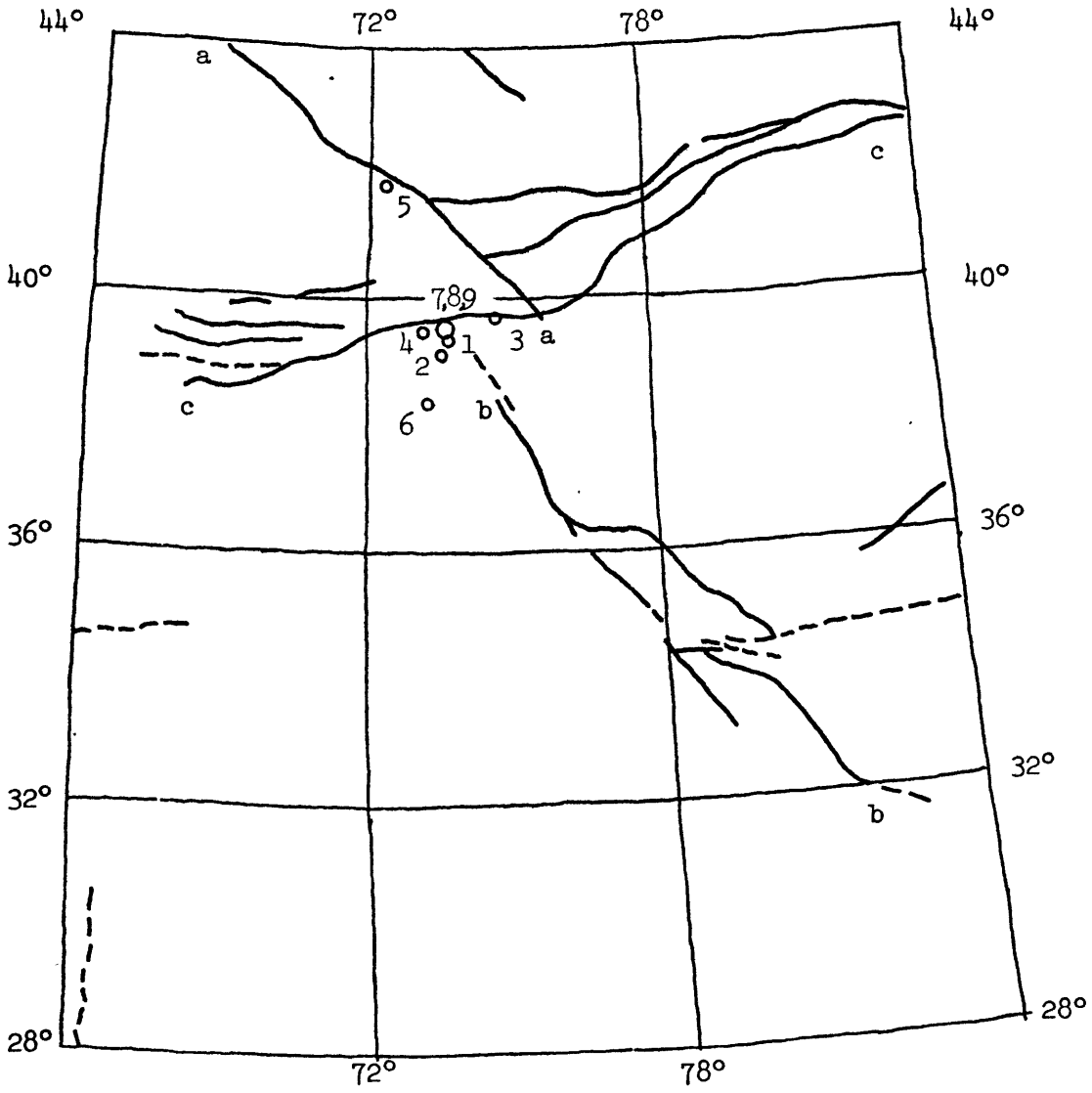

Fig. 5-1.1: Map of faults in Central Asia (after Shirokova, 1974). a-a: Talasso Fergana fault, b-b: Karakoram fault, c-c: Hissar Kokshaal fault, circles are epicenter locations of events in this study.

function time dependence. With these error free spectra as input, the linear inversion returned the following source parameters:

$$h = 1\text{km}$$
$$M_{xx} = 0.45\text{x}10^{25}\text{dynes-cm}$$
$$M_{yy} = 0.45\text{x}10^{25} \quad "$$
$$M_{zz} = -.90\text{x}10^{25} \quad "$$
$$M_{ij} = 0.0 \quad i \neq j$$

As may be seen, the trial depth minimizing the residuals occurred at the true focus of the synthetic data; thus, no bias of the source depth enters by imposing this constraint. However, the moment tensor is considerably different from the starting tensor of the explosive source. This result does show the maximum departure from the double couple source model possible under the imposed constraint. It may be argued that this event does not fall into a class of acceptable models of the earthquake source, and therefore should not be regarded as a natural source. This may form the basis for a discriminant.

2. REGIONALIZATION OF PHASE VELOCITIES

The azimuthal variation of apparent phase velocity in Figure 4-3.2 shows correlation with geologic and physiographic features on the Eurasian continent. For example, phase velocities show a steady decrease in the northwest from stations in Scandinavia

across the northern stable platforms to southern stations in the Mediterranean and the Middle East. There is clear indication of low velocities at many stations across the orogenic belts of southern Asia. The purpose of this section is to regionalize the Eurasian continent in order to explain the observed variation of phase velocity around our reference point. The output of this regionalization is "pure-path" phase velocities which can be used to interpret structure within the separate regions.

With our present dataset we are not in the position to allow the boundaries of the regions to be free parameters, as they are in the "cross-pathing" technique of Santo (1965). Our method of regionalization will be to fix the boundaries based on a reasonable model of the lateral variation of phase velocity. This approach has been used in previous investigations (e.g., Kausel et al., 1974; Forsyth, 1975) to recover the regional variations of phase velocities in oceans.

The correlation that has been noted between the apparent phase velocity and geology suggests a regionalization based principally on surface geologic features which is the essence of Knopoff's (1972) classification of continental phase velocities. Another possibility is to regionalize on the basis of crustal thickness because the dispersion of short period surface waves is very sensitive to this factor.

The map of Eurasia in Figure 5-2.1 summarizes two types of data on which we shall base our regionalization. The contours refer to constant thickness of the earth's crust as measured from

sea level. The shading refers to elevation of the earth's surface relative to sea level. The contours covering the area of the Soviet Union and China are taken from a map compiled by the United States Geologic Survey for the Advanced Research Projects Agency (USGS, 1969). Data for western Europe and India are taken from compilations by Zatopek and Beranek (1975) and Narain (1973), respectively. The elevations are taken from the Times Atlas (1967). The Moho contours were digitized from maps given in the sources mentioned above and replotted on an equal azimuthal projection centered on the reference point. The elevations were transcribed onto this map by hand.

The reliability of this data can be judged to some extent by the data and methods that were used in constructing the USGS map, for example. These are summarized as follows:

a) Deep-seismic sounding results (∿15% area)

b) "Direct-analogy method" which assumes that the crust under geologically similar formations is also similar (e.g., Ural and Appalachian mountains) (∿15-20%)

c) Models based on correlations between tectonics and crustal structure (∿30%)

d) Inference from geology and physiographic features.

In an effort to evaluate the information on this map more quantitatively and to fill in information about the crust in regions not covered by the contours in Figure 5-2.1, we have searched the literature of which a brief review is given below. Major sources of information are drawn from results of surface

wave studies. For many of these studies, we also report the results concerning the structure of the upper mantle. Geographically the review starts in western Europe and moves eastward.

IBERIAN PENINSULA: Payo (1970) obtained Rayleigh wave phase velocities over periods 10-90sec using a tripartite station network involving TOL, PTO, and MAL. The crust and upper mantle structure under this array is found to be quite uniform. The crust is interpreted to be 30km thick. The upper mantle structure of Payo's model IBE shows a 50km thick high velocity lid over a pronounced low velocity zone with shear wave velocity of 4.2km/sec. The upper mantle structure, particularly the lithosphere thickness and distinct low shear velocity in the channel, shows similarities with the structures found in neighboring regions including the Mediterranean.

MEDITERRANEAN SEA REGION: The study by Berry and Knopoff (1967) used Rayleigh wave phase velocities over periods 20-80sec to obtain structure under the western Mediterranean Basin. Payo (1969) measured Rayleigh and Love wave phase velocities over shorter periods 10-50sec for both western and eastern parts of the Mediterranean. Under the center of the western Mediterranean Basin, the crust is 10km thick and the upper mantle was interpreted by Berry and Knopoff to have a 38km thick lid below which a low velocity zone with shear velocity of 4.1km/sec extends to depths of 200km.

THE ALPS: From tripartite arrays formed out of various combinations of five stations in the Alps, Knopoff et al. (1966) measured Rayleigh wave phase velocities over periods 15-80sec in order to obtain a detailed picture of the crust and upper mantle structure. The crust was seen to vary considerably in thickness, with the greatest thickness, 50km, under the crest of the Alps. It thins to 30km to the north and in the west. The upper mantle structure over the entire region was found to have a well developed low velocity zone between depths of 80 and 220km with shear velocity as low as 4.2km/sec. In a study of the western Alps and the Rhinegraben Rift system, Seidl et al. (1970) obtained Rayleigh wave phase velocities over periods 20-100sec using the two station method. Their derived upper mantle structure is very similar to the results of the previous investigation with perhaps slightly lower velocities, 4.1-4.2km/sec, in the channel.

NORTHERN EUROPE: Average phase velocities over an array of stations consisting of MAL, VAL, STU and COP have been reported by Seidl (1971) and an interpretation is given in Seidl et al. (1970b). With the crust constrained to 30km, the latter study obtained an upper mantle structure with a 45km thick lid ($\sim$4.6km/sec) over a low velocity zone with shear velocity of $\sim$4.34km/sec. In the North Sea, Stuart (1978) obtained Rayleigh wave phase velocities over periods 13-127sec and gave an interpretation of the upper mantle with lithosphere thickness of 80-90km and a low velocity zone to depths of 200km, constraining

the crustal thickness to 30km. The velocity of the lid was found to be 4.65 and of the low velocity zone 4.35-4.45km/sec.

It is apparent from these studies that western Europe has been the subject of detailed investigations and that certain conclusions, such as the existence of a well-developed low velocity zone, are shared by all interpretations. There are also indications of lateral variations of the crust and upper mantle between the southern and northern parts. It is the pervasiveness of the low velocity zone in western Europe that dominates the propagation characteristics of not only the fundamental mode Rayleigh wave but also higher modes as shown by Nolet (1975). Nolet found that the Gutenberg model (see Table 2-4.1) satisfactorily fits the observations of phase velocity of six higher mode Rayleigh waves.

SOUTHEASTERN EUROPE: The study by Papazachos et al. (1966) uses refraction and reflection methods on body waves from local earthquakes to determine the crustal structure of Greece and areas neighboring the Adriatic Sea. The crustal thickness varies from 32 to 47km over this area. The Greek peninsula has a mean crustal thickness of 43km and thins to 32km approaching the Adriatic Sea. Under Italy, the crustal thickness is reported to be 45km. The crust in the northeastern regions is seen to thin along a profile from the Carpathians, 45km, approaching the Black Sea, 34km. The northern Aegean Sea and the western part of Turkey have a normal crustal thickness of 33km. The P_n and S_n veloci-

ties over the entire region were found to be 7.87 and 4.55km/sec, respectively.

CARPATHIAN MOUNTAINS: Yurkevich and Volosecky (1969) report Rayleigh wave phase velocities over the periods 20-40sec for paths across the crest of the Carpathian mountains. Their results show that crustal thickness is as great as 50-55km.

SCANDINAVIA AND GREENLAND: Crampin (1964) has measured the phase velocities of higher mode Rayleigh waves between the Uppsala station and WWSSN stations in Scandinavia. For the most part, the crustal thickness under this region appears to be very uniform, having a value of about 40km in agreement with an earlier result determined from fundamental mode Rayleigh wave phase velocities by Tryggvason (1961). Noponen (1966) obtained Rayleigh and Love wave phase velocities in the period range 10-60sec for several paths on the Baltic Shield. Comparison with the velocities on the Canadian Shield (Brune and Dorman, 1963) indicated significant differences both in the crust and upper mantle structure for these two shields. Reviewing body wave and surface wave data collected on Fennoscandia, Penttila (1969) arrives at the following average crustal thicknesses in this region: Finland 39$\pm$3km, Sweden 37km, southern Norway 36km, and Denmark 31km. Thicker crust under the Baltic Shield than under the Canadian Shield may explain the differences in Noponen's phase velocities at short period. On the ice covered Greenland Shield, Rayleigh and Love wave phase velocities were measured over periods 15-50sec between

WWSSN stations GDH, KTG and NOR by Gregersen (1970). The region covered by the profiles was found to have very uniform structure. The interpretation includes a 43km thick crust with upper mantle P- and S-wave velocities of 8.05 and 4.67km/sec, respectively.

THE UKRAINE: Sollogub (1970) reviews the results of refraction and reflection seismic profiles across the Ukraine Shield and neighboring areas including the Dniper-Donetz depression further north of the Black Sea. Over the Ukraine Shield, crustal thickness varys rapidly from 35-60km, which discounts previous results for shield areas being relatively uniform. Sollogub cites evidence for upraised and lowered block layering structure in the crust, deep faulting originating in the upper mantle, and possible low velocity zones in the crust (Pavlenkova, 1969). It is believed that the disturbed nature of the crust and upper mantle in this region is mainly caused by upheavals that occurred in the Tertiary time associated with the Alpine orogeny.

BLACK SEA, CASPIAN SEA AND CAUCASUS: Neprochnov et al. (1970) reviews the geophysical data collected for the Black and Caspian Seas. The crust underlying the center of the Black Sea is as thin as 18-24km. The "sediment-basaltic" crust of the Black Sea has an 8-15km thick sedimentary layer. The Caspian Sea may be divided into two parts: the northern half has typically continental-type crust 35-40km thick and the southern half has slightly thicker crust, 40-45km, with no granitic layer, and extraordinary sedimentary thickness of 25km. P_n velocities under

the Black and Caspian Seas are 8.0-8.2km/sec. In the Caucasus, Ragimov (1969) has measured Rayleigh wave phase velocities over periods 15-40sec. Crustal thickness was determined to be between 45-55km.

RUSSIAN PLATFORM: Rayleigh wave phase velocities over periods 15-40sec have been measured for the interior platform by Bozhko and Starovoit (1969). Savarenski et al. (1969) also give measurements of phase velocity in this region. Both studies found crustal thickness to be 38-40km, favoring the thicker value in the eastern parts of the platform.

URAL MOUNTAINS: Khalevin et al. (1966) report the results of deep seismic sounding on an east-west profile approximately 450km long across the crest of the Ural mountains just south of Sverdlovsk. In this section the crust is seen to vary between 33 and 47km and down warps under the crest of the Urals with amplitudes up to 3-7km. Despite this indication that the Ural mountain has roots, Bouguer anomaly patterns are reported to increase over the Central Urals.

TURKMENIA: The results of deep seismic sounding on a profile 625km long from Kopetdag mountains on the southeastern coast of the Caspian Sea to the Aral Sea are given by Ryaboy (1969). A rather detailed picture of the structure of the crust and upper mantle to depths of 120km is determined. The results show the crust to be 36-38km thick. The velocity of P_n is 8.1km/sec and

deeper in the mantle the P-wave velocity is seen to increase rapidly (9.5km/sec at 110km).

SIBERIAN PLATFORM AND FAR NORTHEAST: We cite two reviews, one covering seismic data, Fotiadi and Ladynin (1974), and the other gravity data, Milashev and Rosenberg (1974), collected over this large region. Fotiadi and Ladynin summarize the results with the synthesis of a contour map of Moho thickness. This shows thick crust 40-45km, under the western Siberian platform, sandwiched between areas of thinner crust, 35-40km, under the western Siberian plate and eastern parts of the Siberian platform. In the southern regions, the crust thickens to 45-50km east of Lake Balkhash. Near Lake Baykal, the crust appears to be about 45km thick on its eastern flank and thins gradually to the east reaching 30-35km along the coastline of the Sea of Okhotsk and opposite to Sakhalin.

Before leaving the discussion of northern Asia, we shall not fail to mention several reviews of the crustal conditions under the entire territory of the USSR from deep seismic sounding given in Kosminskaya et al. (1964) and Belyaevsky et al. (1973) and the detailed compilations of deep seismic sounding results in Vol'vovsky and Vol'vovsky (1975) and interpretations of crustal conditions in many areas of the USSR in Vol'vovsky (1973).

We now return to the west to cover areas of southern and middle Asia.

ARABIAN PENINSULA: Rayleigh wave phase velocities over periods

20-40sec were measured by Niazi (1968) between stations AAE and SHI in order to determine crustal thickness under the Peninsula. A crustal thickness of 35km was obtained. Knopoff and Fouda (1975) inverted Rayleigh wave phase velocities measured between stations SHI-HLW, SHI-JER and SHI-AAE over periods 20-160sec to obtain the crust-upper mantle structure under the northern Arabian Peninsula. Their results show that the crust is between 27-44km thick. They favor a value of 34km provided the S_n velocity over this region is high (4.6km/sec). A well developed low velocity channel is required with the top of the channel found to be 100-140km below the earth's surface.

ZAGROS: Bird (1976) has arrived at crustal thicknesses of 35km under the Mesopotamian Trough to a maximum of 49km under the Crush Zone just north of the Zagros mountains by modeling Bouguer anomalies observed over Iran. The former value is consistent with the results of Knopoff and Fouda (1975). Bird's model for the upper mantle under the Zagros calls for a thick high velocity lithosphere ($\sim$4.65km/sec) which is consistent with group velocities measured in this area (Bird, 1976).

IRANIAN PLATEAU: Rayleigh wave phase velocities were measured between stations MSH and SHI over the range 20-50sec by Canitez and Toksoz (1977). Their phase velocities may be explained by a 45km thick crust overlying a relatively thin lid of 25km with shear wave velocity of 4.5 km/sec.

CENTRAL ASIA: In the territory of the Soviet Union just 50km northwest of the reference point, the crust is found to be 50-70km thick based on observations of Rayleigh wave phase velocity over periods 10-40sec (Savarenskiy and Peshkov, 1968; Savarensky et al., 1969). The Pamir earth model (Table 3-1.2) incorporates a crust based on results of deep seismic sounding (Kosminskaya et al., 1964).

INDIA: The observations of Rayleigh wave phase velocities over periods 20-45sec between stations NDI and LAH in northern India and Pakistan, respectively, are consistent with a high velocity crust and upper mantle very similar to that of the Canadian Shield (Gabriel and Kuo, 1966). The crustal thickness is considered to be slightly greater than the Canadian Shield at a value of 38km. West of this profile over the Indo-Gangetic Basin, Chatterjee (1971) has measured Love wave phase velocities in the period range 20-50sec between stations NDI and SHL. A crustal thickness of 43km is obtained and the velocity of S_n is found to be lower than the previous study at 4.6km/sec. Over the central Indian Peninsula, a crustal thickness of 41km appears to be consistent with group velocities (Bhattacharya, 1974).

HIMALAYAS AND TIBET PLATEAU: This region has been a subject of great interest concerning the nature of its crust and upper mantle. Estimates of crustal thickness range from 50-80km based on observations of group velocity. Under the Himalayan mountains north of the station NDI, Negi and Singh (1973) estimated the

crustal thickness to be 50km. This figure as well as the estimate of 65-70km for Tibet and the Himalayas by Gupta and Narain (1967) are based on group velocities over long paths from events in the Arctic Ocean assuming that the characteristics of the propagation path giving anomalously low velocities is confined to a small portion across the regions of interest. Group velocities measured over paths with a large percentage on the plateau itself have been made by Tung and Teng (1974), Bird (1976), Chun and Yoshii (1977) at long periods and Chen and Molnar (1975) at short periods. Bird gives two interpretations: one model has low shear velocities in the entire crust of thickness 55km and the second model has more normal shear velocities in the lower crust and a crustal thickness of 70km. Both models have low velocity layers in the crust. Chun and Yoshii propose a crustal model 68km thick with low velocity layers. According to Chen and Molnar, the observation of very clear short period waves (4-11sec period) traveling over Tibet with no interference effects requires a very uniform sedimentary layer, which they determine to be 2.5-7km thick.

CHINA: Using the tripartite method of measuring Rayleigh wave phase velocities, Ts'eng and Sung (1963) have obtained velocities (20-30sec period) over a large area of China. They interpret the observations with standard dispersion curves (Press, 1956) to determine crustal thickness. West of Ch'engtu, they found crustal thickness between 50-76km. North of Sian and Nanking, the

values range from 40-55km which are generally thicker than values to the south on the South China plate, 34-44km. Both northern and southern regions have a crust that thins approaching the coastline. Further surface wave studies on China are restricted to measurements of group velocity (Tung and Teng, 1974; Rosenthal and Teng, 1977). On the South China plate, Rosenthal and Teng have inverted group velocities of Love and Rayleigh waves over the period range 10-60sec to obtain crust and upper mantle structure. Their model ASCS1 shows a crustal thickness of 40km. The S_n velocity is $4.5\pm.1$km/sec and the lid is believed to be thin, between 20-30km.

JAPAN: A detailed picture of the crustal thickness under Japan is known from numerous studies of Rayleigh and Love wave phase velocities (Aki, 1961; Aki and Kaminuma, 1963; Kaminuma and Aki, 1963; Kaminuma, 1966). The maximum thickness is 36km under central Honshu and thins to 24km along the coastlines.

It may be concluded that the crustal thicknesses in Figure 5-2.1 agree well with the findings of many independent studies that were touched on in the review above. In my opinion, the uncertainty of the crustal thickness along a contour, as reflected by a standard error, if one could be computed, may be less than 10km. In areas not covered by the present contours, the results of several studies in the review and the surface topography make it possible to deduce reasonable values of the crustal thickness.

We propose a regionalization of the Eurasian continent in-

volving six provinces, one of which is totally confined to the oceans surrounding the continent. The provinces are shown on the map in Figure 5-2.2. The ocean province is found in water depths greater than 1000m. We depart from this choice of boundary only in the case of the path to station CMC in northern Canada in order to preserve the tectonic nature of the province, consisting mainly of ocean floor close to mid-ocean rifts and in marginal seas. The continental divisions may be broadly divided into three types: two of which are associated with tectonically active regions, two with stable regions, and one associated with "transitional" areas between continent and ocean and on the forelands of several orogenic belts. The tectonic regions are generally confined to areas with crustal thickness greater than 45km or to areas having elevation in excess of 1000m. The boundary of the tectonic region in northern China departs from Moho contours to some extent in favor of known elevations over this area. A further division of this tectonic region is defined by the 55km Moho contour. This division also contains the highest topography in Asia. For this reason, we name these two divisions of continental crust in Eurasia the Tectonic province and the Plateau province. The stable continental regions of Eurasia are largely confined to the northern platforms, namely the Russian and Siberian Platforms, and the Indian Peninsula. The northern regions, particularly the Russian Platform, appear to be very uniform as indicated by little variation of the observed phase velocity at Scandinavian stations. Therefore, no further division of

this region appears justified at this time. Our preference is to omit the Indian land mass from the province making up the north platforms because of its separate tectonic history. The two stable regions are called the Indian Shield province which takes in the entire peninsula as far north as the boundary of the Tectonic province and the Northern Platforms and Shields province which includes portions of the Baltic, Greenland, and Canadian Shield areas. The northern limit of the Northern Platforms and Shields province on the Eurasian continent is defined well by the 35km contour, thereby including the Baltic Shield but not the western Siberian Plate. The southern limit abuts the entire length of the Tectonic province's northern boundary following the 45km contour. The last division of the continent is comprised of areas having crustal thickness less than 35km. Generally these areas are found on coastal plains (e.g., China) or on undisturbed crustal blocks bordering folded structures of major orogenic belts. These stable blocks, called forelands (Holmes, 1965), include the Arabian Peninsula and Northern Europe.

We stress the simplicity of this regionalization. It is proposed as a "first order" approximation of the lateral variation of phase velocity on the Eurasian continent. Previous regionalizations of group velocity data by Santo (1965) for Rayleigh waves and Gupta and Sato (1968) for Love waves employed 6 and 7 provinces, respectively, on the Eurasian continent. It should be mentioned that the boundaries of our proposed provinces show mild correlation with the results of the cross-pathing tech-

nique used by Santo and Gupta and Sato, as we would expect. In eastern Europe and the Russian Platform alone, Shechkov (1970) proposes eight provinces on the basis of geology and tectonics to regionalize Love wave group velocities over the period range 18-38sec.

We are not without means of evaluating the adequacy of our proposed regionalization model. Forsyth (1975) suggested using a root-mean-squared error of the theoretical travel time calculated from regionalization models of phase velocity on the Nasca Plate. More specifically, for a regionalization model with m provinces, we calculate a theoretical travel time, t_i, to the i^{th} receiver as follows

$$t_i = \sum_{i=1}^{m} \frac{L_{ij}}{C_j} \qquad (5\text{-}2.1)$$

where L_{ij} is the length of the path in kilometers through the j^{th} province and C_j is the phase velocity in the j^{th} province. It should be understood that this calculated time is a function of frequency because C_j is a function of frequency. The assumption behind this calculation is that the total phase delay at a given point in an inhomogeneous medium is the sum of the phase delays in each homogeneous province (i.e., no phase shifts at the boundaries; Knopoff, 1969). If S_j is the slowness, $1/C_j$, then we define ε_i to be the travel time residual at the i^{th} station

$$\varepsilon_i = t_i^o - \sum_{j=1}^{m} L_{ij} S_j \qquad (5\text{-}2.2)$$

where t_i^o is the observed travel time at the i^{th} station computed using the apparent phase velocities in Appendix C. We solve for the S_j's by the least squares method which minimizes the sum of squared residuals computed for many paths in Eurasia. The root-mean-squared error in the calculated travel time, σ_m, is computed as follows

$$\sigma_m = \sqrt{\frac{\sum^{n} \varepsilon_i^2}{(n-m)}} \qquad (5\text{-}2.3)$$

where n is the number of paths. This RMS error may be used to evaluate the regionalization model by comparing it with the RMS error obtained from the regionalization of phase velocities in oceans, for example.

Table 5-2.1 gives the information about the path lengths in each province for a total of 42 paths emanating from the reference point, as shown on the regionalization map in Figure 5-2.2. In Table 5-2.2, we give the results of calculating the σ_m for regionalization models with an increasing number of divisions. The pyramid structure in Table 5-2.1 shows the method of dividing Eurasia that finally ends with the six provinces described above. For example, Model 1 divides Eurasia into just the continental areas and the ocean province. Model 2 sub-divides the continental area into Tectonic A and Stable A, and so on for other models. In Table 5-2.2, we show the results of Forsyth (1975)

for Rayleigh wave phase velocity regionalization of the Nasca Plate with the calculated RMS error, σ_m for these models. An interesting comparison is between Model 1 of this study and the single division of ocean and continent of Forsyth's. At 40sec period, the RMS error of Model 1 is double that of Forsyth's starting model. Adding one division to the continents to form Tectonic A and Stable A reduces the RMS error by a factor of two at all periods but 90sec. Thus, allowing the major divisions of the earth's surface to be ocean, stable continent and tectonic continent, we can predict the phase travel time of the 40sec Rayleigh wave to no better than an RMS error of 15sec. Allowing for a change in phase velocity with the age of the oceanic lithosphere and with the azimuth of propagation paths relative to the direction of sea floor spreading (directional anisotropy), the travel time in oceans can be predicted to within 5sec (Forsyth, 1975). An RMS error that small cannot be attained on the Eurasian continent with the proposed regionalization model of five continental provinces. We find that sub-dividing Tectonic A into the proposed Tectonic and Plateau provinces (Model 3) improves the RMS error by better than 5sec at the short periods. We infer from the absence of change in σ_m at long periods that the differences between these tectonic provinces is mainly felt by the short period dispersion. On the other hand, the division of Stable A to form Stable B and the Foreland and Coastal Plains province (Model 4) results in small improvement only at the long periods. Our final regionalization model of five continental

provinces has virtually the same σ_m as obtained for Model 4 in Table 5-2.2.

The phase velocity curves of all six provinces obtained from the least squares fit are shown in Figure 5-2.3. The Indian Shield province has the highest phase velocities on the Eurasian continent over the range of periods 26-60sec. At longer periods the Indian Shield has velocities comparable to those of the Northern Platforms and Shields province. The lowest phase velocities in Eurasia at periods shorter than 60sec are those of the Plateau province. These velocities are 8% slower than the phase velocities of the Tectonic province and 20% slower than the Indian Shield's. At the periods 60-70sec, the dispersion curves of the Plateau and Tectonic provinces merge and remain close over the long periods. The phase velocities of the stable provinces consisting of platforms and shields are 5% higher than the velocities of the tectonic provinces out to 90sec period. The phase velocity of the Forelands and Coastal Plains province lies between these two extremes at 90sec. The phase velocity curve of this province is considerably lower than the curves of the other stable provinces for periods longer than 40sec. Finally, the trend of the phase velocity curve of ocean province in the middle period range is flatter than the continental curves which is typical of Rayleigh wave dispersion in the oceans. Its phase velocity at long period is comparable to the velocity found for the tectonic provinces on the Eurasian continent.

For clarity of presentation in Figure 5-2.3, we have drawn

error bars, representing one standard deviation in the calculation of phase velocities, on the values at long period for Tectonic and Platform provinces only. This is done to show that the differences are indeed significant. This observation raises interesting questions about the characteristics of long period dispersion curves in the two major types of continental provinces. In particular, one may ask to what period do differences in the dispersion curves between stable and tectonic regions persist. This is important because it has bearing on the depth of penetration of lateral inhomogenities of the earth's structure. We examine long period dispersion for the remainder of this section.

LONG PERIOD DISPERSION. Measurements of surface wave dispersion for periods longer than 150sec have commonly been made on great-circle paths using one station which records the successive passages of G_2 and G_4, for example. The phase velocity as computed by the formula given in Toksoz and Anderson (1966) is therefore an average value of the Love wave over the entire great-circle path. Variations in the average values were found to be correlated with the composition of the paths, which was defined in terms of ocean, tectonic and shield areas (Toksoz and Anderson, 1966). Tectonic areas were found to have significantly lower Love wave phase velocities than shield areas out to periods longer than 300sec. These values of regional phase velocities were obtained from a least squares fit involving observations

over many great-circle paths of varying composition.

Similar regionalization studies of long period phase velocity dispersion were carried out by Kanamori (1970) and Dziewonski (1970). Kanamori regionalized Rayleigh wave and Love wave phase velocities, and Dziewonski regionalized Rayleigh wave phase and group velocities. Kanamori found that the dispersion in tectonic regions differed significantly from the other regions for both Love and Rayleigh waves. Interestingly, the results of Dziewonski showed significant regional differences in the long period group velocities of Rayleigh waves and not in the phase velocities, in contradiction to the study of Kanamori.

Madariaga and Aki (1972) suggested that the discrepancy in the long period regionalized phase velocities was due to the inadequacy of the ray theoretical approach that is assumed in the method of regionalization. This inadequacy is caused by interference between waves travelling on other great-circle paths. The effect is strongest at the epicenter and antipole where paths converge and produce uncertain phase shifts depending on the heterogeneities along the paths. Recently, Okal (1977) has suggested that lateral variations of the phase velocity in oceans could have been responsible for the discrepancy. His claim is that due to the fact that the paths in Kanamori's dataset contain a larger oceanic fraction and cross more diverse age provinces in the oceans than the paths of Dziewonski's, the effect of assuming one homogeneous province in the regionalization is large enough to cause scatter in Kanamori's results.

We summarize the results of Kanamori, Dziewonski and Okal for Rayleigh wave phase velocities in Figure 5-2.4. In this figure, the results of great-circle path regionalization are shown at periods longer than 150sec for tectonic (+) and shield (x) areas. Okal's dataset includes Kanamori's, Dziewonski's, and some new data. From the results of Okal, it appears that the difference between the phase velocities of the tectonic and shield areas is reduced by accounting for the lateral variation of phase velocities in the oceans. The new regional phase velocities obtained by Okal are consistent with Dziewonski's values which are shown in Figure 5-2.4 only at shortest period ($\sim$175sec) in that regionalization. All of these regional values of phase velocities are reported to be known to better than 1%.

At periods shorter than 150sec in Figure 5-2.4, we give the results of phase velocity measurements using the two station method (--X--) over paths on the North American stable platform, FLO-GOL, and on the Rocky mountains and Colorado Plateau of Western United States, TUC-BOZ (Biswas and Knopoff, 1974). With the accuracy of these measurements reported to be about $\pm$1%, the regionalized values for shield areas at periods longer than 150sec appear to be incompatible with the direct measurements on the North American platform.

Knopoff (1972) points out that the accuracy of the great-circle path regional velocities is probably over-stated because the regionalization of large areas that are broadly classified as shields and are presumed to be homogeneous, averages out the

phase velocity variations along the path in those areas. He goes on to note that from direct measurements of phase velocity along different profiles within a given region the variation in phase velocity at 150sec is observed to be 3-4%. This raises the possibility that stricter regionalization of the continents may uncover significant differences in the long period phase velocities that are presently not obtained from the coarse regionalization models used on great-circle path data.

In an effort to shed light on the differences of long period phase velocities on the Eurasian continent, we studied the long period radiation from event 6. Long period surface waves were excited much more efficiently by event 6 than the shallow events in our dataset. At stations having clear long period wave trains and well-separated higher modes, a spectral analysis indicated that signal strength was reliable to periods as long as 150-160sec.

Long period phase velocities were measured at four stations. Two of the stations, KEV and KBS, have paths containing large percentages, 86% and 63%, respectively, of the stable northern platforms. The path to station CHG consists of 68% in the Tectonic provinces and the remainder in the Coastal Plains province (It should be noted that this latter portion is tectonic in nature, judging from the high seismicity along the path in southeast Asia). The last station, IST, has a path along the southern edge of the Platform province and the boundary of the Tectonic province.

TABLE 5-2.1: PATH LENGTHS IN KILOMETERS THROUGH EURASIAN PROVINCES

	CONTINENT					OCEAN
	TECTONIC A		STABLE A			
			STABLE B			
	TECTONIC	PLATEAU	N. PLATFORMS & SHIELDS	INDIAN SHIELD	FORELANDS & COASTAL PLAINS	OCEAN
CMC	440	100	2666		4092.7	800
COL	770	100	3341		3661.6	
MAT	2532	100			2184.5	742
SHK	2532	100			2546.3	
ANP	1453	1652			1626.9	
HKC	1250	1956			1086.2	
BAG	1216	2023			1428.4	540
DAV	1099	2242			1946.0	1012
CHG	525	1770			1085.0	
SHL	390	1770			188.0	
SNG		1890			2633.6	
NDI	101	810		315		
KOD	338	607		2336.5		
POO	304	540		1445.3		
QUE	535.1	641				
NAI	2430	810			2659.7	
AAE	2936	405			1495.9	
SHI	1930.9	304				
MSH	1056.4	236				
EIL	1687	202			1846.4	
JER	1554	200			1814.8	
TAB	812	200	1368.2			
ATU	2397	100	1810.7			
IST	642	100	1957		1048.9	
AQU	1081	100	3442		301.1	
MAL	1081	100	3374		1602.0	405
TOL	1689	100	3374		1244.8	
TRI	541	100	3374		813.1	
PTO	2364	100	2900		1373.1	
STU	1014	100	2970		1007.6	
VAL	100	100	4353		1765.5	
COP	100	100	4454		87.8	
ESK	100	100	4589		930.6	
KON	100	100	4671.7			
NUR	100	100	3867.3			
UME	100	100	4124.2			
AKU	100	100	4386		771.6	810
KTG	100	100	3746		871.4	1282
KEV	100	100	3746		393.4	
GDH	100	100	4488		1809.8	675
KBS	100	100	3240		1673.8	
NOR	100	100	3500		1530.8	405

TABLE 5-2.2: RMS ERROR, σ_m, IN SECONDS FROM REGIONALIZATION MODELS

MODEL / PERIOD	CONTINENT & OCEAN	STABLE A, TECT. A & OCEAN	STABLE A, TECT., PLATEAU & OCEAN	STABLE B, PLAINS TECT., PLATEAU & OCEAN	FORSYTH(1975) OCEAN & CONTINENT	FORSYTH(1975) 4 OCEAN, 2 CONTINENT, & ANISOTROPY
90s	18.8	10.0	10.1	8.3		6.2
66s	20.9	8.8	9.0	8.0		5.1
40s	33.7	15.2	10.1	9.7	15.1	4.8
34s	38.5	18.0	11.8	11.9		5.5
26s	42.9	21.7	15.7	15.8		6.5

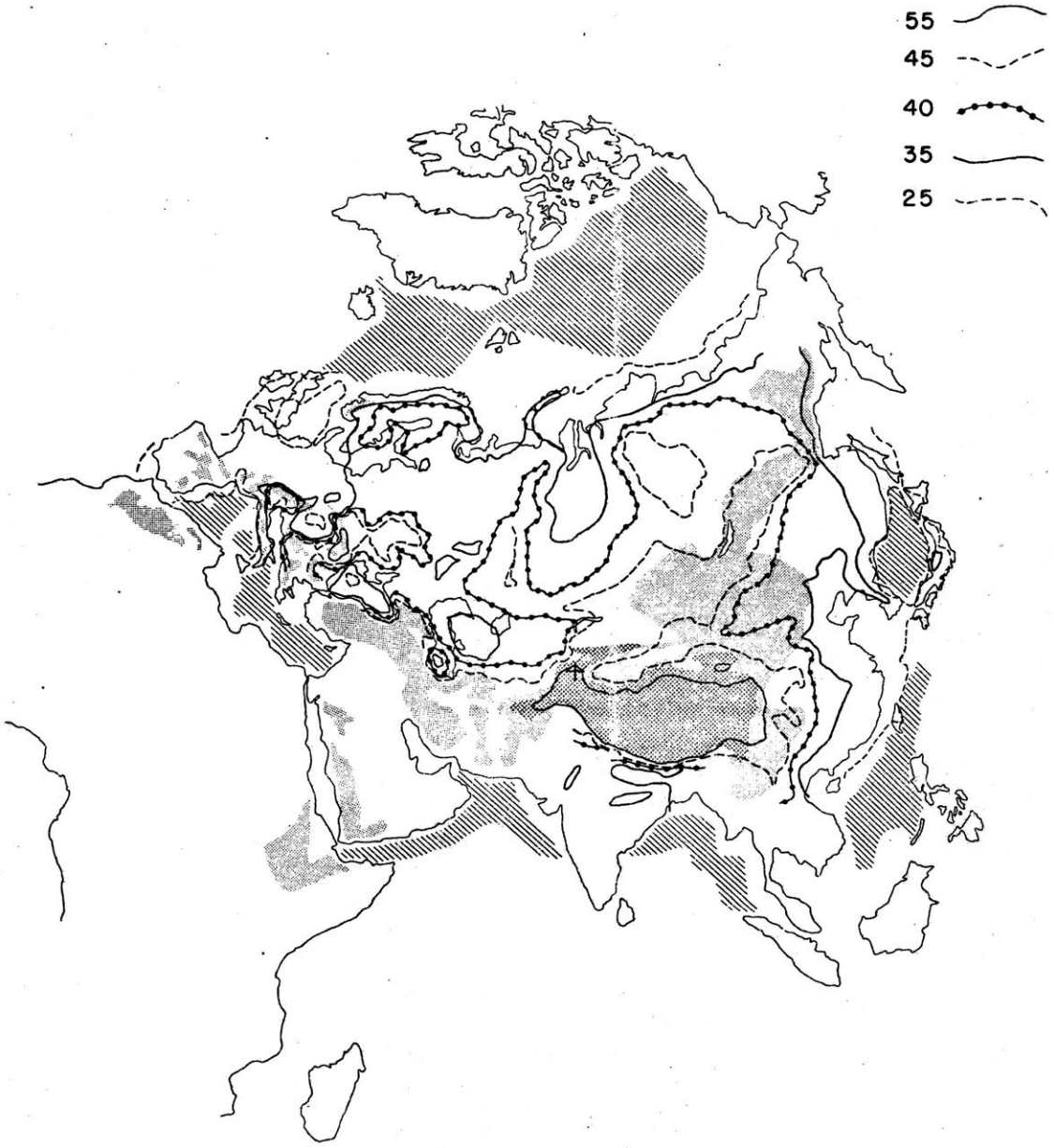

Fig. 5-2.1: Crustal thickness and topography of the Eurasian continent. Legend refers to Moho contours in kilometers. Topography is represented by shading: diagonal lines: <-1000m; no shading: -1000m-1000m; stipple:1000m-3000m; cross-hatch: >3000m.

Fig. 5-2.2: Provinces in the phase velocity regionalization. Diagonal lines: Ocean, stipple (north): Northern Platforms and Shields, stipple (south): Indian Shield, cross-hatch: Tectonic, cross-hatch (inside contour): Plateau, no shading: Forelands and Coastal Plains.

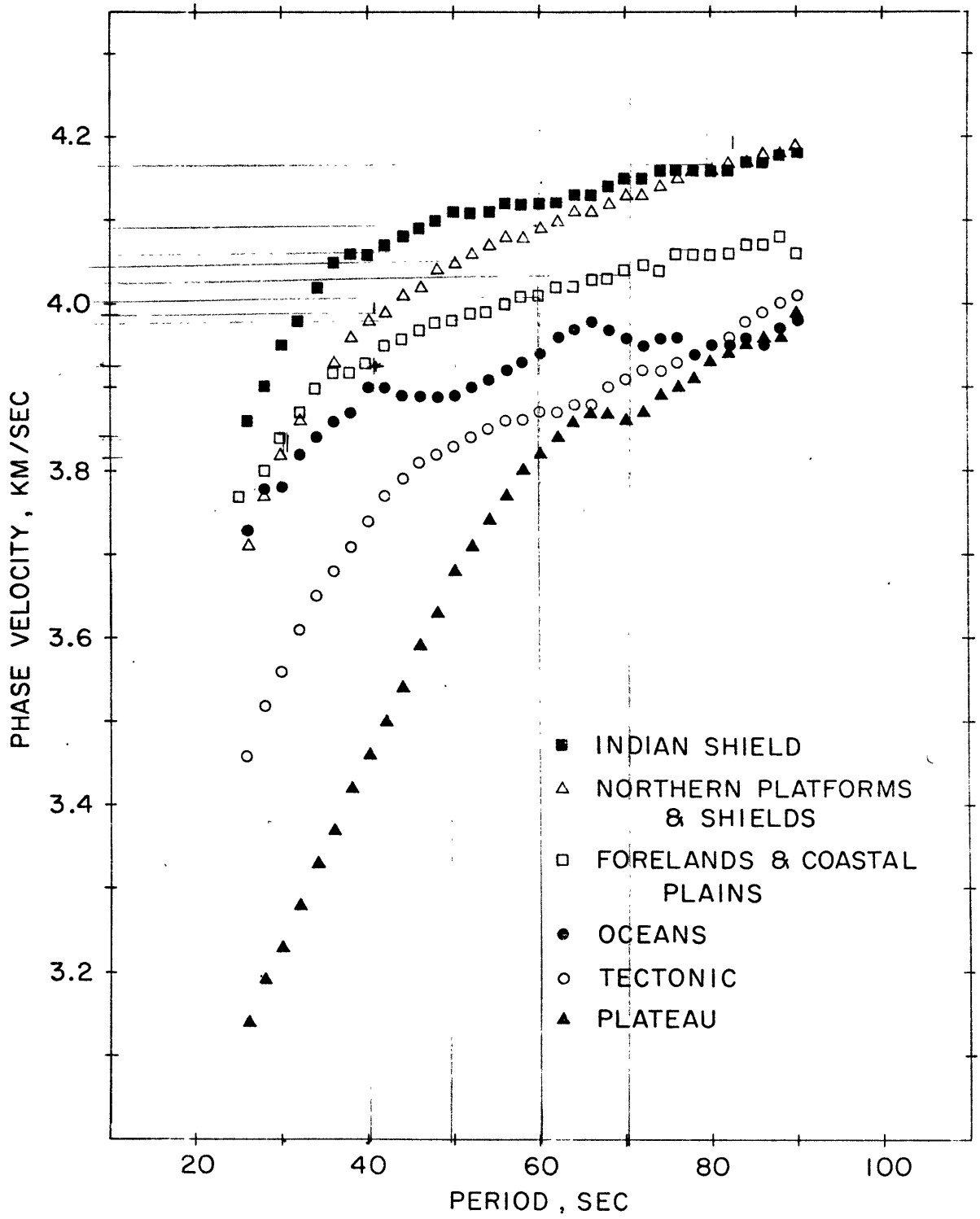

Fig. 5-2.3: Regionalized Rayleigh wave phase velocities.

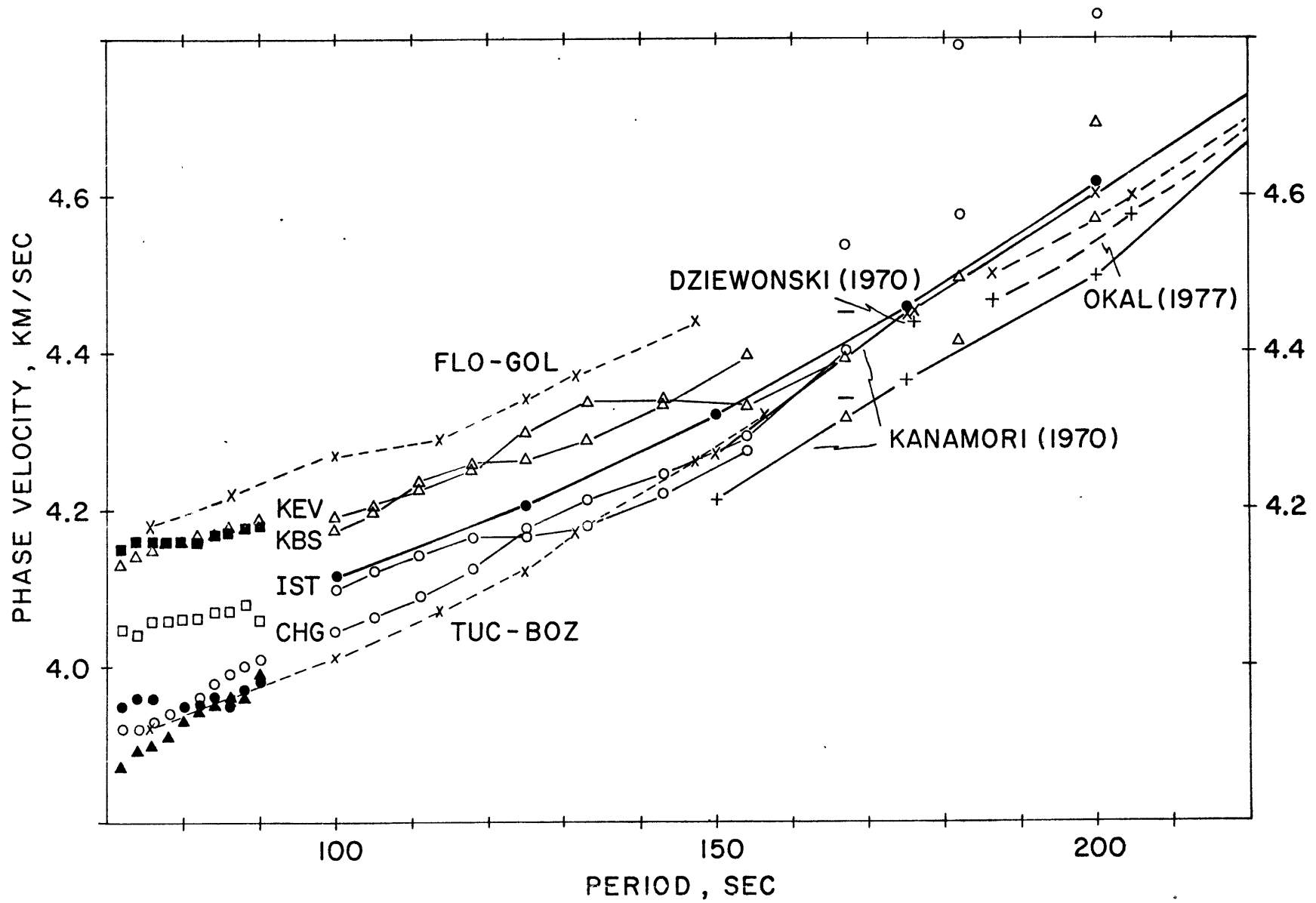

Fig. 5-2.4: Long period Rayleigh wave dispersion. Measurements on profiles FLO-GOL and TUC-BOZ were reported by Biswas and Knopoff (1974). Synthetic curve of Gutenberg model (Table 2-4.1) is shown by (—●—). Horizontal bars at 167sec period indicates range of phase velocity of long period constraint.

The phase velocities are obtained for these four paths via the single station method. The focal phase required by this method was computed using Equation 2-4.1 for the complex source spectrum assuming the source parameters in Table 4-2.6 and a focal depth of 125km. Uncertainty in the focal depth of ±25km was seen to cause less than .03 cycles change in the focal phase.

The results of the phase velocity calculation are plotted in Figure 5-2.4. The reliable measurements are indicated by the points connected with solid lines. The phase velocities for the two northern paths across the Russian Platform are in very close agreement over the period range 100-150sec. The phase velocity curve at station IST appears to be showing systematic differences from CHG at periods shorter than 120sec, but at longer periods they are very close out to 150sec. Thus, the phase velocity curves separate into two groups, one group with stations across the northern platform province and the other with stations in the tectonic provinces of southern Asia. The phase velocities of these groups are about 2% different at 150sec period. At 167sec period, the phase velocities at CHG and KEV are indistinguishable and appear to be in good agreement with the regionalized velocities reported by Dziewonski.

3. INTERPRETATION OF REGIONALIZED PHASE VELOCITIES.

There are major differences in all six regionalized dispersion curves shown in Figure 5-2.3. Lateral variation of crustal

thickness, which was a prime consideration in the regionalization model, is of course responsible for some of these differences. Differences not accounted for by crustal thickness must arise from variations in the structure of the upper mantle. The purpose of this section is to give interpretations of the regionalized phase velocities in terms of the crust and upper mantle structure in each province.

There are two steps taken in this section to arrive at an interpretation. The first step is to compare the regionalized phase velocities with published curves, either observed or theoretical, for other regions. The comparison serves as a guide for making our interpretation. This approach is similar to the interpretation method using "standard curves" (Press, 1956). The limitations of this approach are that a standard curve must exist which satisfactorily fits the observed dispersion and that the matching curve gives an interpretation consistent with imposed constraints.

The second step uses insights gained from the comparisons of standard curves and changes a layered velocity model by trial and error to fit the observed dispersion.

In the trial and error step, we have parameterized the velocity model into the following units; crust, lid, low velocity zone, and base. Except for the crust each unit consists of one homogeneous layer. The depth to the bottom of the base layer is set at 400km below which extends the Gutenberg model as given in Table 2-4.1. Furthermore the bottom of the low velocity zone is

placed at a depth of about 240km. This choice was primarily made to simplify the trial and error fit. At the same time there are many published results (e.g., Monte Carlo inversion of Press (1970)) that show a transition starting about 250km. Also, there have been claims (e.g., Okal, 1977) that below 250km there are no significant differences in the structure between oceans and continents, the implication being that differences between continental regions below this depth are small also. With only the shear velocity of the base layer allowed to vary, we also varied the following parameters in the other units: shear velocity in the lid, β_{lid}, thickness of the lid, h_{lid}, β_{lvz}, and h_{lvz}. In most regions, the parameters of the crustal unit were constrained by the results of the first step, i.e., the comparison with other curves. The fact that the crustal thickness was so constrained and that the base of the low velocity zone was set to 240km meant that the thickness of the lid and low velocity units were not independent but satisfied the following

$$h_{lvz} = 238 - h_{crust} - h_{lid} \qquad (5\text{-}3.1)$$

in kilometers. All of the above considerations of the parameterization simplified the process of the trial and error search and allowed the essential differences between final models of the provinces to be concisely presented.

Constraints were applied to the lid velocity if S_n reportings in the literature were considered applicable to the province

as a whole. All models were required to satisfy the long period dispersion for stable and tectonic regions. Specifically, at 167sec period the phase velocities of all models were required to lie in the range 4.35-4.45km/sec.

Synthetic dispersion curves were computed using the computational technique of Saito (1967) for a spherical earth.

INDIAN SHIELD. In Figure 5-3.1 we compare the Indian Shield dispersion curve with three curves from the literature. The model curve, INDSDS, is from the study of Gabriel and Kuo (1966) and is based on phase velocities observed on northern India, as discussed in the review preceding the regionalization. We find excellent agreement between this curve and our observations for the Indian Shield out to 45sec period. The model, CANSD, obtained by Brune and Dorman (1963) for the Canadian Shield also shows excellent agreement at short period but appears to be too high at long period, although it is not outside the standard deviation of our observations. The last model comes from the study of Bhattacharya (1974) which is based on observations of group velocity of Love and Rayleigh waves. Since a single velocity model could not fit both Love and Rayleigh wave group velocities simultaneously, he proposes an anisotropic model with SV velocity about 5% less than SH velocities in the mantle between depths of 60-160km. The comparison in Figure 5-3.1 shows that the phase velocities predicted by the SV model do not match satisfactorily the observed phase velocities. Our own model, SHIELD-2, is given

in Table 5-3.1 and incorporates the crustal model obtained by Gabriel and Kuo. We constrain the β_{lid} to be 4.72km/sec as imposed by the S_n observations on the Indian Peninsula (Huestis et al., 1973). With a lid thickness of 80km, the same as CANSD, the shear velocity, β_{lvz}, is lower than CANSD by about 0.1km/sec in order to match the phase velocities better over periods 50-90sec period.

NORTHERN PLATFORMS AND SHIELDS. Since large percentages of the paths in this province cross the Russian Platform and the southern portion of the Ural mountains, we give for comparison purposes the short period dispersion curve measured on a profile from Moscow to Sverdlovsk (Savarensky et al., 1969). Although the period range of this comparison is narrow, 26-38sec, there is good agreement as shown in Figure 5-3.1. Comparisons are also shown between two observed curves measured on profiles in the United States: FLO-GOL, as was discussed in the section on long period dispersion, and SHA-LUB across southern United States (Biswas and Knopoff, 1974). Both curves were used by Knopoff (1972) as prime examples of the dispersion in two of his four classifications of continental regions -- shields and aseismic continental regions, respectively. The observed dispersion of stable platforms of Eurasia appears to be closer to the shield classification than the aseismic continent.

The model, PLATFORM-11, is given in Table 5-3.1. The layer parameters in the crust are adopted from Bozhko and Starovoit

(1969). The crust has been thickened from 38km, reported by Bozhko and Starovoit, to 42km because of the contribution of the Urals and the generally thicker crust in other areas. The β_{lid} has been constrained to a value of 4.72km/sec by the observations of Bath (1966) for S_n across the Russian Platform. It should be noted that this value of S_n is the same as that of the Indian Shield. On account of the similarities of the crust in these two provinces there remains just h_{lid} and β_{lvz} to cause differences in the two observed phase velocity curves. The model, PLATFORM-11, has a lid thickness of only 30km, less than half that of SHIELD-2, and shear velocity, β_{lvz}, of 4.55km/sec. With these parameters determined in the lid and low velocity layers, β_{base}, must be less than 4.75km/sec to satisfy the long period constraint.

FORELANDS AND COASTAL PLAINS. For comparison, we show in Figure 5-3.1 two empirical dispersion curves, SHA-LUB, mentioned above, AR (Knopoff and Fouda, 1975), and one synthetic curve based on the Gutenberg model. All of the curves show satisfactory agreement at long periods with the observed dispersion for this province. The disperison on the profile SHA-LUB is low at short periods presumably due to thicker crust under south central United States (Healy and Warren, 1969) approximately 50km, well outside the constraints set by the regionalization. The dispersion, AR, is observed on the Arabian Platform and is seen to be too high at short period. We note also that phase velocity observa-

tions for the North Sea (Stuart, 1978) are also higher at short periods (∿.06km/sec, 26-36sec). Therefore, two parts making up the Forelands and Coastal Plains province are seen to have phase velocities at short period higher than our observed curve. Apparently, other parts, perhaps on the coast of China, have slower phase velocities like that of SHA-LUB. This implies a rather heterogeneous province in so far as the structure affecting short period dispersion, namely crust and lid units. It may not be surprising, therefore, that an "average" continental model such as the Gutenberg model gives the best agreement.

What is characteristic of all the interpretations for these curves is a well developed low velocity zone underlying a high velocity lid (β_{lid}:4.6-4.7km/sec, β_{lvz}:4.3-4.4km/sec). The model PLAINS-6 represents an opposite extreme in terms of these characteristics and is based on the model ASCS-1 given by Rosenthal and Teng (1977) for the South China subplate. In this model, we have adopted the Gutenberg crust and β_{lid} and h_{lid} of 4.5km/sec and 35km, respectively, from model ASCS-1. With β_{lvz} found to be 4.4km/sec the PLAINS-6 model shows a minimum contrast between the lid and low velocity layers that is likely to be found in this province. To meet the long period constraint β_{base} is found to be 4.75km/sec.

TECTONIC PROVINCE. In Figure 5-3.2, empirical phase velocities are shown for profiles TUC-BOZ, GOL-DUG, both in the western United States (Biswas and Knopoff, 1974) and MSH-SHI on the Iranian

Plateau (Canitez and Toksoz, 1977). Both TUC-BOZ and GOL-DUG are mixed paths through the Rocky mountains and the Colorado Plateau, while the synthetic Great Basin curve (Priestley and Brune, 1978) was obtained from phase velocity measurements confined to the Great Basin of Nevada and western Utah. It is apparent that the Great Basin curve does not compare as well as the others. The structure of the Basin and Range obtained by Priestley and Brune shows similarities with structures in rift areas such as the East African Rift. The characteristics of the upper mantle in these areas are thin lid ($\sim$35km) with β_{lid} 4.5km/sec or less, and a low velocity layer with a β_{lvz} of 4.1km/sec extending to depths of about 250km. Based on the better comparison with phase velocities for the paths over mountains and plateaus in western United States, the tectonic provinces of Eurasia may be generally characterized as mountains and plateaus and not as rifts.

The phase velocities of the Iranian Plateau at short period are significantly higher than average velocities in the Tectonic province, as are the phase velocities of the profile TUC-BOZ through western United States. Interestingly, the profile TUC-BOZ samples a much larger portion of the Colorado Plateau than GOL-DUG does (see Figure 2 of Biswas and Knopoff, 1974). These observations suggest that plateau areas have higher phase velocities at short periods than orogenic areas even when crustal thicknesses in these areas are about the same as they appear to be in western United States or southern Eurasia. In the interpretations by Biswas and Knopoff and Canitez and Toksoz, the

crustal units of plateaus are given higher shear velocities than the crustal sections for mountainous areas. For example, Canitez and Toksoz use shear velocities of 3.9km/sec in the lower 28km of the 48km thick crust of the Iranian Plateau. Biswas and Knopoff use velocities of 3.65 and 3.83km/sec for two crustal layers with total thickness of 43km in the interpretation of TUC-BOZ and 3.44 and 3.69km/sec for a total thickness of 45km in the interpretaion of GOL-DUG. These observations have bearing on our discussions of the Plateau province.

Clearly the crustal unit of GOL-DUG is more appropriate for the tectonic province, presumably, due to the number of orogenic belts in Eurasia. In Table 5-3.2 we have incorporated the crustal unit used by Biswas and Knopoff (1974) into our model TECT-6. The value of β_{lid} is 4.55km/sec and h_{lid} is only 35km. The shear velocity, β_{lvz}, is 4.3km/sec. As always without constraints on the S_n, there are trade offs between lid thickness and velocity. An equally acceptable model to the phase velocity data is one in which β_{lid} is 4.45km/sec and h_{lid} is 65km. If we apply the S_n value for the Zagros mountains of 4.65km/sec reported by Bird (1976), a thinner lid ($\sim$5km) than shown for TECT-6 would be called for. In any case, β_{lvz} is about .2km/sec lower than the β_{lvz} of the Northern Platforms and Shields province.

Interestingly, in order to meet the constraint on the long period dispersion, β_{base} of TECT-6 is .2km/sec higher than found for the previous models of stable provinces in Eurasia.

PLATEAU PROVINCE. As discussed in the review given in Section 5-2, studies of surface wave dispersion on the Tibetan plateau, which makes up approximately 60% by area of the Plateau province, have been limited to group velocities. Two of the curves given in Figure 5-3.2 are synthetic curves based on models which fit group velocity data in the literature. The curve, LPB-ARE, is computed from the 70km thick model of the Altiplano proposed by James (1971) from the study of phase velocity dispersion in the Andes mountains region. Also shown is the phase velocity curve of the Pamir model given in Table 3-1.2.

The observed dispersion curve of the Plateau province shows a remarkably uniform drop in the phase velocity over the period range 26-50sec. There is no indication of an upturn in the phase velocities in this range as the curves in the literature have. The slight convex shape of the synthetic curves depends on the period showing a minimum in the group velocity curve. Scatter in the observations of the group velocity (see Bird's Figure 6.4) makes it difficult to locate this minimum. The uniform fall off of the observed phase velocities implies that the group velocity minimum lies at periods shorter than 26sec period which is consistent with the observation of Tung and Teng (1974) but not with those of Chun and Yoshii (1977).

The comparison at longer periods is good for all of the models except for James' which is clearly too low. It should be mentioned that Bird's 55km crustal model (Bird, 1976) fits the observed phase velocities as well as his 70km model shown in Fig-

ure 5-3.2. The success of Bird's proposed models demonstrates a trade off between a thick crust (70km) with high shear velocities in the lower crustal layer (∿3.82km/sec) and a thinner crust (55km) with lower velocities in the crust (∿3.52km/sec). The reason James' model fails is that the crust is thick (70km) and has low velocity (∿3.58km/sec) in the bottom crustal layer. The phase velocity of the Pamir model is too high because the thinner crust (60km) is not compensated by significantly lower velocities in the bottom crustal layer. If we were to choose between the 55km and 70km models, the 70km model would show better consistency with other plateaus, such as the Iranian and Colorado plateaus, because of the higher shear velocities in the 70km thick crust.

Before going on to discuss mantle conditions, the model, PLATEAU-3, as given in Table 5-3.2, shows that the parameters adopted for the crust are the same as those of the Pamir model except that the crustal thickness is 70km. By the excellent comparison this model gives to the observed phase velocities at short period, it appears that a high contrast of shear velocity between the top and bottom crustal layers is an essential feature of PLATEAU-3.

The upper mantle structure of PLATEAU-3 shows little contrast between the lid and the low velocity layers. The shear velocity from the base of the low velocity layer to the base of the crust is essentially a constant between 4.4 and 4.5km/sec. To meet the constraint on the long period dispersion β_{base} must

be 4.9km/sec which is .2km/sec higher than for stable models as was also found for the Tectonic province. Bird's 70km model, which has a layer with velocity 4.26km/sec and thickness 45km immediately below the crust, also satisfies the long period constraint. It offers an interesting contrast to PLATEAU-3, as may be seen in Figure 5-3.3.

OCEAN PROVINCE. We show three curves from the literature in Figure 5-3.2 for comparison with the observed ocean dispersion. The downturn in the velocities at periods shorter than 40sec is more typical of continental dispersion than of oceanic. Therefore we direct our attention to the long periods. The normal ocean basin curve is computed from a model proposed by Weidner (1974) based on Rayleigh wave phase velocity dispersion in the deep ocean basin. These phase velocities are significantly too high. On the other hand, Weidner's observations of phase velocities on the mid-ocean rift are too low at long period. The regionalized phase velocities of Forsyth (1975) for the 0-10m.y. age zone shows good comparison only at long period. Thus, the oceanic province is a combination of young ocean floor and deep ocean basin, probably having a higher percentage of the former than the latter.

SUMMARY. The shear velocity structures of the five continental provinces in Eurasia are plotted in Figure 5-3.4. As mentioned before, our parameterization is very idealized, but does facilitate comparison. We make some comments about the comparison

below.

The difference in lithosphere thickness of the Northern Platforms and the Indian Shield provinces is surprising. The thickness of the Indian Shield lithosphere is typical of other shield areas, while the thickness of platform's lithosphere is unusually thin. This contrast has interesting implications in regard to the indenter hypothesis proposed by Molnar and Tapponnier (1975). Since the lithosphere is the strong portion of the plates, a thick lithosphere under India compared to that of the Eurasian plate may partially explain why Asia underwent massive upheaval while India remained intact.

The low velocity zone under the Indian Shield appears to be better developed than under the Northern Platforms province. This comparison may be relevant in regard to the mobility of the Indian and Eurasian plates since the asthenosphere is a zone of low strength through which the plates move and resistance of the plates' motion may be greater in a higher velocity, presumably, less ductile asthenosphere. The Tectonic province has the lowest shear velocity in the channel of all models shown in Figure 5-3.4. Possible velocity structures of the Coastal Plains province can have equally low velocities in the channel provided β_{lid} is higher.

An interesting comparison between the structures of the stable and tectonic province is β_{base} which is higher by about .2km/sec in tectonic provinces. Dziewonski (1971) finds a similar result in models of shield and tectonic provinces obtained

from interpretations of regionalized long period phase velocities. Specifically, over depths 200-380km, his model T1 shows shear velocity of 4.83km/sec as compared to 4.67km/sec over 240-380km in model S2 for shields. Below 400km the two models were virtually the same. These velocities correspond well to β_{base} of 4.9km/sec and 4.7-4.75km/sec in models of tectonic and stable provinces, respectively.

It is important to consider the non-uniqueness of these results. The comparison of Bird's 70km crust model and Plateau-3 in Figure 5-3.3 illustrates that relaxing the constraint on the base of the low velocity zone, for example, can change the interpretations. Our good comparison with previous results, mentioned above, is in part fortuitous because layer interfaces happen to be chosen in both studies at about 250km. In short, our observed contrast between β_{base} in stable and tectonic provinces does not exclude the possibility of very similar structures at depths below 250km provided that compensations are made at other depths. These compensations may include introducing higher velocity material at shallower depths in tectonic provinces as Bird has done in the model in Figure 5-3.3.

A notable difference between the models in Figure 5-3.3 is the value of S_n velocity. Since S_n does not propagate across the Tibetan Plateau (Molnar and Oliver, 1969), there are no independent estimates of its velocity. Bird proposes low S_n velocities and the existence of a large percentage of partial melt at the base of the crust. The latter is supported by Bird's observa-

TABLE 5-3.1: MEDIUM MODELS OF STABLE EURASIAN PROVINCES

SHIELD - 2

h, km	ρ, g/cm^3	α, km/sec	β, km/sec
0.7	2.30	3.40	1.80
8.0	2.70	5.64	3.47
10.5	2.80	6.15	3.64
18.8	2.85	6.60	3.85
80.0	3.30	8.10	4.72
120.0	3.44	8.20	4.45
162.0	3.56	8.50	4.75

PLATFORM - 11

h, km	ρ, g/cm^3	α, km/sec	β, km/sec
4.0	2.20	4.00	2.00
17.0	2.70	6.00	3.45
21.0	2.90	6.80	3.95
31.0	3.45	8.17	4.72
165.0	3.52	8.40	4.55
162.0	3.56	8.50	4.70

PLAINS - 6

h, km	ρ, g/cm^3	α, km/sec	β, km/sec
19.0	2.74	6.14	3.55
19.0	3.00	6.58	3.80
35.0	3.34	8.17	4.50
165.0	3.41	8.07	4.40
162.0	3.56	8.50	4.75

TABLE 5-3.2: MEDIUM MODELS OF TECTONIC EURASIAN PROVINCES

TECTONIC - 6

h, km	ρ, g/cm^3	α, km/sec	β, km/sec
1.5	2.20	4.00	2.00
1.5	2.41	5.00	2.85
10.0	2.61	5.60	3.43
17.0	2.62	5.65	3.45
18.0	2.97	6.70	3.69
35.0	3.36	7.90	4.55
155.0	3.41	8.07	4.30
162.0	3.56	8.50	4.90

PLATEAU - 3

h, km	ρ, g/cm^3	α, km/sec	β, km/sec
4.0	2.41	4.41	2.55
26.0	2.66	5.50	3.18
40.0	2.90	6.50	3.76
55.0	3.36	7.90	4.45
113.0	3.41	8.07	4.40
162.0	3.56	8.50	4.90

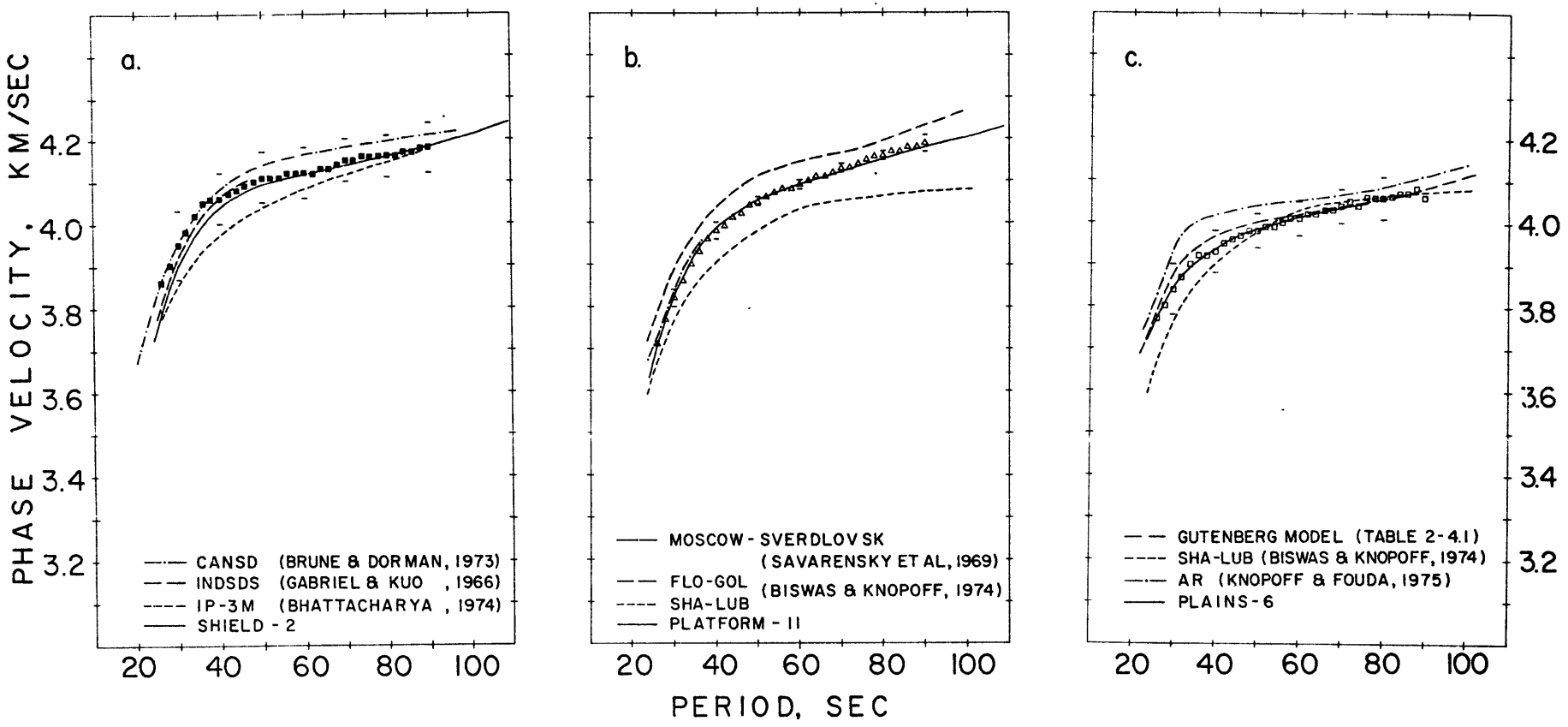

Fig. 5-3.1: Comparison of published phase velocity curves with regionalized phase velocities of stable provinces. a.) Indian Shield province, b.) Northern Platforms and Shields province, c.) Forelands and Coastal Plains province. Error bar represents one standard deviation in the calculation of phase velocity.

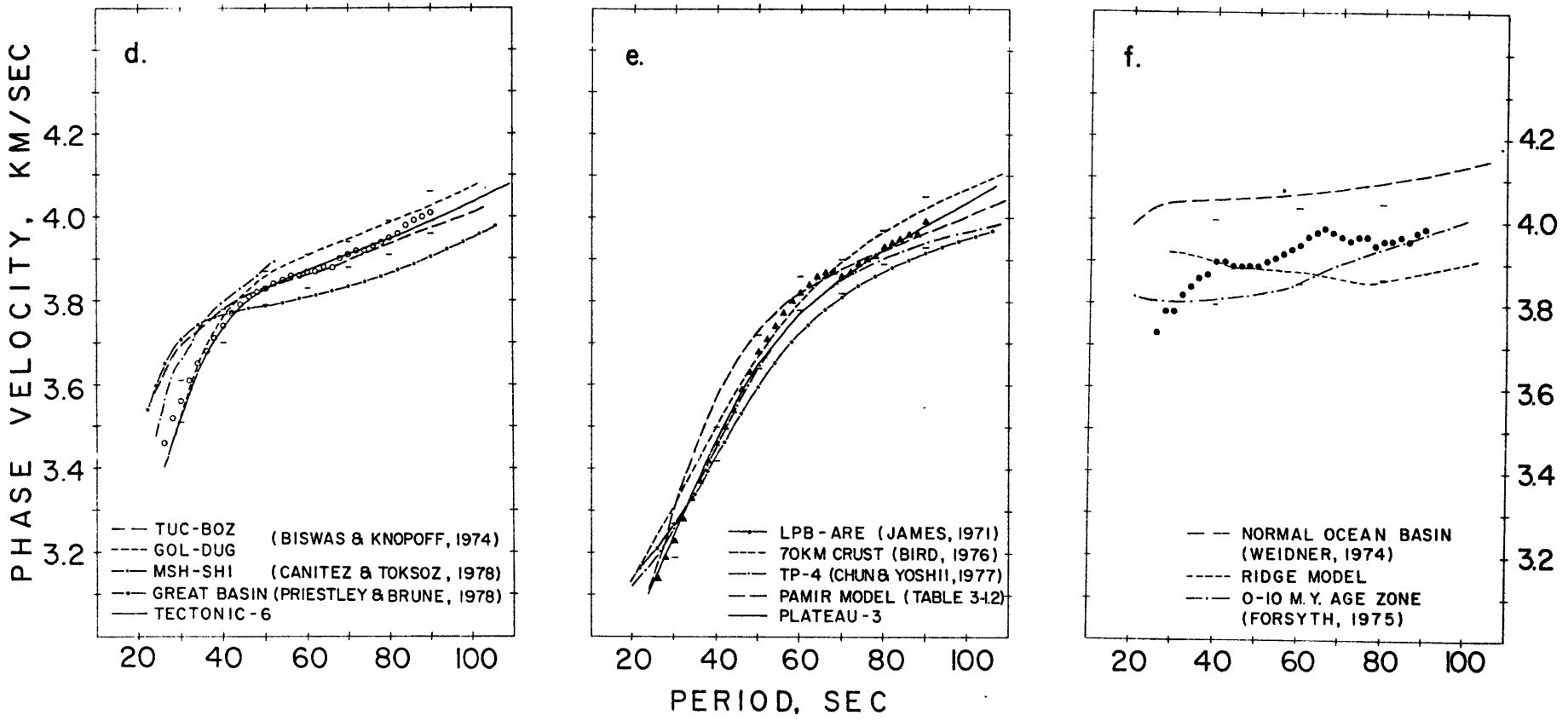

Fig. 5-3.2: Same as Figure 5-3.1 but for tectonic provinces. d.) Tectonic province, e.) Plateau province, f.) Ocean province.

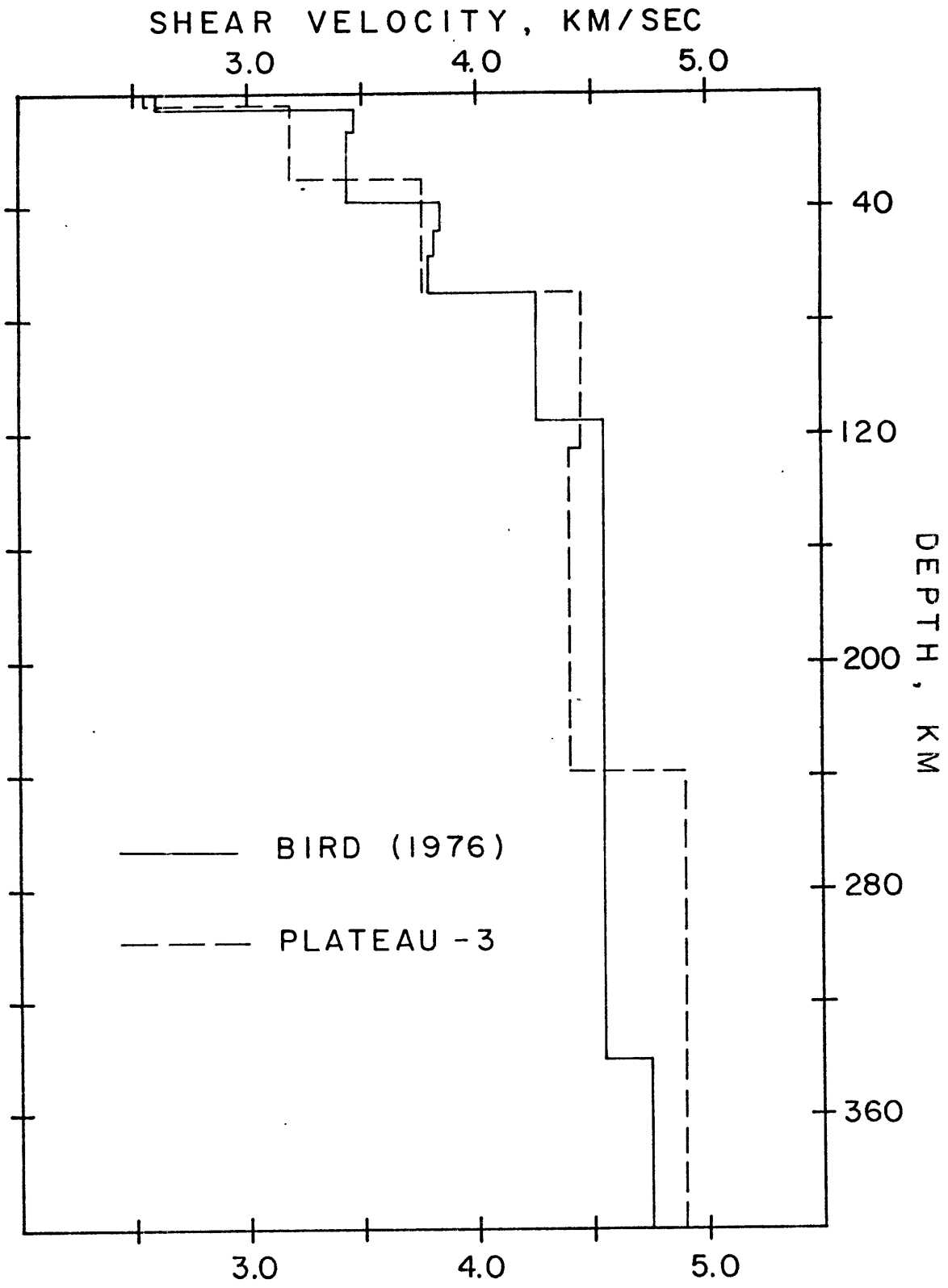

Fig. 5-3.3: Comparison of models of shear velocity structure of plateaus.

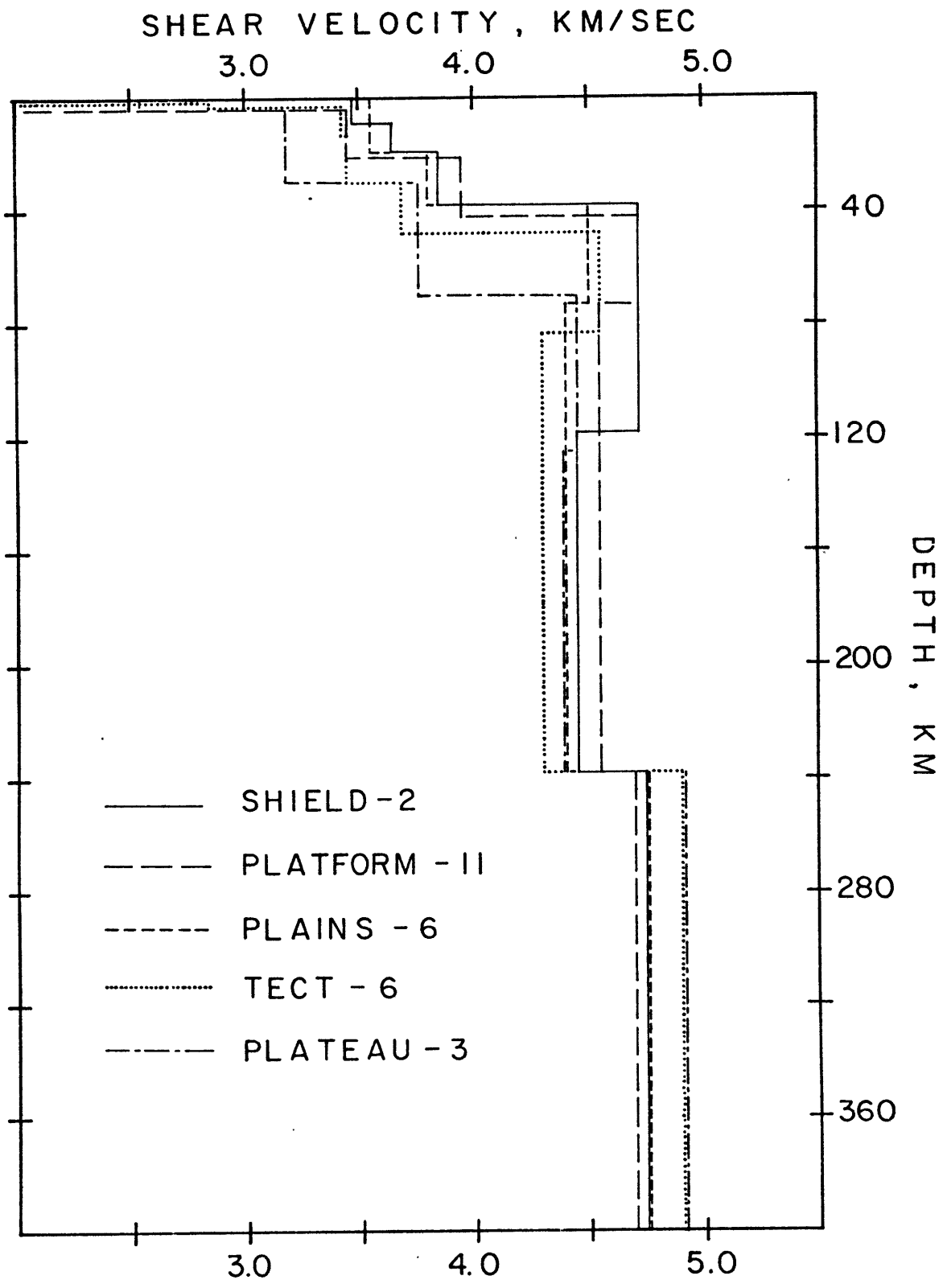

Fig. 5-3.4: Models of shear velocity structure of Eurasian provinces.

tions of strong attenuation of 40-50sec Rayleigh waves over Tibet. In this study we do not find supporting evidence of strong attenuation at these periods on paths over the Tibetan Plateau. This is obvious from the azimuthal plots of attenuation coefficient and phase velocity in Figure 4-3.2 and from plots of attenuation coefficients for stations in southeast Asia (Figure C-14) and in the Far-East (Figure C-15) in Appendix C. In the next section we discuss factors that may be responsible for very low apparent attenuation at long periods on these tectonic paths. In any case, it is interesting to note the similarity of the upper mantle structure of Plateau-3 and the model proposed by James (1971) for the upper mantle under the Altiplano (see Figure 22 in that paper).

4. SURFACE WAVE AMPLITUDE ON EURASIA: EFFECTS OF Q AND HORIZONTAL REFRACTION

The azimuthal variation of surface wave amplitudes reflected in the estimates of attenuation coefficients in Figure 4-3.2 shows strong regional effects. These effects are in general correlated with changes in the apparent phase velocity. For example, the drop in phase velocities over azimuths 290-220^{o} is accompanied by an increase in apparent attenuation, especially at short periods. This is an expected correlation for these propagation effects considering that the lower velocity is, the lower Q may be as in the western United States (Lee and Solomon, 1975).

On other azimuths, however, the sense of change is not as expected. For example, over Tibet where attenuation has been reported to be high in the frequency range .02-.03Hz (Bird, 1976), we observe at 50sec period low velocities but very small, if not negative attenuation coefficients. Along paths east of the reference point, phase velocity is seen to increase over southern to northern China at the same time attenuation also increases. Stations in India record the highest phase velocities in southern Asia and also the highest apparent attenuation. These observations suggest that other factors enter in determining the amplitudes of surface waves in and around the Eurasian continent. We discuss one of these factors, horizontal refraction, in the following sub-section.

HORIZONTAL REFRACTION. McGarr (1969) studied horizontal refraction of surface waves caused by lateral heterogeneities of phase velocity along the wave path. His study is restricted to 20sec period Rayleigh waves over lengthy oceanic paths. Amplitude fluctuations across stations on the coast of western United States were shown to be due to effects of lateral variation of phase velocity causing focusing and defocusing of rays. With the range of phase velocities observed over different paths in Eurasia, serious consideration should be given to lateral refraction of surface waves as a possible interpretation of the amplitude variations.

Although modeling amplitude variations could be very valu-

able in the study of earth structure, the inverse problem of going from a set of amplitude observations to a model of velocity variations is formidable. Here we shall limit ourselves to the forward problem, which is to propose a model of a lateral heterogeneous medium, trace rays through the medium, and compute the amplitudes from the pattern of rays at the observation point.

This is the approach taken by North (1975) and North and Patton (1975). In these studies, the following considerations were made to arrive at a model of lateral variations of phase velocity in Eurasia of finer scale than adopted in the regionalization of phase velocities in Section 2:

a) Lateral variation of crustal thickness; estimates of crustal thickness were obtained from the sources mentioned in Section 5-2.

b) Lateral variation of upper mantle structure; the landforms on and surrounding Eurasia were classified as either shield, platform, foldbelt, or ocean. The upper mantle structure was assumed to conform to Knopoff's (1972) generalization.

c) By a) and b) phase velocities were computed (North, 1975) on a $2^{o}X2^{o}$ grid in latitude and longitude which specified the lateral heterogeneous medium to the computer program that did the ray tracing (Julian, 1970).

In the method of ray tracing cubic splines were used to interpolate the phase velocity and its spacial derivatives between grid points.

The results of the ray tracing at 40sec period is given in Figure 5-4.1. Rays are shot at 5^{o} intervals of azimuth from a source which is very close to the location of the reference point. Although it is not advisable to consider details of the ray pattern reliable as they will change with small changes in the model and location of the source, the broad features are considered to be reliable for qualitative discussion.

The ray pattern east of the source shows the largest departure from the pattern of geometric spreading on a homogeneous sphere, which on this projection would have appeared as straight lines emanating from the source. A gap in the ray pattern implies reduction of ray density, i.e., defocusing, a closure of rays, focusing, and crossing rays implies multipathing. A large gap between azimuths 60 and 90^{o} shows an area of defocusing the source of which is a rapid velocity transition between the Tarim Basin (high velocity) and the Tien Shan and Kun Lun fold belts (low velocity) north and south of the basin, respectively. Focusing occurs on azimuths between 100 and 110^{o}, and in general high ray density is found for azimuths in southeast Asia.

This model predicts lower amplitudes in northern China than in southern China or southeast Asia. The phase velocities which this model predicts (North and Patton, 1975) are higher in the north than in the south. This is qualitatively the variation that is seen in our measurements of attenuation and phase velocity for stations across China and southeast Asia. We might mention that defocusing is mildly suggested by the ray paths south

of the source. Other features of the ray tracing are strong focusing effects caused by low velocities in the Hindu Kush (225-240^{o} azimuth). This gives high amplitudes and perhaps multipathing at NAI, which, recalling results in Chapter 4, was a troublesome station along with AAE due to phase shifts. There is suggestion of lateral refraction causing defocusing in azimuths to Europe and focusing in Scandinavia, but these features and others are mild.

INTRINSIC ATTENUATION. It is apparent that the effects of intrinsic attenuation on amplitudes of surface waves may be masked by the strong effect of lateral refraction. It is important to try to remove or at least minimize the effects of lateral refraction before the interpretation of attenuation data in terms of intrinsic Q. The method of Tsai and Aki (1969) used in Section 4-1 to obtain average Eurasian Q minimizes the effects of lateral refraction because fluctuations in lnA will tend to distribute evenly above and below the average obtained from the slope of the least squares fit. As was shown in Section 4-1 our estimates of average Q are consistent with those obtained by Burton (1974) from Lop Nor nuclear explosions. This increases our confidence in these measurements. Unfortunately, this method is not amenable to obtaining regional Q estimates nor have modifications to do so (Mitchell, 1975) detected regional Q differences between stable and tectonic provinces in Eurasia (Yacoub and Mitchell, 1977).

We attempt to estimate regional attenuation for stable and tectonic provinces in Eurasia by averaging lnA, i.e., η, over a number of stations in a selected azimuthal window. Averaging lnA over azimuth will minimize the effects of lateral refraction provided the window is large enough to sample adequately local variations in the ray density. The size of the window is restricted so that paths are homogeneous in a regionalization sense. For example, we selected stations KEV, NUR, KON and COP to obtain an estimate of Q on the northern platforms. Similarly, we average over stations TAB, JER, MSH, SHI to estimate Q in the tectonic province west of the reference point, and over HKC, ANP, SHK and MAT to estimate Q in the tectonic provinces east of the reference point. We show the station Q observations and the computed average Q for the three datasets in Figure 5-4.2. The variation of the individual values is a measure of the wide fluctuation of the surface wave amplitudes in each dataset.

Comparison of the averages suggests that the Q structures of the stable and tectonic regions are distinctly different. Interestingly, a common feature of all averages is an increasing Q at long periods as was observed for the average Q values obtained by Burton (1974) and by this study.

With the observed Q, we have plotted synthetic curves based on simple models shown in Figure 5-4.3. We have computed the Rayleigh wave Q from the intrinsic Q of the layers in the models using the result of Anderson and Archambeau (1964) and assuming the medium is a Poisson solid with no loss due to compressability

(Anderson et al., 1965). The partial derivatives used in computing the synthetic curves are from velocity models PLATFORM-11 and TECT-6 for the platform and tectonic datasets, respectively.

Considering first the platform dataset, model PLATF-1 is very similar to model MM8 proposed by Anderson et al. (1965). This model features a low Q layer approximately 30km thick immediately below the crust. It is apparent that increasing the Q of this layer from 60 to 500 as we have done in model PLATF-2 considerably improves the fit to the average Q of this dataset. Further improvements can be made by increasing the Q of deeper layers as we show in models in PLATF-3 and -4. As implied by model PLATF-4, no low Q layer in the upper mantle is required by this dataset. Indeed the best fit is obtained by model PLATF-5 for which Q increases with depth.

Model WEST-1, which is similar to MM8, shows a peak at frequencies between .02-.025Hz and does not match the average Q of the western dataset. This is also true of model WEST-2 which has a Q of 30 instead of 60 in the layer below the crust. A model similar to WEST-2 has been proposed by Canitez and Toksoz (1977) to explain the observed Q over the Iranian Plateau. The paths in the western dataset sample a larger region than the Iranian Plateau and the shape of the average Q suggests that a low Q layer must be placed shallower than in models WEST-1 or -2. We see improvement by lowering the Q in the bottom 20km of the 48km crust of TECT-6. Models WEST-3 and -4 demonstrate the shift in the peak of the Rayleigh wave Q to higher frequency as Q is lowered

in the base of the crust. Finally model WEST-5 suggests that Q may increase at shallow depths (>100km) to account for the steep increase in the average Q at low frequencies.

The eastern dataset has an average Q over .02-.04Hz which is similar to that of the western United States except for lower Q at ∿.04Hz. The model MM8 designated here as EAST-1 compares well with observations over much of the frequency range. The peak in the observed Q is matched better by a shallow low Q layer than a broad low Q layer under the crust as comparison between models EAST-1 and -2 shows. Models East-3 and -4 show that typical Q models of western and eastern United States as proposed by Lee and Solomon (1975) compare satifactorily at frequencies less than .025Hz. These models feature high Q in the lithosphere (100-500) and low Q in the asthenosphere (25-50). A model like EAST-1 but with high Q in the lithosphere (see EAST-5) does not fit the eastern dataset as may be seen in Figure 5-4.2.

SUMMARY. We obtained three very different average Q curves for platform, western, and eastern paths across Eurasia. These Q are obtained by averaging the apparent Q on paths to individual stations in order to minimize effects of lateral refraction. For platforms, we find that a Q structure increasing monotonically with depth in the crust and upper mantle gives the best comparison with the observed Q curve. In the crust Q is between 200-300 and between 300-500 in the lid and low velocity layers of the model PLATFORM-11. In the tectonic province west of the refer-

ence point, low Q, ∿60, is found in the bottom 20km of the crust and extends ∿35km into the mantle. High Q (>150) in the asthenosphere of TECT-6 is suggested by the steep increase of Rayleigh wave Q at long periods. East of the reference point a low Q layer is concentrated at the base of the 48km crust in the TECT-6 model. Specifically, Q is ∿60 in the lid when Q in the crust is ∿450. The high Q at long periods suggests that a low Q zone is not associated with a low velocity layer of the model TECT-6.

In southern Asia both east and west of the reference point, there is indication of low Q in the lid of model TECT-6 and of Q increasing below the lid in the asthenosphere. It should be noted that the east-west paths cross several provinces where phase velocities are known to be quite different. No doubt Q varies along these paths also. If we consider a path through two homogeneous regions, one with Q 10 and the other with Q 1000, the apparent Q assuming path lengths are equal in each region, would be about 20. To obtain an apparent Q of about 100, the path length through the low Q region need only be ∿9% of the total path length. This suggests that we need to have finer regionalization of Q before making close comparisons of the Q structures with the velocity structures obtained in Section 5-3.

Nevertheless we might speculate about the implications of the Q on the velocity structures, particularly TECT-6. In examining the nonuniqueness of this model, we found that an equally acceptable model to the phase velocities has a thin lid (∿5km)

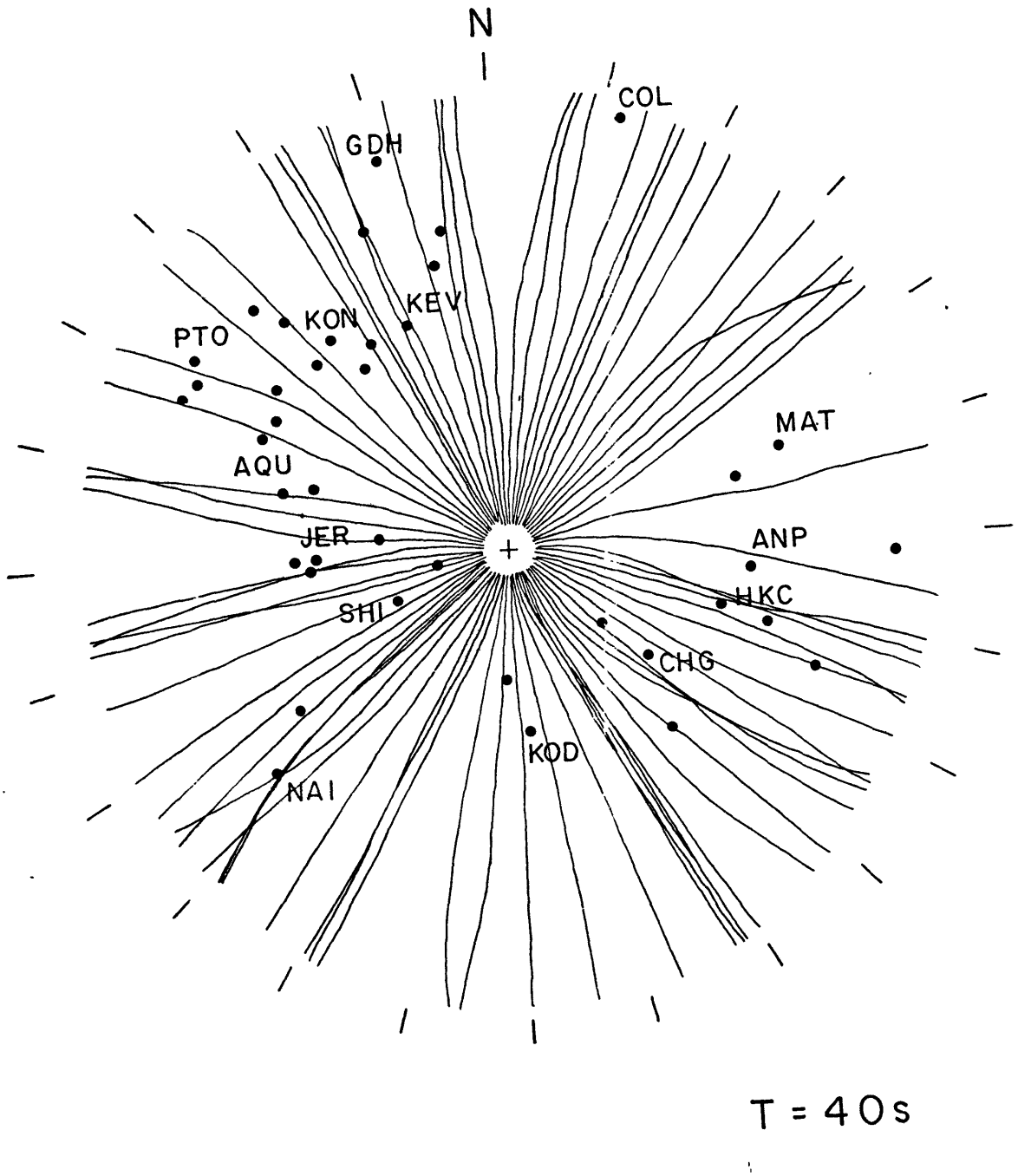

Fig. 5-4.1: Ray paths of 40sec period Rayleigh waves obtained from synthetic ray tracing experiment discussed in the text. Rays leave source (+) at 5° intervals of azimuth. Tick marks are given at 15° intervals.

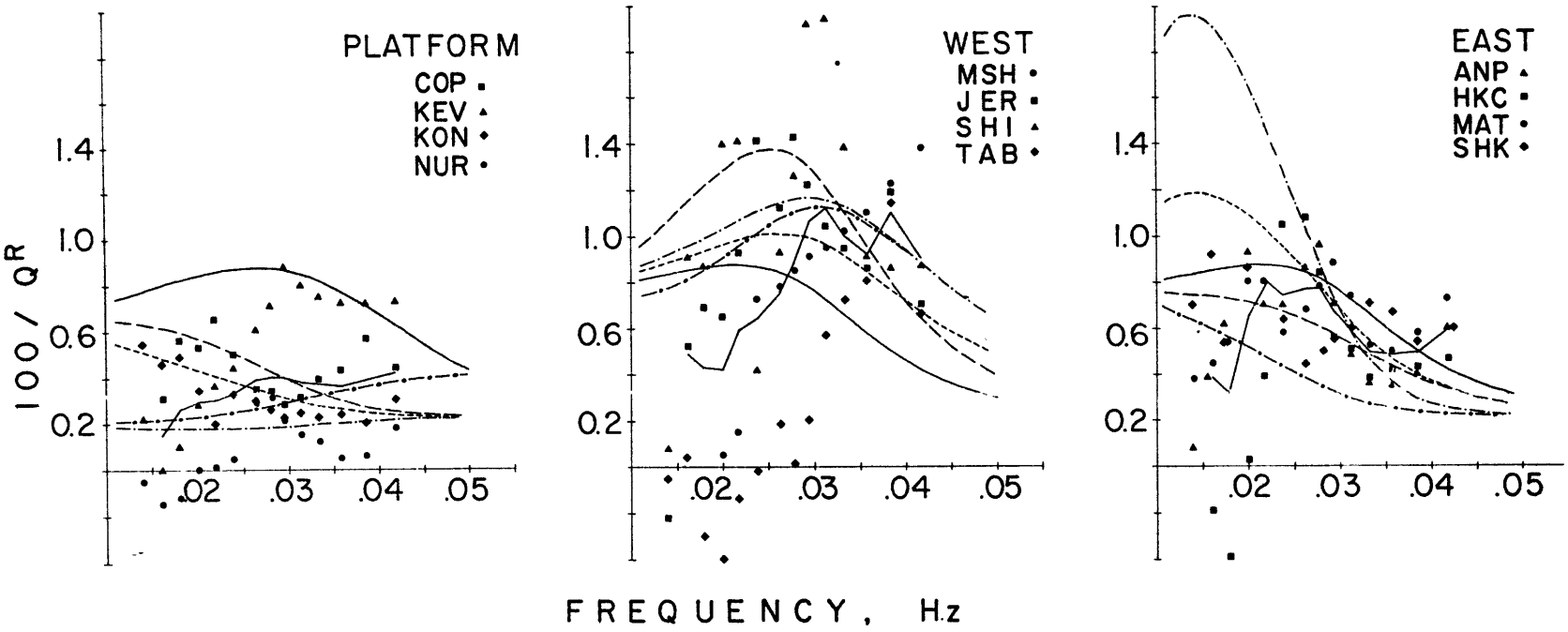

Fig. 5-4.2: Observed Rayleigh wave Q for paths on platforms, west and east of the reference point. Average Q shown by (——). Synthetic curves are for models in Figure 5-4.3. Line definition is by model number: 1 (———), 2 (— — —), 3 (- - - -), 4 (— · — ·), 5 (—o—o).

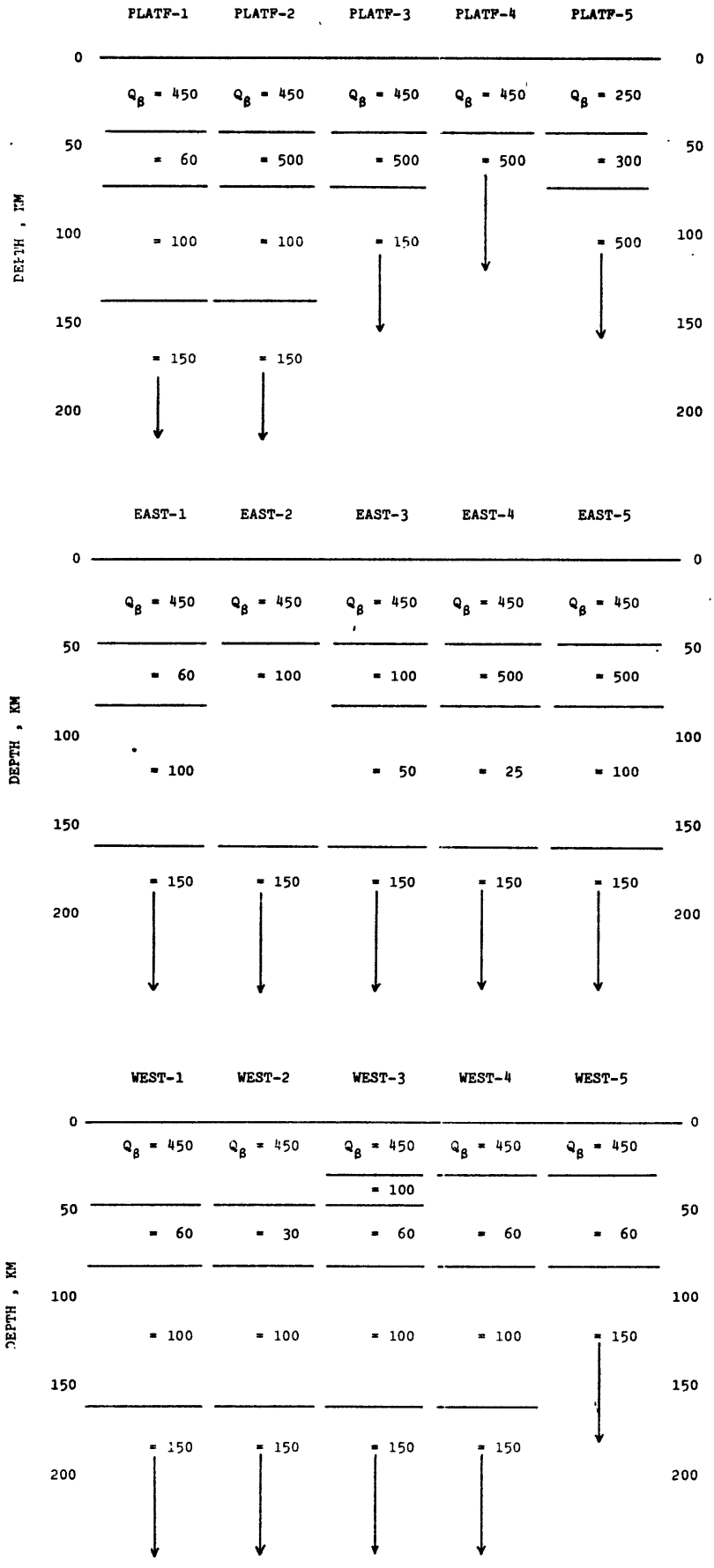

Fig. 5-4.3: Models of Q_β structure giving synthetic curves in Figure 5-4.2.

and high S_n velocity ($\sim$4.65km/sec). A thin lid may be supported by the low Q at the base of the crust in models EAST-1 and WEST-5. Increasing Q at the depths of the low velocity layer of model TECT-6 suggests that the asthenosphere does not extend very deep. Relaxing the constraint on the position of the base of the low velocity layer would permit us to distribute more evenly at shallower depths the high shear velocity in the base layer of this model. In short, the asthenosphere of tectonic provinces of southern Asia may lie at shallow depths under a thin lid with a broad transition zone extending below it.

We speculate that the reason for this could be tied to the tectonic history of this area. With the closing of the Tethys Sea, ocean floor was subducted under the Eurasian plate. This could have cooled the mantle raising its Q and contaminated the mantle with high velocity material. The lithosphere under southern Asia could have been thinned by shear heating due to eddy currents induced in the upper layers of the asthenosphere by the down going slab.

5. FUTURE PROBLEMS

In closing we take this opportunity to mention several possible topics of future research:

a) Reference point movement; establishing more reference points in Eurasia will aid in the study of its structure and tectonics.

b) Q regionalization; more Q data is needed before we look at greater details of its lateral variations under Eurasia.

c) Long period dispersion; very long period phase velocity measurements using the single station method would lead to improved regionalizations to study the structure of the mantle.

BIBLIOGRAPHY

Aki, K., The use of Love waves for the study of earthquake mechanism, J. Geophys. Res., 65, 323-331, 1960a.

Aki, K., Study of earthquake mechanism by a method of phase equalization applied to Rayleigh and Love waves, J. Geophys. Res., 65, 729-740, 1960b.

Aki, K., Interpretation of source functions of circum-Pacific earthquakes obtained from long-period Rayleigh waves, J. Geophys. Res., 65, 2405-2417, 1960c.

Aki, K., Further study of the mechanism of circum-Pacific earthquakes from Rayleigh waves, J. Geophys. Res., 65, 4165-4172, 1960d.

Aki, K., Crustal structure in Japan from the phase velocity of Rayleigh waves, Bull. Earthq. Res. Inst. Tokyo Univ., 39, 255-283, 1961.

Aki, K., Study of Love and Rayleigh waves from earthquakes with fault plane solutions or with known faulting Part I. A phase difference method based on a new model of earthquake source, Bull. Seismol. Soc. Amer., 54, 511-527, 1964.

Aki, K., Generation and propagation of G waves from the Niigata earthquake of June 16, 1964. Part 2. Estimation of earthquake moment, released energy, and stress-strain drop from the G wave spectrum, Bull. Earthq. Res. Inst. Tokyo Univ., 44, 73-88, 1966.

Aki, K., Scaling law of seismic spectrum, J. Geophys. Res., 72, 1217-1231, 1967.

Aki, K., Scaling law of earthquake source time-function, Geophys. J.R. Astr. Soc., 31, 3-25, 1972.

Aki, K. and K. Kaminuma, Phase velocity of Love waves in Japan. Part 1. Love waves from the Aleutian shock of March 9, 1957, Bull. Earthq. Res. Inst. Tokyo Univ., 41, 243-259, 1963.

Aki, K., J. Mendiguren, and Y-B Tsai, Reply to criticism of A. McGarr, J. Geophys. Res., 77, 3827-3830, 1972.

Anderson, D. and C. Archambeau, The anelasticity of the earth, J. Geophys. Res., 69, 2071-2084, 1964.

Anderson, D., A. Ben-Menahem, and C. Archambeau, Attenuation of seismic energy in the upper mantle, J. Geophys. Res., 70, 1441-1448, 1965.

Andrews, D.F., A robust method for multiple linear regression, Technometrics, 16, 523-531, 1974.

Arkhangel'skaya, V. and I. Kuznetsova, Study of the upper portions of the earth's crust in central Asia from dispersion of surface waves, Izv., Earth Physics, 5, 61-65, 1969.

Bath, M., Propagation of S_n and P_n to teleseismic distances, Pure Appl. Geophys., 64, 19-30, 1966.

Belyaevsky, N., A. Borisov, V. Fedynsky, E. Fotiadi, S. Subbotin, and I. Volvovsky, Structure of the earth's crust on the territory of the U.S.S.R., Tectonophysics, 20, 35-45, 1973.

Ben-Menahem, A., Radiation of seismic surface waves from finite moving sources, Bull. Seismol. Soc. Amer., 51, 401-435, 1961.

Ben-Menahem, A. and M.N. Toksoz, Source mechanism from spectra of long period seismic surface-waves 1. Mongolian earthquake of Dec. 4, 1957, J. Geophys. Res., 67, 1943-1955, 1962.

Ben-Menahem, A. and M.N. Toksoz, Source mechanism from spectrums of long-period surface waves 2. The Kamchatka earthquake of Nov. 4, 1952, J. Geophys. Res., 68, 5207-5222, 1963a.

Ben-Menahem, A. and M.N. Toksoz, Source mechanism from spectra of long period seismic surface waves 3. The Alaska earthquake of July 10, 1958, Bull. Seismol. Soc. Amer., 53, 905-919, 1963b.

Berry, M.J. and L. Knopoff, Structure of the upper mantle under the western Mediterranean Basin, J. Geophys. Res., 72, 3613-3626, 1967.

Bhattacharya, S., The crust-mantle structure of the Indian Peninsula from surface wave dispersion, Geophys. J.R. Astr. Soc., 36, 273-283, 1974.

Bird, G.P., Thermal and mechanical evolution of continental convergence zones: Zagros and Himalayas, Ph.D. thesis 422pp., Mass. Inst. of Technol., Cambridge, Ma., 1976.

Biswas, N.N. and L. Knopoff, The structure of the upper mantle under the United States from the dispersion of Rayleigh waves, Geophys. J.R. Astr. Soc., 36, 515-539, 1974.

Bozhko, G.N. and O.E. Starovoit, Phase velocities of Rayleigh waves on the Russian platform, in Proceedings of the Eighth Assembly of the European Seismological Commission, edited by E. Bisztricsany, Budapest, 339-343, 1969.

Brune, J.N. and J. Dorman, Seismic waves and earth structure of the Canadian Shield, Bull. Seismol. Soc. Amer., 53, 167-210, 1963.

Brune, J.N., J.E. Nafe, and J.E. Oliver, A simplified method for the analysis and synthesis of dispersed wave trains, J. Geophys. Res., 65, 287-304, 1960.

Brune, J.N. and P.W. Pomeroy, Surface wave radiation patterns for under-ground nuclear explosions and small-magnitude earthquakes, J. Geophys. Res., 68, 5005-5028, 1963.

Buland, R. and F. Gilbert, Matched filtering for the seismic moment tensor, preprint, 1976.

Bungum, H. and J. Capon, Coda pattern and multipath propagation of Rayleigh waves at NORSAR, Phys. Earth Planet. Interiors, 9, 111-127, 1974.

Burton, P., Estimates of Q^{-1} from seismic Rayleigh waves, Geophys. J.R. Astr. Soc., 36, 167-189, 1974.

Canitez, N. and M.N. Toksoz, Rayleigh wave propagation and structure of the Iranian Plateau, preprint, 1977.

Capon, J., Analysis of Rayleigh-wave multipath propagation at LASA, Bull. Seismol. Soc. Amer., 60, 1701-1731, 1970.

Chatterjee, S.N., On the dispersion of Love waves and crust-mantle structure in the Gangetic Basin, Geophys. J.R. Astr. Soc., 23, 129-138, 1971.

Chen, W.P. and P. Molnar, Short period Rayleigh wave dispersion across the Tibetan Plateau, Bull. Seismol. Soc. Amer., 65, 1051-1057, 1975.

Chouet, B., K. Aki, and M. Tsujiura, Regional variation of the scaling law of earthquake source spectra, Bull. Seismol. Soc. Amer., preprint, 1977.

Chun, K.Y. and T. Yoshii, Crustal structure of the Tibetan Plateau: A surface wave study by a moving window analysis, Bull. Seismol. Soc. Amer., 67, 735-750, 1977.

Claerbout, J.F., Fundamentals of Geophysical Data Processing, McGraw-Hill, San Francisco, Cal., 113 pp, 1976.

Claerbout, J.F. and F. Muir, Robust modeling with erratic data, Geophysics, 38, 826-844, 1973.

Crampin, S., Higher modes of seismic surface waves: Phase velocities across Scandinavia, J. Geophys. Res., 69, 4801-4811, 1964.

Crampin, S., High modes of seismic surface waves: Propagation in Eurasia, Bull. Seismol. Soc. Amer., 56, 1227-1239, 1966.

Dewey, J. and J. Bird, Mountain belts and the new global tectonics, J. Geophys. Res., 75, 2625-2647, 1970.

Dziewonski, A.M., On regional differences in dispersion of mantle Rayleigh waves, Geophys. J.R. Astr. Soc., 22, 289-325, 1970.

Dziewonski, A.M., Upper mantle models from 'Pure-Path' dispersion data, J. Geophys. Res., 76, 2587-2601, 1971.

Dziewonski, A.M. and F. Gilbert, Temporal variation of the seismic moment tensor and the evidence of precursive compression for two deep earthquakes, Nature, 247, 185-188, 1974.

Ewing, M. and F. Press, Determination of crustal structure from phase velocity of Rayleigh waves Part III. The United States, Bull. Geol. Soc. Amer., 70, 229-244, 1959.

Forsyth, D.W., The early structural evolution and anisotropy of the oceanic upper mantle, Geophys. J.R. Astr. Soc., 43, 103-162, 1975.

Forsyth, D.W., Higher-mode Rayleigh waves as an aid to seismic discrimination, Bull. Seismol. Soc. Amer., 66, 827-841, 1976.

Fotiadi, E. and A. Ladynin, The state and the geloogic tasks of combined geophysical studies of the lithospheric structure at depth in Siberia and the Soviet Far East, Geologiya i Geofizika, 15, 144-154, 1974.

Frez, J. and F. Schwab, Structural dependence of the apparent initial phase of Rayleigh waves, Geophys. J.R. Astr. Soc., 44, 311-331, 1976.

Gabriel, V.G. and J.T. Kuo, High Rayleigh wave phase velocities for the New Delhi, India - Lahore, Pakistan profile, Bull. Seismol. Soc. Amer., 56, 1137-1145, 1966.

Gilbert, F., Excitation of the normal modes of the earth by earthquake sources, Geophys. J.R. Astr. Soc., 22, 223-226, 1970.

Gregersen, S., Surface wave dispersion and crust structure in Greenland, Geophys. J.R. Astr. Soc., 22, 29-39, 1970.

Gupta, H.K. and H. Narain, Crustal structure in the Himalayan and Tibet Plateau region from surface wave dispersion, Bull. Seismol. Soc. Amer., 57, 235-248, 1967.

Gupta, H.K. and Y. Sato, Regional characteristics of Love wave group velocity dispersion in Eurasia, Bull. Earthq. Res. Inst. Tokyo Univ., 44, 41-52, 1968.

Gutenberg, B. and C. Richter, Earthquake magnitude, intensity, energy and acceleration, Bull. Seismol. Soc. Amer., 46, 105-145, 1956.

Hagiwara, T., A note on the theory of the electromagnetic seismograph, Bull. Earthq. Res. Inst. Tokyo Univ., 36, 139-164, 1958.

Hamilton, W., The Uralides and the motion of the Russian and Siberian Platforms, Bull. Geol. Soc. Amer., 81, 2553-2576, 1970.

Harkrider, D.G., Surface waves in multilayered elastic media I. Rayleigh and Love waves from buried sources in a multilayered elastic half-space, Bull. Seismol. Soc. Amer., 54, 627-679, 1964.

Haskell, N.A., Radiation pattern of Rayleigh waves from a fault of arbitrary dip and direction of motion in a homogeneous medium, Bull. Seismol. Soc. Amer., 53, 619-642, 1963.

Healy, J. and D. Warren, Explosion seismic studies in North America, in The Earth's Crust and Upper Mantle, edited by P.J. Hart, AGU Monograph, 13, 208-220, 1969.

Hill, R., Robust regression when there are outliers in the carriers, Ph.D Thesis, Harvard University, Cambridge, Ma., 289pp., 1977.

Holmes, A., Principles of Physical Geology, Ronald Press Co., New York, 1288pp, 1965.

Huber, P.J., Robust statistics: A review, Annals of Mathematical Statistics, 43, 1041-1067, 1972.

Huestis, S., P. Molnar, and J. Oliver, Regional S_n velocities and shear velocity in the upper mantle, Bull. Seismol. Soc. Amer., 63, 469-475, 1973.

James, D.E., Andean crustal and upper mantle structure, J. Geophys. Res., 76, 3246-3271, 1971.

Julian, B., Ray tracing in arbitrarily heterogeneous media, Technical Note 1970-45, Lincoln Lab., Mass. Inst. of Technol., 1970.

Kaminuma, K., The crust and upper mantle structure in Japan, Bull. Earthq. Res. Inst. Tokyo Univ., 44, 495-510, 1966.

Kaminuma, K. and K. Aki, Crustal structure in Japan from the phase velocity of Rayleigh waves Part 2. Rayleigh waves from the Aleutian shock of March 9, 1957, Bull. Earthq. Res. Inst. Tokyo Univ., 41, 217-241, 1963.

Kanamori, H., Velocity and Q of mantle waves, Phys. Earth Planet. Interiors, 2, 259-275, 1970.

Kausel, E.G., A.R. Leeds, and L. Knopoff, Variations of Rayleigh wave phase velocity across the Pacific ocean, Science, 186, 139-141, 1974.

Khalevin, N., V. Druzhinin, V. Rybalka, E. Nezolenova, and L. Chudakova, The results of deep seismic sounding of the earth's crust in the middle Urals, Izv., Earth Physics, 4, 36-44, 1966.

Khalturin, V., T. Rautian, and P. Molnar, The spectral content of Pamir-Hindu Kush intermediate depth earthquakes: evidence for a high-Q zone in the upper mantle, J. Geophys. Res., 82, 2931-2943, 1977.

Knopoff, L., Phase and group slowness in inhomogeneous media, J. Geophys. Res., 74, 1701, 1969.

Knopoff, L., Observation and inversion of surface wave dispersion, Tectonophysics, 13, 497-519, 1972.

Knopoff, L. and A.A. Fouda, Upper mantle structure under the Arabian Peninsula, Tectonophysics, 26, 121-134, 1975.

Knopoff, L., S. Muller, and W.L. Pilant, Structure of the crust and upper mantle in the Alps from the phase velocity of Rayleigh waves, Bull. Seismol. Soc. Amer., 56, 1009-1044, 1966.

Kosminskaya, I. and Y. Riznichenko, Seismic studies of the earth's crust in Eurasia, Research in Geophysics, 2, 81-122, edited by H. Odishaw, MIT Press, Cambridge, Ma., 1964.

Kropotkin, P., Eurasia as a composite continent, Tectonophysics, 12, 261-266, 1971.

Landisman, M., A. Dziewonski, and Y. Sato, Recent improvements in the analysis of surface wave observations, Geophys. J.R. Astr. Soc., 17, 369-403, 1969.

Lee, W. and S. Solomon, Inversion schemes for surface wave attenuation and Q in the crust and upper mantle, Geophys. J.R. Astr. Soc., 43, 47-71, 1975.

Lowes, F.J., A comment on 'Statistical estimates of amplitude and phase', Geophys. J.R. Astr. Soc., 22, 227-228, 1970.

Madariaga, R. and K. Aki, Spectral splitting of toroidal-free oscillations due to lateral heterogenity of the earth's structure, J. Geophys. Res., 77, 4421-4431, 1972.

McCowan, D.W., Moment tensor representation of surface wave sources, Geophys. J.R. Astr. Soc., 44, 595-599, 1976.

McEvilly, T.V., Central United States crust-upper mantle structure from Love and Rayleigh wave phase velocity inversion, Bull. Seismol. Soc. Amer., 54, 1997-2015, 1964.

McGarr, A., Amplitude variations of Rayleigh waves -- horizontal refraction, Bull. Seismol. Soc. Amer., 59, 1307-1334, 1969.

Mendiguren, J., Focal mechanism of a shock in the middle of the Nazca plate, J. Geophys. Res., 76, 3861-3879, 1971.

Mendiguren, J., Inversion of surface wave data in source mechanism studies, J. Geophys. Res., 82, 889-894, 1977.

Mendiguren, J. and K. Aki, Source mechanism of the deep Colombian earthquake of July 31, 1970 from the free oscillation data, preprint, 1978.

Milashev, A. and V. Rozenberg, The crustal structure and distribution of kimberlites on the Siberian platform, Geologiya i Geofizika, 15, 61-73, 1974.

Mitchell, B.J., Radiation and attenuation of Rayleigh waves from the southeastern Missouri earthquake of October 21, 1965, J. Geophys. Res., 78, 886-899, 1973.

Mitchell, B.J., Regional Rayleigh wave attenuation in North America, J. Geophys. Res., 80, 4904-4916, 1975.

Molnar, P. and J. Oliver, Lateral variations of attenuation in the upper mantle and discontinuities in the lithosphere, J. Geophys. Res., 74, 2648-2682, 1969.

Molnar, P., T. Fitch, and F. Wu, Fault plane solutions of shallow earthquakes and contemporary tectonics in Asia,E Earth and Planetary Science Letters, 19, 101-112, 1973.

Molnar, P. and P. Tapponnier, Cenozoic tectonics of Asia: Effects of a continental collision, Science, 189, 419-426, 1975.

Morse, P.M. and H. Feshbach, Methods of Theoretical Physics, Part I, McGraw-Hill, New York, N.Y., 997pp., 1953.

Narain, H., Crustal structure of the Indian subcontinent, Tectonophysics, 20, 249-260, 1973.

Negi, J.G. and V.P. Singh, Love wave dispersion analysis for the crustal structure of laterally inhomogeneous Himalayas, Bull. Seismol. Soc. Amer., 63, 1163-1172, 1973.

Neprochnov, Y., I. Kosminskaya, and Y. Malovitsky, Structure of the crust and upper mantle of the Black and Caspian Seas, Tectonophysics, 10, 517-538, 1970.

Ni, J., Contempory tectonics in the Tien Shan region, preprint, 1978.

Niazi, M., Crustal thickness in central Saudi Arabian Peninsula, Geophys. J.R. Astr. Soc., 15, 545-547, 1968.

Nolet, G., Higher Rayleigh modes in western Europe, Geophys. Res. Letters, , 2, 60-62, 1975.

Noponen, I., Surface wave phase velocities in Finland, Bull. Seismol. Soc. Amer., 56, 1093-1104, 1966.

North, R., Surface wave raytracing across Eurasia, Semiannual Techn. Summary, Lincoln Lab., Mass. Inst. of Technol., June, 1975.

North, R. and H. Patton, Modeling Rayleigh wave phase velocities and amplitudes in Eurasia, Semiannual Techn. Summary, Lincoln Lab., Mass. Inst. of Technol., December, 1975.

Okal, E., The effect of intrinsic ocean upper mantle heterogeneity on regionalization of long period Rayleigh wave phase velocities, Geophys. J.R. Astr. Soc., 49, 357-370, 1977.

Papazachos, B., P. Comninakis, and J. Drakopoulos, Preliminary results of an investigation of crustal structure in southeastern Europe, Bull. Seismol. Soc. Amer., 56, 1241-1268, 1966.

Patton, H.J., A note on the source mechanism of the southeastern Missouri earthquake of October 21, 1965, J. Geophys. Res., 81, 1483-1486, 1976.

Pavlenkova, N., Velocity profile of the earth's crust in the central Ukraine, Izv., Earth Physics, 6, 21-30, 1969.

Payo, G., Crustal structure of the Mediterranean Sea Part II. Phase velocity and travel times, Bull. Seismol. Soc. Amer., 59, 23-42, 1969.

Payo, G., Structure of the crust and upper mantle in the Iberian Shield by means of a long period triangular array, Geophys. J.R. Astr. Soc., 20, 493-508, 1970.

Penttila, E., Structure of the earth's crust in Finland as revealed by data on the propagation velocities of seismic waves, Izv., Earth Physics, 5, 17-23, 1969.

Pilant, W.L. and L. Knopoff, Observations of multiple seismic events, Bull. Seismol. Soc. Amer., 54, 19-39, 1964.

Pisarenko, V.F., Statistical estimates of amplitude and phase corrections, Geophys. J.R. Astr. Soc., 20, 89-98, 1970.

Press, F., Determination of crustal structure from phase velocity of Rayleigh waves, Bull. Geol. Soc. Amer., 67, 1647-1658, 1956.

Press, F., Regionalized earth models, J. Geophys. Res., 75, 6575-6581, 1970.

Press, F., A. Ben-Menahem, and M.N. Toksoz, Experimental determination of earthquake fault length and rupture velocity, J. Geophys. Res., 66, 3471-3485, 1961.

Priestley, K. and J. Brune, Surface waves and the structure of the great basin of Nevada and western Utah, preprint, 1978.

Ragimov, S.S., The phase velocities determination method and the earth's crust depth estimation in Azerbaijan by Rayleigh waves, in Proceedings of the Eighth Assembly of the European Seismological Commission, edited by E. Bisztricsany, Budapest, 212-215, 1969.

Randall, M. and L. Knopoff, The mechanism at the focus of deep earthquakes, J. Geophys. Res., 26, 4965-4976, 1970.

Remington, R. and M. Schork, Statistics with Applications to the Biological and Health Sciences, Prentice-Hall, Inc., Englewood Cliffs, N.J., 418pp, 1970.

Richardson, R. and S. Solomon, Apparent stress and stress drop for intraplate earthquakes and tectonic stress in the plates, Pure Appl.Geophys., 115, 317-331, 1977.

Rosenthal, R. and T. Teng, A surface wave study of the South-China subplate, Techn. Report No 77-9, Univ of S. Calif., 1977.

Ryaboy, V., Structure of the earth's crust and upper mantle in the central regions of Turkmenia according to deep seismic sounding data, in Proceedings of the Eighth Assembly of the European Seismological Commission, edited by E. Bisztricsany, Budapest, 216-221, 1969.

Saito, M., Excitation of free oscillations and surface waves by a point source in a vertically heterogeneous earth, J. Geophys. Res., 72, 3689-3699, 1967.

Santo, T., Lateral variation of Rayleigh wave dispersion character Part II. Eurasia, Pure Appl. Geophys., 62, 67-80, 1965.

Savarenskiy, Y.F. and A.B. Peshkov, The use of surface wave velocities for selection of models of crustal structure, Izv., Earth Physics, 10, 79-87, 1968.

Savarensky, E.F., G.N. Bozhko, T.I. Kukhtikova, A.B. Peshkov, I.I. Popov, B.N. Shechkov, O.I. Yurkevich, and L.M. Yudakova, On the earth structure in some regions of the USSR from surface waves data, Pure Appl. Geophys., 73, 99-119, 1969.

Seidl, D., Spezielle Probleme der Ausbreitung seismischer Oberflachenwellen, mit Beobachtungsbeispielen aus Europa, D. Sc. Thesis, Univ. of Karlsruhe, 105pp., 1971.

Seidl, D., H. Reichenbach, and S. Mueller, Dispersion investigation of Rayleigh waves in the Rhine Graben Rift System, in Graben Problems, edited by H. Illes and S. Muller, Stuggart, 203-206, 1970.

Seidl, D., S. Mueller, and H. Reichenbach, Dispersion and absorption of seismic surface waves and the structure of the upper mantle based on observations in Europe, in Proceedings of the Twelfth General Assembly of the European Seismo. Comm., Luxembourg, Sept., 1970, Communs Obs. r. Belg., Ser. A, 13, 198-199, 1970b.

Shechkov, B.N., Group velocities of surface waves on trajectories in Eurasia, Izv., Earth Physics, 8, 80-87, 1970.

Shirokova, Y., A detailed study of the stresses and fault planes at earthquake foci of central Asia, Izv., Earth Physics, 11, 707-717, 1974.

Sollogub, V., On certain regularities of crustal structure associated with the major geologic features of southeastern Europe, Tectonophysics, 10, 549-559, 1970.

Stuart, G., The upper mantle structure of the North Sea region from Rayleigh wave dispersion, Geophys. J.R. Astr. Soc., 52, 367-382, 1978.

Times of London, Atlas of the World, John Bartholomew and Son, Ltd, Edinburgh, 1967.

Toksoz, M.N. and D.L. Anderson, Phase velocities of long period surface waves and structure of the upper mantle 1. Great-circle Love and Rayleigh wave data, J. Geophys. Res., 71, 1649-1658, 1966.

Tryggvason, E., Crustal thickness in Fennoscandia from the phase velocities of Rayleigh waves, Ann. Geofis., 14, 267-293, 1961.

Tsai, Y-B. and K. Aki, Simultaneous determination of the seismic moment and attenuation of seismic surface waves, Bull. Seismol. Soc. Amer., 59, 275-287, 1969.

Tsai, Y-B. and K. Aki, Precise focal depth determination from amplitude spectra of surface waves, J. Geophys. Res., 75, 5729-5743, 1970.

Tseng, J-S. and Z. Sung, Phase velocities of Rayleigh waves in China, Acta Geophys. Sinica, 12, 148-165, 1963.

Tung, J.P. and T. Teng, Surface wave studies on crustal and mantle structure of China, Techn. Report No.74-2, Univ. of S. Calif., 1974.

United States Geological Survey, Atlas of Asia and Eastern Europe to Support Detection of Underground Nuclear Testing Part V. Crust and Mantle Conditions, edited by R. Rodriquez, February, 1969.

Volvovski, I., Seismic Studies of the Earth's Crust in the U.S.S.R., Nedra, Moscow, 290pp, 1973.

Volvovski, I. and B. Volvovski, Cross-sections of the Earth's Crust in the Territory of the U.S.S.R., Plotted from Deep Seismic Soundings, Sovetskoe Radio, Moscow, 268pp., 1975.

Weidner, D.J., Rayleigh waves from mid-ocean ridge earthquakes: source and path effects, Ph.D. thesis 253pp., Mass. Inst. of Technol., Cambridge, Ma., 253pp., 1972.

Weidner, D.J., Rayleigh wave phase velocities in the Atlantic ocean, Geophys. J.R. Astr. Soc., 36, 105-139, 1974.

Weidner, D.J. and K. Aki, Focal depth and mechanism of mid-ocean ridge earthquakes, J. Geophys. Res., 78, 1818-1831, 1973.

Yacoub, N. and B. Mitchell, Attenuation of Rayleigh wave amplitudes across Eurasia, Bull. Seismol. Soc. Amer., 67, 751-769, 1977.

Yurkevich, O.I. and B.I. Volosecky, Determination of the thickness of the earth's crust in the Carpathians from the dispersion of the surfaces waves from Chilean earthquake in 1960, in Proceedings of the Eighth Assembly of the European Seismological Commission, edited by E. Bisztricsany, Budapest, 285-292, 1969.

Zatopek, A. and B. Beranek, Geophysical synthesis and crustal structure in central Europe, Studia Geophys. Geod., 19, 121-133, 1975.

APPENDIX A

TECHNIQUES APPLIED TO INVERT FOR THE SEISMIC MOMENT TENSOR

INVERSION WITH CONSTRAINTS. Let us rewrite Equation 2-4.3 in compact form:

$$\alpha_{ik} = b_0 x_0(\omega_k) + b_1 x_1(\theta_i, \omega_k) + b_2 x_2(\theta_i, \omega_k) + \varepsilon^{\alpha}_{ik}$$

and (A.1)

$$\beta_{ik} = b_4 x_4(\theta_i, \omega_k) + b_5 x_5(\theta_i, \omega_k) + \varepsilon^{\beta}_{ik}$$

where b_i's are model parameters to be determined (in our case, the moment components) and x_i's are functions of the independent variables, azimuth and frequency, once we have chosen a trial focal depth.

If we choose to determine b_i's at a given frequency, ω_k, the first equation in A.1 is a second-order regression equation with a constant term b_0' where $b_0' = b_0 x_0(\omega_k)$. The other equation in A.1 is also second order, however a constant term is missing. If we choose to determine b_i's over a range of frequencies, the equations in A.1 become third order and second order regression equations, respectively, both missing constant terms.

We can treat the absence of the constant term by carrying out the regression under the constraint that the constant term

equal zero. As an example, let us consider the second order regression on the imaginary data when we desire to estimate b_4 and b_5 at a given frequency. Calling the constant in the equation, b_3, we first write the error matrix of n observations

$$\begin{bmatrix} \varepsilon_1^{\beta} \\ \varepsilon_2^{\beta} \\ \\ \\ \varepsilon_n^{\beta} \end{bmatrix} = \begin{bmatrix} \beta_1 & -1 & -x_{41} & -x_{51} \\ \beta_2 & -1 & -x_{42} & -x_{52} \\ & & & \\ & & & \\ \beta_n & -1 & -x_{4n} & -x_{5n} \end{bmatrix} \begin{bmatrix} 1 \\ b_3 \\ b_4 \\ b_5 \end{bmatrix}$$

where we have dropped the subscript k to simplify notation. The least squares solution of this over-determined system of equations is obtained by minimizing the sum of squared errors, i.e.

$$\min E = [\varepsilon_1^{\beta} \; \varepsilon_2^{\beta} \; \cdots \; \varepsilon_n^{\beta}] \begin{bmatrix} \varepsilon_1^{\beta} \\ \varepsilon_2^{\beta} \\ \vdots \\ \varepsilon_n^{\beta} \end{bmatrix}$$

We write E in matrix form as follows

$$\begin{aligned} E &= \underset{\sim}{\varepsilon}^T \underset{\sim}{\varepsilon} \\ &= (\underset{\sim}{B} \underset{\sim}{X})^T \underset{\sim}{B} \underset{\sim}{X} \\ &= \underset{\sim}{X}^T \underset{\sim}{B}^T \underset{\sim}{B} \underset{\sim}{X} \end{aligned}$$

where T denotes transpose and

$$\underset{\sim}{\varepsilon} = \begin{bmatrix} \varepsilon_1^{\beta} \\ \varepsilon_2^{\beta} \\ \vdots \\ \varepsilon_n^{\beta} \end{bmatrix} \qquad \underset{\sim}{X} = \begin{bmatrix} 1 \\ b_3 \\ b_4 \\ b_5 \end{bmatrix}$$

$$\underset{\sim}{B} = \begin{bmatrix} \beta_1 & -1 & -x_{41} & -x_{51} \\ \beta_2 & -1 & -x_{42} & -x_{52} \\ \vdots & & & \\ \beta_n & -1 & -x_{4n} & -x_{5n} \end{bmatrix}$$

Following Claerbout (1976) the least squares solution to a system of n equations and k constraint equations reduces to minimizing a quantity E of the form

$$E = \underset{\sim}{X}^T \underset{\sim}{B}^T \underset{\sim}{B} \underset{\sim}{X} + 2\underset{\sim}{\lambda} \underset{\sim}{G} \underset{\sim}{X}$$

where $\underset{\sim}{G}$ is a matrix containing k constraint equations and $\underset{\sim}{\lambda}$ is a matrix of Lagrange multipliers. The method of Lagrange multipliers called upon here is the same as that applied to the variational integral under constraint conditions (e.g. Morse and Feshbach, 1953, pp 276-280). We can write the constraint equation in our case as follows

$$[0 \ 1 \ 0 \ 0] \begin{bmatrix} 1 \\ b_3 \\ b_4 \\ b_5 \end{bmatrix} = 0$$

from which the constraint matrix is identified to be

$$\underset{\sim}{G} = [0\ 1\ 0\ 0].$$

We proceed to find the normal equations by taking $\partial E/\partial b_3$, $\partial E/\partial b_4$, $\partial E/\partial b_5$ and and $\partial E/\partial \lambda$ and requiring that

$$\frac{\partial E}{\partial b_3} = \frac{\partial E}{\partial b_4} = \frac{\partial E}{\partial b_5} = \frac{\partial E}{\partial \lambda} = 0$$

where $\underset{\sim}{\lambda} = [\ \lambda\ ]$. With λ an unknown, the normal equations can be written in matrix form as follows

$$\begin{bmatrix} 0 & 1 & 0 & 0 & 0 \\ r_{10} & r_{11} & r_{12} & r_{13} & 1 \\ r_{20} & r_{21} & r_{22} & r_{23} & 0 \\ r_{30} & r_{31} & r_{32} & r_{33} & 0 \end{bmatrix} \begin{bmatrix} 1 \\ b_3 \\ b_4 \\ b_5 \\ \lambda \end{bmatrix} = [0] \qquad \text{(A.2)}$$

where

$$r_{10} = -\Sigma\beta_i \qquad r_{11} = n \qquad r_{12} = \Sigma x_{4i} \qquad r_{13} = \Sigma x_{5i}$$

$$r_{20} = -\Sigma\beta_i x_{4i} \qquad r_{21} = r_{12} \qquad r_{22} = \Sigma x_{4i}^2 \qquad r_{23} = \Sigma x_{4i} x_{5i}$$

$$r_{30} = -\Sigma\beta_i x_{5i} \qquad r_{31} = r_{13} \qquad r_{32} = r_{23} \qquad r_{33} = \Sigma x_{5i}^2$$

If we define the following matrix,

$$\underset{\sim}{M} = \begin{bmatrix} 1 & 0 & 0 & 0 \\ r_{11} & r_{12} & r_{13} & 1 \\ r_{21} & r_{22} & r_{23} & 0 \\ r_{31} & r_{32} & r_{33} & 0 \end{bmatrix}$$

then the solution to these normal equations is written

$$\begin{bmatrix} b_3 \\ b_4 \\ b_5 \\ \lambda \end{bmatrix} = \underset{\sim}{M}^{-1} \begin{bmatrix} 0 \\ -r_{10} \\ -r_{20} \\ -r_{30} \end{bmatrix}$$

It is apparent from examination of the first normal equation in A.2 that b_3 must be identically zero in this solution.

ROBUST METHODS. Noise on the seismogram may cause multiplicative errors that can seriously bias the estimates of the tensor elements (Section 3-2). This is not surprising because in carrying out the inversion we assumed that errors are additive in the complex spectrum (Equation 2-4.3 and A.1). In the case of our actual data, this assumption may not be valid over the entire frequency range of interest. At long periods, where we expect it is, the presence of just a few bad points was seen to significantly affect the results of inversion (Section 4-2). Under these circumstances, robust methods may be very useful. This section describes a robust regression method applied in this paper.

There are many such methods (for a review, see Huber, 1972), and the following discussion, based on Hill (1976), just scratches the surface of this topic.

As a starting point let us find the estimation of the location parameter, μ, by minimizing the quantity, Δ.

$$\min_{\theta} \Delta = \sum_{i=1}^{n} \rho\left(\frac{x_i-\theta}{S}\right) \qquad \text{(A.3)}$$

where x_i, i=1,...n, are observed samples of the probability density $F\left(\frac{x-\mu}{\sigma}\right)$, S is an estimate of dispersion, σ, and θ, is called the M-estimate of μ. The function $\rho(\xi)$ is called the loss function and writing

$$\psi(\xi) = \frac{d\rho}{d\xi}$$

we can satisfy A.3 by solving the following equation for θ

$$\sum_{i=1}^{n} \psi\left(\frac{x_i-\theta}{S}\right) = 0.$$

When $\rho(\xi) = \xi^2$, the minimization is least squares in which case the M-estimate equals the sample mean. It is common practice to define the function $\psi(\xi)$, which will be "robust" to the erratic data point. For example, a well-known function is the

"Huber ψ" -

$$\psi^{H}(\xi) = \begin{cases} \xi, & |\xi| \leq k \\ -k, & \xi < -k \\ k, & \xi > k \end{cases}$$

where k is constant. We shall return to the function ψ momentarily.

In regard to the regression problem, the M-estimate of a model parameter is defined analogously

$$\min_{b_j} \sum_{i=1}^{n} \rho\left(\frac{y_i - x_{ij}b_j}{S}\right)$$

where y_i i=1,2,...n are observations depending on the variables x_{ij}, S is an estimate of the dispersion of the residuals, ε_i, $\varepsilon_i = y_i - x_{ij}b_j$, and b_j is the M-estimate of the model parameter, B_j. The minimization is satisfied by solving

$$\sum_{i=1}^{n} x_{ij}\psi\left(\frac{y_i - x_{ij}b_j}{S}\right) = 0 \qquad (A.4)$$

for b_j. For $\psi(\xi) = \xi$, the minimization reduces to the normal equations of the least squares method. For $\psi(\xi) \neq \xi$, the problem is non-linear, and a solution can be found by iteration. Letting $w(\xi) = \frac{\psi(\xi)}{\xi}$, we substitute for ψ in Equation A.4

$$\sum_{i=1}^{n} x_{ij}\left(\frac{y_i - x_{ij}b_j}{S}\right) \quad w\left(\frac{\varepsilon_i}{S}\right) = 0.$$

This can be written as a matrix equation

$$\underset{\sim}{X}^T \underset{\sim}{W} \underset{\sim}{Y} - \underset{\sim}{X}^T \underset{\sim}{W} \underset{\sim}{X} \underset{\sim}{b} = 0$$

where $\underset{\sim}{W}$ is a nxn diagonal matrix such that $W_{ii} = w(\frac{\varepsilon_i}{S})$. These matrix equations are the normal equations for the weighted least squares. The solution to these equations is

$$\underset{\sim}{b} = (\underset{\sim}{X}^T \underset{\sim}{W} \underset{\sim}{X})^{-1} \underset{\sim}{X}^T \underset{\sim}{W} \underset{\sim}{Y}$$

The M-estimates of the regression parameters may be obtained by applying iterative, reweighted least squares such that

$$\underset{\sim}{b}^i = (\underset{\sim}{X}^T\underset{\sim}{W} [\frac{\underset{\sim}{Y}-\underset{\sim}{X}\underset{\sim}{b}^{(i-1)}}{S}] \underset{\sim}{X})^{-1}\underset{\sim}{X}^T\underset{\sim}{W}[\frac{\underset{\sim}{Y}-\underset{\sim}{X}\underset{\sim}{b}^{(i-1)}}{S}] \underset{\sim}{Y}$$

This scheme in general converges to a minimun. However, there may be more than one minimum and the particular solution that is reached will depend on the initial estimate, $\underset{\sim}{b}^o$.

The problem of finding an initial estimate is important and, at the same time, it is the biggest weakness of robust methods. In general, the initial estimate should also be robust. For example, the sample median is considered a satisfactory initial estimate of the location. In regression, an approach to finding an initial estimate is not widely agreed upon. One possibility is the estimate which minimizes the sum absolute value of the residuals. Known as the L_1 norm solution, Claerbout and Muir (1973) have described an algorithm applicable to multiple regression.

The function, $\psi(\xi)$, determines the robust properties of the M-estimate. Many functional forms have been proposed and a few, such as the Huber ψ, have been well studied. A class of ψ functions called "redescending" have emerged as favorites in the applications field because of their very robust qualities. The redescending sine function Andrews (1974) is defined as follows

$$\psi^{S}(\xi) = \begin{cases} 0 , & |\xi| \geq \pi c \\ \sin\frac{\xi}{c} , & |\xi| < \pi c \end{cases}$$

where $\xi_i = \frac{\varepsilon_i}{S}$, ε_i is the residual, S is the estimate of the dispersion of the residuals, and c is a constant. Redescending functions yield stronger robust estimates than ψ^{H} because large scaled residuals are heavily "down-weighted". Notice that the argument of ψ involves the scaled residuals. In order to be effective, the estimate of S must be robust as in the following computation

$$S = \text{median } \{\varepsilon_i - \text{median}\{\varepsilon_i\}\}$$

On the basis of this discussion and my experience with these techniques, the following procedure was found to give satisfactory results:

1. An initial estimate, b^{o}, was obtained using L_1 norm.
2. The residuals were scaled using a robust estimate of S.

3. Weights, W_{ii}, were computed using the redescending sine function. A value of 1.5 is suitable for c.
4. The final estimates, reported in this paper, were taken to be the weighted least squares solution after one iteration, i.e. b_j^1.

We show the final result at each frequency as a dashed line in the figures of real and imaginary data in Chapter 4 and Appendix B. The procedure is the same whether it is applied to data at a single frequency or across the frequency band. However, in the latter situation we weight observations across frequency also. If S_k is the dispersion of the residuals at frequency k, the suitable weight, $W_{ii,k}$ is

$$W_{ii,k} = W_{ii}/S_k^2$$

The final results when the method is applied across the frequency band are shown by solid lines or otherwise noted in the figure captions.

APPENDIX B

ILLUSTRATIONS OF OBSERVED REAL AND IMAGINARY PARTS WITH CALCULATED CURVES

In this appendix, the observed real and imaginary parts of the source spectrum are plotted as a function of azimuth with the theoretical curves calculated for parameters determined by the linear inversions. We sampled the spectrum at six frequencies (1/60, 1/50, 1/40, 1/34, 1/30 and 1/26Hz). The observations, corresponding to α_{ik} and β_{ik} in Equation 2-4.3, are shown by solid dots on six separate plots per page. On each plot we show two calculated curves. The dashed curve is the result of the linear inversion applied to the data in that plot only (i.e. at a fixed frequency). The solid curve is obtained by inverting the data at all frequencies simultaneously and corresponds to the calculated amplitudes for the trial depth that minimized the residuals on the residual curves in Figure 4-2.15. We give the estimates of the moment tensor elements at this depth in Table 4-2.5. The robust method described in Appendix A was used in all of the inversions. The illustrations are presented in numerical order of the event.

Note: There are two sets of illustrations for event 9. The first set (Figures B-9a and 9b) has three curves in each plot, the solid and dot-dash curves referring to the results in Table 4-2.4 for 10 and 15km, respectively. The second set (Figures

B-9a' and 9b') pertains to the results of the relocation in Table 4-2.4 (see Section 4-2). Event 7 has an extra imaginary part (Figure B-7b) corresponding to the ISC origin time. A 2sec correction has been made to this origin time in Figures B-7a and B-7b' (see Section 4-2).

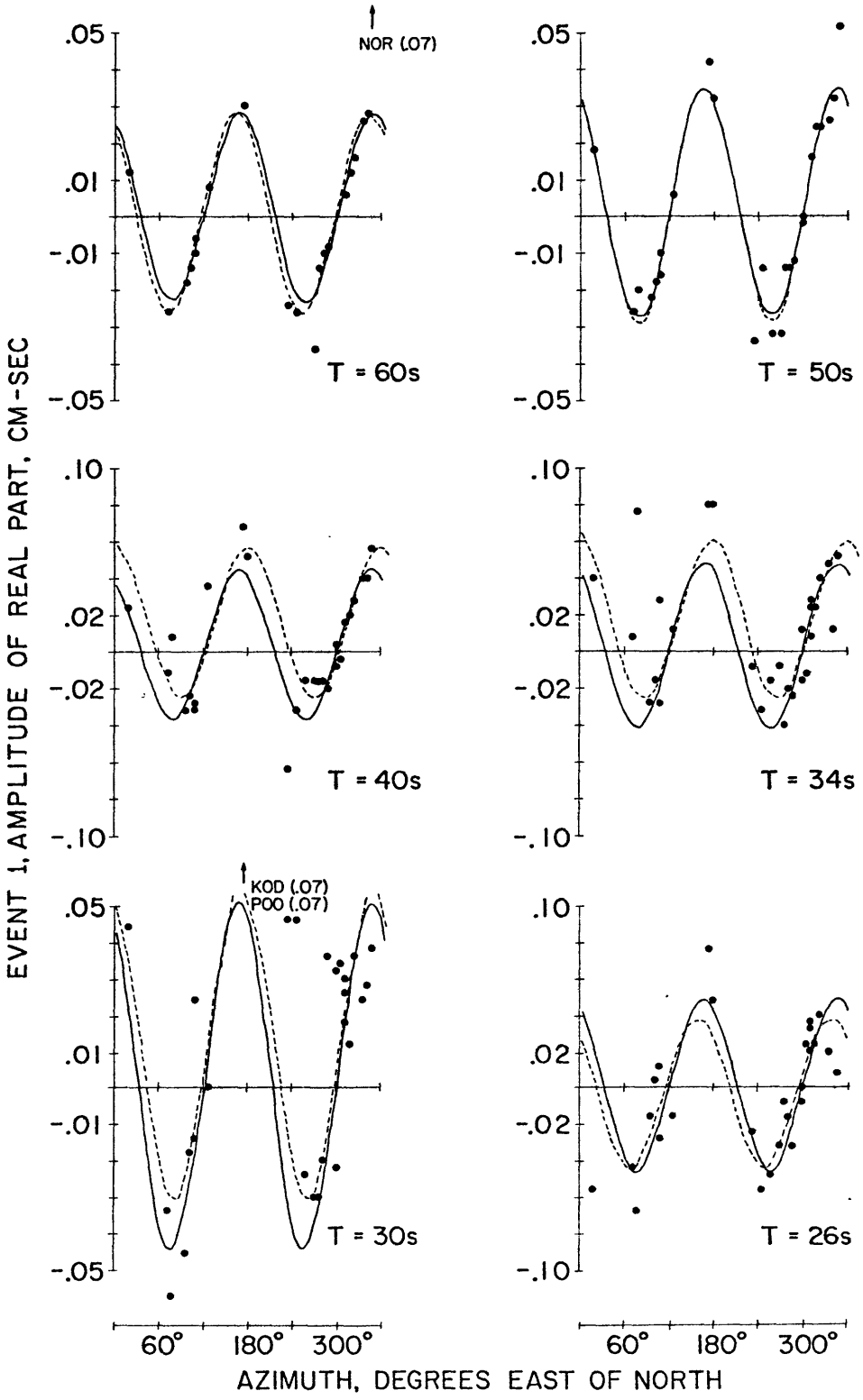
NOR (07)
T = 60s
T = 50s
T = 40s
T = 34s
KOD (07)
POO (07)
T = 30s
T = 26s
.05
.01
-.01
-.05
.10
.02
-.02
-.10
60°
180°
300°
EVENT 1, AMPLITUDE OF REAL PART, CM-SEC
AZIMUTH, DEGREES EAST OF NORTH

FIGURE B-1a

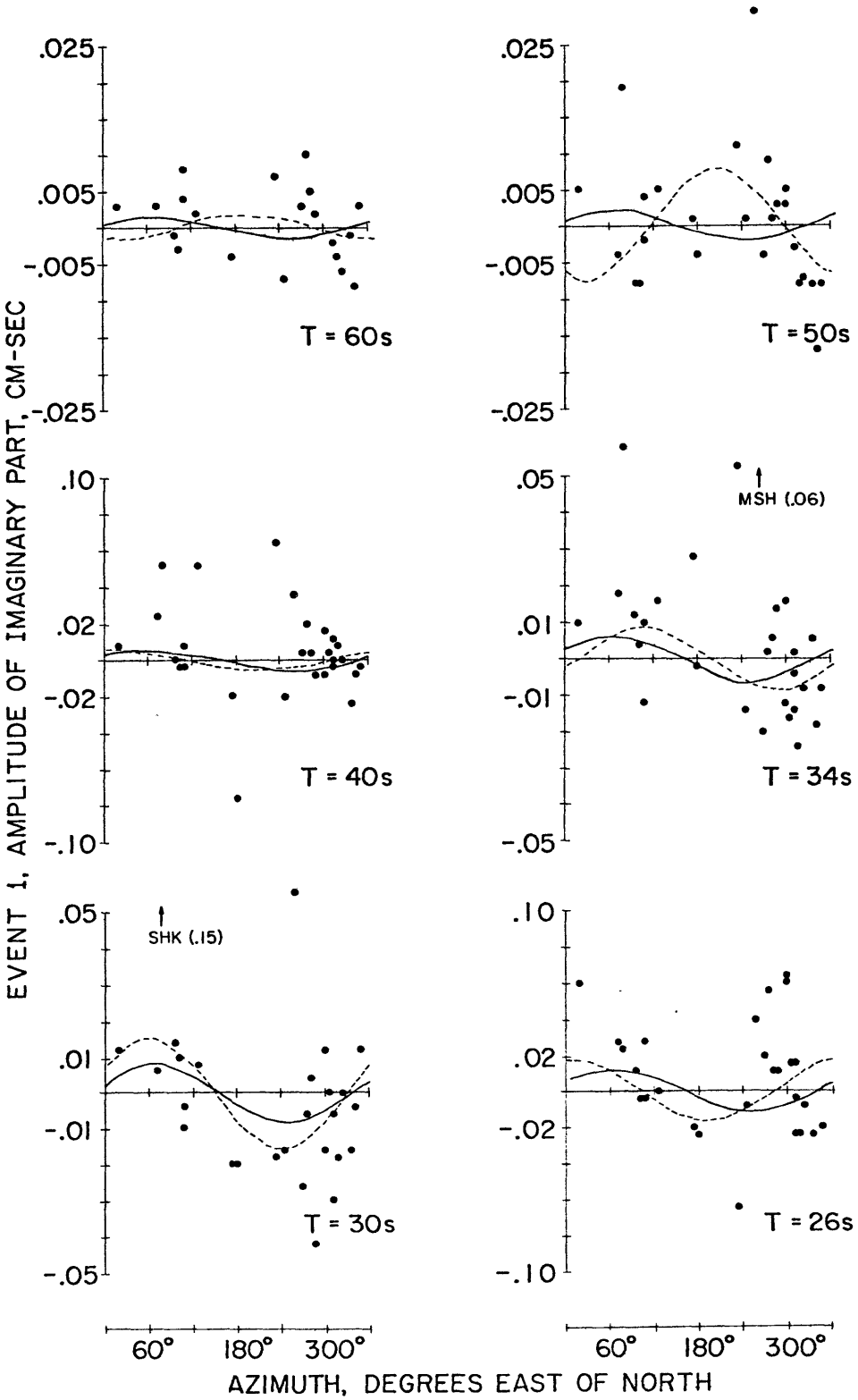
.025
.005
-.005
-.025
T = 60s
T = 50s
.10
.02
-.02
-.10
T = 40s
.05
.01
-.01
-.05
MSH (.06)
T = 34s
SHK (.15)
T = 30s
T = 26s
60°
180°
300°
EVENT 1, AMPLITUDE OF IMAGINARY PART, CM-SEC
AZIMUTH, DEGREES EAST OF NORTH

FIGURE B-1b

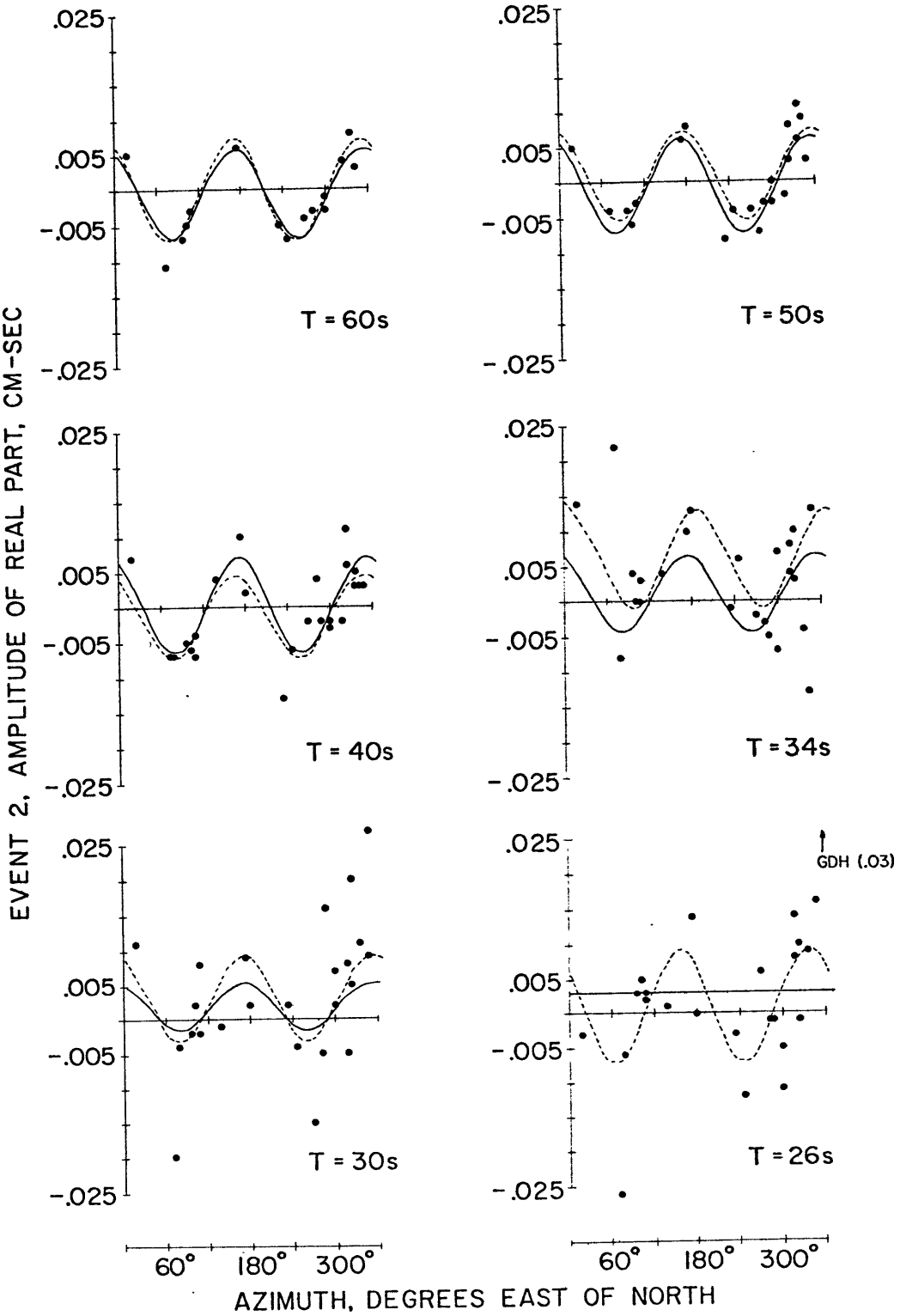
.025
.005
-.005
-.025
T = 60s
T = 50s
T = 40s
T = 34s
T = 30s
T = 26s
GDH (.03)
EVENT 2, AMPLITUDE OF REAL PART, CM-SEC
60°
180°
300°
AZIMUTH, DEGREES EAST OF NORTH

FIGURE B-2a

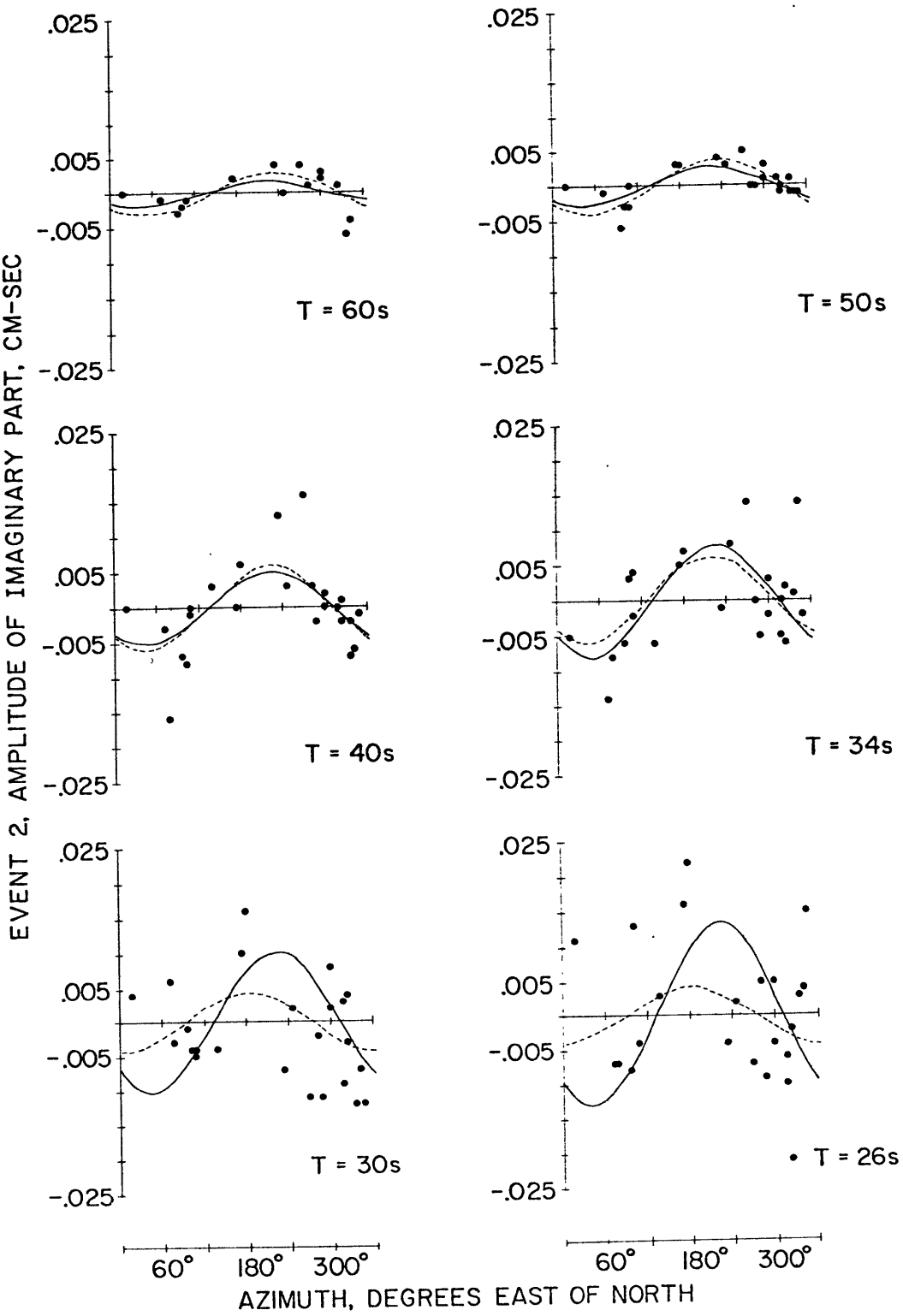
.025
.005
-.005
-.025
T = 60s
T = 50s
T = 40s
T = 34s
T = 30s
T = 26s
EVENT 2, AMPLITUDE OF IMAGINARY PART, CM-SEC
60°
180°
300°
AZIMUTH, DEGREES EAST OF NORTH

FIGURE B-2b

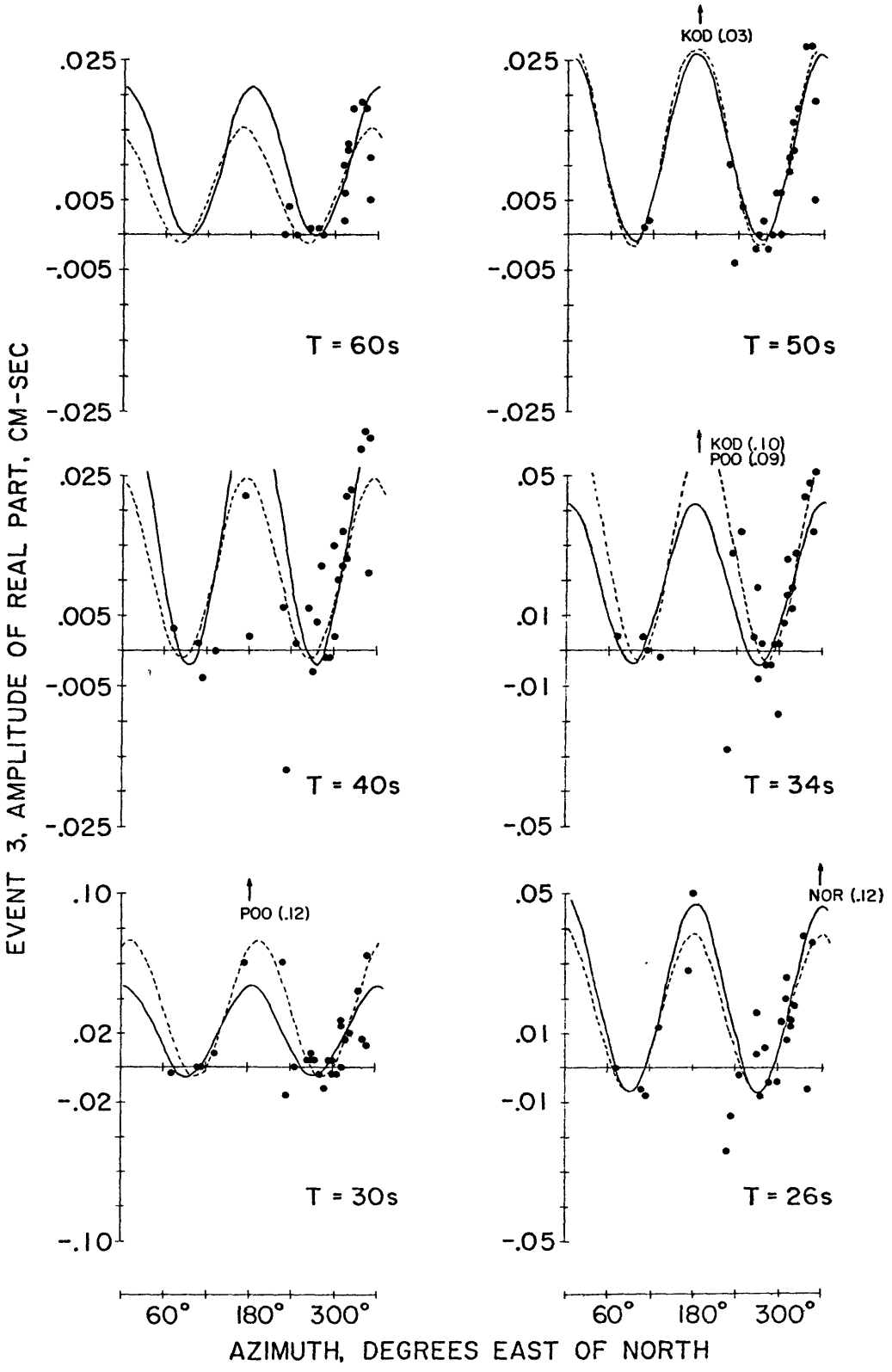
KOD (.03)
.025
.005
-.005
-.025
T = 60s
T = 50s
KOD (.10)
POO (.09)
.05
.01
-.01
-.05
T = 40s
T = 34s
POO (.12)
NOR (.12)
.10
.02
-.02
-.10
T = 30s
T = 26s
60°
180°
300°
EVENT 3, AMPLITUDE OF REAL PART, CM-SEC
AZIMUTH, DEGREES EAST OF NORTH

FIGURE B-3a

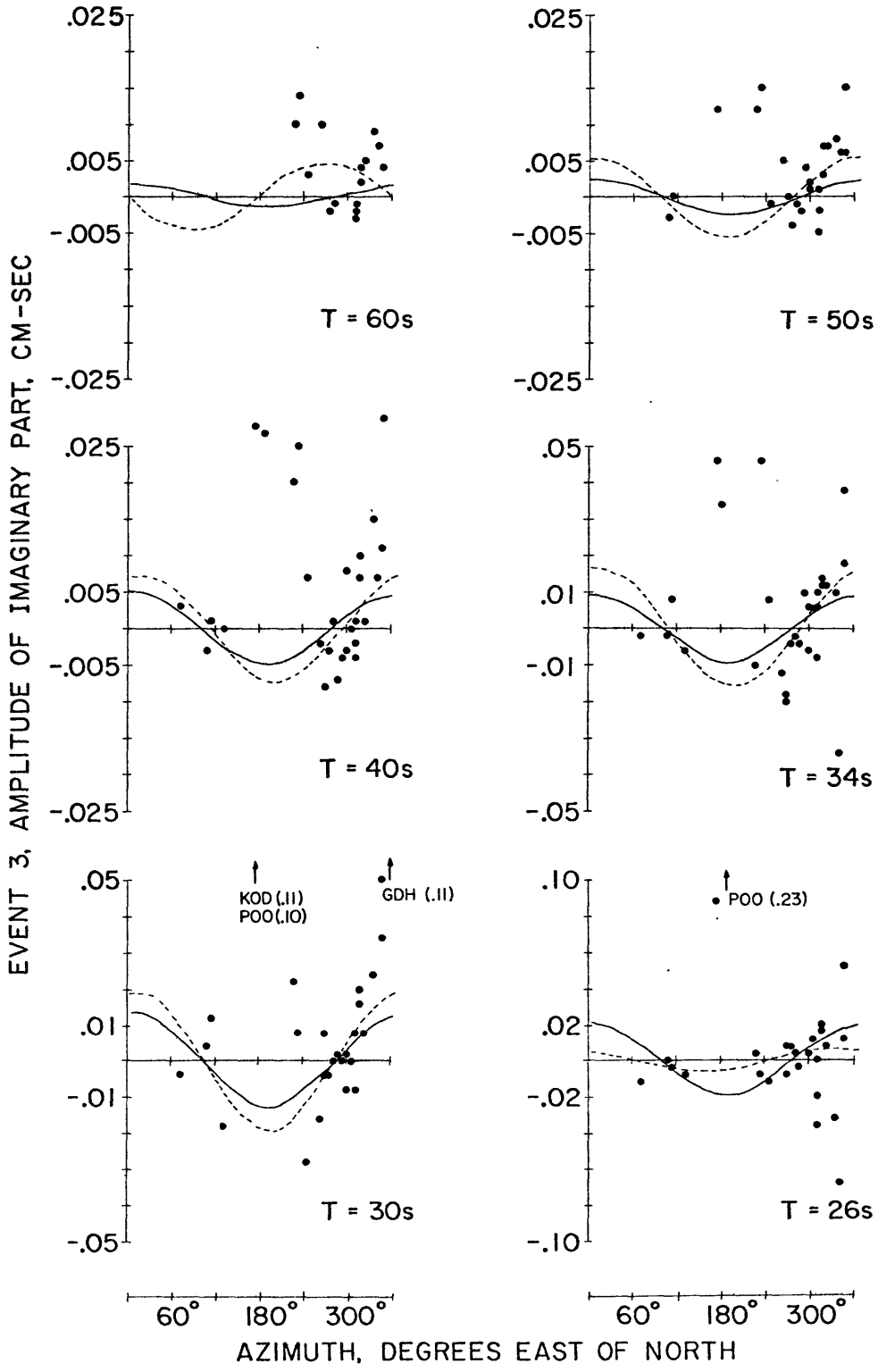
.025
.005
-.005
-.025
T = 60s
T = 50s
.05
.01
-.01
-.05
T = 40s
T = 34s
KOD (.11)
POO(.10)
GDH (.11)
.10
.02
-.02
-.10
POO (.23)
T = 30s
T = 26s
60°
180°
300°
EVENT 3, AMPLITUDE OF IMAGINARY PART, CM-SEC
AZIMUTH, DEGREES EAST OF NORTH

FIGURE B-3b

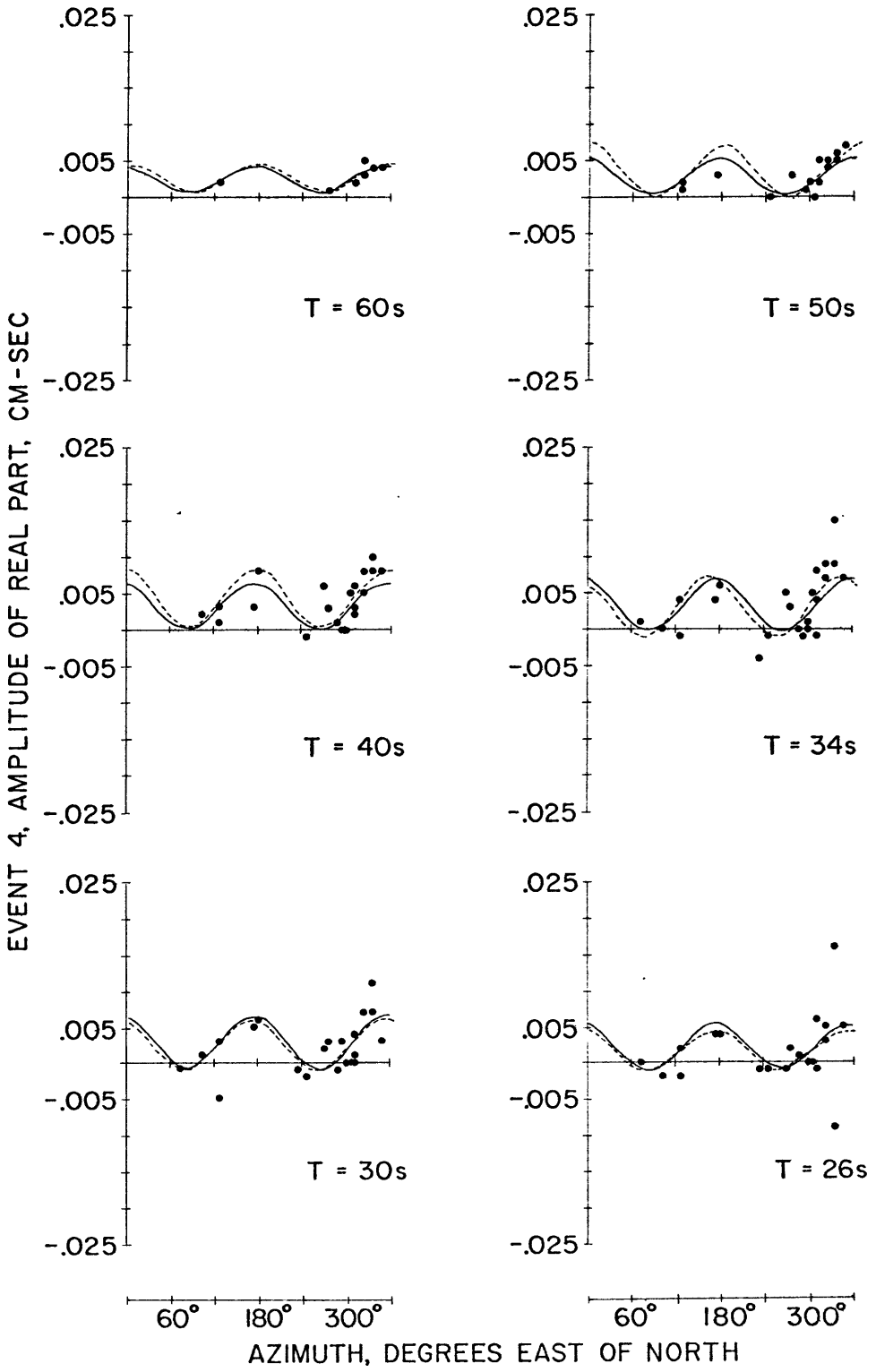
.025
.005
-.005
-.025
T = 60s
T = 50s
T = 40s
T = 34s
T = 30s
T = 26s
EVENT 4, AMPLITUDE OF REAL PART, CM-SEC
60°
180°
300°
AZIMUTH, DEGREES EAST OF NORTH

FIGURE B-4a

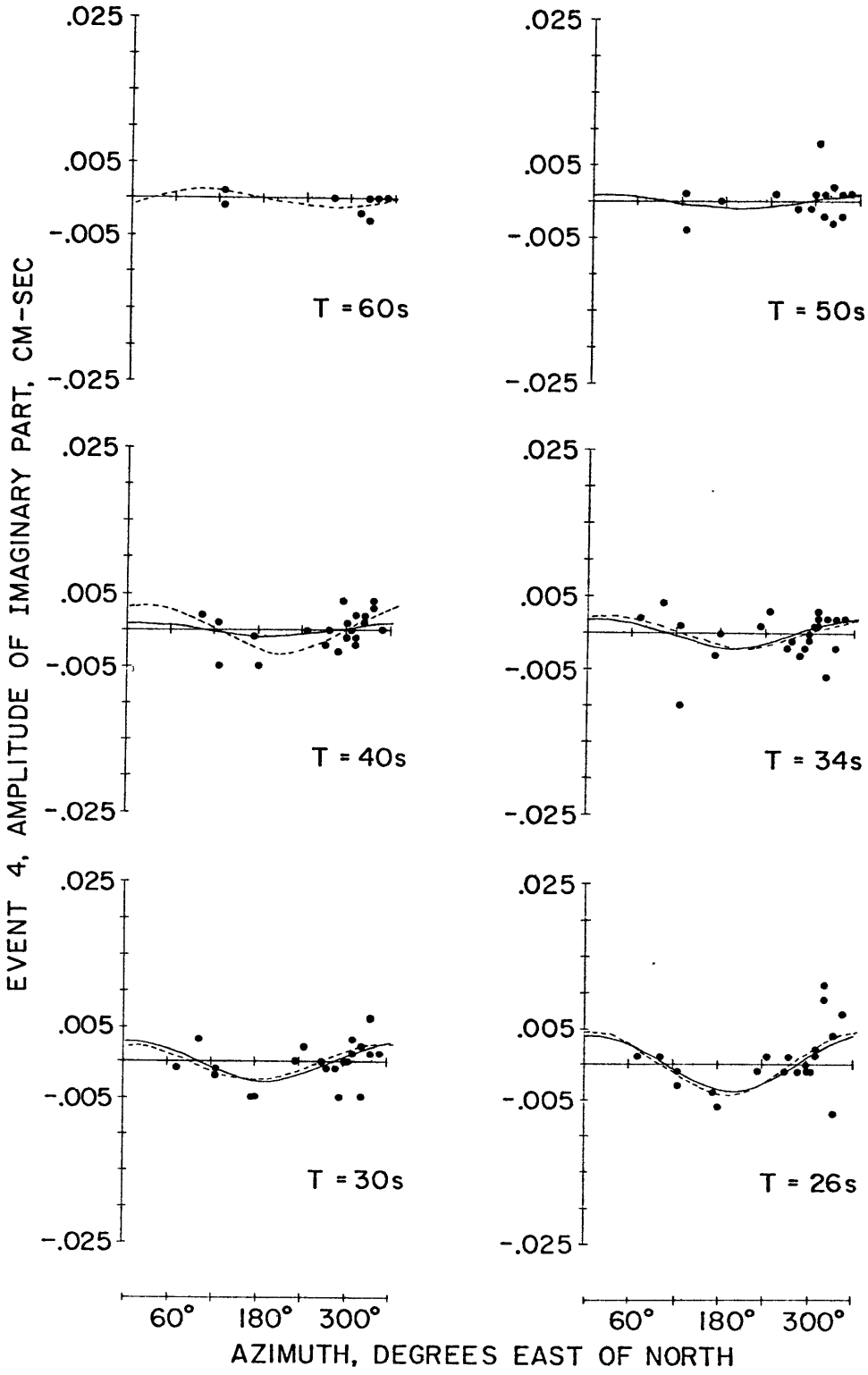
.025
.005
-.005
-.025
T = 60s
T = 50s
T = 40s
T = 34s
T = 30s
T = 26s
EVENT 4, AMPLITUDE OF IMAGINARY PART, CM-SEC
60°
180°
300°
AZIMUTH, DEGREES EAST OF NORTH

FIGURE B-4b

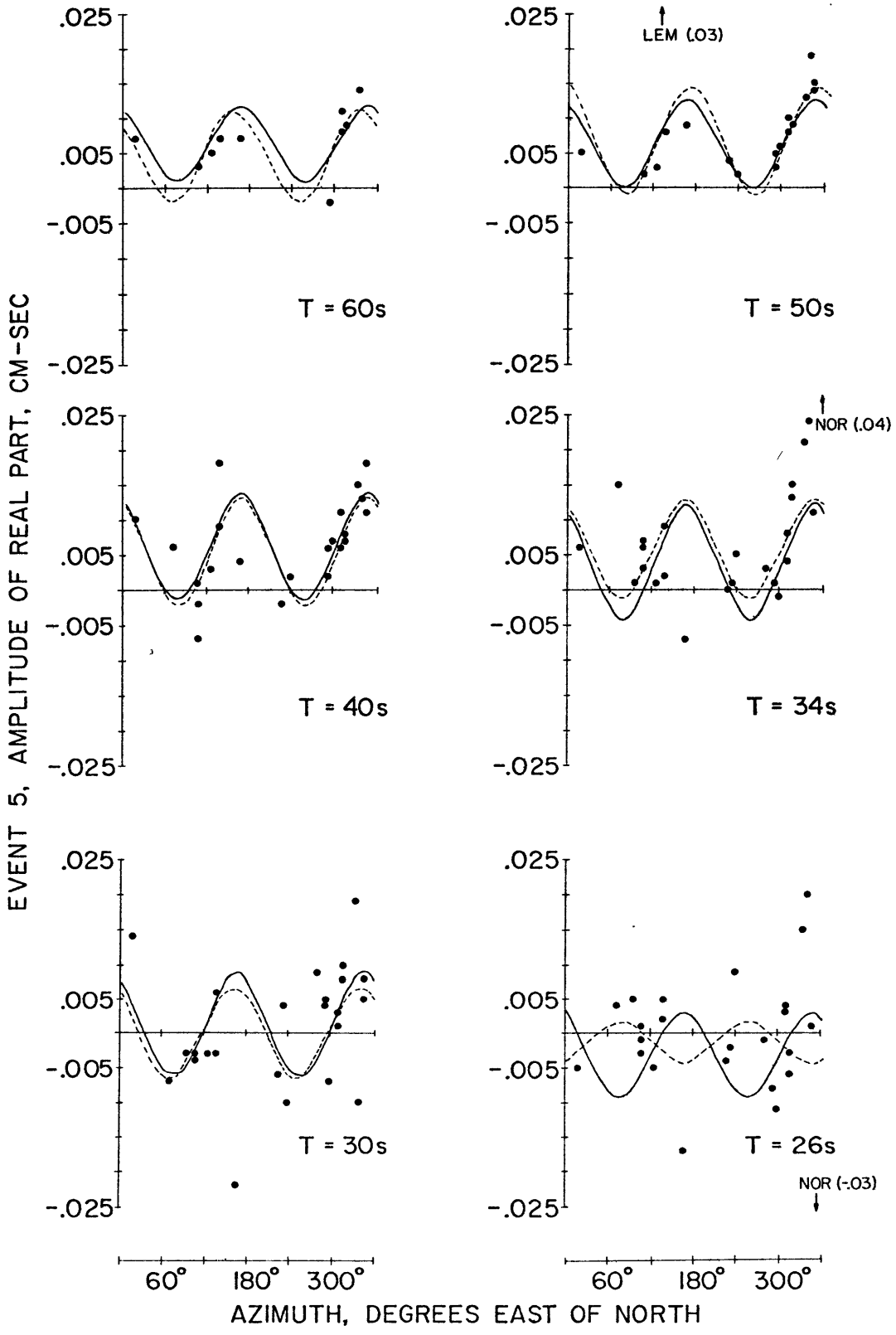
.025
.005
-.005
-.025
T = 60s
LEM (.03)
T = 50s
T = 40s
NOR (.04)
T = 34s
T = 30s
T = 26s
NOR (-.03)
60°
180°
300°
EVENT 5, AMPLITUDE OF REAL PART, CM-SEC
AZIMUTH, DEGREES EAST OF NORTH

FIGURE B-5a

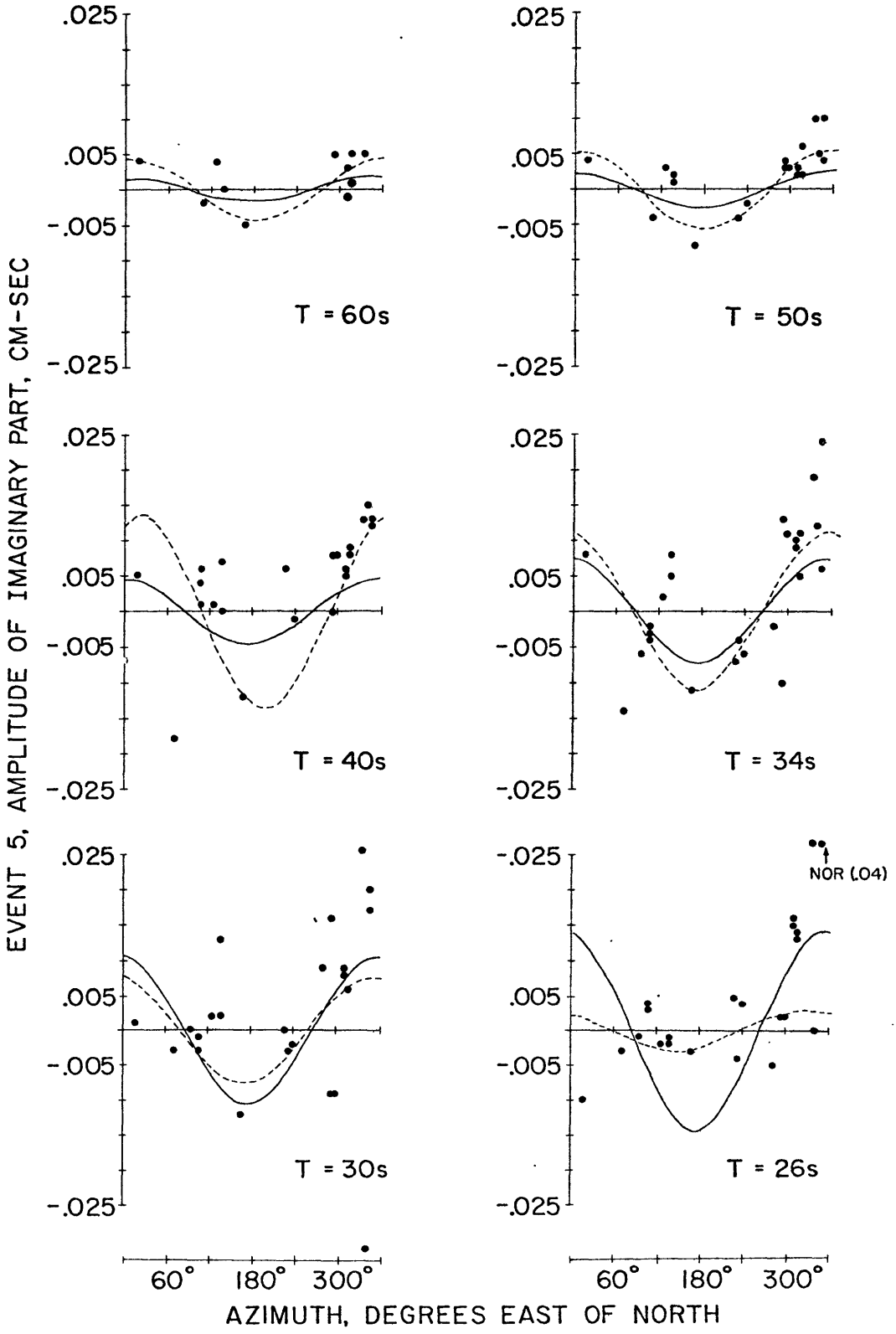
.025
.005
-.005
-.025
T = 60s
T = 50s
T = 40s
T = 34s
T = 30s
T = 26s
NOR (04)
EVENT 5, AMPLITUDE OF IMAGINARY PART, CM-SEC
60°
180°
300°
AZIMUTH, DEGREES EAST OF NORTH

FIGURE B-5b

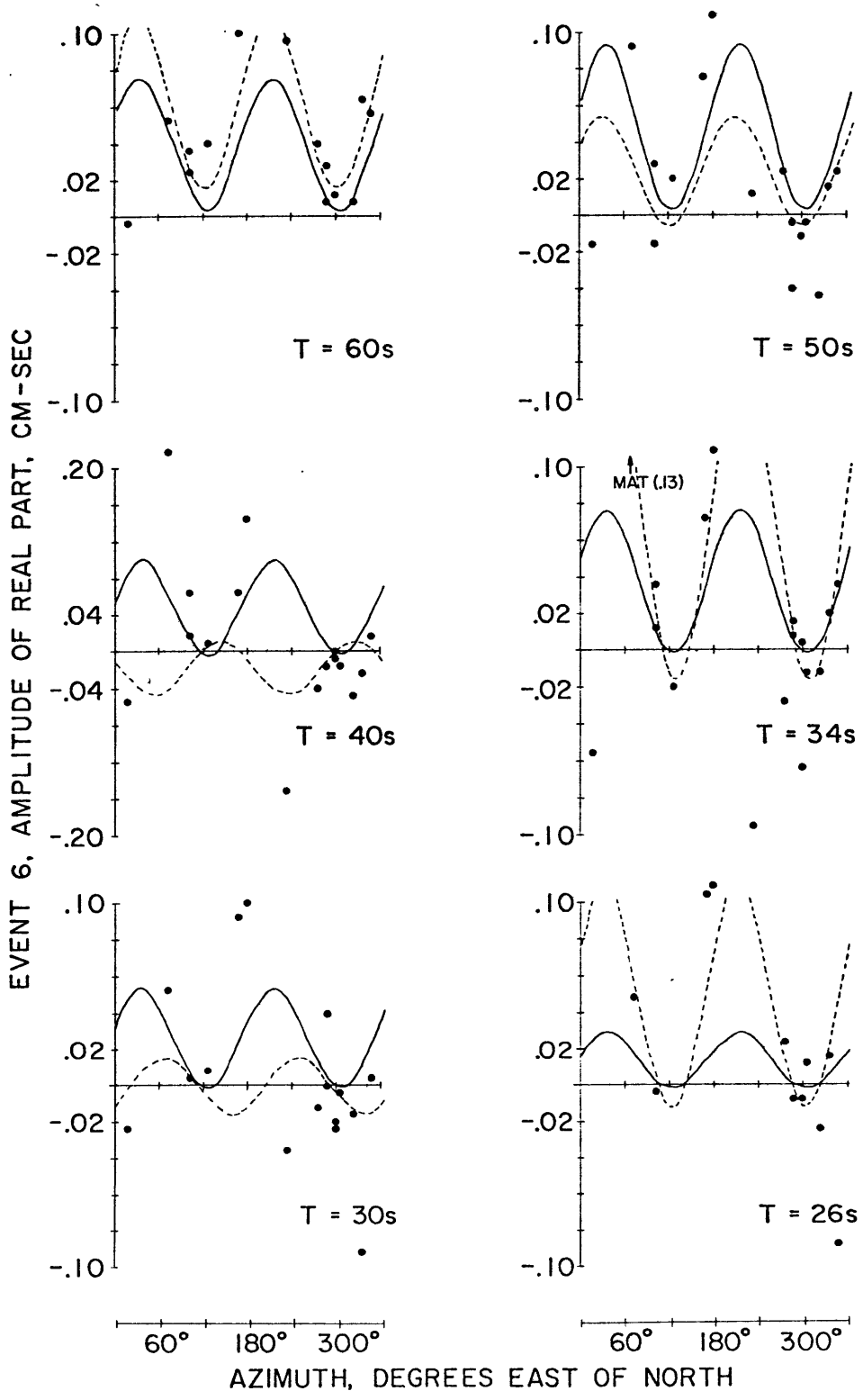
.10
.02
-.02
-.10
T = 60s
T = 50s
.20
.04
-.04
-.20
T = 40s
MAT (13)
T = 34s
T = 30s
T = 26s
EVENT 6, AMPLITUDE OF REAL PART, CM-SEC
60°
180°
300°
AZIMUTH, DEGREES EAST OF NORTH

FIGURE B-6a

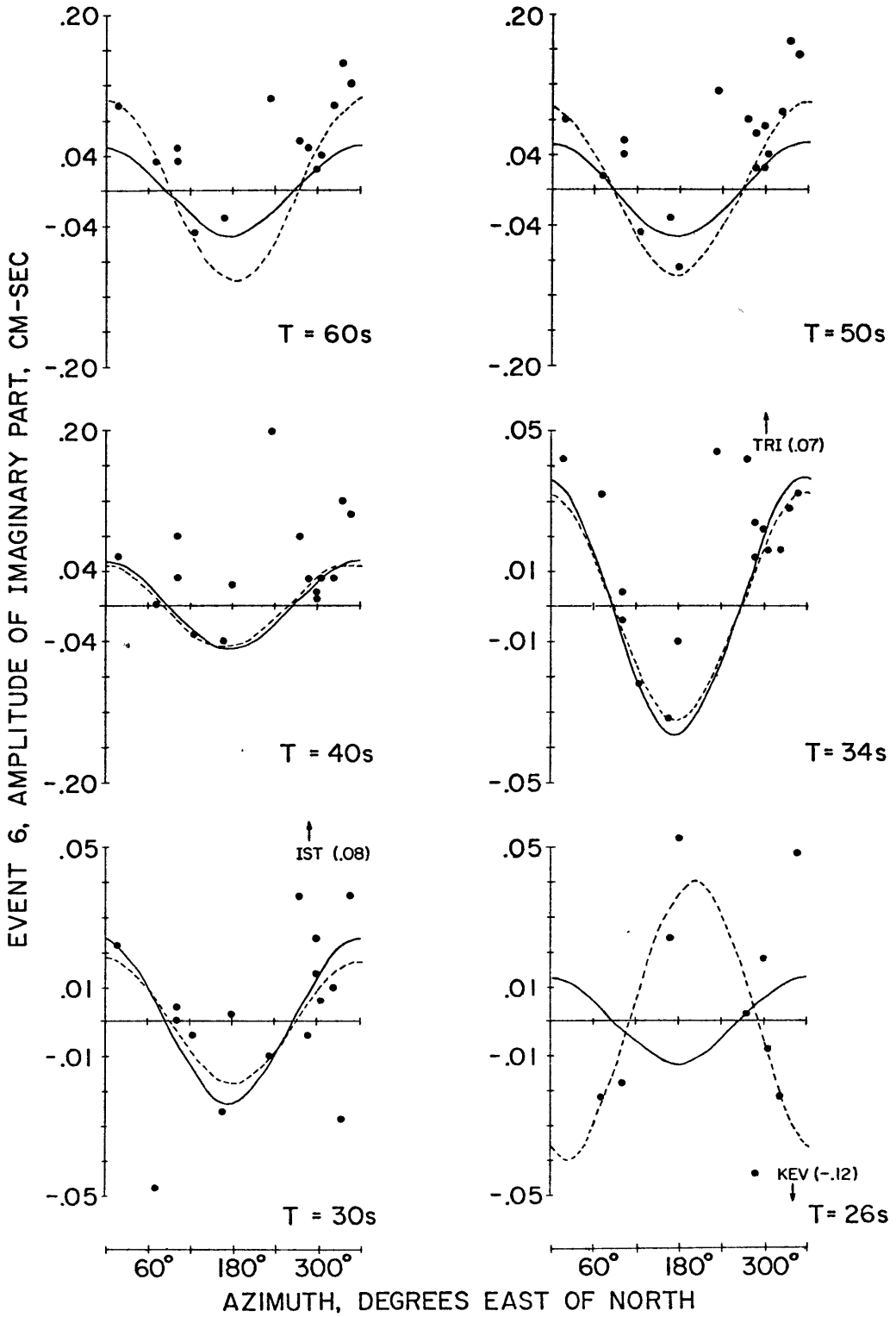
EVENT 6, AMPLITUDE OF IMAGINARY PART, CM-SEC
.20
.04
-.04
-.20
T = 60s
T = 50s
T = 40s
TRI (.07)
.05
.01
-.01
-.05
T = 34s
IST (.08)
T = 30s
KEV (-.12)
T = 26s
60°
180°
300°
AZIMUTH, DEGREES EAST OF NORTH

FIGURE B-6b

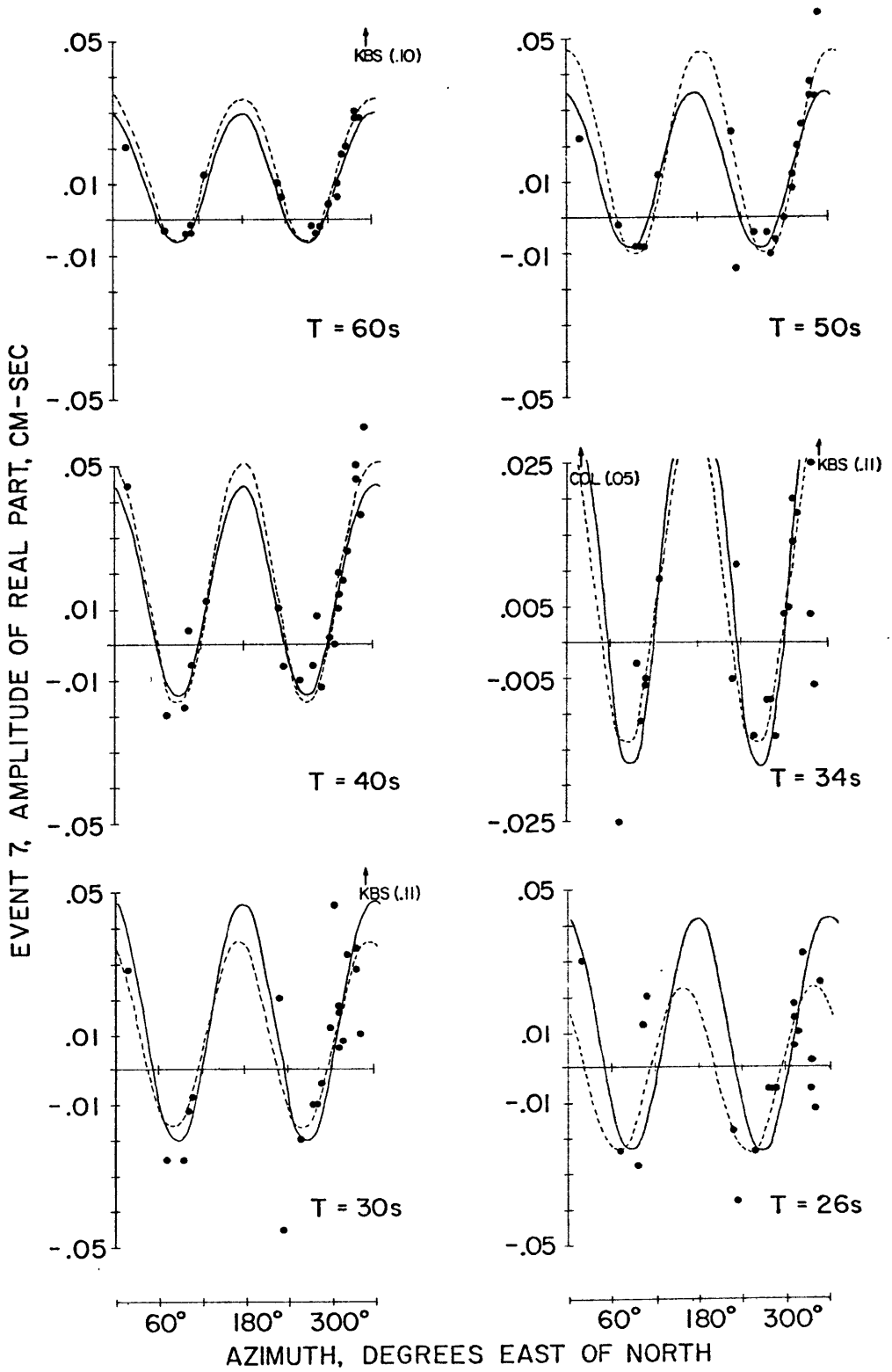
KBS (.10)
T = 60s
T = 50s
T = 40s
COL (05)
KBS (.11)
T = 34s
KBS (.11)
T = 30s
T = 26s
.05
.01
-.01
-.05
.025
.005
-.005
-.025
60°
180°
300°
EVENT 7, AMPLITUDE OF REAL PART, CM-SEC
AZIMUTH, DEGREES EAST OF NORTH

FIGURE B-7a

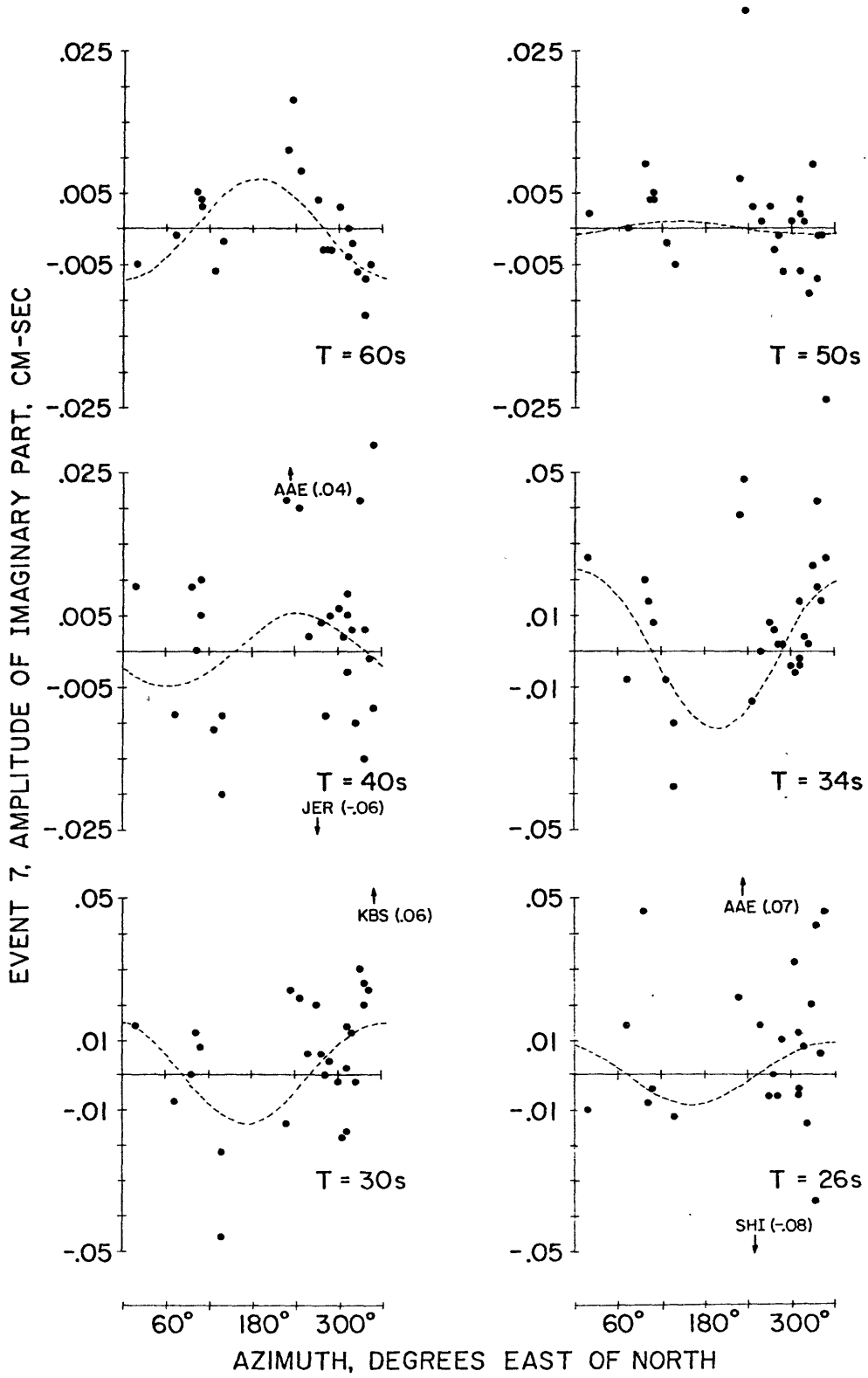
.025
.005
-.005
-.025
T = 60s
T = 50s
AAE (.04)
.05
.01
-.01
-.05
T = 40s
JER (-.06)
T = 34s
KBS (.06)
AAE (.07)
T = 30s
T = 26s
SHI (-.08)
60°
180°
300°
EVENT 7, AMPLITUDE OF IMAGINARY PART, CM-SEC
AZIMUTH, DEGREES EAST OF NORTH

FIGURE B-7b

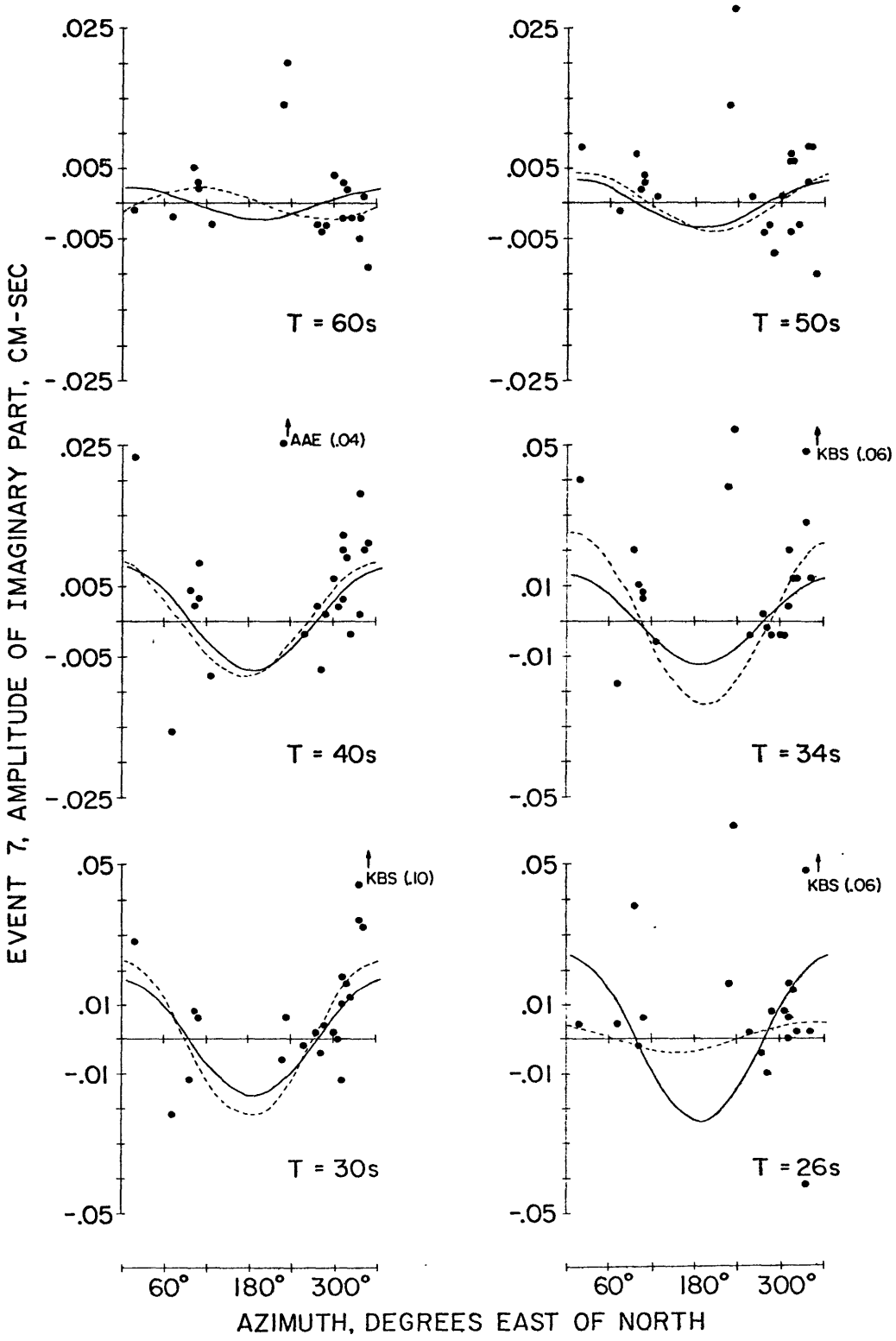
.025
.005
-.005
-.025
T = 60s
T = 50s
AAE (.04)
KBS (.06)
.05
.01
-.01
-.05
T = 40s
T = 34s
KBS (.10)
KBS (.06)
T = 30s
T = 26s
60°
180°
300°
EVENT 7, AMPLITUDE OF IMAGINARY PART, CM-SEC
AZIMUTH, DEGREES EAST OF NORTH

FIGURE B-7b'

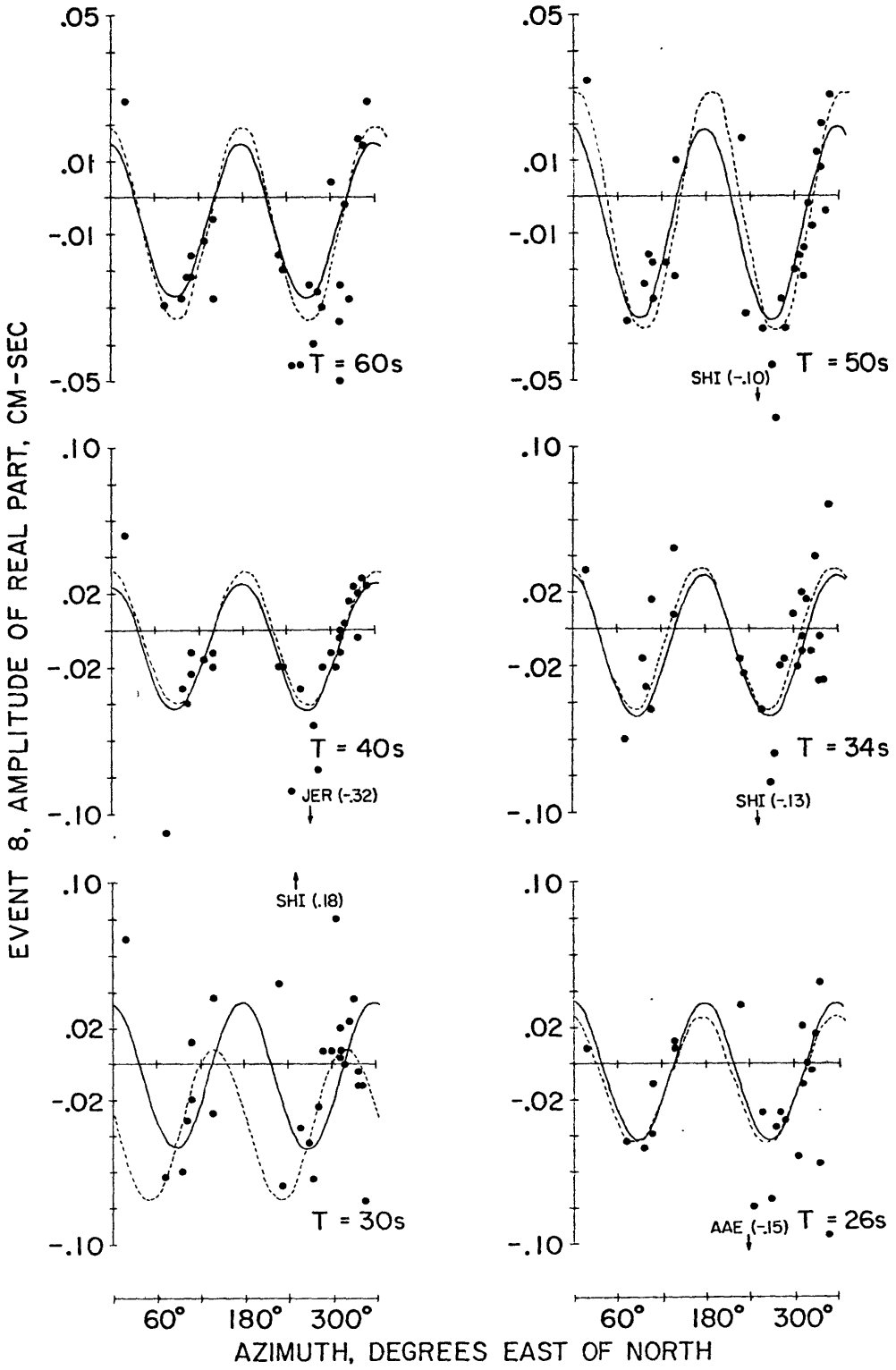
.05
.01
-.01
-.05
T = 60s
T = 50s
SHI (-.10)
.10
.02
-.02
-.10
T = 40s
JER (-.32)
T = 34s
SHI (-.13)
SHI (.18)
T = 30s
AAE (-.15)
T = 26s
60°
180°
300°
EVENT 8, AMPLITUDE OF REAL PART, CM-SEC
AZIMUTH, DEGREES EAST OF NORTH

FIGURE B-8a

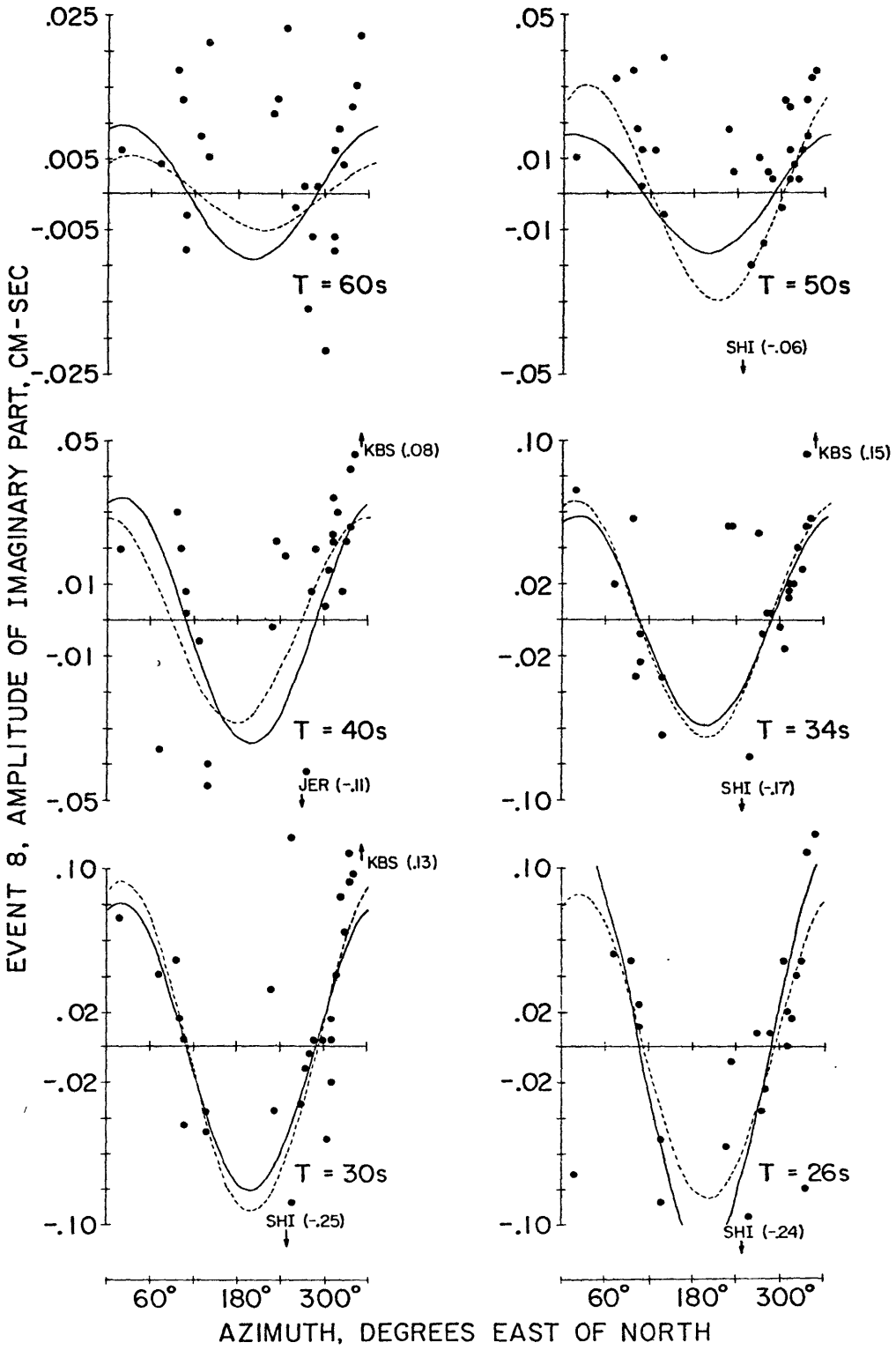
.025
.005
-.005
-.025
T = 60s
.05
.01
-.01
-.05
T = 50s
SHI (-.06)
.05
.01
-.01
-.05
KBS (.08)
T = 40s
JER (-.11)
.10
.02
-.02
-.10
KBS (.15)
T = 34s
SHI (-.17)
.10
.02
-.02
-.10
KBS (.13)
T = 30s
SHI (-.25)
.10
.02
-.02
-.10
T = 26s
SHI (-.24)
60°
180°
300°
AZIMUTH, DEGREES EAST OF NORTH
EVENT 8, AMPLITUDE OF IMAGINARY PART, CM-SEC

FIGURE B-8b

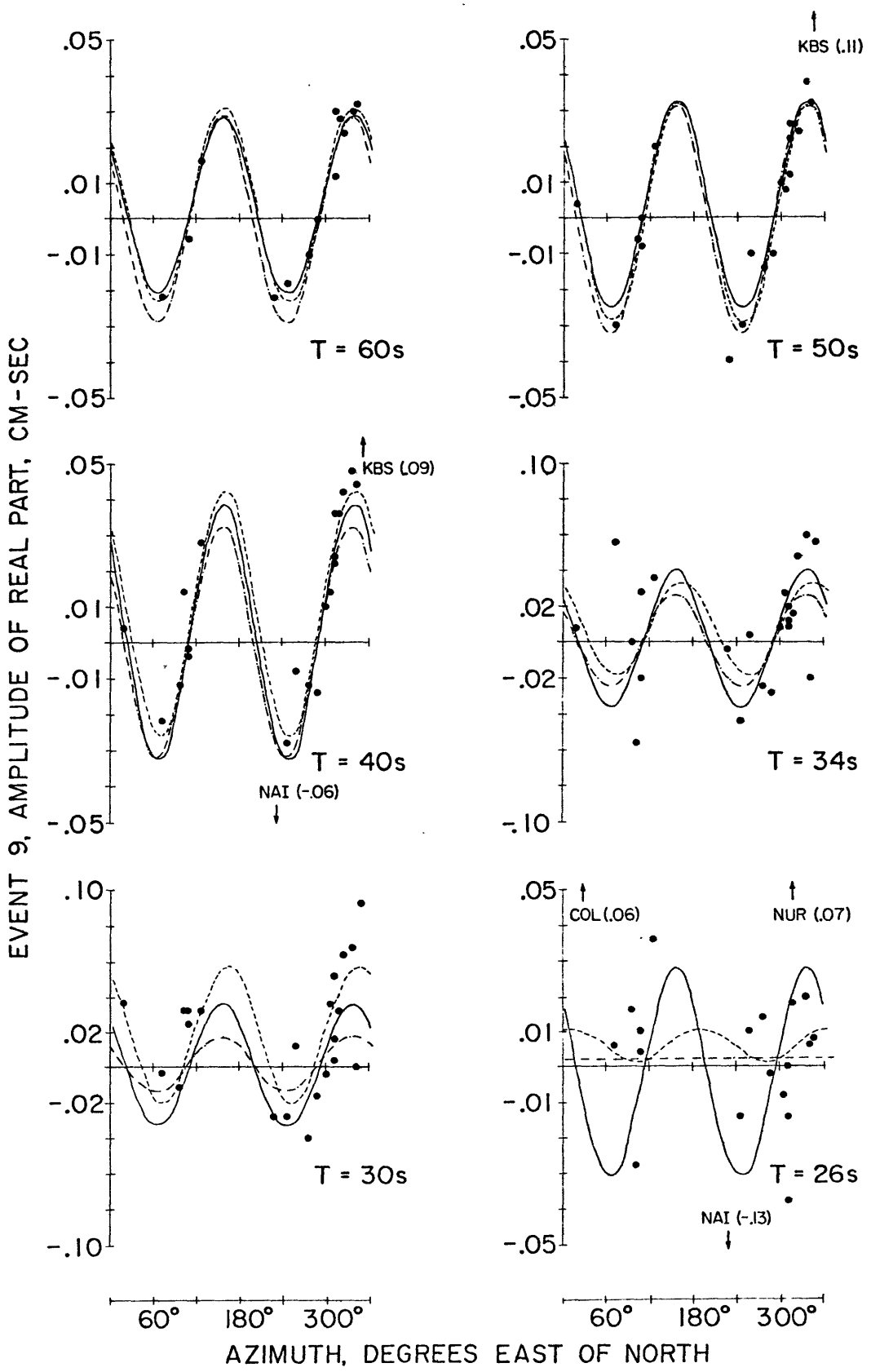
EVENT 9, AMPLITUDE OF REAL PART, CM-SEC
.05
.01
-.01
-.05
T = 60s
KBS (.11)
T = 50s
KBS (.09)
T = 40s
NAI (-.06)
.10
.02
-.02
-.10
T = 34s
COL (.06)
NUR (.07)
T = 30s
T = 26s
NAI (-.13)
60°
180°
300°
AZIMUTH, DEGREES EAST OF NORTH

FIGURE B-9a

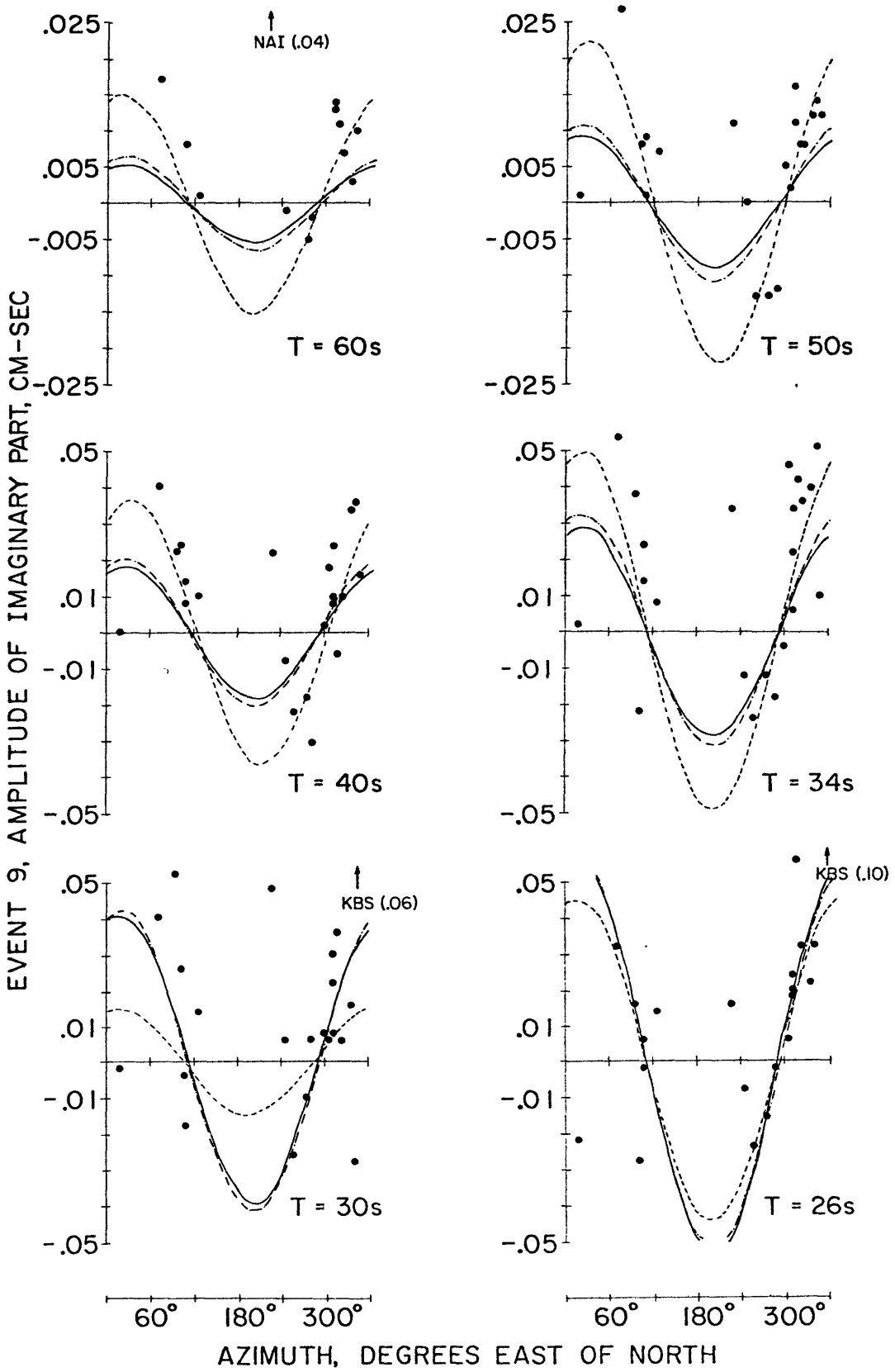
NAI (.04)
T = 60s
T = 50s
T = 40s
T = 34s
KBS (.06)
KBS (.10)
T = 30s
T = 26s
.025
.005
-.005
-.025
.05
.01
-.01
-.05
60°
180°
300°
EVENT 9, AMPLITUDE OF IMAGINARY PART, CM-SEC
AZIMUTH, DEGREES EAST OF NORTH

FIGURE B-9b

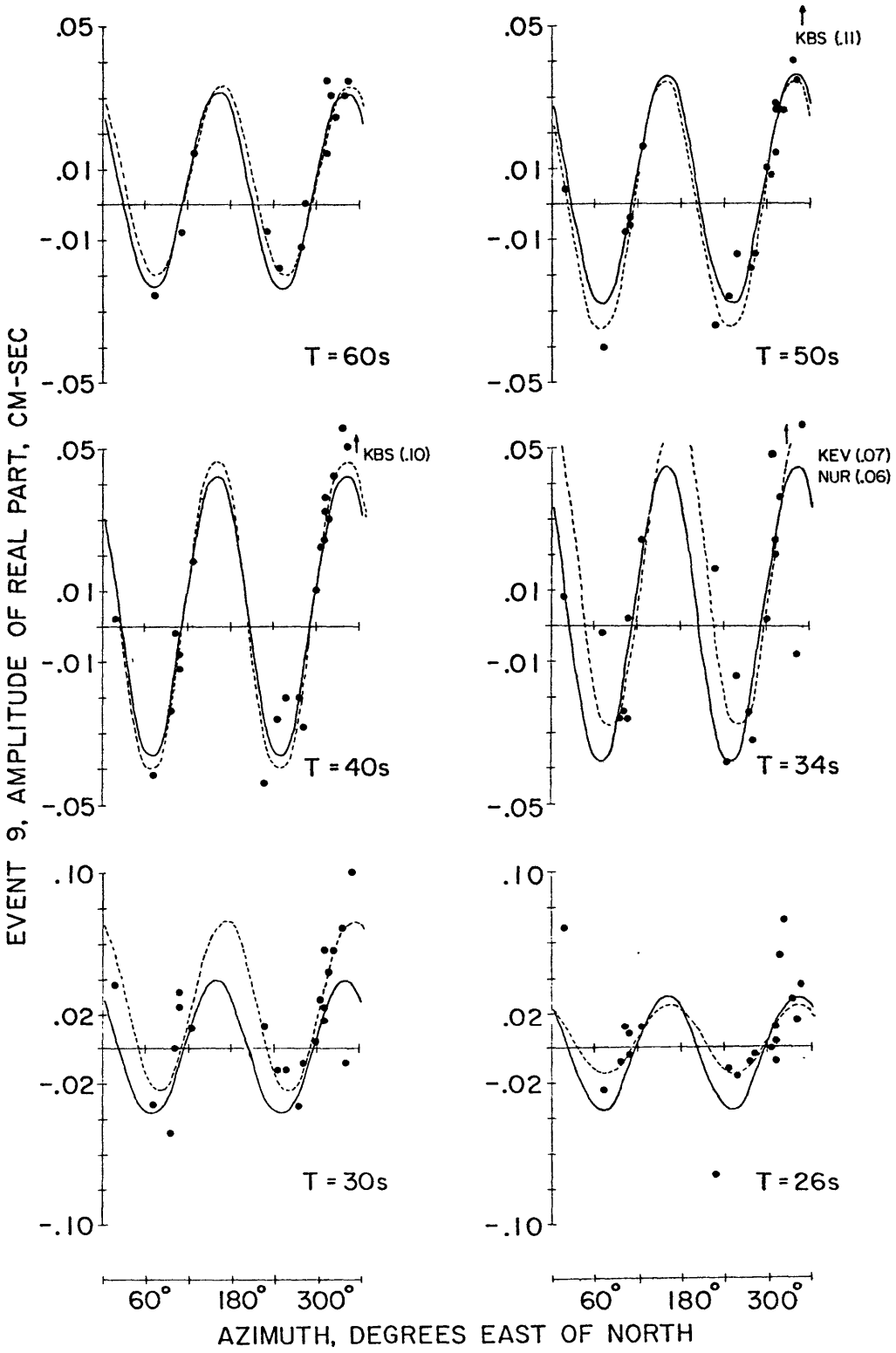
EVENT 9, AMPLITUDE OF REAL PART, CM-SEC
.05
.01
-.01
-.05
T = 60s
KBS (.11)
T = 50s
KBS (.10)
T = 40s
KEV (.07)
NUR (.06)
T = 34s
.10
.02
-.02
-.10
T = 30s
T = 26s
60°
180°
300°
AZIMUTH, DEGREES EAST OF NORTH

FIGURE B-9a'

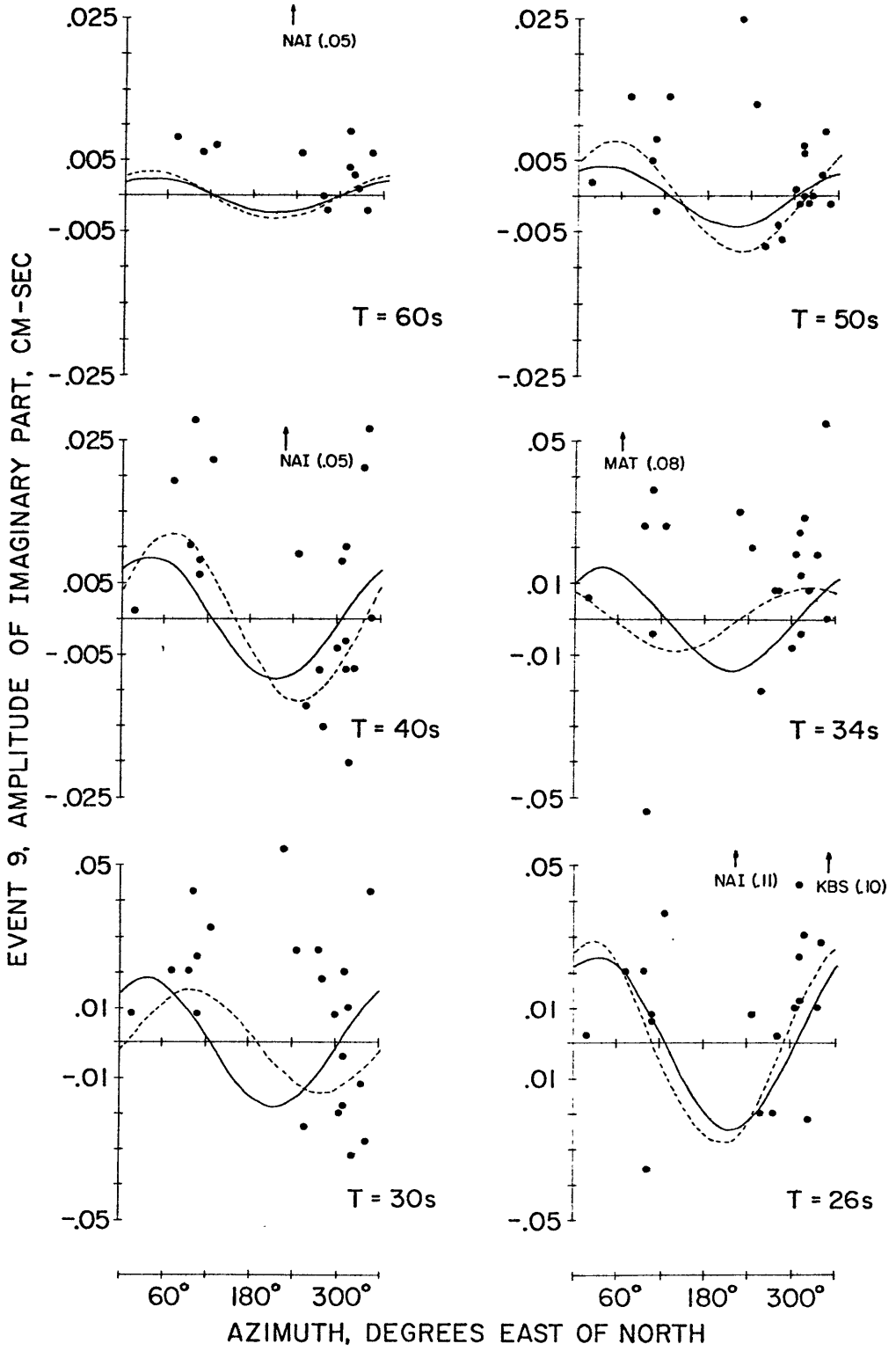
.025
.005
-.005
-.025
NAI (.05)
T = 60s
T = 50s
NAI (.05)
T = 40s
.05
.01
-.01
-.05
MAT (.08)
T = 34s
NAI (.11)
KBS (.10)
T = 30s
T = 26s
60°
180°
300°
EVENT 9, AMPLITUDE OF IMAGINARY PART, CM-SEC
AZIMUTH, DEGREES EAST OF NORTH

FIGURE B-9b'

APPENDIX C

APPARENT PHASE VELOCITIES AND ATTENUATION COEFFICIENTS

Phase velocities are computed by Equation 4-3.1. Phase velocity curves are grouped in Figures C-1 through C-8 according to the geographic location of the stations. Attenuation coefficients are computed using Equation 4-3.2 based on the results of calculating H_{ik} two ways. The attenuation based on MLE is shown in Figures C-9 through C-15 as open circles connected with solid or dashed lines. A dashed line is used when the standard error in the calculation of $\hat{\phi}_{ik}$ (Equation 2-5.19) exceeds $\pi/2$ radians. For smaller phase errors, a solid line is used. The attenuation based on LAV (i.e., log averaging) is shown by solid dots. Error bars represent one standard deviation in the calculation of attenuation based on the LAV result (Equation 2-5.19). Station groups follow the discussion given in Section 4-3.

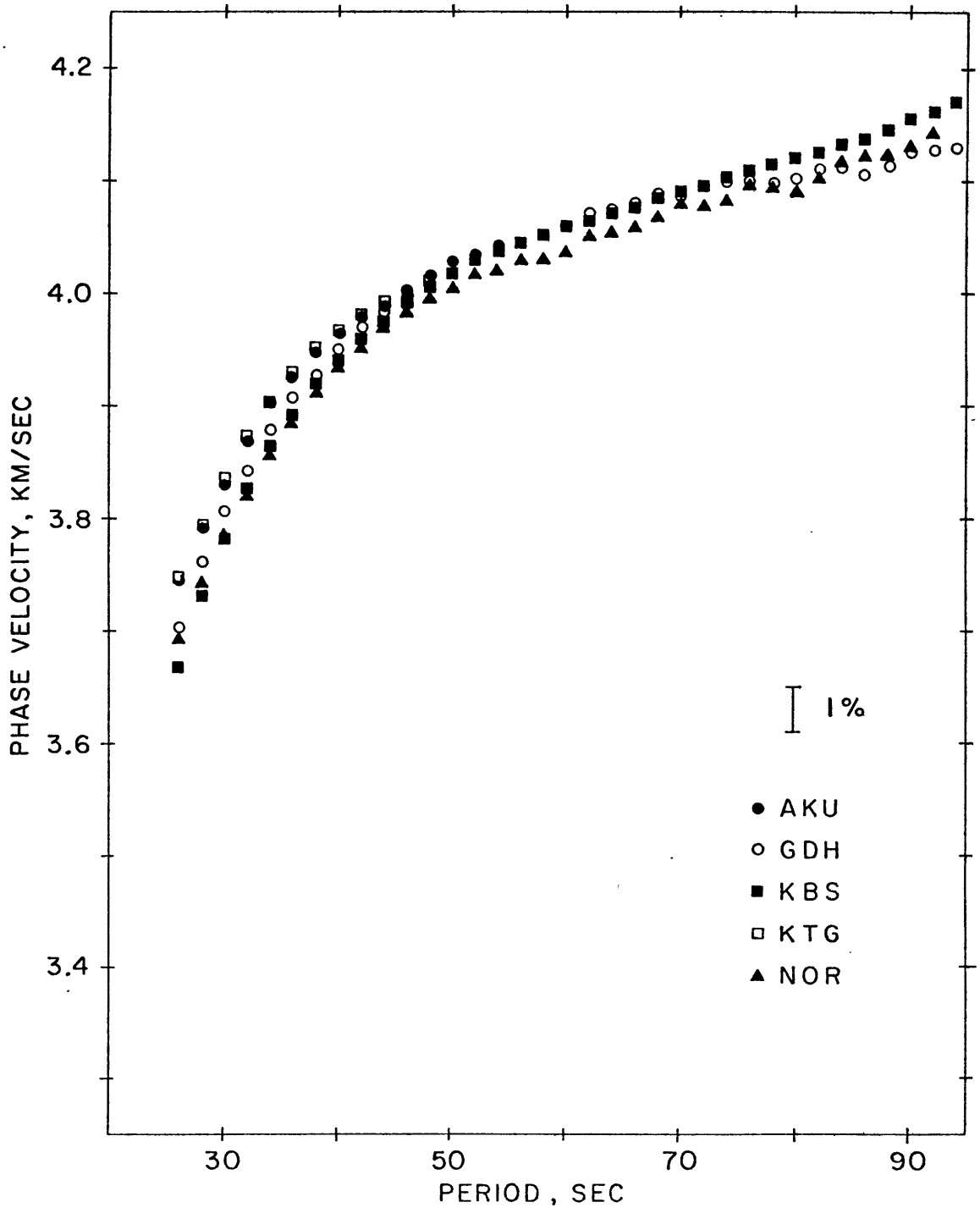
4.2
4.0
3.8
3.6
3.4
PHASE VELOCITY, KM/SEC
30
50
70
90
PERIOD, SEC
1%
AKU
GDH
KBS
KTG
NOR

FIGURE C-1

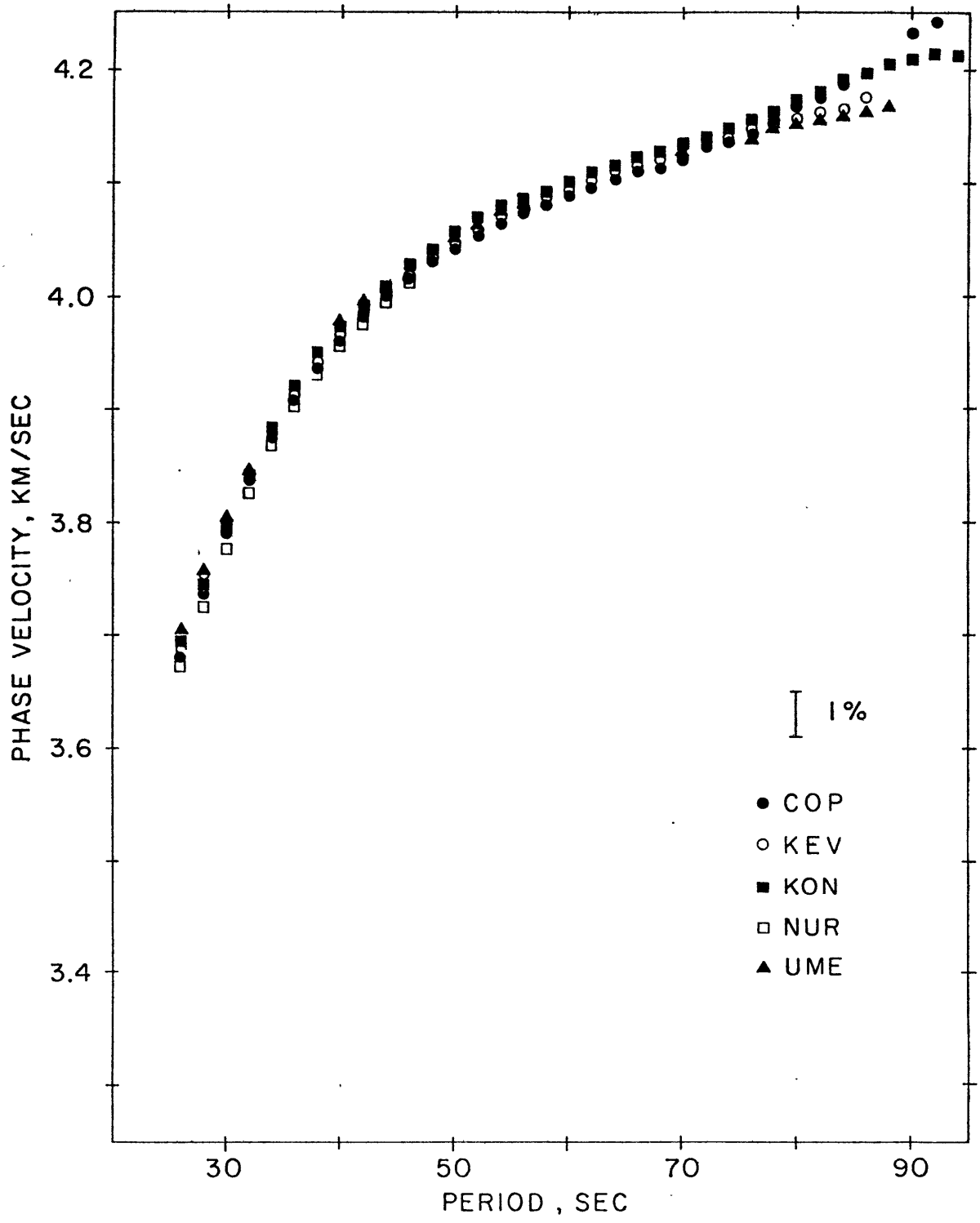
4.2
4.0
3.8
3.6
3.4
PHASE VELOCITY, KM/SEC
30
50
70
90
PERIOD , SEC
1%
COP
KEV
KON
NUR
UME

FIGURE C-2

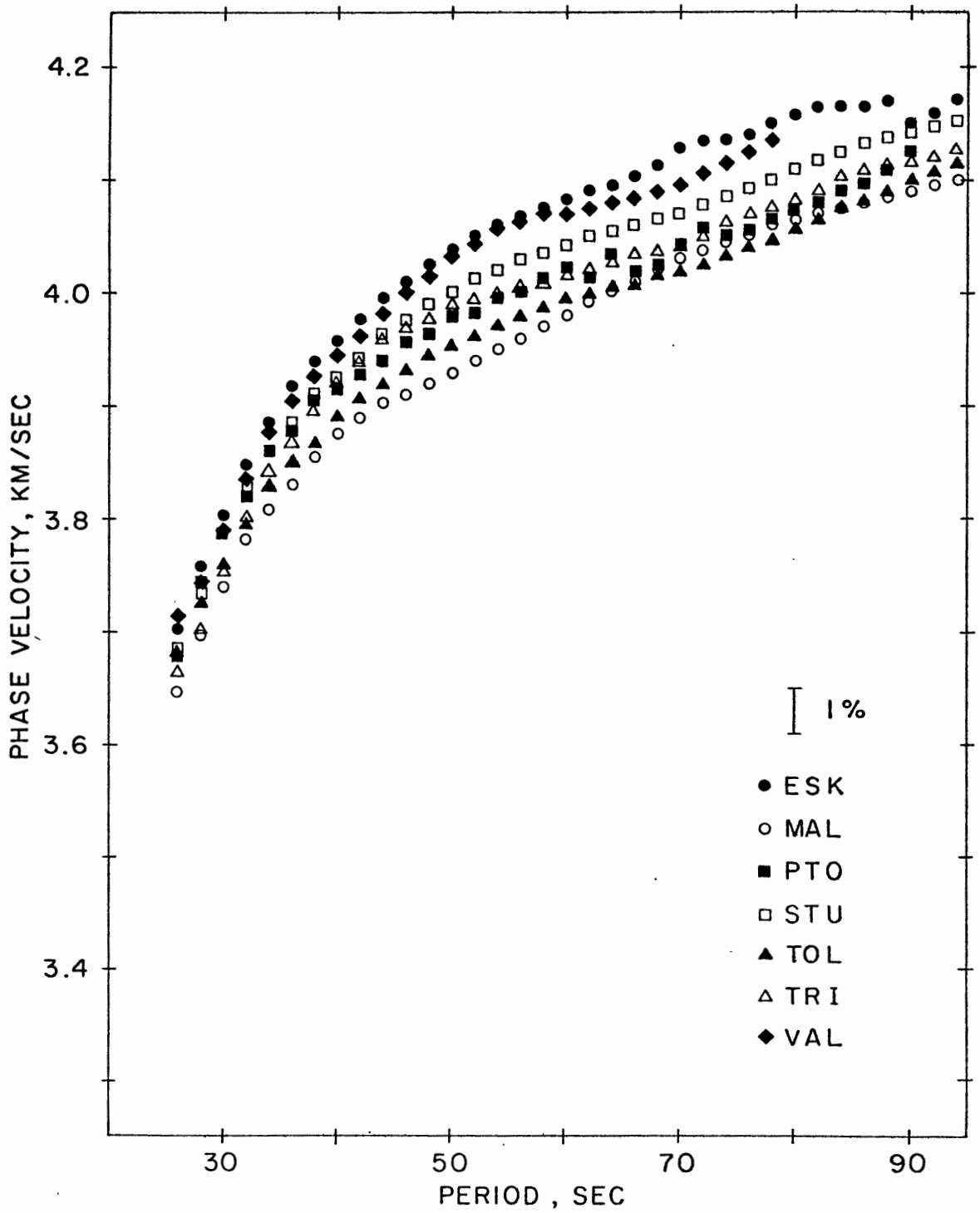
4.2
4.0
3.8
3.6
3.4
PHASE VELOCITY, KM/SEC
30
50
70
90
PERIOD , SEC
1%
ESK
MAL
PTO
STU
TOL
TRI
VAL

FIGURE C-3

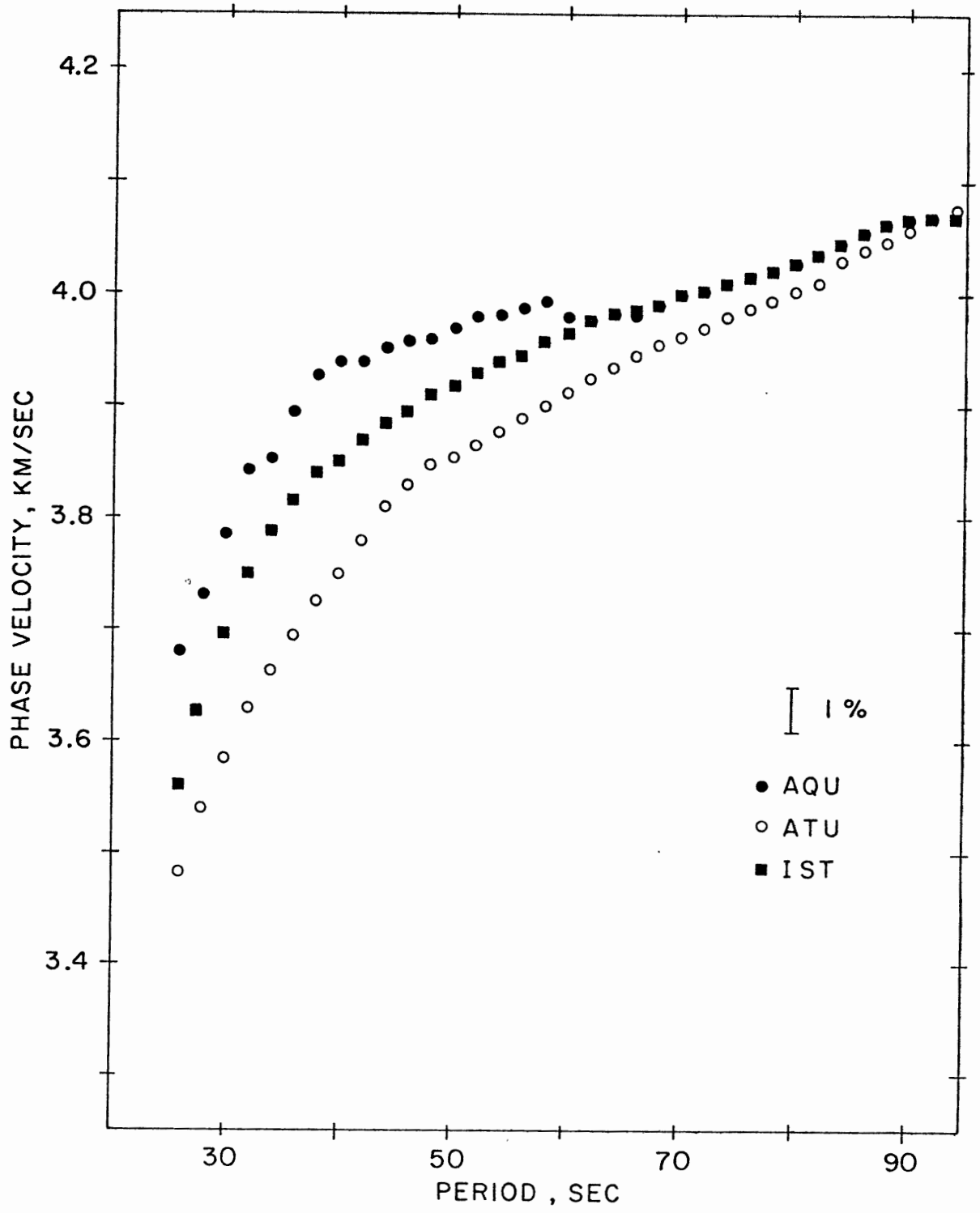
4.2
4.0
3.8
3.6
3.4
PHASE VELOCITY, KM/SEC
30
50
70
90
PERIOD, SEC
1 %
AQU
ATU
IST

FIGURE C-4

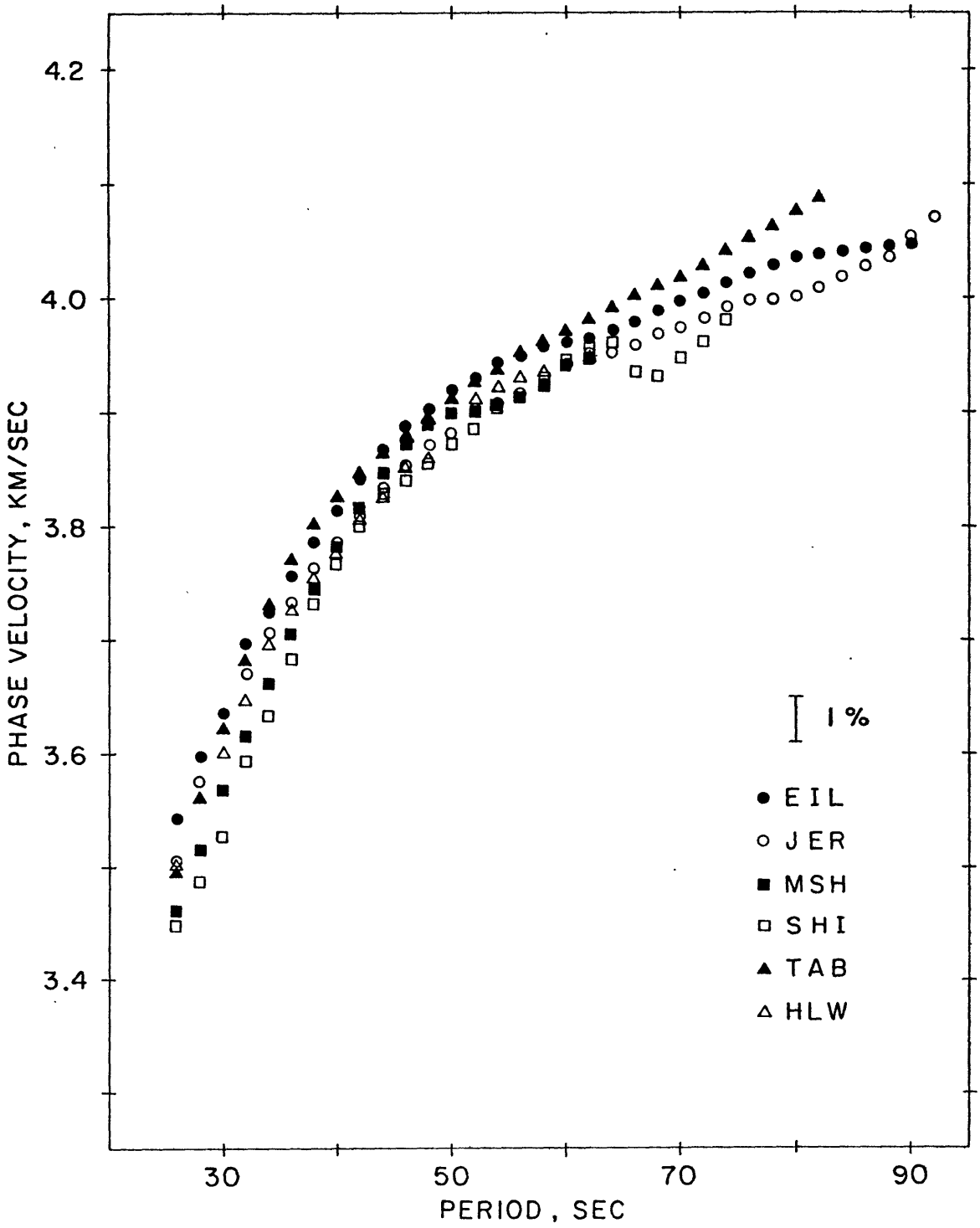
4.2
4.0
3.8
3.6
3.4
PHASE VELOCITY, KM/SEC
30
50
70
90
PERIOD, SEC
1 %
EIL
JER
MSH
SHI
TAB
HLW

FIGURE C-5

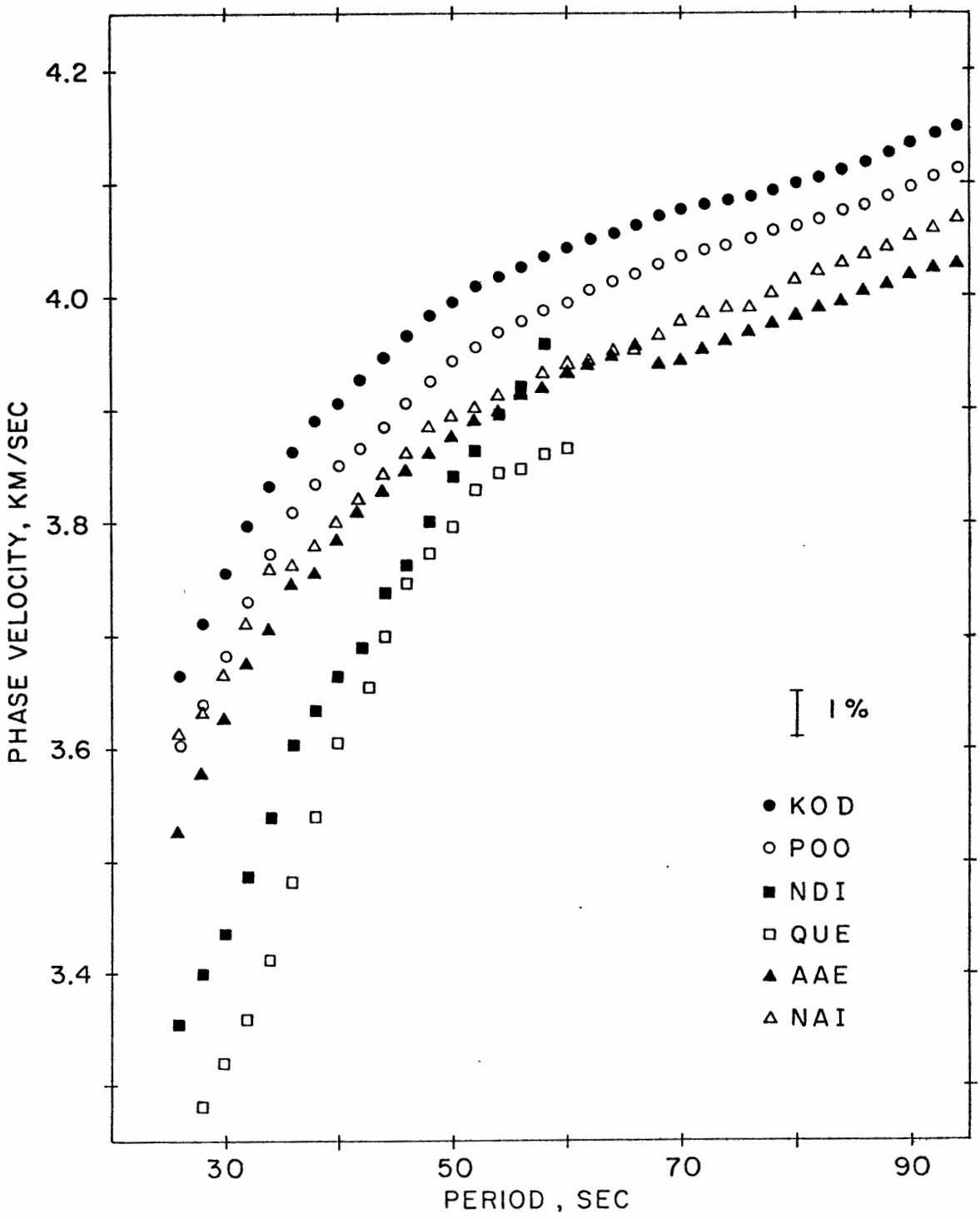
4.2
4.0
3.8
3.6
3.4
PHASE VELOCITY, KM/SEC
30
50
70
90
PERIOD , SEC
1%
KOD
POO
NDI
QUE
AAE
NAI

FIGURE C-6

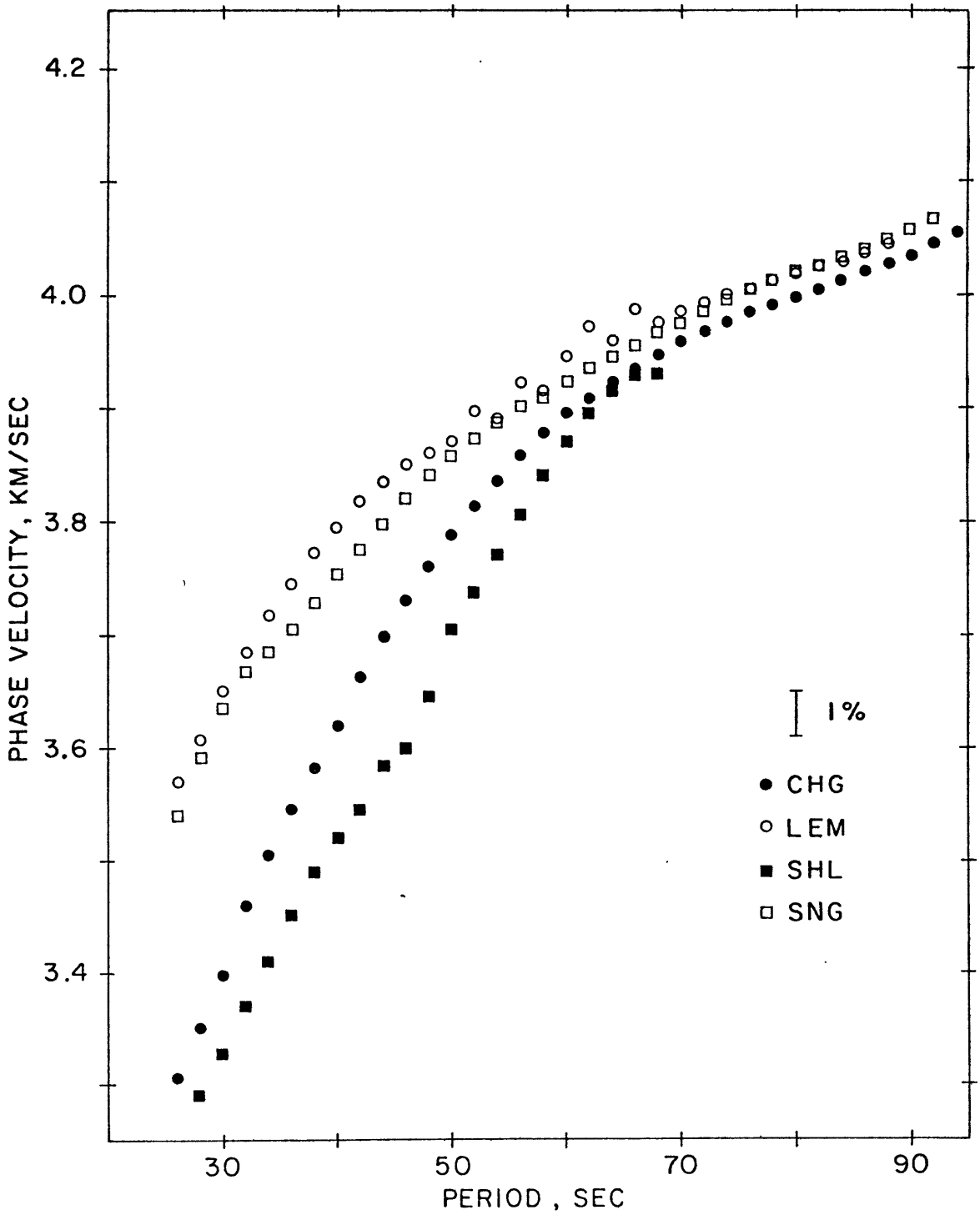
4.2
4.0
3.8
3.6
3.4
PHASE VELOCITY, KM/SEC
30
50
70
90
PERIOD, SEC
1%
CHG
LEM
SHL
SNG

FIGURE C-7

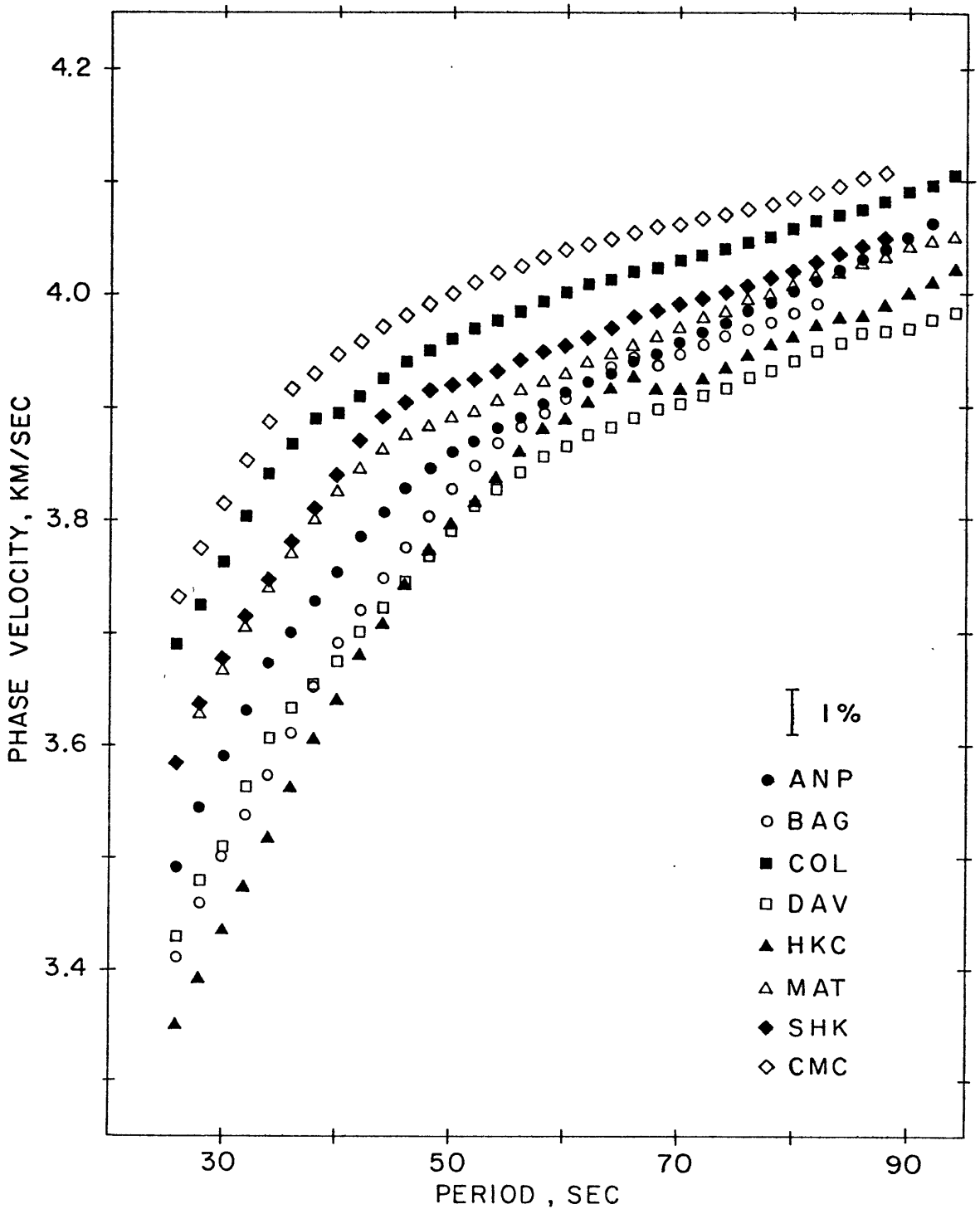
4.2
4.0
3.8
3.6
3.4
PHASE VELOCITY, KM/SEC
30
50
70
90
PERIOD, SEC
1%
ANP
BAG
COL
DAV
HKC
MAT
SHK
CMC

FIGURE C-8

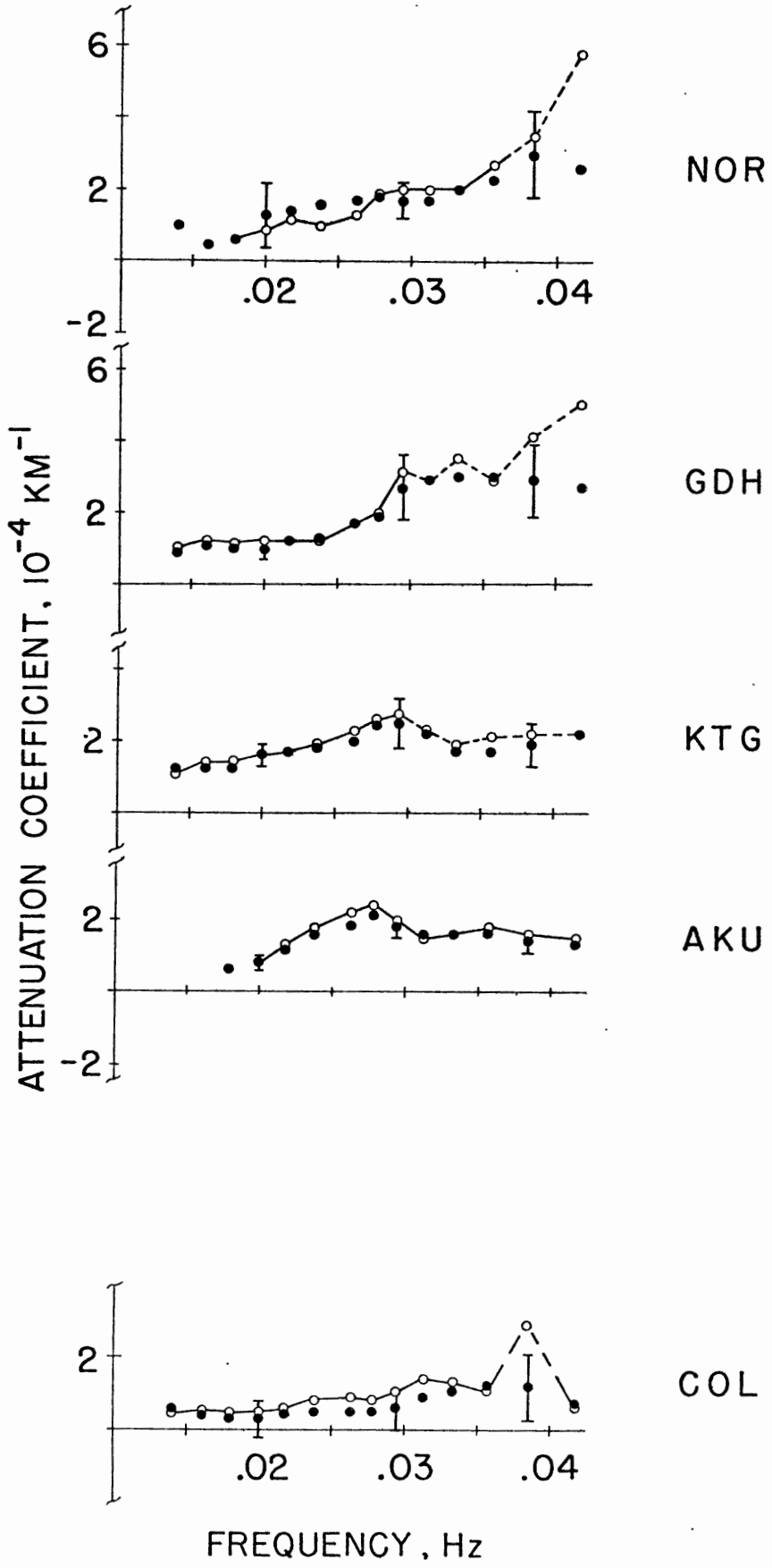
6
2
-2
.02
.03
.04
NOR
6
2
GDH
2
KTG
2
-2
AKU
ATTENUATION COEFFICIENT, 10^{-4} KM^{-1}
2
.02
.03
.04
COL
FREQUENCY, Hz

FIGURE C-9

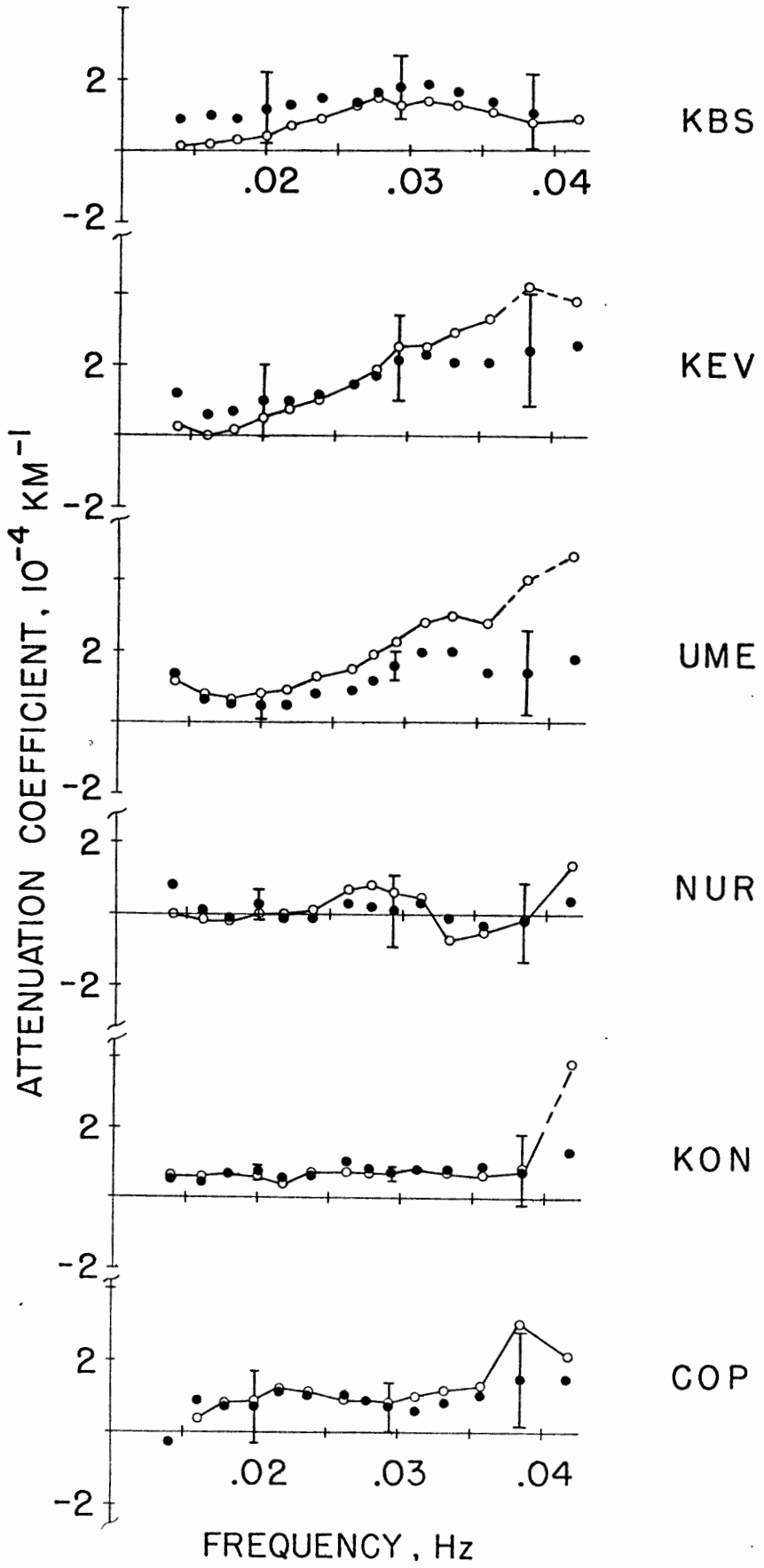
KBS
KEV
UME
NUR
KON
COP
2
-2
.02
.03
.04
ATTENUATION COEFFICIENT, 10^{-4} KM^{-1}
FREQUENCY, Hz

FIGURE C-10

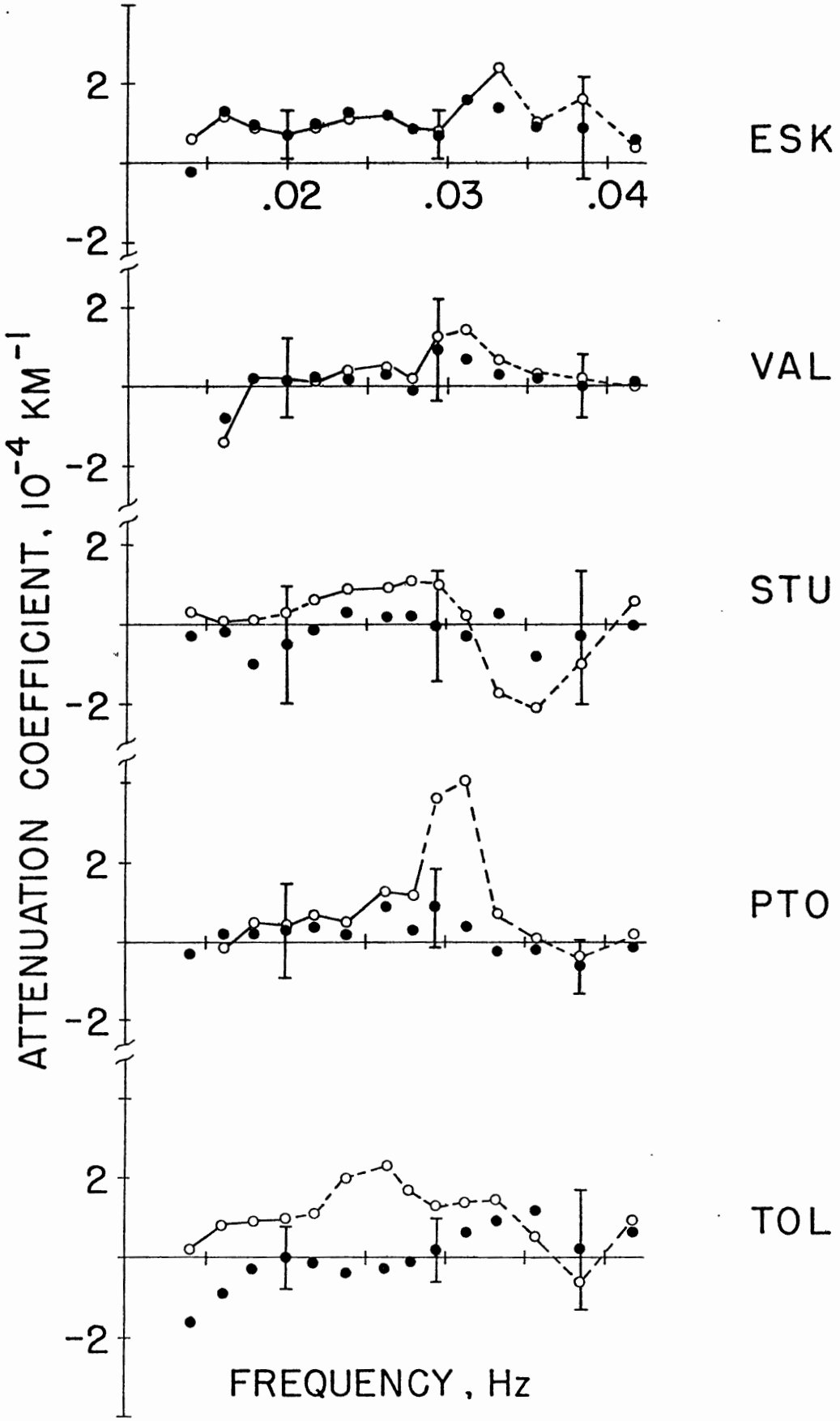
ESK
VAL
STU
PTO
TOL
2
-2
.02
.03
.04
ATTENUATION COEFFICIENT, 10^{-4} KM^{-1}
FREQUENCY, Hz

FIGURE C-11

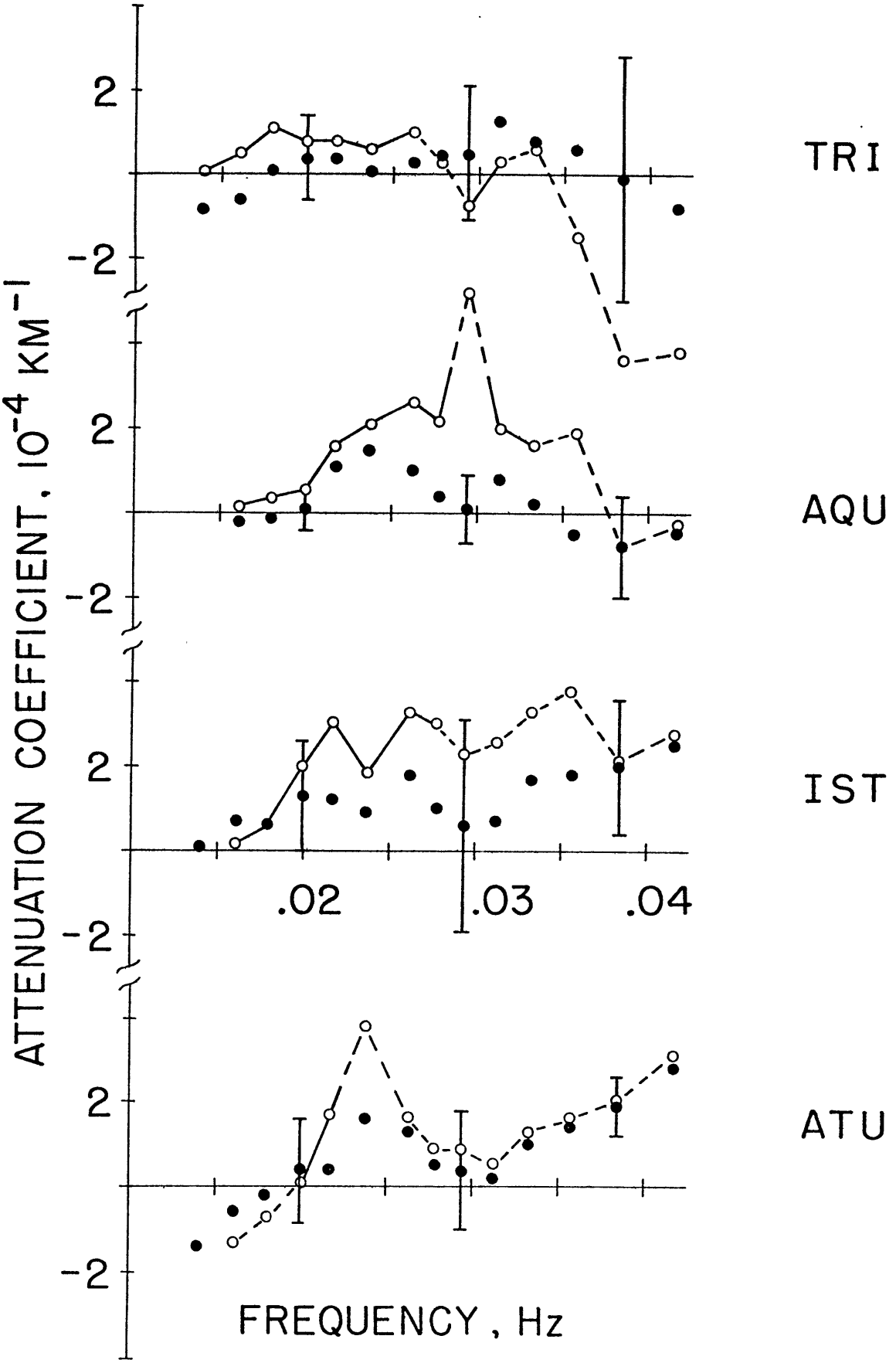
ATTENUATION COEFFICIENT, 10^{-4} KM^{-1}
2
-2
TRI
AQU
IST
ATU
.02
.03
.04
FREQUENCY, Hz

FIGURE C-12

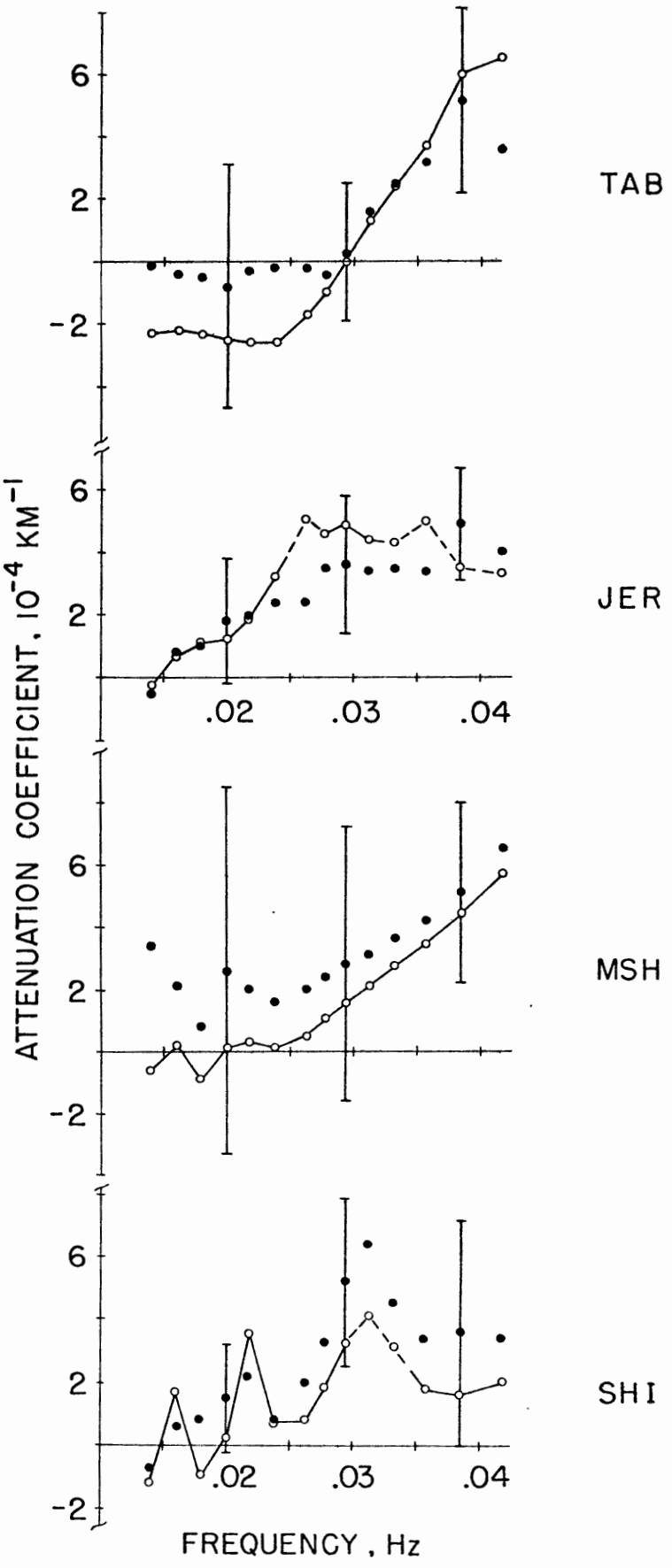
ATTENUATION COEFFICIENT, 10^{-4} KM^{-1}
6
2
-2
TAB
JER
MSH
SHI
.02
.03
.04
FREQUENCY, Hz

FIGURE C-13

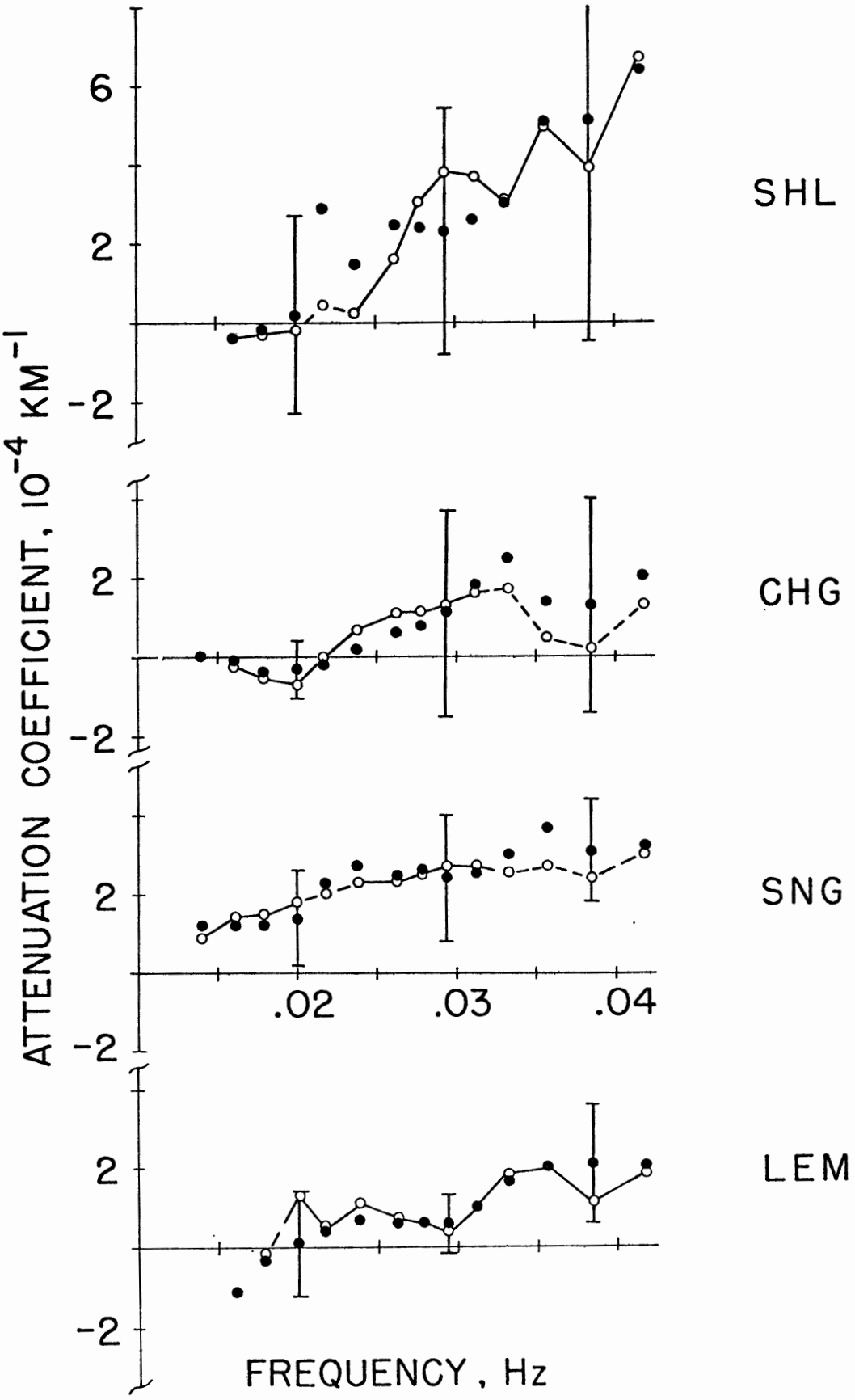
ATTENUATION COEFFICIENT, 10^{-4} KM^{-1}
6
2
-2
SHL
2
-2
CHG
2
-2
SNG
.02
.03
.04
2
-2
LEM
FREQUENCY, Hz

FIGURE C-14

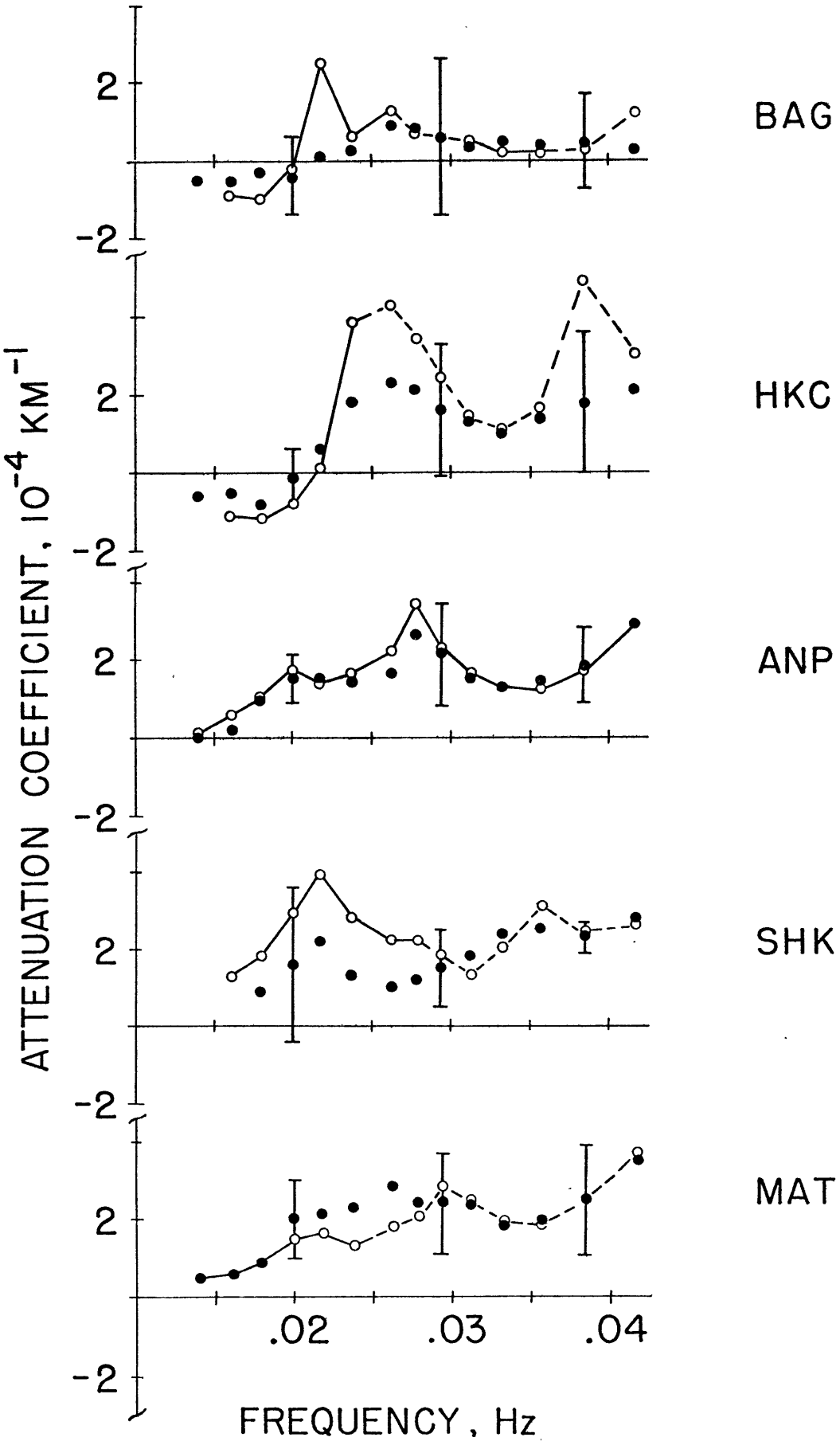
BAG
HKC
ANP
SHK
MAT
2
-2
.02
.03
.04
ATTENUATION COEFFICIENT, 10^{-4} KM^{-1}
FREQUENCY, Hz

FIGURE C-15